2023-05-01

Isotopic Insights Into Water Of Condensation, Cross-Formation Water Flow, And Natural Hydrocarbon Migration In Sedimentary Basins

Lisa J. Molofsky

University of Texas at El Paso

Recommended Citation

Molofsky, Lisa J., "Isotopic Insights Into Water Of Condensation, Cross-Formation Water Flow, And Natural Hydrocarbon Migration In Sedimentary Basins" (2023). *Open Access Theses & Dissertations*. 3827.
https://scholarworks.utep.edu/open_etd/3827

ISOTOPIC INSIGHTS INTO WATER OF CONDENSATION, CROSS-FORMATION WATER FLOW, AND NATURAL HYDROCARBON MIGRATION IN SEDIMENTARY BASINS

LISA J. MOLOFSKY

Doctoral Program in Geological Sciences

APPROVED:

Mark A. Engle, Ph.D., Chair

Lin Ma, Ph.D.

Katherine Giles, Ph.D.

Wen-Yee Lee, Ph.D.

Stephen L. Crites, Jr., Ph.D.
Dean of the Graduate School

Dedication

This thesis is dedicated to my amazing mother, Dorothy, whose affection and support have been unwavering all these years. You show us the way!

ISOTOPIC INSIGHTS INTO WATER OF CONDENSATION, CROSS-FORMATION WATER FLOW, AND NATURAL HYDROCARBON MIGRATION IN SEDIMENTARY BASINS

by

LISA J. MOLOFSKY, M.S.

DISSERTATION

Presented to the Faculty of the Graduate School of
The University of Texas at El Paso
in Partial Fulfillment
of the Requirements
for the Degree of

DOCTOR OF PHILOSOPHY

Department of Geological Sciences
THE UNIVERSITY OF TEXAS AT EL PASO
May 2023

Acknowledgements

I'd like to express my great thanks to my advisor, Dr. Mark Engle, for his expert guidance and good humor. It was early conversations with Mark that prompted me to pursue this PhD, and now, many, many excellent conversations later, I remain grateful for my good luck. I also want to thank my mom and dad who have lovingly supported me, and my children, with their time, energy, and sustenance throughout this project. Special appreciation goes to my brother, Adam, who sacrificed a week's vacation to assist me in sampling natural gas seeps; to my brother and sister-in-law Ari and Anna, who housed me through the birth of my twins in San Francisco; and to Sofia, whose care for the twins has made a huge difference. To Sarah, whose friendship buoys me up: thank you! Most importantly, thanks to my children and to my husband, Jared, who have all been patient on weekends and evenings as I worked toward the completion of this PhD – I love you very much.

I'd also like to acknowledge my committee members, Lin Ma, Katherine Giles, and Wen-Yee Lee, as well as Benjamin Brunner at the University of Texas at El Paso, Diego Fernandez at the University of Utah, and each of my colleagues who worked with me on this research. The time they spent engaging in scientific discussions, analyzing data, and reviewing my writing is greatly appreciated. My colleagues include, first and foremost, Buddy Wylie and Tom Wagner of Coterra Energy Inc., who I have known for more than a decade, and consider savvy scientists and friends; and Eric Daniels and Daniel Segal of Chevron Technical Center, whose expertise have been instrumental in my exploration of brine and gas chemistry. In addition, my evaluation of natural gas seepage geochemistry was greatly improved by discussions with Giuseppe Etiope, at the Istituto Naxionale di Geofisica e Vulcanologia.

A special thanks goes to my first big boss and mentor John Connor at GSI for his encouragement to pursue this PhD, and all of the thought-provoking and entertaining discussions about my latest discoveries. I also thank Mark Hemingway at GSI for lending me his golden ear for language, or rather, his silver tongue. His instruction has significantly improved my writing and sharpened my wit. To April Villagomez at GSI, my sincere appreciation for your tutelage in ArcGIS!

Last but not least, I would like to acknowledge Coterra Energy and other energy companies who provided funding and data for the work presented in this dissertation. Access to sampling locations and assistance with sampling was also generously provided by Carbon Energy Corporation (Vaughn Thompson), Humboldt Redwood Company (Keith Lackey and Arron Cox), Green Diamond Resource Co. (Jason Woodward), La Brea Tar Pits & Museum (Regan Dunn and Karin Rice), and John T. Williams. I would also like to thank Gregg Wilkerson for his contribution to the field sampling program, and Michael Abrams for his insightful feedback.

Abstract

This dissertation applies geochemical tools to track the movement, transformation, and behavior of water and gases in hydrocarbon-bearing sedimentary basins. During petroleum exploration and production, hydrocarbons are generated at the surface along with other fluids naturally present in the formation, such as formation water. In addition, where hydraulic fracturing is used to stimulate shale gas and oil production, a percentage of the injected fracturing fluid also returns to the surface. Understanding the origin and movement of these water sources, as well as targeted and non-targeted hydrocarbon gases is critical to evaluating reservoir performance and properly managing fluids at the surface. However, tracking fluid migration in deep sedimentary basins is not a simple task, as it can be significantly affected by geologic, chemical, microbial, and anthropogenic processes. This dissertation provides a framework for evaluating three types of fluid occurrence or movement that can affect our interpretation of fluid origin during hydrocarbon production:

1) Identification of water condensing out of the gas phase (i.e., water of condensation) as a potentially significant component of produced water from shale gas wells.
2) Detection of recent cross-formation flow of deep formation waters; and
3) Distinguishing between gas seepage at the surface due to natural pathways (i.e., natural seeps) vs. anthropogenic pathways.

In the first study, I show that isotopes of water, in concert with salinity, can be utilized to identify water of condensation as a source of fluid in produced water from Marcellus shale gas wells in the Appalachian Basin. In the second study, I utilize a combination of ^{228}Ra/^{226}Ra and ^{87}Sr/^{86}Sr ratios to identify recent cross-formation flow that is supplying "out-of-zone" water into Marcellus shale gas wells. My third study presents a strategy for the application of isotopic and

molecular methods to distinguish between naturally seeping hydrocarbon gases (and associated water, where present) and anthropogenic releases in hydrocarbon-bearing basins throughout California. Collectively, these approaches hold promise for unraveling water and gas origin and chemistry in a variety of settings within hydrocarbon-bearing basins.

Table of Contents

List of Tables

List of Figures

List of Illustrations

Chapter 1: Introduction

The production of hydrocarbons may be reasonably characterized as an exercise in controlling and managing various fluids—natural gas, crude oil, formation fluids and produced water, hydrocarbon condensates, and others. When unexpected movement or changes in the chemistry of such fluids occur, these can generate consequences that range from inconvenient through expensive to potentially hazardous. Therefore, geochemical tools to track fluid movement can be critical for proper planning and management at oil and gas production sites. However, understanding fluid origin, and the processes that affect fluid chemistry, is complicated by complex geologic histories of fluid movement and chemical alteration in hydrocarbon-bearing sedimentary basins (Carpenter, 1978; Etiope et al., 2009; Kharaka and Hanor, 2007; Rostron and Arkadakskiy, 2014; Saller and Stueber, 2021; Schoell, 1988). Additionally, anthropogenic activities, such as hydraulic fracturing and fluid disposal or storage, can also affect fluid chemistry and movement. Deciphering these natural and anthropogenic processes is essential to understanding fluid history in deep sedimentary basins. Such an understanding can also be useful in evaluating the performance of hydrocarbon-producing wells and reservoirs, as well as enhancing approaches to management of fluids co-produced with targeted hydrocarbons (Chaudhary et al., 2019; Engle et al., 2014; Saller and Stueber, 2021; Veil, 2012).

In this dissertation, I explore three types of fluid occurrence or movement that can affect the interpretation of fluid origin (primarily that of water and gas) during hydrocarbon production, and propose various geochemical and isotopic tools to help anticipate, identify, and manage them. These are:

- Identification of water of condensation as a potentially significant component of produced water from shale gas production.

- Characterization of cross-formational flow of formation waters, particularly during unconventional gas or enhanced oil production
- Distinguishing between gas seepage at the surface due to natural vs. anthropogenic pathways.

BEHAVIOR AND CONTROLS OF FORMATION FLUID CHEMISTRY IN SEDIMENTARY BASINS

Physical processes that control formation fluid movement

There are a number of physical processes that have been documented to control formation fluid movement within sedimentary basins. These can largely be grouped into three categories: i) compression and compaction stresses that reduce pore volume, ii) processes that result in an increase in fluid volume, and iii) fluid movement as a result of differences in density, concentration, or hydraulic head (Osborne and Swarbrick, 1997).

Reduced pore volume occurs as a result of sediment loading (vertical compression) and tectonic forces (horizontal compression). These processes drive mechanical compaction (physical rearrangement of grains, which generally occurs up to depths of 2-3 km) and chemical compaction (diagenetic cementation, which predominates at greater depths) (Dickinson, 1953; Osborne and Swarbrick, 1997). The loss of pore volume and associated increase in pore pressure forces the expulsion of pore fluid from the rock into overlying or underlying formations. In cases where fluids cannot be expelled fast enough (e.g. rapid burial or tectonic compression of formations with limited permeability), pore pressure may build above hydrostatic pressure, a state known as disequilibrium compaction.

Changes in fluid volume can also drive fluid movement. Increased fluid volume can result from mineral diagenesis, catagenesis of organic matter to create hydrocarbons, and aquathermal expansion. Important diagenetic mineral transformations include the conversion of smectite to illite, i.e. “clay dewatering”, and the conversion of gypsum (hydrated calcium-sulfate) to anhydrite in evaporite sequences. Smectite-to-illite conversion is estimated to increase pore-water content by a maximum of 4 to 6.6%. This transformation generally occurs at depths of 3-5 km and temperatures >65°C (Bjorlykke, 1998; Bruce, 1984; Osborne and Swarbrick, 1997). The conversion of gypsum to anhydrite results in the loss of 39% of mineral-bound water by volume, and may take place at various depths, though generally temperatures >40°C (MacDonald, 1953; Osborne and Swarbrick, 1997). Catagenesis, or the thermal breakdown of organic kerogens to form hydrocarbons, can also generate significant fluid volume in the form of buoyant liquid hydrocarbons and gas, residue, and by-products (Polutranko, 1998). Volume increases associated with catagenesis are reported to range from 3% to as high as 25% (Meissner, 1978; Ungerer et al., 1990). Aquathermal expansion describes the volumetric expansion of water as temperatures increase; however, this process likely has a minimal effect on pore water volume in most hydrogeologic settings (e.g., Osborne and Swarbrick, 1997).

Fluid movement can also occur as a result of density differences, concentration differences, and hydraulic gradients. Density differences are commonly driven by salinity variations, such as those associated with the dissolution of evaporite beds (Thornton and Wilson, 2007), and the presence of petroleum hydrocarbons, which are characterized by a significantly lower density than water (Atashbari, 2016; Bird et al., 2006; Heald, 1988). Concentration differences in fluid can also drive the movement of water, but not solutes, across a semipermeable membrane such as a shale (Marine and Fritz, 1981). However, “membrane filtration” is largely considered to be a minor control, if at all, on fluid salinities in sedimentary basins (Hanor, 1994). Lastly, differences in hydraulic head can drive substantial vertical and horizontal fluid movement. Hydraulic head is the pressure exerted by water at a point above a vertical datum, usually sea level. In cases where water enters an aquifer at higher elevation and is subsequently transported to lower elevations beneath an impermeable layer (i.e., within a confined aquifer), hydraulic head can exceed hydrostatic pressure. Similarly, pore pressure can exceed hydrostatic pressure as a result of compaction, mineral diagenesis, and other processes described previously. In such situations, where a pathway is available, water will move upwards in the direction of lower pressure. Conversely, during periods of basin uplift, the removal of geologic overburden during erosion and incision can result in a lower hydraulic head, and the downward movement of meteoric waters (e.g., Kim et al., 2022).

Natural controls on formation fluid geochemistry

Below the zone of shallow groundwater circulation, the chemistry of formation fluids in sedimentary basins can change significantly during the basins' geochemical, hydrologic, thermal, and tectonic history. At the most basic level, water sources in sedimentary basins include seawater and meteoric water (assuming formation fluid has not been altered by anthropogenic activities such as injection) (Carpenter, 1978; Kharaka and Hanor, 2007).

The salinity of formation fluids can vary both within a basin and within a single formation or reservoir, ranging from a few milligrams per liter (mg/L) to over 400,000 mg/L total dissolved solids (TDS) (Blondes et al., 2019; Kharaka and Hanor, 2007). 'Brines' are characterized as formation water with salinity exceeding that of average seawater (TDS>35,000 mg/L). Most deep sedimentary basin brines are marine in origin, and exhibit Na-Ca-Cl water type (Carpenter, 1978; Kharaka and Hanor, 2007; Lowenstein et al., 2003). The salinity in these brines is largely thought to originate from seawater, the incorporation of "bitterns", i.e., remnant seawater that remains after the precipitation of marine evaporites, or the dissolution of those evaporites (Carpenter, 1978). Other important processes that affect formation fluid chemistry include mixing, rock-water interaction, bacterial activity, interaction with organic matter, and diffusion (Carpenter, 1978; Kharaka and Hanor, 2007).

In confined basins, the evaporation of seawater drives the precipitation of evaporite minerals (gypsum, halite, $MgSO_4$, potassium salts). This process leaves the remnant seawater water depleted in certain ions that are incorporated into salts, and enriched in others that are not (Carpenter, 1978). For example, bromine does not form any salts of its own, and substitutes very little in the mineral matrix of other salts; as such, during the formation of evaporites, bromine becomes progressively concentrated in the remnant fluid phase, and can serve as an index of evaporation (Carpenter, 1978; Dresel and Rose, 2010). The dissolution of evaporites can also yield high salinity that largely reflects the parent salt (e.g., halite dissolution yields approximately equal molar abundances of Na and Cl). For example, evaporite dissolution is an important factor in formation fluid composition in the Gulf Coast basin, where halite-dominated salt domes are common (Bennett and Hanor, 1987). Because sedimentary basin formation fluids are mobile, mixing of different formation fluids with one another, and with meteoric water, is common (Kharaka and Hanor, 2007). In the latter case, the addition of relatively fresh meteoric water serves to dilute brine concentrations, although the ratios of ions may change very little (e.g., Dresel and Rose, 2010).

Rock-water interactions control the concentrations of many minor constituents, as well as some major ions (e.g., calcium and magnesium) in fluids. Significant rock-water interactions include: i) dolomitization which can enrich Ca^{2+} and deplete Mg^{2+} in brines; ii) albitization of plagioclase feldspar, which results in higher Ca^{2+} and lower Na^{+} fluid concentrations (Kharaka and Hanor, 2007); iii) smectite to illite conversion and gypsum to anhydrite conversion, both which release interstitial water (Bjorlykke, 1998; MacDonald, 1953); iv) silica alteration, which results in the loss of Mg, K, and Na and gain of Li in fluids (e.g., Vigier et al., 2009); v) the breakdown of marine kerogen, which releases iodide and bromide and isotopically light boron into fluids (e.g., Engle et al., 2016); vi) O and H isotope exchange between water and clay minerals, and O exchange with carbonate minerals (McCrea, 1950; O'Neil and Kharaka, 1976); and vii) decay of U and Th in minerals to produce soluble radium (Fisher, 1998; Kraemer and Reid, 1984).

Lastly, fluid geochemistry can be impacted by the presence of reactive organic species (i.e., organic acids), which act as buffering agents and form complexes with various metals (e.g., with Al, Fe, Pb, and Zn) (Kharaka and Hanor, 2007). Additionally, the breakdown of organic material by microbial activity can alter ion abundances in fluids, consuming ions that act as electron acceptors (O_2, NO_3^{1-}, Fe^{3+}, Mn^{4+}, SO_4^{2-}), and producing others as reaction biproducts (e.g., Fe^{2+}, S^{2-}).

Anthropogenic controls on formation fluid chemistry

Because the majority of deep fluid samples originate from oil and gas wells which coproduce formation fluids with the targeted hydrocarbons, anthropogenic controls on fluid chemistry are an important consideration. When not properly sealed, the presence of deep artificial penetrations (e.g., oil and gas wells) can provide artificial pathways for fluids to move between otherwise disconnected formations. Fluids can also be introduced during the injection of wastewater for permanent disposal in porous formations deep underground. The majority of this wastewater is produced water from oil and gas extraction, although it may also include stormwater and agricultural drainage, industrial wastewater, hazardous and radioactive wastes, and carbon dioxide (U.S. EPA, 2022). In addition, fluids may be introduced to extract desirable minerals or metals (e.g., solution mining of salt), or improve hydrocarbon production (e.g., via the injection of water, steam, gas, or chemicals) (U.S. Dept. of Energy, 2022). In particular, hydraulic fracturing involves in the injection of millions of gallons of fracturing fluid to fracture relatively impermeable shales and tight mudstones, stimulating gas and oil production. Fracturing fluid generally contains >90% water (composed of fresh water, produced water, or mixtures thereof), with <2% chemical additives, and >8% proppant to hold the fractures open (FracFocus, 2022). Commonly, between 50 to 95% of the water remains permanently trapped underground (King, 2012).

Approaches to understanding formation fluid origin and subsurface processes using geochemical tools

Various geochemical tools have been applied during investigations into the origin and processes affecting deep fluids in sedimentary basins. At a fundamental level, these include evaluation of the fluid's chemical composition, with a focus on the relative abundances of major cations (Ca, Mg, Na, K, Ba, Sr), and anions (SO_4, Cl, HCO_3/CO_3, and Br), as well as important trace elements (e.g., B, Li, I) (e.g., Carpenter, 1978; Dresel and Rose, 2010; Engle et al., 2020; Hanor and McIntosh, 2006; Williams et al., 2001). More recently, researchers have noted that compositional data plots are subject to potential false correlations, as changes in the abundance of one component necessarily changes the abundance of another (Engle and Rowan, 2013). To avoid erroneous interpretation, compositional data can be transformed to one of the family of log ratio transformations, which are not subject to the same numerical errors (Engle and Rowan, 2014).

A variety of isotopic methods have also been applied to trace fluid origin, including: $\delta^{2}H$ and $\delta^{18}O_{H2O}$, $\delta^{13}C_{DIC}$, $\delta^{34}S$ and $\delta^{18}O_{SO4}$, $\delta^{37}Cl$, $^{87}Sr/^{86}Sr$, $\delta^{7}Li$, $\delta^{11}B$, $^{228}Ra/^{226}Ra$, ^{3}H, ^{14}C, ^{36}Cl, ^{81}Br (Birkle, 2016; Blondes et al., 2020; Engle et al., 2020; Engle and Rowan, 2014; Nicot et al., 2020, 2018; Phan et al., 2016; Rostron and Arkadakskiy, 2014; Rowan et al., 2011; Saller and Stueber, 2021; Stotler et al., 2021; Warner et al., 2012). For example, within the Appalachian Basin, Sr isotopes have been used to effectively distinguish between brines originating from the Upper

Devonian Venango formation versus those from the Middle Devonian Marcellus Shale (Chapman et al., 2012). Similarly, water isotopes (δ^2H and δ^{18}O) have been shown to be a simple approach to discerning formation fluids formed from seawater evaporation from those with a significant meteoric water component (e.g., Rostron and Arkadakskiy, 2014; Saller and Stueber, 2021). Nevertheless, the success of these tools as isotopic tracers can vary significantly from basin to basin, and within localized geographic areas, depending on the diversity of fluids, lithologies, and processes acting on fluid composition.

With the rapid expansion of hydraulic fracturing for shale gas and tight oil, there is a wealth of new produced water chemical data available from shales. This data provides a fresh look at the processes affecting shale water chemistry and origin. The second and third chapters of this dissertation focus on interpretation of produced water data from the Marcellus Shale in northeastern Pennsylvania, one of the most productive shale gas plays in the world (EIA, 2021).

The Marcellus is characterized by relatively low water saturation, and much of the injected fracturing fluid (>85%) is imbibed into the formation (Bryndzia and Fay, 2016; U.S. EPA, 2015). Of the injected fluid that is returned to surface, the majority is produced during the first few weeks to months of flowback, after which the rate of water production rapidly declines. This decrease in volume is accompanied by a steep increase in salinity, as well as evolving δ^{18}O and ^{87}Sr/^{86}Sr values, widely interpreted to represent the transition from water dominated by injection fluid to that dominate by formation water (Capo et al., 2014; Chapman et al., 2012; Haluszczak et al., 2013; Phan et al., 2020; Rowan et al., 2015). Similar trends of decreasing water production accompanied by increasing salinity, which generally stabilizes after the first year, are evident in most shale gas plays with available time-series produced water data (e.g., Haluszczak et al., 2013; Rowan et al., 2015). As such, later-stage produced water chemistry is widely interpreted to represent the shale formation fluid end-member, and forms the basis for much of the interpretation of shale water origin and history.

In the second and third chapters, I explore two important exceptions to this trend. First, a subset of Marcellus Shale gas wells exhibits a later-stage (i.e., six months or more) reversal in salinity, suddenly producing fresher water over time, while still maintaining very low rates of water production. I hypothesize that this reversal is due to contributions from fresh water condensing out of the gas phase, i.e., water of condensation, a concept that is explored in Chapter 2. The third chapter focuses on a subset of Marcellus wells that fall on the opposite end of the spectrum; specifically, wells that produce water with consistently elevated salinity (i.e. >100,000 mg/L TDS) and higher water production rates, with no decline in water production over time. There have been reports that water production at these wells represents cross-formation flow from more permeable underlying or overlying formations. I show that a combination of Ra and Sr isotopes in produced water, as well as lithologic measurements of U and Th in rocks, can be used as effective tools to extract information on cross-formation flow.

BEHAVIORS AND CONTROLS OF NATURAL GAS GEOCHEMISTRY IN SEDIMENTARY BASINS

Physical processes that control hydrocarbon gas movement

In Chapter 4, I focus on the geochemistry of natural gas seeps, and the changes that occur during migration from reservoir to surface. Hydrocarbon migration is largely divided into: i) ‘expulsion migration,’ in which hydrocarbons are expelled from the source rock, and ii) ‘post-expulsion migration,’ during which hydrocarbons migrate from a source rock to permeable reservoir rocks, between reservoirs, or from reservoir(s) to surface. Expulsion migration is driven by pressure related to compaction in the upper 2 km of burial, as well as the development of overpressure within the formation due to hydrocarbon generation (or other processes that generate pressures greater than hydraulic head, as discussed above). Within this setting, most gases and lighter oil components are thought to migrate in a gaseous solution by buoyancy-driven flow through permeable pathways (e.g., microfractures, joints, and faults) (Hunt, 1995; Nemčok, 2016). Hydrocarbons can also diffuse out of source rocks in the direction of lower concentration, though diffusion is a remarkably slow process (Smith et al., 1971). Similarly, natural gases can migrate entrained in water, although this is largely thought to be important only for methane and possibly ethane due to the limited solubilities of most oils and hydrocarbon gases (Hunt, 1995).

Post-expulsion migration is primarily driven by hydrocarbon buoyancy (Hunt, 1995). During migration through the rock matrix, buoyant upward flow of gas must overcome capillary entry pressure, i.e., the pressure needed to displace water held in pore spaces by capillary forces (Mann et al., 1997). However, formation overpressure commonly drives the opening of pre-existing fractures well before capillary entry pressures are met. This is why many petroleum-bearing formations leak over time (Hunt, 1995).

The upward migration of hydrocarbons largely proceeds through joints, faults, and lineaments at the surface, where all three are formed when rocks are subject to stress. Hydrocarbons can also migrate along unconformities, which can serve as permeable migration pathways (Mann et al., 1997). For this reason, many natural seeps are found at surface expressions of unconformities.

Reservoirs are accumulations of hydrocarbons within a trap, i.e. a permeable rock located beneath an impermeable seal. Traps can be structural (e.g., anticlines, salt domes, or faults that align impermeable rocks next to permeable reservoirs), and/or stratigraphic (e.g., unconformities) (Hunt, 1995). Stacked reservoirs are typically associated with vertical migration via faults and fractures, and frequently contain oil or gas originating from the same source rock (Hunt, 1995). In contrast, lateral migration along unconformities can result in the long-distance transport (e.g. several hundred miles) of hydrocarbons from the source rock (e.g., Peters et al., 2007).

The natural migration of gases from reservoir to surface is referred to as natural gas seepage, which is commonly divided into macroseepage and microseepage. Macroseepage represents the substantial flow of hydrocarbons via preferential pathways to surface (e.g., 10^{-1} to 10^{3} tonnes per year). Such seeps were the basis for the initial discovery of many petroleum-bearing basins worldwide (Hodgson, 1987). Macroseeps may be dry (just produce gas), or co-produce fluids (oil and/or water) and are typically associated with channeled flow via fault systems to surface. By contrast, microseepage represents the pervasive, slow, and invisible transport of gas vertically upwards, likely related to the buoyancy of microbubbles (Klusman and Saeed, 1996). A third category, miniseepage, describes the diffuse flow of gas in the vadose zone around macroseeps (Etiope, 2015).

Artificial pathways for hydrocarbon gas migration

The unintended migration of natural gas from reservoir to surface, i.e. “stray gas migration,” can occur via deep artificial penetrations and pathways that bypass natural seals on reservoirs. These include improperly plugged and abandoned hydrocarbon production and injection wells, or active wells with well integrity issues, such as faulty/absent cement or compromised casing (Davies et al., 2014; Harrison, 1983). They may also include deep water supply wells that serve as secondary pathways for the upward migration of gas that has already escaped into the deeper subsurface. Similarly, naturally occurring faults and fractures can serve as secondary pathways for gas migration (Dusseault and Jackson, 2014; Lackey et al., 2017; Llewellyn, 2014; Molofsky et al., 2021).

Many oil and gas fields contain multiple gas-bearing formations throughout the vertical stratigraphy. Even when certain formations are not targeted for production, gases from these strata may enter the well annulus and move buoyantly upwards if cement is compromised or absent (e.g., Davies et al., 2014; Lackey et al., 2017). As a result, evaluating the origin of stray gas migration frequently requires chemical characterization of the gas to differentiate potential source reservoirs.

Controls on primary gas geochemistry

Natural gases are characterized as ‘primary’, i.e., gas originating from a single source, or ‘secondary’, i.e., gases that are mixed or altered. This section focuses on the controls on primary gas geochemistry. Primary natural gases are divided into three genetic types: “microbial”, “thermogenic”, and “abiogenic”. These types are distinguished by the process of formation, which largely dictates the molecular and isotopic composition. Microbial gas forms at temperatures less than 70°C by two distinct pathways: fermentation of acetate (landfills, swamps, marshes, and other near-surface environments); and CO_2 reduction (marine environments, glacial drift deposits, and within petroleum reservoirs) (Whiticar, 1994). Microbial gas is dominated by methane (>99% of hydrocarbons), with ethane comprising less than 0.1% (if present at all), and propane and heavier hydrocarbon gases comprising <0.001% (Taylor et al., 2000). Importantly, microbial gas formed by fermentation also contains CO_2, which is produced in approximately equal molar concentrations to methane (e.g., $CH_3COO^- + H^+ \rightarrow CH_4 + CO_2$) (Whiticar, 1994).

Thermogenic gas forms from the abiotic breakdown of organic matter under high temperature and pressures at depth. This process, called catagenesis, occurs when short-chain hydrocarbons are cleaved off of heavier organic compounds (kerogen), and subsequently saturated to yield light alkanes (methane (CH_4 or “C1”), ethane (C_2H_6 or “C2”), propane (C_3H_8 or “C3”), butane (C_4H_{10} or “C4”), pentane (C_5H_{12} or “C5”) and hexane (C_6H_{14} or “C6”)). Thermogenic gas commonly contains >1% C2+ hydrocarbons, though the specific molecular and isotopic composition of thermogenic gases is largely controlled by a combination of source kerogen and thermal maturation (i.e., the extent of heat-driven reactions that alter the organic material). Kerogen sources for natural gas include algal material (type I, oil prone), mixed terrestrial and marine material (type II, oil and gas prone), and woody terrestrial material (type III, gas prone). At lower thermal maturities, the $\delta^{13}C$ value of C1 is closest to that of the parent kerogen, with C2-C6+ exhibiting increasing $\delta^{13}C$ values in order of mass (Hunt, 1995). As thermal maturity increases, $\delta^{13}C$ values of all hydrocarbons (C1 – C6+) become increasingly enriched relative to kerogen. At the same time, differences between hydrocarbon $\delta^{13}C$ values narrow and disappear completely at highest temperatures (Hunt, 1995).

The maximum paleotemperature and time of exposure controls the characterization of gases as early mature, oil associated/mature, late mature, or overmature (Whiticar, 1994). Early mature thermogenic gas is relatively dry (<5% C2+); however, as gas generation proceeds through the oil window into mature thermogenic gas, C2+ abundance can increase dramatically. The C2+ abundance falls again in late mature thermogenic (LMT) gas as continued thermal cracking breaks down higher-chain hydrocarbons (Whiticar, 1994).

Nonhydrocarbon gases, such as CO_2, H_2S, N_2, H_2, and He can co-occur with primary thermogenic hydrocarbon gases. CO_2 forms from the thermal breakdown of organic matter, as a biproduct of the reaction between kaolinite and carbonates to produce chlorite, and from carbonate decomposition during contact with high temperature magma (Hunt, 1995). Additional CO_2 can be generated during post-genetic alteration, described in more detail in the discussion of secondary gas geochemistry. H_2S originates from the thermal cracking of sulfur-bearing kerogen, degradation of high sulfur oil, or sulfate reduction in pore water (Hunt, 1995). Oxidation of ammonia or nitrogen-bearing organic compounds (e.g., by reaction with ferric oxide) can produce high-nitrogen gases (e.g., >30% N_2) (Hunt, 1995; Whiticar, 1994). Mantle off-gassing is another potential source of N_2, H_2, and He, and mantle-derived He has been detected in fluids at the surface associated with the San Andreas fault and companion faults in California (e.g., Boles et al., 2015; Kennedy et al., 1997). However, it is more likely that all three gases are actively generated within the reservoir, either via reactions or in the case of ^4He, through the radioactive decay of U and Th (Hunt, 1995; Whiticar, 1994; Zhou and Ballentine, 2006)

Abiogenic methane originates within the mantle or deep within the earth's crust from inorganic reactions. Recent research indicates it can also be produced during gas-water-rock reactions in low-temperature (<100°C) continental settings (Etiope and Sherwood Lollar, 2013). It is largely thought to be an insignificant contributor of methane on earth, and is most commonly observed at mid-ocean-ridge (MOR) hydrothermal systems (Schoell, 1988).

Controls on secondary gas geochemistry

Secondary gases represent those that have been altered by post-genetic processes. These processes can occur during migration from the source rock to the reservoir, between reservoirs, or from reservoir to surface. Important post-genetic processes are discussed briefly below and described in more detail in Chapter 4.

Secondary mixing of natural gases is common, and may include mixtures of gases originating from different source rocks, exhibiting different thermal maturities, or formed by different processes all together (i.e., microbial degradation vs. thermal cracking) (Whiticar, 1994). Mixtures of microbial and thermogenic gases in deeper strata are frequently observed where microbial gases are buried with the formation. Similarly, mixtures of thermogenic gases are common in basins with complex hydrocarbon generation histories (Schoell, 1988).

Microbes that oxidize hydrocarbon gases are widespread in the subsurface; as such, the microbial oxidation of methane and other hydrocarbon gases is possible wherever electron acceptors are available for microbially mediated reactions. Microbial oxidation of hydrocarbon gases can proceed aerobically (where O_2 serves as the electron acceptor), or anaerobically (where dissolved NO_3^-, Fe^{3+}, Mn^{4+}, and SO_4^{2-} serve as electron acceptors). Oxidation results in changes to the relative abundances of hydrocarbon gases, as well as their isotopic composition. For example, Pallasser (2000) showed that anaerobic microbial oxidation preferentially consumes C3 and n-alkanes. In addition, both aerobic and anaerobic microbial oxidation results in the predictable enrichment of carbon and hydrogen isotopes in the remaining hydrocarbon gases (Coleman et al., 1981; Whiticar, 1999). Abiogenic oxidation of hydrocarbon gases occurs at temperatures >80°C as a result of oxidation by Fe^{3+} bearing minerals and thermochemical sulfate reduction (TSR). Though significantly less common than microbial oxidation, this process also results in increased $\delta^{13}C$ values of C1-C5 hydrocarbons (Etiope et al., 2009).

Secondary methanogenesis following petroleum degradation is an important, if not the primary, source of CO_2 in oil-associated natural gases. This process occurs within petroleum reservoirs, and in migration pathways that contain petroleum, where the microbial oxidation (biodegradation) of petroleum and heavy hydrocarbons produces CO_2 as a reaction byproduct. This CO_2 can then be utilized in 'secondary methanogenesis,' or the creation of microbial methane via the CO_2 reduction pathway. Unlike microbial methane produced by CO_2 reduction in glacial drift deposits, methane produced during secondary methanogenesis exhibits a $\delta^{13}C$ isotopic composition consistent with thermogenic gas (Brown, 2011). The CO_2 that remains after secondary methanogenesis is markedly enriched in the heavier ^{13}C isotope, exhibiting $\delta^{13}C$ values in excess of +10‰ (Etiope, 2009a).

Migration fractionation refers to the molecular fractionation of C1-C6+ hydrocarbons during solution and sorption. Specifically, because C2 and C3 exhibit higher solubilities than C1, these compounds preferentially enter solution when free-phase gas comes into contact with water (Klusman and Saeed, 1996). Similarly, C2+ hydrocarbons have been observed to preferentially sorb to (or become entrapped in) mineral surfaces and organic materials (Abrams, 2020, 2017; Abrams and Dahdah, 2010; Bernard et al., 2001; Bjoroy and Ferriday, 2001; Deville et al., 2003; Etiope, 2015; Horvitz, 1985, 1972; Whiticar, 2001). As a result of solubility or sorption fractionation during migration, free-phase gas can exhibit C2+ loss.

Isotopic and molecular fractionation of hydrocarbon gases by diffusion occurs where concentration gradients are the primary driver of gas movement, rather than advective flow. Diffusion is not thought to be an important mechanisms for gas transport in most settings (e.g. Hunt, 1995); nevertheless, where present, diffusion results in a lighter isotopic and molecular composition of migrating gas (more C1, and depleted $\delta^{13}C$ values) (Prinzhofer and Battani, 2003).

Approaches to understanding hydrocarbon gas origin and subsurface processes using geochemical tools

Variations in the geochemistry (molecular and isotopic composition) of natural gases is used to gain insight into gas origin (process of formation, source rocks), thermal maturity (e.g., temperature of hydrocarbon generation), and secondary processes that can alter gas composition (e.g., microbial oxidation). For such interpretations, researchers generally utilize diagrams that incorporate the ratios of the molecular abundances of gases, and the isotopic composition of hydrocarbon and non-hydrocarbon gases. Common diagrams include a plot of $\delta^{13}C$-C1 vs. C1/(C2+C3) (Bernard et al., 1977); $\delta^{2}H$-C1 vs. $\delta^{13}C$-C1 (Schoell, 1983); $\delta^{13}C$-C1 vs. $\delta^{13}C$-CO_2 (Gutsalo and Plotnikov, 1981); $\delta^{13}C$-C2 vs. $\delta^{13}C$-C1 and $\delta^{13}C$-C3 vs. $\delta^{13}C$-C2 (Whiticar, 1994);

and 1/Cx vs. δ^{13}Cx (Chung et al., 1988). Most recently, Milkov and Etiope (2018) provided revised genetic diagrams for the first three plots, which are the most commonly utilized during interpretation of natural gas chemistry. These revised plots were based on over 20,000 reservoir gas samples from 76 countries and 21 territories. By comparison, there is relatively limited information on the molecular and isotopic composition of natural gas seepage, with data available for only a small number of the over 10,000 estimated onshore natural seeps (Etiope, 2009b). Because many oil and gas fields were discovered in areas of natural seepage (Hodgson, 1987), understanding the chemical characteristics of naturally seeping fluids is important for discerning these natural phenomena from anthropogenic releases associated with oil and gas extraction.

With a particularly high density of natural gas seep occurrence across its petroleum-bearing basins, California is a model setting for expanding our understanding of the chemistry of onshore natural gas seeps. Specifically, California is home to more than 130 natural gas seeps and at least 400 additional oil seeps (Hodgson, 1987). The fourth chapter of this dissertation presents a strategy for the largescale examination and synthesis of the molecular and isotopic composition of natural gas seepage in California, including newly collected data from 18 sample locations. This approach focuses on improving our understanding of the characteristics and processes that affect natural gas seepage chemistry, where this information is important for distinguishing natural seepage from anthropogenic impacts in areas of oil and gas extraction.

REFERENCES

Abrams, M.A., 2020. Marine seepage variability and its impact on evaluating the surface migrated hydrocarbon seep signal. Mar. Pet. Geol. 121, 104600. https://doi.org/10.1016/j.marpetgeo.2020.104600

Abrams, M.A., 2017. Evaluation of near-surface gases in marine sediments to assess subsurface petroleum gas generation and entrapment. Geosci. 7. https://doi.org/10.3390/geosciences7020035

Abrams, M.A., Dahdah, N.F., 2010. Surface sediment gases as indicators of subsurface hydrocarbons - examining the record in laboratory and field studies. Mar. Pet. Geol. 27, 273–284. https://doi.org/10.1016/j.marpetgeo.2009.08.005

Atashbari, V., 2016. Origin of overpressure and pore pressure prediction in carbonate reservoirs of the Abadan Plain Basin. The University of Adelaide.

Bennett, S.C., Hanor, J.S., 1987. Dynamics of subsurface salt dissolution at the Welsh Dome, Louisiana Gulf Coast, in: Lerche, I., O'Brien, J.J. (Eds.), Dynamical Geology of Salt and Related Structures. Academic press, New York, pp. 653–677.

Bernard, B., Brooks, J.M., Sackett, W.M., 1977. A geochemical model for characterization of hydrocarbon gas sources in marine sediments, in: Proceedings of the Annual Offshore Technology Conference, Houston, Texas, May 1977. https://doi.org/10.4043/2934-ms

Bernard, B.B., Brooks, J.M., Zumberge, J., 2001. Determining the Origin of Gases in Near-Surface Sediments, in: AAPG Hedberg Conference "Near-Surface Hydrocarbon Migration: Mechanisms and Seepage Rates" September 16-19, 2001, Vancouver, BC, Canada. pp. 1–4.

Bird, R.B., Stewart, W.E., Lightfoot, E.N., 2006. Transport Phenomena, Revised 2nd Edition. John Wiley Sons, Inc.

Birkle, P., 2016. Recovery rates of fracturing fluids and provenance of produced water from hydraulic fracturing of Silurian Qusaiba hot shale, northern Saudi Arabia, with implications on fracture network. Am. Assoc. Pet. Geol. Bull. 100. https://doi.org/10.1306/02101615120

Bjorlykke, K., 1998. Clay mineral diagenesis in sedimentary basins—a key to the prediction of rock properties; examples from the North Sea Basin. Clay Min. 33, 15–34.

Bjoroy, M., Ferriday, I., 2001. Surface geochemistry as an exploration tool: A comparison of results using different analytical techniques. Near-Surface Hydrocarb. Migr. Mech. Seepage Rates.

Blondes, M.S., Gans, K.D., Engle, M.A., Kharaka, Y.K., Reidy, M.E., Saraswathula, V., Thordsen, J.J., Rowan, E.L., Morrissey, E.A., 2019. U.S. Geological Survey National Produced Waters Geochemical Database v2.3 [Data set]. U.S. Geological Survey [WWW Document]. USGS Data Source. https://doi.org/10.5066/F7J964W8

Blondes, M.S., Shelton, J.L., Engle, M.A., Trembly, J.P., Doolan, C.A., Jubb, A.M., Chenault, J.C., Rowan, E.L., Haefner, R.J., Mailot, B.E., 2020. Utica shale play oil and gas brines: Geochemistry and factors influencing wastewater management. Environ. Sci. Technol. 54, 13917–13925. https://doi.org/10.1021/acs.est.0c02461

Boles, J.R., Garven, G., Camacho, H., Lupton, J.E., 2015. Mantle helium along the Newport-Inglewood fault zone, Los Angeles Basin, California: A leaking paleo-subduction zone. Geochem. Geophys. Geosyst. 16, 2364–2381.

Brown, A., 2011. Identification of source carbon for microbial methane in unconventional gas reservoirs. Am. Assoc. Pet. Geol. Bull. 95, 1321–1338. https://doi.org/10.1306/01191110014

Bruce, C.H., 1984. Smectite dehydration—its relation to structural development and hydrocarbon accumulation in northern Gulf of Mexico Basin. Am. Assoc. Pet. Geol. Bull. 68, 673–683.

Bryndzia, L.T., Fay, M.C., 2016. Geochemical analysis of Returned Treatment Waters (RTW) associated with shale gas production in the Appalachian Basin (USA) and Deep Basin (Canada): Potential use of Total Dissolved Solids (TDS) and Oxygen isotope data for assessing Water:Rock ratios..., in: SPE/AAPG/SEG Unconventional Resources Technology Conference 2016. https://doi.org/10.15530/urtec-2016-2455905

Capo, R.C., Stewart, B.W., Rowan, E.L., Kolesar Kohl, C.A., Wall, A.J., Chapman, E.C., Hammack, R.W., Schroeder, K.T., 2014. The strontium isotopic evolution of Marcellus Formation produced waters, southwestern Pennsylvania. Int. J. Coal Geol. 126, 57–63. https://doi.org/10.1016/j.coal.2013.12.010

Carpenter, A.B., 1978. Origin and Chemical Evolution of Brines in Sedimentary Basins, in: Johnson, K.S., Russel, J.A. (Eds.), Oklahoma Geological Survey Circular 79: Thirteenth Annual Forum on the Geology of Industrial Minerals. pp. 60–77. https://doi.org/10.2118/7504-MS

Chapman, E.C., Capo, R.C., Stewart, B.W., Kirby, C.S., Hammack, R.W., Schroeder, K.T., Edenborn, H.M., 2012. Geochemical and strontium isotope characterization of produced waters from Marcellus Shale natural gas extraction. Environ. Sci. Technol. 46, 3545–3553. https://doi.org/10.1021/es204005g

Chaudhary, B.K., Sabie, R., Engle, M.A., Xu, P., Willman, S., Carroll, K.C., 2019. Spatial variability of produced-water quality and alternative-source water analysis applied to the Permian Basin, USA. Hydrogeol. J. 27, 2889–2905. https://doi.org/10.1007/s10040-019-02054-4

Chung, H.M., Gormly, J.R., Squires, R.M., 1988. Origin of gaseous hydrocarbons in subsurface environments: Theoretical considerations of carbon isotope distribution. Chem. Geol. 71, 97–104. https://doi.org/10.1016/0009-2541(88)90108-8

Coleman, D.D., Risatti, J.B., Schoell, M., 1981. Fractionation of carbon and hydrogen isotopes by methane-oxidizing bacteria. Geochim. Cosmochim. Acta 45, 1033–1037. https://doi.org/10.1016/0016-7037(81)90129-0

Davies, R.J., Almond, S., Ward, R.S., Jackson, R.B., Adams, C., Worrall, F., Herringshaw, L.G., Gluyas, J.G., Whitehead, M.A., 2014. Oil and gas wells and their integrity: Implications for shale and unconventional resource exploitation. Mar. Pet. Geol. 56, 239–254. https://doi.org/10.1016/j.marpetgeo.2014.03.001

Deville, E., Battani, A., Griboulard, R., Guerlais, S., Lallemant, S., Mascle, A., Prizhofer, A., Schmitz, J., Statement, G., Setting, S., 2003. Processes of Mud Volcanism in the Barbados-Trinidad Compressional System : New structural , Thermal and Geochemical Data. AAPG Search and Discovery Article #30017.

Dickinson, G., 1953. Geological Aspects of Abnormal Reservoir Pressures in Gulf Coast Louisiana. Am. Assoc. Pet. Geol. Bull. 37, 410–432. https://doi.org/10.1306/5ceadc6b-16bb-11d7-8645000102c1865d

Dresel, P., Rose, A.W., 2010. Chemistry and origin of oil and gas well brines in western Pennsylvania. Pennsylvania Geol. Surv., 4th Ser. Open File Rep. OFOG 10-01.0 48.

Dusseault, M., Jackson, R., 2014. Seepage pathway assessment for natural gas to shallow groundwater during well stimulation, in production, and after abandonment. Environ. Geosci. 21, 107–126. https://doi.org/10.1306/eg.04231414004

EIA, 2021. Petroleum & Other Liquids: Drilling Productivity Report [WWW Document]. URL https://www.eia.gov/petroleum/drilling/

Engle, M.A., Cozzarelli, I.M., Smith, B.D., 2014. USGS Investigations of Water Produced During Hydrocarbon Reservoir Development, USGS Fact Sheet 2014-3104.

Engle, M.A., Doolan, C.A., Pitman, J.A., Varonka, M.S., Chenault, J., Orem, W.H., Mcmahon, P.B., Jubb, A.M., 2020. Origin and geochemistry of formation waters from the lower Eagle Ford Group, Gulf Coast Basin, south central Texas. Chem. Geol. 550, 119754. https://doi.org/10.1016/j.chemgeo.2020.119754

Engle, M.A., Reyes, F.R., Varonka, M.S., Orem, W.H., Ma, L., Ianno, A.J., Schell, T.M., Xu, P., Carroll, K.C., 2016. Geochemistry of formation waters from the Wolfcamp and " Cline " shales: Insights into brine origin, reservoir connectivity, and fluid flow in the Permian Basin, USA. Chem. Geol. 425, 76–92. https://doi.org/10.1016/j.chemgeo.2016.01.025

Engle, M.A., Rowan, E.L., 2014. Geochemical evolution of produced waters from hydraulic fracturing of the Marcellus Shale, northern Appalachian Basin: A multivariate compositional data analysis approach. Int. J. Coal Geol. 126, 45–56. https://doi.org/10.1016/j.coal.2013.11.010

Engle, M.A., Rowan, E.L., 2013. Interpretation of Na–Cl–Br Systematics in Sedimentary Basin Brines: Comparison of Concentration, Element Ratio, and Isometric Log-ratio Approaches. Math Geosci. 45, 87–101. https://doi.org/10.1007/s11004-012-9436-z

Etiope, G., 2015. Natural Gas Seepage: The Earth's Hydrocarbon Degassing. Springer International Publishing, Switzerland.

Etiope, G., 2009a. Natural emissions of methane from geological seepage in Europe. Atmos. Environ. 43, 1430–1443. https://doi.org/10.1016/j.atmosenv.2008.03.014

Etiope, G., 2009b. GLOGOS, A New Global Onshore Gas-Oil Seeps Dataset. Search Discov.

70071.

Etiope, G., Feyzullayev, A., Milkov, A. V., Waseda, A., Mizobe, K., Sun, C.H., 2009. Evidence of subsurface anaerobic biodegradation of hydrocarbons and potential secondary methanogenesis in terrestrial mud volcanoes. Mar. Pet. Geol. 26, 1692–1703. https://doi.org/10.1016/j.marpetgeo.2008.12.002

Etiope, G., Sherwood Lollar, B., 2013. Abiotic methane on earth. Rev. Geophys. 51, 276–299. https://doi.org/10.1002/rog.20011

Fisher, R.S., 1998. Geological and Geochemical Controls on Naturally Occurring Radioactive Materials (NORM) in Produced water from Oil, Gas, and Geothermal Operations. Environ. Geosci. 5, 139–150. https://doi.org/1075-9565/98/$10.50/0

FracFocus, 2022. What Is Fracturing Fluid Made Of? [WWW Document]. FracFocus Chem. Discl. Regist. URL https://www.fracfocus.org/learn/what-is-fracturing-fluid-made-of (accessed 3.13.23).

Gutsalo, L.K., Plotnikov, A.M., 1981. Carbon isotopic composition in the CH4-CO2 system as a criterion for the origin of methane and carbon dioxide in Earth natural gases (in Russian). Dokl. Akad. Nauk 259, 470–473.

Haluszczak, L.O., Rose, A.W., Kump, L.R., 2013. Geochemical evaluation of flowback brine from Marcellus gas wells in Pennsylvania, USA. Appl. Geochemistry 28. https://doi.org/10.1016/j.apgeochem.2012.10.002

Hanor, J.S., 1994. Geofluids: Origin of saline fluids in sedimentary basins, in: Parnell, J. (Ed.), Geological Society Special Publication No. 78. pp. 151–174.

Hanor, J.S., McIntosh, J.C., 2006. Are secular variations in seawater chemistry reflected in the compositions of basinal brines? J. Geochemical Explor. 89, 153–156.

https://doi.org/10.1016/j.gexplo.2005.11.054

Harrison, S.S., 1983. Evaluating System for Ground-Water Contamination Hazards Due to Gas-Well Drilling on the Glaciated Appalachian Plateau. Groundwater 21, 689–700. https://doi.org/10.1111/j.1745-6584.1983.tb01940.x

Heald, C.C. (Ed.), 1988. Cameron Hydraulic Data: A Handy Reference on the Subject of Hydraulics and Steam - 17th Edition. Ingersoll-Rand.

Hodgson, S.F., 1987. Onshore Oil & Gas Seeps in California, Publication No. TR26.

Horvitz, L., 1985. Geochemical exploration for petroleum. Science (80-.). 229, 821–827. https://doi.org/10.1126/science.229.4716.821

Horvitz, L., 1972. Vegetation and Geochemical Prospecting for Petroleum. Am. Assoc. Pet. Geol. Bull. 56, 925–940. https://doi.org/10.1306/819a409a-16c5-11d7-8645000102c1865d

Hunt, J.M., 1995. Petroleum Geochemistry and Geology, 2nd ed. W.H. Freeman and Company, New York.

Kennedy, B.M., Kharaka, Y.K., Evans, W.C., Ellwood, A., DePaolo, D.J., Thordsen, J., Ambats, G., Mariner, R.H., 1997. Mantle fluids in the San Andreas fault system, California. Science (80-.). 278, 1278–1281. https://doi.org/10.1126/science.278.5341.1278

Kharaka, Y.K., Hanor, J.S., 2007. Deep fluids in the continents: 1. Sedimentary Basins, in: Treatise on Geochemistry. Pergamon, Oxford, pp. 1–48.

Kim, J., Ferguson, G., Person, M., Jiang, W., Lu, Z., Ritterbusch, F., Yang, G., Tyne, R., Bailey, L., Ballentine, C., Reiners, P., McIntosh, J., 2022. Krypton-81 Dating Constrains Timing of Deep Groundwater Flow Activation. Geophys. Res. Lett. 49, 1–11.

King, G.E., 2012. Hydraulic fracturing 101: What every representative, environmentalist, regulator, reporter, investor, university researcher, neighbor and engineer should know about estimating frac risk and improving frac performance in unconventional, SPE 152596, in: SPE Hydraulic Fracturing Technology Conference, Soc. of Pet. Eng., Woodlands, Tex. pp. 1–80.

Klusman, R.W., Saeed, M.A., 1996. Comparison of Light Hydrocarbon Microseepage Mechanisms, in: Schumacher, D., Abrams, M.A. (Eds.), Hydrocarbon Migration and Its Near-Surface Expression: AAPG Memoir 66. pp. 157–158.

Kraemer, T.F., Reid, D.F., 1984. The occurrence and behavior of radium in saline formation water of the U.S. Gulf Coast region. Chem. Geol. 46, 153–174. https://doi.org/10.1016/0009-2541(84)90186-4

Lackey, G., Rajaram, H., Sherwood, O.A., Burke, T.L., Ryan, J.N., 2017. Surface Casing Pressure As an Indicator of Well Integrity Loss and Stray Gas Migration in the Wattenberg Field, Colorado. https://doi.org/10.1021/acs.est.6b06071

Llewellyn, G.T., 2014. Evidence and mechanisms for Appalachian Basin brine migration into shallow aquifers in NE Pennsylvania, USA. Hydrogeol. J. 22, 1055–1066. https://doi.org/10.1007/s10040-014-1125-1

Lowenstein, T.K., Hardie, L.A., Timofeff, M.N., Demicco, R.V., 2003. Secular variation in seawater chemistry and the origin of calcium chloride basinal brines. Geology 31, 857–860.

MacDonald, G.J.F., 1953. Anhydrite-gypsum equilibrium relations. Am. J. Sci. 251, 884–898.

Mann, U., Hantschel, T., Schaefer, R.G., Kroos, B., Leythaeuser, D., Littke, R., Sachsenhofer, R.F., 1997. Petroleum Migration: Mechanisms, Pathways, Efficiencies and Numerical Simulations, in: Welte, D.H., Horsfield, B., Baker, D.R. (Eds.), Petroleum and Basin Evolution. Springer, Berlin, Heidelberg, pp. 403–520.

Marine, I.W., Fritz, S.J., 1981. Osmotic Model to Explain Anomalous Hydraulic Heads. Water

Resour. Res. 17, 73–82.

McCrea, J.M., 1950. On the Isotopic Chemistry of Carbonates and a Paleotemperature Scale On the Isotopic Chemistry of Carbonates and a Paleotemperature Scale. J. Chem. Phys. 18, 849–857. https://doi.org/10.1063/1.1747785

Meissner, F.F., 1978. Petroleum geology of the Bakken Formation, Williston Basin, North Dakota and Montana, in: Proceedings of 1978 Williston Basin Symposium, September 24-27, Montana Geological Society, Billings.

Milkov, A. V, Etiope, G., 2018. Organic Geochemistry Revised genetic diagrams for natural gases based on a global dataset of >20,000 samples. Org. Geochem. 125, 109–120. https://doi.org/10.1016/j.orggeochem.2018.09.002

Molofsky, L.J., Connor, J.A., Van De Ven, C.J.C., Hemingway, M.P., Richardson, S.D., Strasert, B.A., McGuire, T.M., Paquette, S.M., 2021. A review of physical, chemical, and hydrogeologic characteristics of stray gas migration: Implications for investigation and remediation. Sci. Total Environ. 779, 146234. https://doi.org/10.1016/j.scitotenv.2021.146234

Nemčok, M., 2016. Models of hydrocarbon migration, in: Rifts and Passive Margins: Structural Architecture, Thermal Regimes, and Petroleum Systems. Cambridge University Press, Cambridge, pp. 442–472.

Nicot, J., Eichhubl, P., Scanlon, B.R., 2020. Origin of low salinity, high volume produced waters in the Wolfcamp Shale (Permian), Delaware Basin, USA. Appl. Geochemistry 122, 104771. https://doi.org/10.1016/j.apgeochem.2020.104771

Nicot, J., Gherabati, A., Darvari, R., Mickler, P., 2018. Salinity Reversal and Water Freshening in the Eagle Ford Shale, Texas, USA. ACS Earth Sp. Chem. 2, 1087–1094.

https://doi.org/10.1021/acsearthspacechem.8b00095

O'Neil, J.R., Kharaka, Y.K., 1976. Hydrogen and oxygen isotope exchange reactions between clay minerals and water. Geochim. Cosmochim. Acta 40, 241–246. https://doi.org/10.1016/0016-7037(76)90181-2

Osborne, M.J., Swarbrick, R.E., 1997. Mechanisms for Generating Overpressure in Sedimentary Basins: A Reevaluation. Am. Assoc. Pet. Geol. Bull. 81, 1023–1041.

Pallasser, R.J., 2000. Recognizing biodegradation in gas/oil accumulations through the δ13C compositions of gas components. Org. Geochem. 31, 1363–1373. https://doi.org/10.1016/S0146-6380(00)00101-7

Peters, K.E., Magoon, L.B., Lampe, C., Hosford Scheirer, A., Lillis, P.G., Gautier, D.L., 2007. A four-dimensional petroleum systems model for the San Joaquin Basin Province, California. USGS Prof. Pap. 1713, 35pp.

Phan, T.T., Capo, R.C., Stewart, B.W., Macpherson, G.L., Rowan, E.L., Hammack, R.W., 2016. Factors controlling Li concentration and isotopic composition in formation waters and host rocks of Marcellus Shale, Appalachian Basin. Chem. Geol. 420, 162–179. https://doi.org/10.1016/j.chemgeo.2015.11.003

Phan, T.T., Hakala, J.A., Sharma, S., 2020. Application of isotopic and geochemical signals in unconventional oil and gas reservoir produced waters toward characterizing in situ geochemical fluid-shale reactions. Sci. Total Environ. 714, 1–17. https://doi.org/10.1016/j.scitotenv.2020.136867

Polutranko, A.J., 1998. Causes of Formation and Distribution of Abnormally High Formation Pressure in Petroleum Basins of Ukraine, in: Law, B.E., Ulmishek, G.F., Slavin, V.I. (Eds.), Abnormal Pressures in Hydrocarbon Environments.

Prinzhofer, A., Battani, A., 2003. Gas isotopes tracing: An important tool for hydrocarbons exploration. Oil Gas Sci. Technol. 58, 299–311. https://doi.org/10.2516/ogst:2003018

Rostron, B., Arkadakskiy, S., 2014. Fingerprinting "stray" formation fluids associated with hydrocarbon exploration and production. Elements 10, 285–290. https://doi.org/10.1190/ice2015-2211363

Rowan, E.L., Engle, M.A., Kirby, C.S., Kraemer, T.F., 2011. Radium Content of Oil- and Gas-Field Produced Waters in the Northern Appalachian Basin (USA): Summary and Discussion of Data, USGS Scientific Investigations Report 2011–5135.

Rowan, E.L., Engle, M.A., Kraemer, T.F., Schroeder, K.T., Hammack, R.W., Doughten, M.W., 2015. Geochemical and isotopic evolution of water produced from Middle Devonian Marcellus shale gas wells, Appalachian Basin, Pennsylvania. Am. Assoc. Pet. Geol. Bull. 99, 181–206. https://doi.org/10.1306/07071413146

Saller, A.H., Stueber, A.M., 2021. Evolution of formation waters in the Permian Basin, United States: Late Permian evaporated seawater to Neogene meteoric water. Am. Assoc. Pet. Geol. Bull. 102, 401–428. https://doi.org/10.1306/0504171612517157

Schoell, M., 1988. Multiple origins of methane in the earth. Chem. Geol. 71, 1–10.

Schoell, M., 1983. Genetic Characterization of Natural Gases. Am. Assoc. Pet. Geol. Bull. 67, 2225–2238. https://doi.org/10.1306/AD46094A-16F7-11D7-8645000102C1865D

Smith, J.E., Erdman, J. g., Morris, D.A., 1971. Migration, accumulation and retention of petroleum in the earth, in: Proceedings of Eighth World Petroleum Congress, Moscow. Applied Science Publishers, London, pp. 13–26.

Stotler, R.L., Kirk, M.F., David Newell, K., Goldstein, R.H., Frape, S.K., Gwynne, R., 2021. Stable bromine isotopic composition of coal bed methane (CBM) produced water, the occurrence of enriched 81Br, and implications for fluid flow in the midcontinent, USA. Minerals 11. https://doi.org/10.3390/min11040358

Taylor, S.W., Sherwood Lollar, B., Wassenaar, L.I., 2000. Bacteriogenic Ethane in Near-Surface Aquifers : Implications for Leaking Hydrocarbon Well Bores. Environ. Sci. Technol. 34, 4727–4732.

Thornton, M.M., Wilson, A.M., 2007. Topography-driven flow versus buoyancy-driven flow in the U.S. midcontinent: implications for the residence time of brines. Geofluids 7, 69–78.

U.S. Dept. of Energy, 2022. Enhanced Oil Recovery [WWW Document]. URL https://www.energy.gov/fecm/enhanced-oil-recovery (accessed 3.13.23).

U.S. EPA, 2022. General Information About Injection Wells [WWW Document]. URL https://www.epa.gov/uic/general-information-about-injection-wells (accessed 3.13.23).

U.S. EPA, 2015. Case Study Analysis of the Impacts of Water Acquisition for Hydraulic Fracturing on Local Water Availability, EPA/600/R-14/179.

Ungerer, P., Burrus, J., Doligez, B., Chent, P.Y., Bessis, F., 1990. Basin evaluation by two-dimensional modeling of heat transfer, fluid flow, hydrocarbon generation, and migration. Am. Assoc. Pet. Geol. Bull. 74, 309–335.

Veil, J., 2012. U . S . Produced Water Volumes and Management Practices in 2012.

Vigier, N., Gislason, S.R., Burton, K.W., Millot, R., Mokadem, F., 2009. The relationship between riverine lithium isotope composition and silicate weathering rates in Iceland. Earth Planet. Sci. Lett. 287, 434–441. https://doi.org/10.1016/j.epsl.2009.08.026

Warner, N.R., Jackson, R.B., Darrah, T.H., Osborn, S.G., Down, A., Zhao, K., White, A., Vengosh, A., 2012. Geochemical evidence for possible natural migration of Marcellus Formation brine to shallow aquifers in Pennsylvania. Proc. Natl. Acad. Sci. U. S. A. 109, 11961–11966. https://doi.org/10.1073/pnas.1121181109

Whiticar, M.J., 2001. Characterization and Application of Sorbed Gas by Microdesorption CF-IRMS, in: AAPG Hedberg Conference "Near-Surface Hydrocarbon Migration: Mechanisms and Seepage Rates" September 16-19, 2001, Vancouver, BC, Canada. pp. 1–3.

Whiticar, M.J., 1999. Carbon and hydrogen isotope systematics of bacterial formation and oxidation of methane. Chem. Geol. 161, 291–314. https://doi.org/10.1016/S0009-2541(99)00092-3

Whiticar, M.J., 1994. Correlation of Natural Gases with Their Sources, in: Magoon, L.B., Dow, W.G. (Eds.), The Petroleum System - From Source to Trap. AAPG Memoir.

Williams, L.B., Hervig, R.L., Wieser, M.E., Hutcheon, I., 2001. The Influence of organic matter on the boron isotope geochemistry of the Gulf Coast sedimentary basin, USA. Chem. Geol. 174, 445–461. https://doi.org/10.1016/S0009-2541(00)00289-8

Zhou, Z., Ballentine, C.J., 2006. 4He dating of groundwater associated with hydrocarbon reservoirs. Chem. Geol. 226, 309–327.

Chapter 2: Evidence for Water of Condensation: A Third Source of Water in Shale Gas Wells

Published in AAPG Bulletin (2023) 107(4): 629-641.

ABSTRACT

Prior geochemical studies have reported that produced waters from shale gas and tight oil are a mixture of injected fluids and formation waters, with the latter dominating after the initial return of injected fluids. The assumption that later-stage produced water is largely representative of formation waters forms the basis of the current understanding of the source and behavior of deep fluids in shales and mudstones. Here, for the first time, I demonstrate the role of a third significant source of produced water in Marcellus Shale gas wells: water vapor condensing out of the gas phase. 'Water of condensation' is characterized by negligible salinity and an isotopically light composition (i.e., low $\delta^{18}O$ and $\delta^{2}H$). For wells with low daily produced water-to-gas volumes, water of condensation can mask the composition of downhole fluids (which represent an evolving mixture of injection fluid and formation water). End-member mixing between downhole fluids and water vapor in equilibrium with these fluids at reservoir temperatures can replicate the observed isotopic and chloride compositions of produced water samples. Results demonstrate that water of condensation, which occurs in surface samples from virtually all natural gas production systems, can significantly influence the composition of produced water in gas wells with low water production rates (a common feature of mature shale gas wells). The impact of water of condensation on produced water composition should be considered when investigating the nature and composition of deep formation waters in low permeability gas reservoirs.

INTRODUCTION

Investigations of produced water composition from oil and gas wells have provided insight into the movement and behavior of fluids in sedimentary basins, mineral diagenesis and hydrocarbon maturation, tectonic-related fluid redistribution, and the origin and conditions of evaporite sequence formation (e.g., Carpenter, 1978; Barnaby et al., 2004; Dresel and Rose, 2010; Rowan et al., 2015; Stewart et al., 2015; Phan et al., 2016; Renock et al., 2016; Chaudhary et al., 2019; Blondes et al., 2020). Until recently, this research has included minimal data from low-permeability shales and mudstones, which represent the most abundant types of sedimentary rock on the planet. This has changed markedly in the last 10-15 years with the emergence of produced water data from shale gas and tight oil reservoirs accessed by hydraulic fracturing. The Marcellus Shale, a hugely productive shale gas play in the United States yielding $34\text{x}10^9$ ft^3 ($97\text{x}10^7$ m^3) of gas per day (EIA, 2021), is one of the most well studied plays. It exhibits relatively low water saturation, with some considering it to contain negligible quantities of mobile water (Bryndzia and Fay, 2016). In fact, Marcellus Shale gas wells commonly only return between 8% and 12% of the volume of injected fracturing fluids back to surface over the life of the well (the remaining injected fluids are thought to be imbibed into the formation) (U.S. EPA, 2015). Despite this, the Marcellus has generated significant insight on fluid behavior in shales. Time-series produced water data from Marcellus Shale gas wells typically exhibit a pattern of rapidly increasing salinity and increasing δ^{18}O values, as well as shifting $^{87}\text{Sr}/^{86}\text{Sr}$ values, during the first few weeks to months of production, with the composition and salinity stabilizing by the end of the first year (Capo et al., 2014; Chapman et al., 2012; Haluszczak et al., 2013; Phan et al., 2020; Rowan et al., 2015). Based on geochemical interpretation of the corresponding brine composition, this increase in salinity is not caused by dissolution of salts (Rowan et al. 2015; Haluszczak et al. 2013). Rather, these compositional changes have primarily been attributed to a transition from generation of mostly injected water (hydraulic fracturing fluids, which often contain meteoric water) immediately after hydraulic fracturing to mostly naturally-occurring formation water as well production continues (e.g., Phan et al., 2020; Rowan et al., 2015). Studies of the behavior or composition of fluids from the Marcellus or other lower permeability sedimentary units generally assume that hydraulic fracturing fluids and natural formations waters are the only significant end-members, and collect samples to target one or the other (e.g., Chapman et al., 2012; Haluszczak et al., 2013; Rostron and Arkadakskiy, 2014; Rowan et al., 2015; Wright et al., 2019). Based on new evidence presented here, however, in some cases the composition of later-stage produced fluids may be strongly influenced by a third end-member: fresh water condensing out of the gas phase ("water of condensation").

Geochemical evidence for water of condensation was first demonstrated in deep (>3000 m, 100° - 150°C) conventional Gulf Coast reservoirs by Kharaka et al. (1977a, 1977b) and Poulson et al. (1995). Specifically, they reported that produced waters impacted by this process exhibited low salinity, silica depletion, isotopically light $\delta^{18}O$ values, and unusual behavior of geothermometers. By comparison, the Marcellus Shale is a shallower (1,500 to 2,750 m depth in areas of current production, EPA, 2011) unconventional shale gas system with lower present-day reservoir temperatures (approximately 35 to 75 °C) and relatively low water saturation. There has been scant other work on the influence of water of condensation on produced water composition, and I am not aware of any evaluation of the impact of water of condensation on the isotopic and chemical composition of produced water in shale gas plays.

Here, I show produced water isotopic and compositional data from Marcellus Shale gas wells in northeastern Pennsylvania that exhibit a later-stage (i.e., six months or more) shift to lower

$\delta^{18}O$ and δ^2H values and decreased salinity. This pattern inverts the typically reported trend of increasing salinity that stabilizes after the first year of production. I explain this newly observed pattern through a mass balance isotope model (using $\delta^{18}O$ and δ^2H of water) and demonstrate that it is likely the evolution of a produced water composition resulting from increasing contributions from water condensing out of the gas phase.

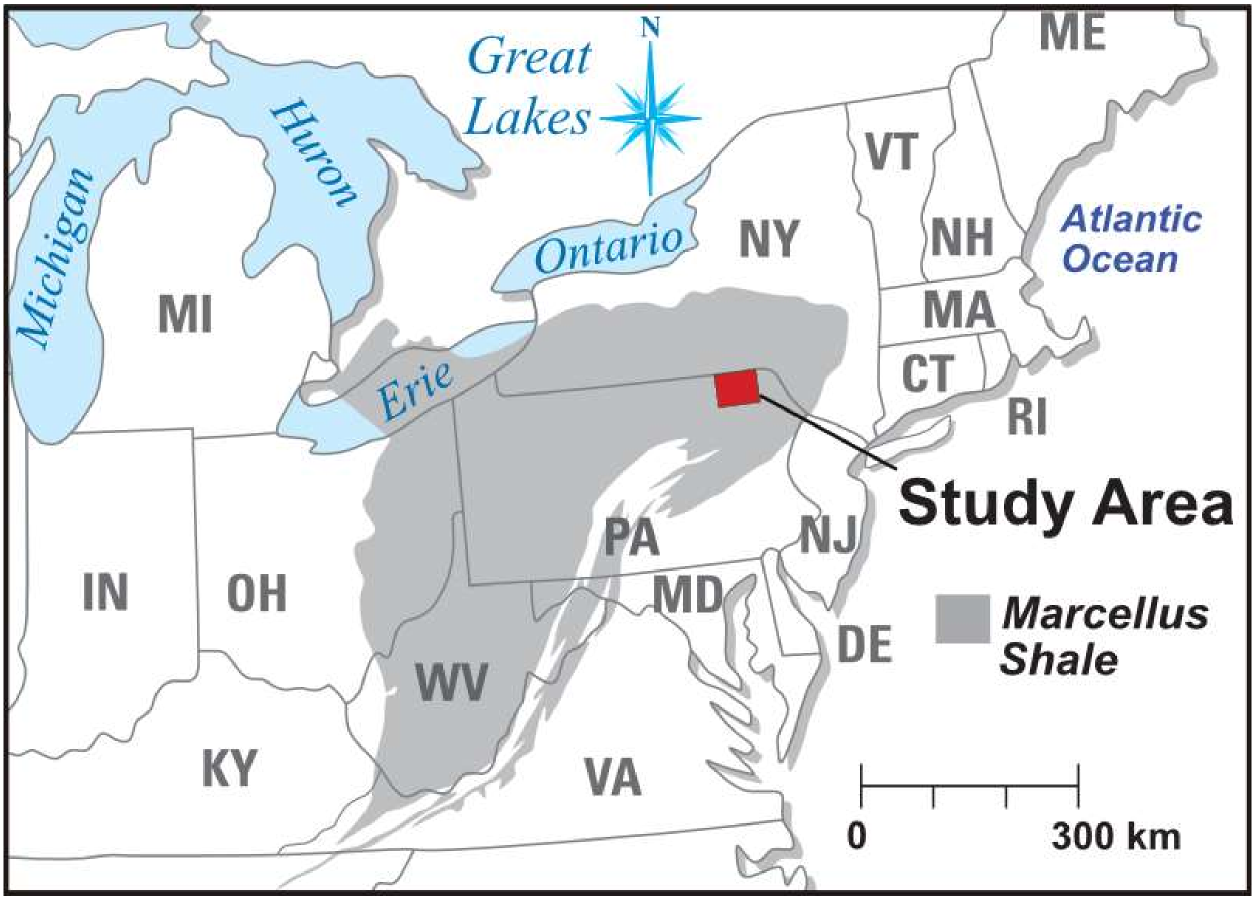

Figure 2.1: Susquehanna County in Pennsylvania where samples were collected for this study, and extent of Marcellus Shale (modified from Rowan et al. 2015, based on Milici and Swezey, 2006).

MATERIALS AND METHODS

Produced water data presented in this study ($\delta^{18}O$, $\delta^{2}H$, Cl, total dissolved solids (TDS), and average ratios of daily water vs. gas production) originate from Marcellus gas wells located in Susquehanna County, Pennsylvania (Figure 2.1). The Marcellus was deposited in the foreland basin of the Acadian orogenic belt circa 390 million years ago. Within the study area, the Marcellus is located at approximately 5500-7500 ft below ground level (1676-2286 m) and ranges from 160 to 480 ft thick (49-146 m). Present-day reservoir temperatures range from ~45°C in north/northwest Susquehanna County to ~75°C in south/southeast Susquehanna County, though the majority of sampled Marcellus gas wells produce from targeted zones with temperatures between 55°C and 65°C (average of 60°C). The Marcellus is dominated by black shale, but also contains interbedded limestone and lighter shales. There is no evidence of halite or other salt deposits within the Marcellus in the study area.

Data collected and presented in this study include: 1) discrete produced water samples from 230 Marcellus Shale gas wells (Table 2.1), and 2) time-series produced water samples from three Marcellus Shale gas wells (Well A – 26 samples, Well B - 25 samples, and Well C - 25 samples) that started producing in July 2019 (Tables 2.2, 2.3, and 2.4). This study also presents analysis of blended injection fluid utilized during hydraulic fracturing of Wells A, B, and C (3 samples total, 1 per well), comprised of >90% freshwater and <10% treated produced water (Tables 2.2, 2.3, and 2.4). These samples were collected before fracturing additives were added. However, because additives comprise <1% of injection fluid the water isotopic composition of the blended injection fluid should be largely representative of hydraulic fracturing fluid. Lastly, eight freshwater samples were collected from Susquehanna County permitted freshwater sources regularly utilized by the operator for fracturing fluid water supply (Table 2.5).

The 230 individual produced water samples originated from wells that had been in production from five days to 4,408 days (~12 years) at the time of collection. For the purposes of this paper, I define samples from wells in production for 6 months (~180 days) or more as "later-stage" production (190 wells, or 83% of samples). If multiple samples were available from each well, the most recent sample that met data quality assurance criteria within 10% charge balance was utilized (Reed and Mariner, 1991). Hydraulic fracturing was utilized to stimulate gas production in all wells; however, 11 of the 230 wells had vertical rather than horizontal wellbores, and were stimulated using one to three stages of injection fluid as opposed to five or more (Table 2.1). The time-series data from the three Marcellus wells represent produced water composition during the first three months following initial production, as well as two additional samples collected at 15 months and 16 months after production began. All produced water samples were collected directly from the water discharge port of the sealed gas-water separator into laboratory-supplied bottles. In accordance with the operator's standard of practice, water samples were not filtered prior to collection. Water isotope analysis ($\delta^{18}O$ and $\delta^{2}H$) was performed at Isotech Laboratories (Champaign, Illinois) by vacuum distillation followed by continuous flow-isotope ratio mass spectrometry (CF-IRMS), with a reported 1σ values of ±0.1‰ and ±2.0‰ for $\delta^{18}O$ and $\delta^{2}H$, respectively. Samples were analyzed for Cl and specific gravity at Environmental Service Laboratories, Inc. (Indiana, Pennsylvania) or at Green Analytical Laboratories (Durango, Colorado). Total dissolved solids concentrations (TDS) were calculated as the sum of all major ions.

Average daily water and gas production, measured with an Emerson R100 Coriolis meter and ABB Totalflow XMV meter, respectively, was evaluated for each well in this study for the relevant sampling dates. Specifically, daily water and gas volume measurements for the seven days prior to the sampling event, the day of the sampling event itself, and the seven days after the sampling event were averaged. The ratio of daily water production and gas production was then calculated based on these respective 15-day moving averages.

RESULTS

The $\delta^{18}O$ and $\delta^{2}H$ composition of the freshwater samples plot along the local meteoric water line for Pennsylvania (Figures 2.2A, B, and C) (Kendall and Coplen, 2001). Because injection fluid is comprised of >90% freshwater, its isotopic composition largely reflects that of fresh surface water, with some minor deviation associated with the significantly smaller (<10%) recycled produced water component. For all three wells with time-series data, produced water samples from the first day of production exhibited an isotopic composition that is relatively close to the injection fluid (Figures 2.2A, B, and C). Over the first three months of production, the isotopic composition becomes progressively heavier, and at the same time, TDS rises to 40,000 to ~80,000 mg/L (depending on the well). I interpret this change as a transition from produced water dominated by injection fluid to one comprised of an increasing percentage of higher salinity Marcellus formation fluid. This trend is consistent with previous interpretations from other time-series produced water investigations from shale gas and tight oil wells, which show produced water samples fall on a mixing line between injection fluid and Marcellus formation fluid (Chapman et al., 2013; Farrell et al., 2017; Haluszczak et al., 2013; Oetjen et al., 2018; Rosenblum et al., 2017; Rowan et al., 2015).

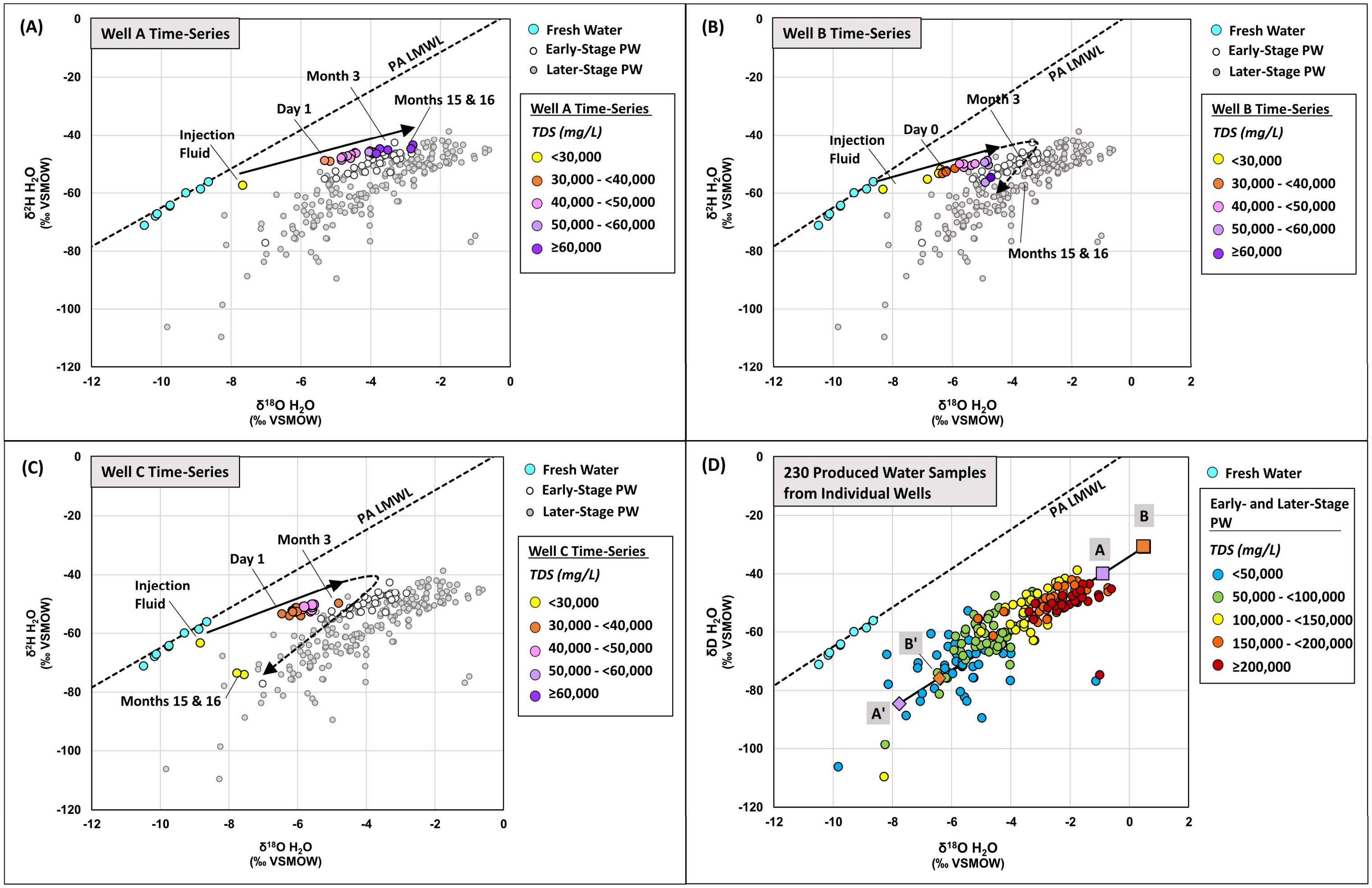

Figure 2.2: Water δ^2H vs. δ^{18}O values for A) Well A time-series data, B) Well B time-series data, C) Well C time-series data, and D) 230 produced water samples from Marcellus Shale gas wells sampled once each in Susquehanna County. Arrows on figures A-C indicate sequence of samples relative to time. Figure D also shows hypothetical mixing lines A-A' (purple) and B-B' (orange). On all plots, freshwater samples are shown as turquoise circles. Day 0 refers to samples collected during the first 24 hours of production. A single later-stage produced water sample with a δ2H value less than -120‰ was removed for plotting purposes.

At 15 and 16 months after production began, samples from Well A follow the previous pattern of increasing $\delta^{18}O$ and $\delta^{2}H$ values and TDS concentrations with time (Figure 2.2A). However, for Wells B and C samples, there is a shift to lighter $\delta^{18}O$ and $\delta^{2}H$ compositions, along the trend of later-stage produced water samples (the gray circles) (Figures 2.2B and C). Later-stage produced water samples generally exhibit a decline in salinity (Figure 2.2D) as their isotopic composition of water shifts from heavier to lighter $\delta^{18}O$ and $\delta^{2}H$ compositions. However, their water isotopic composition does not trend back towards the local meteoric water line, but roughly parallel to the local meteoric water line. This suggests the loss of salinity is not due to greater proportions of relatively fresh returned injection fluid.

I propose that this trend of increasingly lighter $\delta^{18}O$ and $\delta^{2}H$ and less saline later-stage produced water represents a third step in the evolution of produced water composition in some shale gas basins with low mobile water content: dilution of produced waters by water condensing out of the gas phase. Based on equilibrium conditions, a Marcellus production gas at a representative reservoir temperature of ~60°C is estimated to hold 0.2 bbls of water vapor per 10^{6} ft^{3} gas (1.1 m^{3} water/10^{6} m^{3} gas) (per the chart of the water content of sweet natural gases in McKetta and Wehe, 1958). The full range of reservoir temperatures in the study area (45°C to 75°C) results in only minor changes to this estimate (0.1 to 0.3 bbls water/10^{6} ft^{3} gas, or 0.6 to 1.7 m^{3} water/10^{6} m^{3} gas, respectively) (Table A.1). This water vapor, which is relatively fresh, condenses as temperatures decrease due to adiabatic expansion and lower geothermal temperatures once fluids leave the reservoir and/or at the surface when processed through a gas-water separator.

Changes in daily produced water-to-gas volumes over time support this hypothesis. Specifically, water volumes are higher (Figure 2.3A) during the first ~10 days of production as larger volumes of injected fracturing fluid are returned to the surface, then decrease over time as the well transitions to producing formation fluids mixed with remnant injection fluids. Very low daily ratios of water-to-gas production (e.g., <1 bbl water/10^6 ft^3 gas per day, or <5.6 m^3 water/10^6 m^3 gas per day) indicate that the well is producing little water relative to gas, as exhibited 15 and 16 months after production began at Wells B and C. Based on estimates of the amount of water vapor contained in Marcellus gas in the study area, a significant fraction of that water (~20%) is comprised of water condensing out of the gas phase.

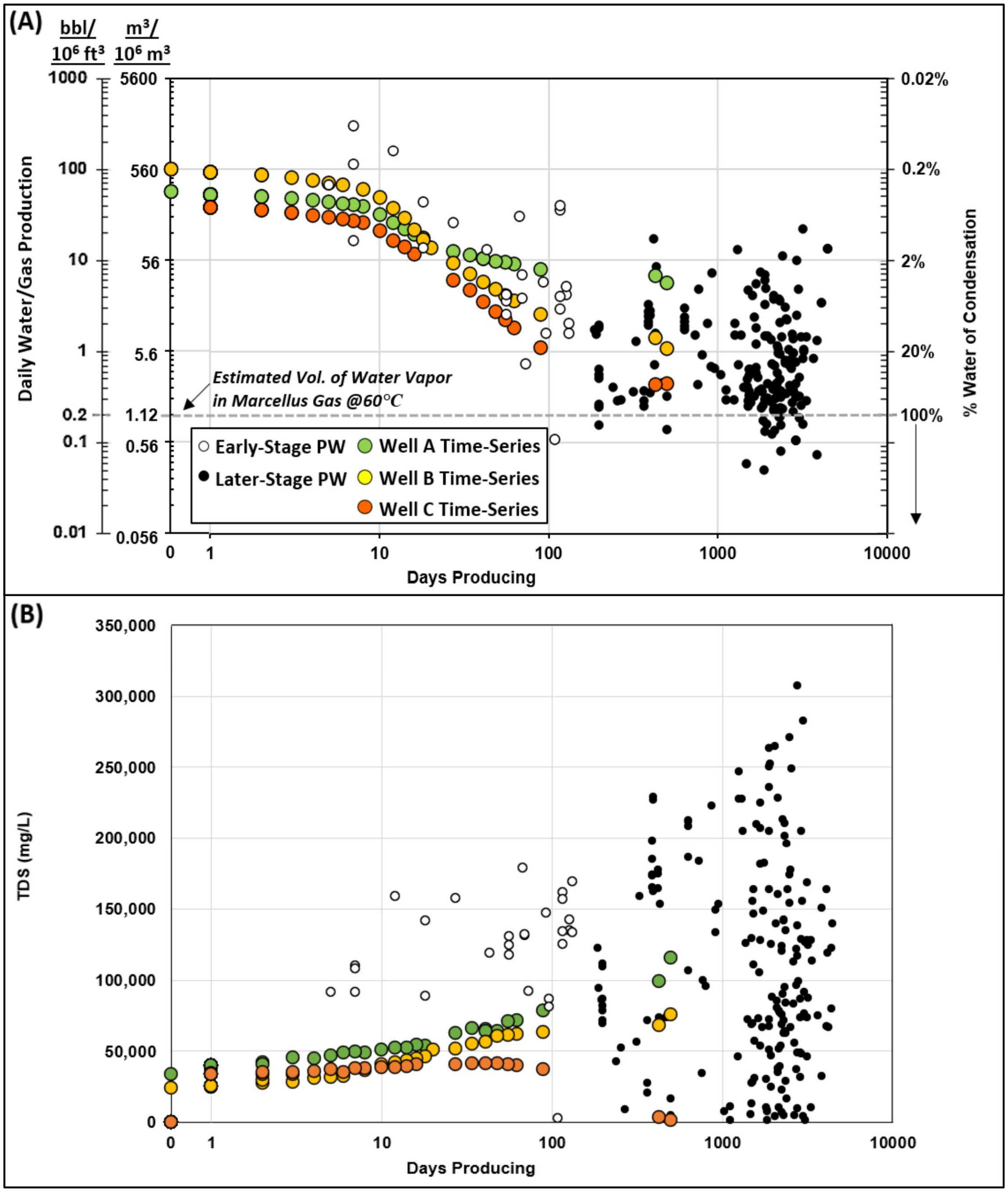

Figure 2.3: A) Daily water-to-gas production ratio (15 day moving average) vs. days producing, and B) TDS concentration vs. days producing for Wells A, B, and C time-series data and 230 produced water samples from Marcellus Shale gas wells sampled once each in Susquehanna County.

For Wells A, B, and C, daily water-to-gas production ratios rapidly decline during the first three months of production in concert with increasing TDS concentrations (Figures 2.3A and B, Figure A.1) representing a decline in the volume of injected fluid being returned to surface and a relative increase in the proportion of produced water comprised of formation fluid with high dissolved solids content. However, the three wells display different trends in daily water-to-gas ratios 15 and 16 months after production began, concomitant with significant changes in their water isotopic compositions (Figures 2.2A, B, and C). The water-to-gas ratio for Well A remains >1 bbl water/10^6 ft^3 gas (>5.6 m^3 water/10^6 m^3 gas), and samples continue to exhibit increasing TDS concentrations. This, along with a continuation in increasingly heavier water isotopes, suggests that Well A's produced water continues to be dominated by a significant fraction of formation fluids. The water-to-gas ratio for Well B declines to ~1 bbl water/10^6 ft^3 gas (~5.6 m^3 water/10^6 m^3 gas) at 15 and 16 months after production began, indicating that produced water from Well B is now approximately 80% downhole fluids, and 20% water of condensation. In this well, TDS concentrations still remain elevated at ~70,000 mg/L, reflecting a notable formation fluid component. In contrast, Well C displays a distinct decrease in the water-to-gas ratio 15 and 16 months after production began (to <0.5 bbls/10^6 ft^3 gas per day, or <2.8 m^3 water/10^6 m^3 gas per day). This correlates with a decrease in TDS concentrations, reflecting the fact that produced water from the well is now strongly influenced (≥40%) by water of condensation.

Because later-stage produced water samples from Marcellus wells were obtained six months or more after production began, the shift from primarily injection fluid (lower TDS, larger volumes) to formation fluid/injection fluid mix (higher TDS, smaller volumes) is not observed (Figure 2.2). Rather, in these samples, the highest daily water-to-gas ratio is associated with the highest TDS concentration (Figure A.1), suggesting that in a subset of wells, formation fluids continue to be produced in larger volumes over time (e.g., from certain permeable sub-strata of the Marcellus or from more transmissive underlying or overlying formations). In contrast, later-stage produced water samples that exhibit lower TDS and lower water-to-gas ratios are inferred to be increasingly dominated by water of condensation.

Of import, samples from Wells A, B, and C reach different maximum TDS and correspondingly heavier water isotope values before “rolling over” due to dilution from water condensing out of the gas phase. As noted above, this rollover occurs when the relative production of downhole fluids (comprised of a mixture of injection fluid and formation fluid) is small, such that water condensing out of the gas phase is a non-negligible component of total water production. I define a rollover point as the position on the oxygen-hydrogen isotope plot where the trajectory of the variation in the composition of the water reverses, becoming isotopically lighter with time (see Figures 2.2B and C). Based on this model, there are three key fluid components in this system: injection fluid, formation fluid, and water of condensation. However, all three water sources do not mix concurrently as would be the case in a ternary mixing model with independent, static end-members. Rather, this system represents a sequential bivariate mixing model, whereby the composition of the third source of water (water of condensation) necessarily forms from an evolving mixture of the first two sources (formation water and injection fluid) and correspondingly exhibits a dynamic and variable composition. As such, rollover points represent the specific injection water/formation water mixture at the time when water of condensation becomes an appreciable component of produced water.

The composition of water of condensation can be modeled by isotopic equilibrium between downhole fluids and water vapor, and plots on a line with a consistent slope (as described in the "End-Member Mixing" discussion below). Therefore, the isotopic composition of any produced water samples should plot on one of two intersecting lines: a) the mixing line between injection fluid and formation fluid, where this line represents the range of possible downhole fluid compositions, and b) the mixing line between downhole fluid at a given time and water vapor formed from that fluid. By this same logic, if a sample is suspected to be influenced by water of condensation, the downhole fluid composition can be determined by extending a line with a predictable slope through the sample affected by water of condensation until it intersects the mixing line between injection fluid and formation fluids. The relative contribution of water of condensation in a produced water sample can also be estimated by determining the approximate volume of water vapor contained within the volume of gas produced on a daily basis (per charts of the water content of natural gases at different reservoir temperatures), as a proportion of the total daily volume of water produced.

As observed in Figures 2.2B and C, rollover points appear at different compositions after differing amounts of production time for different wells. This variability likely reflects the composition and relative availability of movable water within the reservoir at different locations (which in turn is a function of a number of factors including water saturation, porosity, intrinsic permeability, and fracture density and connectivity, among others). For example, wells targeting units with lower volumes of movable water and higher imbibition rates are more likely to exhibit lower water-to-gas production ratios and more dilute water (containing a higher proportion of injection fluids). Such wells would experience rollover earlier than wells that continue to produce appreciable volumes of endogenous movable formation fluids or exogenous (out-of-zone) formation waters into later-stage production.

Other factors that could influence the isotopic composition of later-stage water include rock-water isotope interactions, variable fluid composition within the Marcellus, the presence of out-of-zone fluids, and fracturing fluid hits from nearby wells. However, none of these sufficiently explain the data. O'Neil and Kharaka (1976) showed that in order for isotope exchange to occur between waters and clay minerals at reservoir conditions, it takes a year or more at much higher temperatures (>100°C), and thus much faster reaction rates, than what is present in the Marcellus in the study area. At approximately half the reservoir temperature, it is improbable that such reactions are occurring on a timeframe consistent with this data (Rowan et al., 2015). With respect to variable fluid composition within the Marcellus and possible contributions from out-of-zone fluids, both are expected to exhibit relatively high salinity, generally similar major elemental composition, and isotopically heavy water (e.g., Osborn and McIntosh, 2010). As such, neither are consistent with the production of relatively fresh and isotopically light water. Similarly, hits of fracturing fluids from nearby wells would produce both an isotopically distinct composition (see Figure 2.2) and an anticipated increase in the rate of water vs. gas production, neither of which is observed in later-stage production.

END-MEMBER MIXING

To test my hypothesis that water of condensation represents a third significant source of later-stage produced water, I evaluated how well the observed data can be recreated, assuming a simple end-member mixture between downhole fluids and water of condensation. For this exercise, I assume a downhole fluid end-member that falls on the mixing line between injection fluid and Marcellus formation fluid with $\delta^{18}O$ and $\delta^{2}H$ values of -0.9‰ and -39.9‰, respectively (point A, Figure 2.2D). Point A was selected as an end-member because it represents the intersection of the mixing line between injection fluids and formation fluids (best-fit line to time-series data from

Well A) and the larger trend of produced water samples that extend down and to the left of this line (best-fit line for 190 later-stage produced water samples). The other end-member (point A' on Figure 2.2D) is calculated from Point A based on the isotopic composition of water vapor assumed to be in isotopic equilibrium with downhole fluid at typical reservoir temperature (~60°C) (per the temperature-dependent equilibration fractionation factors provided in Majoube, 1971, and utilized in Beaudoin and Therrien, 2021; $\delta^{18}O$ water-vapor $10^3\ln\alpha = 6.9$, δ^2H water-vapor $10^3\ln\alpha = 47.6$). I assume that nearly all water vapor is condensed as liquid water by the time the gas is processed through the separator. Based on that assumption, water of condensation will exhibit a nearly identical isotopic composition to water vapor. As seen on Figure 2.2D, the isotopic composition of most samples plot on a line between these two end-members.

However, I also needed to confirm that a mixture of these two end members was internally consistent with other physical and geochemical data. To that end, I compared the mixing percentage of water of condensation and downhole fluids calculated based on water isotopes to those based on: 1) daily ratios of water-to-gas production (Figure 2.4A) and 2) conservative chloride concentrations (Figure 2.4B). Mixing percentages based on water isotopes were calculated by finding the orthogonal projection of each sample's isotopic composition onto the A-A' mixing line. For daily ratios of water-to-gas production, I assume that every 10^6 ft^3 gas can carry ~0.20 bbls of water vapor (estimated per McKetta and Wehe, 1958 using a reservoir temperature of ~60°C). For chloride concentrations, I assume water of condensation contains negligible chloride, and downhole fluids contain 120,000 mg/L chloride, where the latter was estimated based on chloride concentrations of produced water samples plotting close to Point A.

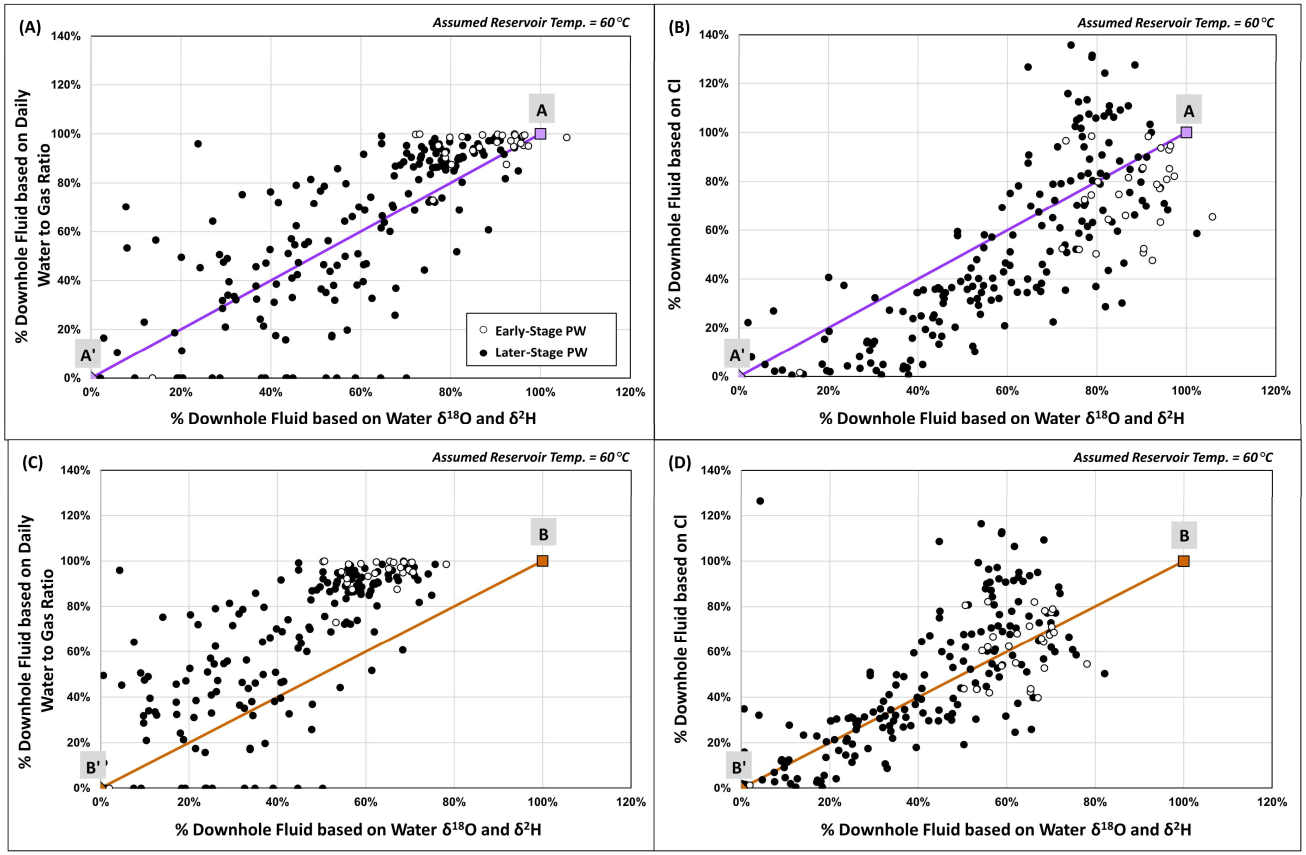

Figure 2.4: Estimated percentages of formation fluids based on A) the daily ratios of water-to-gas production and B) conservative Cl concentrations, versus the $\delta^{18}O$ and $\delta^{2}H$ composition of produced water using end-member mixing model A-A’, and C) the daily ratios of water-to-gas production and D) conservative Cl concentrations, versus the $\delta^{18}O$ and $\delta^{2}H$ composition of produced water using end-member mixing model B-B’. Values with negative proportions removed for plotting purposes. Due to variability in downhole fluid composition, in rare instances, the calculated percentage of downhole fluid based on the $\delta^{18}O$ and $\delta^{2}H$ composition and Cl concentration was greater than 100%.

As shown on Figure 2.4A, mixing percentages for the respective daily water-to-gas ratio and water isotope mass-balance methods generally fall along a 1:1 comparison line, suggesting that both parameters can be reasonably estimated from this simple mixing model. However, the comparison of Cl and water isotope data along a 1:1 line are less consistent. Specifically, roughly three-fourths of my data plot below the 1:1 comparison line for the respective Cl and water isotope mass balance methods, suggesting a moderate discrepancy between the two (Figure 2.4B). Samples whose data plot above the 1:1 comparison line exhibit higher salinity than those that plot below the line. These more saline samples also originate from wells with higher relative daily water production rates, indicative of a more mobile formation fluid component. I infer that these samples represent a range of downhole fluid compositions, both in-zone and out-of-zone, that are relatively unaffected by a small component of water of condensation. The variability in composition may reflect different mixtures of formation fluid and injection fluid within the Marcellus, or differences in the relative proportion or source of formation waters from more permeable out-of-zone strata (potentially accessed by faults and fractures). By comparison, samples whose data plot below the 1:1 line in Figure 2.4B generally exhibit lower chloride concentrations and originate from wells with lower relative daily water production rates. For this subset, I infer that a better mixing model fit may be obtained by increasing the assumed $\delta^{18}O$ and $\delta^{2}H$ values of the downhole fluid end-member, or decreasing the assumed chloride concentration. To increase the $\delta^{18}O$ and $\delta^{2}H$ end-member values, I must either assume that 1) there is a source of mobile downhole fluids that exhibit a heavier $\delta^{18}O$ and $\delta^{2}H$ values than Point A, or 2) the water isotopic composition of downhole fluids is altered during the course of production. It is unlikely that there is a source of mobile fluids with a heavier $\delta^{18}O$ and $\delta^{2}H$ values than produced water samples that plot near Point A, which is consistent with the heaviest values reported in the literature for Marcellus produced waters (Osborn and McIntosh, 2010; Rowan et al., 2015). Rather, I suggest that a secondary process could be altering the composition of downhole fluids over time at these wells, such as Raleigh-type fractionation. Specifically, as water vapor is formed and removed from the reservoir during production, the remaining downhole fluids would become enriched in the heavier isotopes and theoretically more saline over time. The effects of Raleigh-fractionation would only be evident where there was little mobile water to start with. In this case, I assume enriched $\delta^{18}O$ and $\delta^{2}H$ values of 0.5‰ and -30.8‰, respectively, and an associated chloride concentration of 140,000 mg/L for the end-member (Point B). Using this downhole fluid composition, and assuming equilibrium fractionation at 60°C, the water vapor is calculated to exhibit $\delta^{18}O$ and $\delta^{2}H$ values of water represented by Point B' (Figure 2.2D). Based on these end-members, samples with lower chloride concentrations and/or daily water-to-gas production ratios (i.e., those that plotted below the 1:1 line in Figure 2.4B) generally exhibit a better fit. That is, the mixing percentages calculated based on chloride concentrations and water isotopes are more equally distributed about the 1:1 comparison line (Figure 2.4D). However, mixing percentages calculated based on the daily water-to-gas ratios and water isotopes are notably less consistent (Figure 2.4C).

If instead of increasing the assumed $\delta^{18}O$ and $\delta^{2}H$ end-member values, I decrease the chloride concentration (e.g., to 60,000 mg/L, as might occur in wells that exhibit lower produced water chloride concentrations when the water isotopic composition rolls over), a similar trend is observed to that developed when Rayleigh fractionation is invoked. Specifically, samples with lower chloride concentrations and/or daily water-to-gas production ratios (i.e., those that plotted below the 1:1 line in Figure 2.4B) generally exhibit a better fit to the mixing model (Figures A.2 and A3). In reality, I anticipate that there are multiple mixing lines that could adequately describe the spread of data shown in Figure 2.2D, depending on the timing in the life cycle of the well and the range of conditions encountered in the reservoir. As an example of the latter, if I use the lower-end or upper-end reservoir temperatures (45°C and 75°C, respectively), the isotopic composition of water vapor in isotopic equilibrium with the downhole fluid shifts by up to ±2.1% for $\delta^{18}O$ and ±18.1‰ for $\delta^{2}H$ (see Table A.1 and Figure A.4). This shift is parallel or sub-parallel to the mixing line shown in Figure 2.2D, such that the slope of the A-A' mixing line remains relatively unchanged even though the calculated mixing percentages of water of condensation and downhole fluids change in accordance with the shifting end-members (Figures A.4, A.5, and A.6). Given the complexities of the study area and the number of samples presented here, it is unlikely that a single simple mathematical relationship can fully explain or even reasonably fit individual data points. Nevertheless, using a range of typical conditions, I can reasonably replicate large-scale trends across the study area in a manner that supports the hypothesis that produced water composition reflects an evolving mixture of downhole fluids and water of condensation.

CONCLUSIONS

This study provides the first evidence of the later-stage transition (i.e., six months or more) in the geochemical and isotopic composition of shale gas produced water from higher salinity and enriched $\delta^{18}O$ and $\delta^{2}H$ water to lower salinity and isotopically light water that is not consistent with simple mixing between formation water and injected fracturing fluids, but rather the addition of water condensing out of the gas phase. Key findings include the following:

1) Time-series produced water data from three Marcellus Shale gas wells in Susquehanna County, Pennsylvania, indicate an early transition (i.e., first 6 months of production) from produced water comprised of primarily injected fracturing fluids (low salinity, isotopically

light) to that containing a significant component of naturally-occurring formation water (high salinity, isotopically heavy).

2) This early transition is followed by a later-stage shift (i.e., six months or more) or “rollover” to produced water characterized by increasing proportions of water of condensation (lower TDS, isotopically light water). This shift in produced water composition is most common in Marcellus Shale gas wells producing relatively low water-to-gas production ratios (e.g., <1 bbl/10^6 ft^3 or <5.6 $m^3/10^6$ m^3), consistent with the expected water content of Marcellus gas at equilibrium conditions at reservoir temperature of ~60°C (~0.2 bbl/10^6 ft^3 gas or 1.1 $m^3/10^6$ m^3).
3) Simple end-member mixing models between injected fluids, formation water, and water of condensation largely recreate observed $\delta^{18}O$ and δ^2H compositions, chloride concentrations, and water-to-gas production ratios, suggesting the mechanism provides internally consistent interpretations.
4) Different wells experience rollover at different times, TDS concentrations, and water isotopic compositions likely as a result of differences in the availability of movable water and associated downhole fluid composition.
5) For produced water samples with a significant component of water of condensation, the downhole fluid water isotopic composition can be determined by extending a line with a predictable slope (calculated based on isotopic equilibrium between water and water vapor at reservoir temperature) through the sample affected by water of condensation until it intersects the mixing line between injection fluid and formation fluids. The relative contribution of water of condensation in a produced water sample can also be estimated by

determining the volume of water vapor contained within any daily volume of gas, as a fraction of the total water produced.

This work counters the widely reported finding that later-stage produced water from shale gas wells is largely dominated by formation fluids, an assumption which underpins much of the basic insight about movement and processes involving deep fluids from shales (e.g., Capo et al., 2014; Rowan et al., 2015; Phan et al., 2016; Blondes et al., 2020). Rather, this study demonstrates that in shale gas plays with low water production rates, the relatively small volume of downhole fluids (comprised of formation water and remnant injection fluid) produced at the surface may be significantly diluted by water condensing out of the gas phase as production continues. The fact that the majority of produced water samples in this study are affected by water of condensation suggest that this phenomenon could be commonplace during mature production from gas reservoirs with low permeability and/or water saturation, and should be accounted for when evaluating the nature and composition of deep formation waters in such reservoirs.

Table 2.1: Chemical analyses of 230 produced water samples from Marcellus Shale gas wells sampled once each.

Well	Sample Date	Days Producing	Daily Water/Gas 15 Day Moving Avg.		$\delta^{18}O$ (‰ VSMOW)	$\delta^{2}H$ (‰ VSMOW)	Chloride (mg/L)	TDS (mg/L)
			bbl/10^6ft^3	m^3/10^6m^3				
1V	9/22/2020	4393	0.0	0.0	-3.06	-48.8	44300	79700
2V	9/22/2020	4393	0.0	0.0	-1.76	-38.7	70400	122200
3V	9/22/2020	4084	0.0	0.0	-5.09	-60.6	38400	67200
4V	9/22/2020	4408	13.7	76.8	-2.18	-41.6	82000	139800
5V	12/14/2017	3373	0.0	0.0	-8.28	-109.6	63000	113800
6V	9/22/2020	4163	0.0	0.0	-3.11	-46.6	71500	119200
7	12/6/2017	2760	1.0	5.5	-8.51	-156.2	189000	307200
8V	12/19/2017	3156	0.0	0.0	-3.48	-47.1	76000	128100
9	12/6/2017	3029	0.0	0.0	-6.48	-74.0	44900	76500
10	11/29/2017	3158	0.2	0.9	-7.06	-83.7	26600	46100
11V	9/22/2020	4076	3.5	19.7	-1.77	-42.4	93000	163700
12V	9/22/2020	4180	0.0	0.0	-3.28	-46.1	36200	66600
13	12/12/2017	2867	0.1	0.6	-4.00	-67.4	19000	31900
14	12/14/2017	2915	0.0	0.0	-3.20	-62.9	71300	128400
15V	11/28/2017	2956	0.0	0.0	-1.44	-45.6	90700	155300
16	10/21/2020	3849	0.1	0.4	-1.13	-76.8	18400	32700
17V	11/29/2017	2976	4.9	27.4	-1.00	-74.7	177000	282500
18	12/6/2017	3004	0.5	3.0	-8.25	-98.6	44500	74500
19	12/13/2017	2858	0.4	2.5	-7.54	-88.6	28200	49200
20	11/21/2017	2754	0.2	1.3	-5.57	-82.2	5840	9600
21	11/29/2017	2864	0.3	1.8	-3.86	-58.1	51500	86800
22	11/29/2017	2805	0.4	2.0	-4.12	-60.8	57500	98800
23	11/21/2017	2773	0.4	2.3	-2.31	-48.2	81700	138100
24	11/21/2017	2734	0.3	1.6	-4.98	-89.4	20400	36800
25	12/19/2017	1842	0.2	1.0	-5.84	-67.5	785	1300
26	3/13/2019	3191	1.0	5.7	-3.33	-47.5	52200	87300
27	12/13/2017	1870	0.1	0.3	-5.20	-65.0	30400	51000
28	10/14/2020	3814	1.3	7.4	-1.95	-42.0	85200	150300
29	11/29/2017	2722	1.6	8.8	-2.91	-49.5	68400	121600
30	9/29/2020	3645	0.9	4.8	-5.87	-61.5	42900	75000
31	11/29/2017	2636	0.8	4.5	-5.53	-69.5	32700	55800
32	11/21/2017	2296	0.2	1.1	-3.56	-58.3	83200	142400
33	11/30/2017	2355	0.2	0.9	-5.28	-71.8	17500	28900
34	11/18/2017	2352	0.2	1.4	-4.88	-60.5	48200	84100
35	10/28/2020	3306	0.3	1.7	-5.85	-70.1	5860	10300
36	11/8/2018	2329	0.3	1.8	-3.59	-54.2	55200	95200
37	11/18/2017	2235	0.4	2.2	-3.84	-59.3	68600	120500
38	11/18/2017	2235	0.4	2.1	-3.56	-57.2	69600	123700
39	11/28/2017	2346	0.4	2.1	-4.44	-61.4	37300	62300
40	11/28/2017	2346	0.1	0.5	-2.46	-53.3	78100	135000

Note: V = Vertical wellbore

Table 2.1: Continued.

Well	Sample Date	Days Producing	Daily Water/Gas 15 Day Moving Avg.		δ^{18}O (‰ VSMOW)	δ^{2}H (‰ VSMOW)	Chloride (mg/L)	TDS (mg/L)
			bbl/10^{6}ft^{3}	m^{3}/10^{6}m^{3}				
41	11/21/2017	2472	0.8	4.6	-3.04	-53.0	86800	153800
42	11/18/2017	2516	0.3	1.9	-4.28	-64.1	38400	66400
43	11/21/2017	2381	1.5	8.3	-2.44	-50.1	113000	195900
44	11/21/2017	2472	0.8	4.3	-2.38	-49.7	100000	173900
45	9/30/2020	3193	1.1	6.0	-3.24	-62.9	69300	124700
46	11/21/2017	2504	2.3	13.0	-1.84	-45.5	102000	177600
47	9/29/2020	3020	0.3	1.9	-3.67	-57.5	54700	91300
48	12/14/2017	2215	0.3	1.8	-4.34	-60.4	30700	53600
49	12/5/2017	2395	0.2	1.3	-5.49	-83.6	9600	16300
50	11/21/2017	2272	1.1	6.2	-1.35	-43.4	120000	213400
51	9/23/2020	3334	1.5	8.2	-2.54	-50.3	76400	127700
52	12/12/2017	2319	1.0	5.3	-4.31	-64.2	36100	64100
53	3/13/2019	2303	0.5	2.8	-4.77	-54.6	43900	71800
54	11/20/2017	1825	0.4	2.0	-6.13	-73.7	5180	8500
55	11/30/2017	1835	0.3	1.5	-5.43	-67.7	4250	7400
56	9/29/2020	3160	0.8	4.7	-5.70	-66.6	41400	73800
57	10/29/2018	2305	0.2	1.4	-5.55	-60.4	35100	62500
58	10/29/2018	2305	0.2	1.1	-6.15	-75.8	2810	5000
59	10/23/2018	2226	0.5	2.6	-6.70	-60.6	12300	22700
60	10/23/2018	2226	0.3	1.8	-8.19	-67.7	3790	6600
61	11/28/2017	1744	0.4	2.1	-2.76	-57.6	90200	148500
62	9/21/2020	3163	22.6	126.6	-5.12	-55.4	105000	168200
63	11/28/2017	2073	0.7	4.2	-2.61	-50.8	84300	139700
64	11/21/2017	2132	4.2	23.4	-4.24	-53.0	94700	160000
65	10/23/2018	2226	0.6	3.3	-4.98	-58.4	38500	68800
66	10/23/2018	2226	1.2	6.6	-5.25	-54.1	41900	75700
67	12/13/2017	2119	0.2	1.3	-5.25	-75.7	22300	37600
68	11/9/2020	2897	2.5	14.2	-5.45	-52.8	26900	47900
69	10/22/2018	2148	0.3	1.7	-4.24	-61.2	44400	78100
70	9/23/2020	3079	1.5	8.1	-2.65	-50.6	70500	126200
71	9/23/2020	3079	0.3	1.5	-6.58	-79.3	686	1200
72	10/12/2020	2865	0.8	4.3	-5.14	-56.5	41500	73900
73	10/22/2018	2144	0.1	0.8	-4.01	-65.3	29000	51800
74	10/22/2018	2144	0.2	1.4	-4.87	-66.2	5850	10100
75	10/14/2020	2756	1.4	7.9	-5.01	-59.9	69700	117200
76	11/20/2017	1880	0.3	1.7	-3.09	-56.7	93900	163300
77	11/20/2017	1880	3.3	18.5	-1.75	-49.9	136000	236100
78	11/20/2017	1880	1.5	8.3	-1.40	-49.5	157000	263200
79	9/21/2020	2916	10.1	56.9	-3.18	-50.3	122000	204500
80	12/13/2017	1712	0.5	3.0	-5.67	-64.0	39700	66600

Table 2.1: Continued.

Well	Sample Date	Days Producing	Daily Water/Gas 15 Day Moving Avg.		δ^{18}O (‰ VSMOW)	δ^{2}H (‰ VSMOW)	Chloride (mg/L)	TDS (mg/L)
			bbl/10^6ft^3	m^3/10^6m^3				
81	10/12/2020	3003	0.2	1.1	-5.28	-75.6	2380	4300
82	11/21/2017	1950	0.3	1.8	-4.14	-61.7	48800	88100
83	9/14/2020	2630	0.7	3.9	-4.39	-62.4	46800	83200
84	11/30/2017	1669	1.2	6.8	-2.20	-50.9	126000	207200
85	10/29/2018	1944	0.5	2.5	-5.42	-62.8	24400	46800
86	11/20/2017	1806	0.2	1.4	-4.02	-76.6	6050	10500
87	11/20/2017	1806	0.4	2.2	-5.09	-71.1	17400	30400
88	12/13/2017	1876	0.1	0.8	-4.57	-64.5	43100	72000
89	9/28/2020	2716	0.7	3.8	-4.58	-57.8	55900	96600
90	12/13/2017	1884	0.3	1.7	-4.03	-71.2	38800	67700
91	12/13/2017	465	0.5	2.6	-5.02	-64.6	43700	73400
92	10/14/2020	2770	0.4	2.1	-4.26	-67.3	28600	49000
93	11/30/2017	1673	0.6	3.3	-2.78	-55.7	109000	181300
94	11/8/2018	2088	0.1	0.7	-4.21	-60.1	44800	80600
95	11/28/2017	1510	0.3	1.9	-5.18	-64.5	16000	28000
96	12/13/2017	1626	0.3	1.8	-4.49	-66.2	42600	72900
97	9/7/2017	1490	0.4	2.4	-4.74	-66.8	41400	68500
98	10/28/2020	2637	0.4	2.4	-6.99	-81.0	2610	4600
99	10/12/2020	2621	1.1	6.0	-3.41	-51.9	64700	112800
100	9/7/2017	1490	0.5	2.9	-2.75	-44.9	79400	129200
101	12/12/2017	1499	0.3	1.6	-4.28	-60.3	41400	69200
102	12/21/2017	1672	0.7	3.8	-6.42	-81.2	32300	53600
103	12/12/2017	1499	4.8	26.9	-2.97	-49.9	85500	155400
104	11/29/2017	1642	2.4	13.4	-4.02	-57.4	61300	105100
105	12/12/2017	1295	13.2	74.1	-1.04	-47.3	127450	227700
106	12/21/2017	1672	1.9	10.4	-3.40	-49.6	73800	128100
107	12/12/2017	1492	0.3	1.4	-5.18	-67.4	7900	13100
108	12/7/2017	1471	0.1	0.3	-5.71	-80.4	3150	5400
109	12/20/2017	1518	0.6	3.1	-2.76	-55.5	83900	146400
110	12/20/2017	1518	0.6	3.6	-2.80	-52.4	94950	163900
111	12/20/2017	1518	0.4	2.1	-3.33	-60.2	63400	110400
112	9/21/2020	2547	2.2	12.5	-2.23	-51.8	139000	248800
113	9/30/2020	2322	3.6	20.2	-2.02	-50.6	127000	210200
114	11/28/2017	1410	0.4	2.3	-4.45	-65.0	43000	72500
115	12/21/2017	1369	1.5	8.5	-3.17	-54.3	74200	126100
116	10/28/2020	2412	11.3	63.2	-2.43	-44.3	95700	163700
117	11/28/2017	1116	0.3	1.7	-5.64	-70.3	775	1400
118	11/28/2017	1116	0.4	2.1	-5.62	-71.4	6550	11200
119	9/21/2020	2473	3.1	17.2	-2.17	-51.5	163000	271100
120	10/14/2020	2166	0.4	2.5	-5.19	-63.2	43800	77000

Table 2.1: Continued.

Well	Sample Date	Days Producing	Daily Water/Gas 15 Day Moving Avg.		δ^{18}O (‰ VSMOW)	δ^{2}H (‰ VSMOW)	Chloride (mg/L)	TDS (mg/L)
			bbl/10^{6}ft^3	m^3/10^{6}m^3				
121	9/30/2020	2322	2.1	11.8	-2.45	-52.8	113000	201100
122	11/20/2017	1249	2.0	11.5	-1.02	-48.2	149000	247000
123	11/20/2017	1249	1.5	8.5	-1.83	-49.7	129000	227300
124	12/20/2017	1319	0.7	4.0	-2.49	-51.0	122959	204900
125	10/6/2020	1945	1.5	8.3	-3.52	-52.4	73100	125400
126	10/28/2020	1554	0.3	1.6	-6.24	-71.4	16700	31000
127	9/30/2020	2122	0.2	1.3	-6.12	-65.0	20400	35200
128	9/23/2020	2261	1.0	5.5	-3.95	-59.2	48400	90200
129	12/7/2017	1240	0.3	1.7	-5.01	-64.5	27100	45800
130	10/14/2020	2165	0.7	4.0	-4.45	-66.0	23300	38900
131	12/12/2017	908	0.7	3.9	-3.23	-54.6	80900	133000
132	9/29/2020	2283	3.8	21.4	-3.65	-49.9	84200	141600
133	9/30/2020	1886	6.2	34.7	-1.78	-49.0	127000	204800
134	9/30/2020	2127	3.8	21.4	-2.75	-51.7	139000	228000
135	9/23/2020	2104	0.4	2.2	-6.20	-75.6	48800	85200
136	3/13/2019	1544	0.6	3.6	-4.54	-47.6	34400	57300
137	11/29/2017	946	0.7	3.7	-3.29	-54.5	89800	153400
138	11/29/2017	635	2.2	12.1	-1.60	-47.7	130000	208200
139	11/29/2017	635	3.0	17.0	-1.85	-43.8	108000	186300
140	11/29/2017	635	2.4	13.5	-1.57	-43.5	124000	211500
141	9/30/2020	1668	5.6	31.2	-2.28	-50.7	135000	225000
142	11/29/2017	632	1.9	10.7	-1.60	-48.2	128000	212200
143	9/29/2020	2040	1.4	7.6	-1.84	-49.4	158000	264600
144	12/21/2017	316	0.4	2.1	-5.62	-68.1	32100	56600
145	12/12/2017	1028	0.6	3.1	-6.23	-72.4	4020	7400
146	3/13/2019	1483	0.4	2.3	-5.65	-71.8	16800	27800
147	9/23/2020	2044	0.3	1.6	-9.83	-106.2	2480	4200
148	10/28/2020	1885	7.0	39.4	-0.61	-45.2	153000	250500
149	10/14/2020	1768	7.5	42.2	-2.22	-44.6	108000	182500
150	11/30/2017	865	2.1	11.6	-1.93	-47.6	133000	222800
151	9/30/2020	1900	5.0	27.9	-3.23	-55.7	152000	252100
152	10/14/2020	1933	0.2	0.9	-6.10	-60.9	15000	24700
153	11/20/2017	363	0.3	1.6	-5.63	-71.5	12800	20600
154	11/20/2017	363	0.3	1.4	-5.63	-71.2	16000	27500
155	11/20/2017	363	0.4	2.1	-4.82	-63.9	41300	71500
156	11/29/2017	388	2.1	12.0	-2.75	-49.5	107000	173600
157	11/29/2017	388	2.0	11.0	-2.55	-47.8	98700	173100
158	11/29/2017	388	2.8	15.6	-2.72	-49.2	96500	164700
159	9/16/2020	1587	4.2	23.5	-2.26	-47.6	115000	209400
160	11/29/2017	388	2.5	14.0	-2.31	-50.3	118000	198100

Table 2.1: Continued.

Well	Sample Date	Days Producing	Daily Water/Gas 15 Day Moving Avg.		δ^{18}O (‰ VSMOW)	δ^{2}H (‰ VSMOW)	Chloride (mg/L)	TDS (mg/L)
			bbl/10^6ft^3	m^3/10^6m^3				
161	11/28/2017	96	0.0	0.0	-3.95	-48.4	50700	86400
162	11/28/2017	96	1.6	9.0	-4.05	-47.6	47600	81300
163	11/29/2017	388	3.3	18.7	-2.24	-46.5	106000	184900
164	11/30/2017	326	1.3	7.4	-2.83	-48.4	94800	158800
165	12/20/2017	126	4.3	23.9	-3.18	-46.3	85250	142400
166	12/20/2017	126	5.2	29.1	-3.30	-46.5	80900	134500
167	11/21/2017	394	2.5	14.2	-1.79	-46.5	131000	226600
168	11/21/2017	394	2.8	15.7	-1.65	-45.7	133000	228900
169	11/21/2017	394	0.4	2.0	-2.91	-51.4	96400	162100
170	12/21/2017	27	26.2	146.9	-2.83	-46.4	92900	157600
171	12/20/2017	69	3.9	21.7	-3.38	-47.1	77150	131600
172	12/20/2017	69	7.0	39.4	-3.64	-47.3	78900	132200
173	12/4/2017	131	1.6	9.0	-3.83	-52.3	79900	133600
174	12/20/2017	418	1.4	7.7	-2.66	-48.4	100000	174700
175	12/20/2017	418	0.7	4.0	-3.15	-50.3	98800	164300
176	11/20/2017	254	0.3	1.6	-5.92	-66.2	29900	52100
177	11/20/2017	239	0.4	2.3	-5.18	-57.8	25100	42900
178	9/16/2020	131	2.1	11.5	-3.44	-52.9	98500	168900
179	12/12/2017	196	0.6	3.6	-5.21	-57.1	46250	85700
180	12/12/2017	189	1.6	8.8	-4.57	-53.6	51400	94000
181	9/30/2020	804	0.9	5.3	-4.62	-61.3	53400	95700
182	10/23/2018	198	0.3	1.5	-4.73	-54.1	45900	81600
183	10/23/2018	198	0.6	3.1	-5.53	-59.1	37600	69700
184	10/23/2018	198	0.2	0.9	-5.09	-55.5	41400	71800
185	10/23/2018	198	0.5	2.9	-4.78	-55.5	48000	86300
186	10/23/2018	198	0.2	1.4	-5.12	-58.9	43600	78300
187	10/22/2018	43	13.4	75.1	-3.32	-42.6	65400	119200
188	10/15/2018	56	2.6	14.5	-4.16	-52.8	74500	130700
189	10/15/2018	56	3.7	20.5	-4.09	-49.9	66000	117600
190	10/15/2018	56	4.2	23.8	-4.66	-53.3	72600	124200
191	3/13/2019	185	1.8	9.8	-3.32	-49.1	75800	122500
192	10/23/2018	198	1.8	10.2	-3.93	-50.7	62600	111200
193	10/12/2020	918	7.3	41.1	-2.21	-43.8	83900	149300
194	10/23/2018	198	2.0	11.1	-4.19	-51.6	61000	109400
195	9/28/2020	759	0.4	2.5	-5.89	-64.1	19900	34600
196	10/21/2020	733	1.5	8.6	-2.25	-48.3	109000	183200
197	10/5/2020	428	8.7	48.6	-2.19	-44.2	86700	153400
198	9/14/2020	628	1.7	9.8	-3.58	-53.4	61600	106500
199	9/10/2020	768	4.9	27.3	-2.64	-46.0	55800	99400
200	9/23/2020	267	0.3	1.7	-6.50	-67.9	5020	8700

Table 2.1: Continued.

Well	Sample Date	Days Producing	Daily Water/Gas 15 Day Moving Avg.		$\delta^{18}O$ (‰ VSMOW)	$\delta^{2}H$ (‰ VSMOW)	Chloride (mg/L)	TDS (mg/L)
			bbl/10^6ft^3	m^3/10^6m^3				
201	5/2/2019	5	68.0	381.7	-5.32	-55.1	52400	91500
202	7/25/2019	7	115.0	645.0	-3.75	-48.4	52400	91700
203	7/25/2019	7	16.7	93.8	-4.48	-51.3	64400	109700
204	7/25/2019	7	305.9	1716.1	-3.59	-47.0	63300	107700
205	7/19/2019	67	30.7	172.2	-3.15	-48.1	98400	179100
206	12/18/2019	116	36.1	202.3	-3.16	-46.2	94600	161600
207	12/18/2019	116	40.5	227.5	-3.34	-47.0	93700	156900
208	10/14/2020	417	17.3	97.2	-2.42	-44.2	102000	177000
209	11/18/2020	495	0.3	1.9	-7.13	-70.6	2890	5000
210	11/18/2020	495	0.5	2.6	-8.14	-77.9	1130	2000
211	11/18/2020	495	0.1	0.8	-7.15	-72.3	9760	16500
212	9/10/2020	426	1.6	9.1	-4.40	-51.7	42500	73500
213	11/19/2020	496	1.4	7.7	-4.19	-53.0	49800	90200
214	11/19/2020	496	2.9	16.2	-3.10	-46.9	59200	103900
215	10/28/2020	108	0.1	0.6	-7.02	-77.1	1610	2800
216	10/12/2020	92	5.9	33.0	-3.26	-48.6	85600	147100
217	7/30/2020	18	13.9	77.8	-5.01	-52.5	50300	89000
218	7/30/2020	18	44.6	250.0	-3.74	-49.8	81600	141800
219	11/19/2020	496	5.7	32.0	-2.49	-42.9	67300	114700
220	10/12/2020	351	0.3	1.8	-5.97	-74.2	1160	2200
221	10/12/2020	351	7.7	43.2	-2.37	-42.5	76700	130100
222	12/18/2019	116	4.0	22.7	-3.65	-46.0	82200	133700
223	12/18/2019	116	3.0	16.6	-4.25	-50.6	74800	125100
224	2/17/2020	12	162.6	912.4	-4.99	-55.0	96600	159000
225	9/21/2020	229	0.4	2.5	-4.60	-61.3	96400	164600
226	9/16/2020	206	16.5	92.8	-2.61	-50.2	137000	241200
227	9/16/2020	206	1.7	9.3	-3.39	-53.0	118000	214300
228	9/30/2020	73	0.7	4.1	-4.48	-53.9	52100	92300
229	12/7/2017	1541	25.9	145.1	-0.72	-44.8	120000	192300
230	9/23/2020	2562	115.8	649.8	-0.72	-46.2	118000	186000

Table 2.2: Chemical analyses of Well A injection fluid and time-series produced water samples.

Well	Matrix	Sample Date	Days Producing	Daily Water/Gas 15 Day Moving Avg.		$\delta^{18}O$ (‰ VSMOW)	$\delta^{2}H$ (‰ VSMOW)	Chloride (mg/L)	TDS (mg/L)
				bbl/10^6ft^3	m^3/10^6m^3				
A	Injection Fluid	5/7/2019	--	--	--	-7.67	-57.3	17400	30000
A	Produced Water	7/12/2019	0	57.1	320.1	-5.32	-48.8	19600	33500
A	Produced Water	7/13/2019	1	53.5	300.3	-5.17	-49.1	22300	38600
A	Produced Water	7/13/2019	1	53.5	300.3	-4.85	-47.9	23300	40200
A	Produced Water	7/14/2019	2	50.7	284.6	-4.84	-48.7	24200	42000
A	Produced Water	7/14/2019	2	50.7	284.6	-4.80	-47.5	22900	40300
A	Produced Water	7/15/2019	3	48.2	270.2	-4.67	-47.2	26600	45200
A	Produced Water	7/16/2019	4	46.1	258.4	-4.77	-47.8	26100	44800
A	Produced Water	7/17/2019	5	44.2	248.2	-4.58	-48.1	26800	46900
A	Produced Water	7/18/2019	6	42.5	238.6	-4.56	-46.8	27500	48700
A	Produced Water	7/19/2019	7	40.9	229.7	-4.42	-46.3	28400	49200
A	Produced Water	7/20/2019	8	39.6	222.4	-4.45	-46.1	28700	49200
A	Produced Water	7/22/2019	10	31.9	179.0	-4.67	-47.9	29700	51000
A	Produced Water	7/24/2019	12	26.1	146.3	-4.18	-46.8	29900	52500
A	Produced Water	7/26/2019	14	22.2	124.6	-4.24	-46.7	30000	52600
A	Produced Water	7/28/2019	16	19.7	110.4	-4.25	-45.9	30000	54600
A	Produced Water	7/30/2019	18	17.7	99.4	-4.24	-47.9	30700	53500
A	Produced Water	8/8/2019	27	12.8	71.5	-4.05	-45.9	36000	62900
A	Produced Water	8/15/2019	34	11.6	65.1	-3.93	-46.1	37900	66100
A	Produced Water	8/22/2019	41	10.6	59.6	-4.02	-45.5	37600	65400
A	Produced Water	8/22/2019	41	10.6	59.6	-3.95	-46.5	38500	63800
A	Produced Water	8/29/2019	48	10.0	55.9	-3.90	-45.9	39800	63900
A	Produced Water	9/5/2019	55	9.5	53.6	-3.84	-46.4	40600	71100
A	Produced Water	9/12/2019	62	9.2	51.5	-3.74	-44.8	42000	71600
A	Produced Water	10/9/2019	89	8.0	45.1	-3.51	-45.2	46800	78300
A	Produced Water	9/9/2020	425	6.8	38.3	-2.85	-44.8	56900	98900
A	Produced Water	11/19/2020	496	5.8	32.4	-2.79	-43.5	65900	115400

Table 2.3: Chemical analyses of Well B injection fluid and time-series produced water samples.

Well	Matrix	Sample Date	Days Producing	Daily Water/Gas 15 Day Moving Avg.		δ^{18}O (‰ VSMOW)	δ^{2}H (‰ VSMOW)	Chloride (mg/L)	TDS (mg/L)
				bbl/10^{6}ft^3	m^3/10^{6}m^3				
B	Injection Fluid	5/2/2019	--	--	--	-8.33	-58.7	9670	16000
B	Produced Water	7/12/2019	0	99.9	560.7	-6.84	-55.2	13700	24100
B	Produced Water	7/13/2019	1	93.1	522.5	-6.45	-53.3	14000	24600
B	Produced Water	7/13/2019	1	93.1	522.5	-6.46	-53.2	15200	25300
B	Produced Water	7/14/2019	2	87.1	488.4	-6.39	-51.8	15700	27300
B	Produced Water	7/14/2019	2	87.1	488.4	-6.30	-52.7	17000	29300
B	Produced Water	7/15/2019	3	81.0	454.5	-6.39	-52.6	16600	28300
B	Produced Water	7/16/2019	4	75.8	425.2	-6.21	-52.7	18700	31100
B	Produced Water	7/17/2019	5	71.5	401.1	-6.20	-52.3	18100	31400
B	Produced Water	7/18/2019	6	67.5	378.8	-6.34	-53.3	18800	32700
B	Produced Water	7/20/2019	8	60.3	338.4	-5.92	-51.5	21200	36500
B	Produced Water	7/22/2019	10	49.0	275.0	-5.76	-49.9	23100	40500
B	Produced Water	7/24/2019	12	38.1	213.6	-5.62	-50.0	24500	42300
B	Produced Water	7/26/2019	14	29.4	165.0	-5.62	-51.2	25400	43200
B	Produced Water	7/28/2019	16	21.6	121.4	-5.24	-49.9	25100	45000
B	Produced Water	7/30/2019	18	17.0	95.3	-5.37	-50.5	26100	46400
B	Produced Water	8/1/2019	20	13.9	78.0	-5.42	-51.8	30100	50700
B	Produced Water	8/8/2019	27	9.5	53.2	-5.23	-49.8	29200	51500
B	Produced Water	8/15/2019	34	7.3	40.7	-5.16	-50.0	31600	55100
B	Produced Water	8/22/2019	41	5.8	32.7	-5.04	-49.1	33100	56200
B	Produced Water	8/29/2019	48	4.9	27.3	-4.92	-49.4	35400	60200
B	Produced Water	9/5/2019	55	4.1	23.2	-4.83	-48.8	35600	61500
B	Produced Water	9/12/2019	62	3.6	20.4	-4.87	-49.3	36300	62000
B	Produced Water	10/9/2019	89	2.6	14.7	-4.79	-50.3	36800	63600
B	Produced Water	9/9/2020	425	1.4	8.1	-4.90	-56.3	40800	68400
B	Produced Water	11/18/2020	495	1.1	6.1	-4.71	-54.6	42700	75900

Table 2.4: Chemical analyses of Well C injection fluid and time-series produced water samples.

Well	**Matrix**	**Sample Date**	**Days Producing**	**Daily Water/Gas 15 Day Moving Avg.**		**$\delta^{18}O$ (‰ VSMOW)**	**$\delta^{2}H$ (‰ VSMOW)**	**Chloride (mg/L)**	**TDS (mg/L)**
				bbl/10^{6}ft^3	**m^3/10^{6}m^3**				
C	Injection fluid	5/17/2019	--	--	--	-8.84	-63.3	7760	13200
C	Produced water	7/13/2019	1	38.6	216.7	-6.24	-54.1	19200	34600
C	Produced water	7/13/2019	1	38.6	216.7	-6.14	-52.7	18500	33600
C	Produced water	7/13/2019	1	38.6	216.7	-6.46	-53.4	19000	33800
C	Produced water	7/14/2019	2	35.9	201.3	-6.18	-53.2	19100	33700
C	Produced water	7/14/2019	2	35.9	201.3	-6.16	-52.5	20200	35400
C	Produced water	7/15/2019	3	33.5	187.9	-6.01	-52.6	19700	33900
C	Produced water	7/15/2019	3	33.5	187.9	-6.16	-52.3	20000	35000
C	Produced water	7/16/2019	4	31.7	177.7	-6.06	-52.9	20300	35700
C	Produced water	7/17/2019	5	30.1	169.1	-6.04	-51.3	21000	37000
C	Produced water	7/18/2019	6	28.7	161.0	-6.16	-52.3	20200	35400
C	Produced water	7/19/2019	7	27.4	153.6	-6.06	-51.3	21600	37500
C	Produced water	7/20/2019	8	26.3	147.3	-6.04	-51.5	21600	37600
C	Produced water	7/22/2019	10	21.4	120.0	-5.85	-50.9	22100	38500
C	Produced water	7/24/2019	12	16.8	94.3	-5.86	-52.0	22100	38800
C	Produced water	7/26/2019	14	14.2	79.6	-4.81	-49.8	22100	39000
C	Produced water	7/28/2019	16	11.9	67.0	-5.81	-51.0	23800	40300
C	Produced water	8/8/2019	27	6.1	34.3	-5.58	-50.3	23100	40600
C	Produced water	8/15/2019	34	4.7	26.5	-5.60	-50.5	23400	41200
C	Produced water	8/22/2019	41	3.5	19.8	-5.53	-50.3	23800	41200
C	Produced water	8/29/2019	48	2.8	15.5	-5.58	-51.1	23500	41100
C	Produced water	9/5/2019	55	2.2	12.6	-5.59	-52.1	23000	40700
C	Produced water	9/12/2019	62	1.8	10.3	-5.63	-52.8	22800	39700
C	Produced water	10/9/2019	89	1.1	6.2	-5.91	-54.1	20900	37000
C	Produced water	9/9/2020	425	0.4	2.5	-7.77	-73.5	2070	3700
C	Produced water	11/18/2020	495	0.4	2.5	-7.56	-74.0	716	1400

Table 2.5: Chemical analyses of freshwater samples.

Source	Sample Date	$\delta^{18}O$ (‰ VSMOW)	$\delta^{2}H$ (‰ VSMOW)	Chloride (mg/L)	TDS (mg/L)
1	6/6/2019	-8.88	-58.6	12	50
2	6/6/2019	-8.65	-56.1	7	49
3	3/14/2019	-9.30	-59.9	11	44
4	3/14/2019	-10.17	-67.9	18	69
5	3/14/2019	-10.49	-71.1	30	126
6	3/14/2019	-9.76	-64.5	22	76
7	3/14/2019	-10.12	-67.1	17	66
8	3/14/2019	-9.75	-64.2	25	79

REFERENCES

Barnaby, R.J., Oetting, G.C., Gao, G., 2004. Strontium isotopic signatures of oil-field waters: Applications for reservoir characterization. Am. Assoc. Pet. Geol. Bull. 88, 1677–1704. https://doi.org/10.1306/07130404002

Beaudoin, G., Therrien, P., 2021. AlphaDelta Stable Isotope Fractionation Calculator [WWW Document]. URL http://www2.ggl.ulaval.ca/cgi-bin/alphadelta/alphadelta_4alpha.cgi

Blondes, M.S., Shelton, J.L., Engle, M.A., Trembly, J.P., Doolan, C.A., Jubb, A.M., Chenault, J.C., Rowan, E.L., Haefner, R.J., Mailot, B.E., 2020. Utica shale play oil and gas brines: Geochemistry and factors influencing wastewater management. Environ. Sci. Technol. 54, 13917–13925. https://doi.org/10.1021/acs.est.0c02461

Bryndzia, L.T., Fay, M.C., 2016. Geochemical analysis of Returned Treatment Waters (RTW) associated with shale gas production in the Appalachian Basin (USA) and Deep Basin (Canada): Potential use of Total Dissolved Solids (TDS) and Oxygen isotope data for assessing Water:Rock ratios..., in: SPE/AAPG/SEG Unconventional Resources Technology Conference 2016. https://doi.org/10.15530/urtec-2016-2455905

Capo, R.C., Stewart, B.W., Rowan, E.L., Kolesar Kohl, C.A., Wall, A.J., Chapman, E.C., Hammack, R.W., Schroeder, K.T., 2014. The strontium isotopic evolution of Marcellus Formation produced waters, southwestern Pennsylvania. Int. J. Coal Geol. 126, 57–63. https://doi.org/10.1016/j.coal.2013.12.010

Carpenter, A.B., 1978. Origin and Chemical Evolution of Brines in Sedimentary Basins, in: Johnson, K.S., Russel, J.A. (Eds.), Oklahoma Geological Survey Circular 79: Thirteenth Annual Forum on the Geology of Industrial Minerals. pp. 60–77. https://doi.org/10.2118/7504-MS

Chapman, E.C., Capo, R.C., Stewart, B.W., Hedin, R.S., Weaver, T.J., Edenborn, H.M., 2013. Strontium isotope quantification of siderite, brine and acid mine drainage contributions to abandoned gas well discharges in the Appalachian Plateau. Appl. Geochemistry 31, 109–118. https://doi.org/10.1016/j.apgeochem.2012.12.011

Chapman, E.C., Capo, R.C., Stewart, B.W., Kirby, C.S., Hammack, R.W., Schroeder, K.T., Edenborn, H.M., 2012. Geochemical and strontium isotope characterization of produced waters from Marcellus Shale natural gas extraction. Environ. Sci. Technol. 46, 3545–3553. https://doi.org/10.1021/es204005g

Chaudhary, B.K., Sabie, R., Engle, M.A., Xu, P., Willman, S., Carroll, K.C., 2019. Spatial variability of produced-water quality and alternative-source water analysis applied to the Permian Basin, USA. Hydrogeol. J. 27, 2889–2905. https://doi.org/10.1007/s10040-019-02054-4

Dresel, P., Rose, A.W., 2010. Chemistry and origin of oil and gas well brines in western Pennsylvania. Pennsylvania Geol. Surv., 4th Ser. Open File Rep. OFOG 10-01.0 48.

EIA, 2021. Petroleum & Other Liquids: Drilling Productivity Report [WWW Document]. URL https://www.eia.gov/petroleum/drilling/

EPA, 2011. Natural Gas Drilling in the Marcellus Shale: NPDES Program Frequently Asked Questions.

Farrell, J., Williams, R., Prabhu, R., Makarychev-Mikhailov, S., Kreimeier, W., 2017. Interrogating flowback chemistry for damage markers in the Eagle Ford, in: SPE/AAPG/SEG Unconventional Resources Technology Conference 2017. https://doi.org/10.15530/urtec-2017-2674419

Haluszczak, L.O., Rose, A.W., Kump, L.R., 2013. Geochemical evaluation of flowback brine from Marcellus gas wells in Pennsylvania, USA. Appl. Geochemistry 28. https://doi.org/10.1016/j.apgeochem.2012.10.002

Kendall, C., Coplen, T.B., 2001. Distribution of oxygen-18 and deuteriun in river waters across the United States. Hydrol. Process. 15, 1363–1393. https://doi.org/10.1002/hyp.217

Kharaka, Y.K., Callender, E., Carothers, W.W., 1977a. Geochemistry of geopressured geothermal waters from the Texas Gulf Coast. Third Geopress. Energy Conf. 1, 121–166.

Kharaka, Y.K., Callender, E., Wallace, R.H., 1977b. Geochemistry of geopressured geothermal waters from the Frio Clay in the Gulf Coast region of Texas. Geology 5, 241–244. https://doi.org/10.1130/0091-7613(1977)5<241:GOGGWF>2.0.CO;2

Majoube, M., 1971. Fractionnement en oxygene-18 et en deuterium entre l’eau et sa vapeur. J. Chem. Phys. 1423–1436. https://doi.org/10.1051/jcp/1971681423

McKetta, J.J., Wehe, A.H., 1958. Use this chart for the water content of natural gases. Pet. Refin. 37, 153–154.

Milici, R.C., Swezey, C.S., 2006. Assessment of Appalachian basin oil and gas resources: Devonian shale Middle and Upper Paleozoic total petroleum system: U.S. Geological

Survey Open File Report 2006-1237. https://doi.org/10.3133/ofr20061237

O'Neil, J.R., Kharaka, Y.K., 1976. Hydrogen and oxygen isotope exchange reactions between clay minerals and water. Geochim. Cosmochim. Acta 40, 241–246. https://doi.org/10.1016/0016-7037(76)90181-2

Oetjen, K., Chan, K.E., Gulmark, K., Christensen, J.H., Blotevogel, J., Borch, T., Spear, J.R., Cath, T.Y., Higgins, C.P., 2018. Temporal characterization and statistical analysis of flowback and produced waters and their potential for reuse. Sci. Total Environ. 619–620. https://doi.org/10.1016/j.scitotenv.2017.11.078

Osborn, S.G., McIntosh, J.C., 2010. Chemical and isotopic tracers of the contribution of microbial gas in Devonian organic-rich shales and reservoir sandstones, northern Appalachian Basin. Appl. Geochemistry 25, 456–471. https://doi.org/10.1016/j.apgeochem.2010.01.001

Phan, T.T., Capo, R.C., Stewart, B.W., Macpherson, G.L., Rowan, E.L., Hammack, R.W., 2016. Factors controlling Li concentration and isotopic composition in formation waters and host rocks of Marcellus Shale, Appalachian Basin. Chem. Geol. 420, 162–179. https://doi.org/10.1016/j.chemgeo.2015.11.003

Phan, T.T., Hakala, J.A., Sharma, S., 2020. Application of isotopic and geochemical signals in unconventional oil and gas reservoir produced waters toward characterizing in situ geochemical fluid-shale reactions. Sci. Total Environ. 714, 1–17. https://doi.org/10.1016/j.scitotenv.2020.136867

Poulson, S.R., Ohmoto, H., Ross, T.P., 1995. Stable isotope geochemistry of waters and gases (CO2, CH4) from the overpressured Morganza and Moore-Sams fields, Louisiana Gulf Coast. Appl. Geochemistry 10, 407–417. https://doi.org/10.1016/0883-2927(95)00014-B

Reed, M.J., Mariner, R.H., 1991. Quality control of chemical and isotopic analyses of geothermal water samples, in: Proceedings Sixteenth Workshop Geothermal Reservoir Engineering, January 23-25, 1991. Sixteenth Workshop on Geothermal Reservoir Engineering, Stanford University, pp. 9–13.

Renock, D., Landis, J.D., Sharma, M., 2016. Reductive weathering of black shale and release of barium during hydraulic fracturing. Appl. Geochemistry 65, 73–86. https://doi.org/10.1016/j.apgeochem.2015.11.001

Rosenblum, J., Nelson, A.W., Ruyle, B., Schultz, M.K., Ryan, J.N., Linden, K.G., 2017. Temporal characterization of flowback and produced water quality from a hydraulically fractured oil and gas well. Sci. Total Environ. 596–597. https://doi.org/10.1016/j.scitotenv.2017.03.294

Rostron, B., Arkadakskiy, S., 2014. Fingerprinting “stray” formation fluids associated with hydrocarbon exploration and production. Elements 10, 285–290. https://doi.org/10.1190/ice2015-2211363

Rowan, E.L., Engle, M.A., Kraemer, T.F., Schroeder, K.T., Hammack, R.W., Doughten, M.W., 2015. Geochemical and isotopic evolution of water produced from Middle Devonian Marcellus shale gas wells, Appalachian Basin, Pennsylvania. Am. Assoc. Pet. Geol. Bull. 99, 181–206. https://doi.org/10.1306/07071413146

Stewart, B.W., Chapman, E.C., Capo, R.C., Johnson, J.D., Graney, J.R., Kirby, C.S., Schroeder, K.T., 2015. Origin of brines, salts and carbonate from shales of the Marcellus Formation: Evidence from geochemical and Sr isotope study of sequentially extracted fluids. Appl. Geochemistry 60, 78–88. https://doi.org/10.1016/j.apgeochem.2015.01.004

U.S. EPA, 2015. Case Study Analysis of the Impacts of Water Acquisition for Hydraulic

Fracturing on Local Water Availability, EPA/600/R-14/179.

Wright, S., Franks, S., Pantano, J., Kloska, M., Wolters, J., 2019. Understanding Dynamic Production Contribution from Hydraulically Fractured Middle Bakken and Three Forks Wells in the Williston Basin, ND Using Time-Lapsed Geochemistry, in: Proceedings of the 7th Unconventional Resources Technology Conference, Denver, Colorado, 22-24 July 2019. https://doi.org/10.15530/urtec-2019-142

Chapter 3: A Combined $^{228}Ra/^{226}Ra$ and $^{87}Sr/^{86}Sr$ Approach to Identify Cross-Formation Flow in Sedimentary Basin Systems

ABSTRACT

Fluid composition in deep hydrocarbon-bearing sedimentary basins can be affected by a wide range of biological, chemical, physical, and geological processes, and as a result, very few (if any) formations contain connate water (i.e., water trapped during deposition) (Engle et al., 2020). Identifying the origin of formation waters is important for understanding the controls on and behavior of fluid movement in deeper sedimentary systems. In oil and gas reservoirs, information on fluid origin can be useful in evaluating reservoir and individual well performance, as well as enhancing approaches to produced water management. In addition, evidence of fluid transport across formations can inform fluid migration induced by anthropogenic activities (e.g., associated with CO_2 sequestration or oil and gas extraction). To identify relatively recent (<16,000 years) cross-formation flow in sedimentary basin fluids, I propose a new method to evaluate deep fluid sources based on the combined behavior of $^{228}Ra/^{226}Ra$ and $^{87}Sr/^{86}Sr$ in waters relative to ratios of Th/U and Rb/Sr in lithologic samples from potential source formations. This approach is applied to evaluate the origin of produced fluids from Marcellus Shale gas wells in Pennsylvania, in the northern Appalachian Basin. A combination of $^{228}Ra/^{226}Ra$ and $^{87}Sr/^{86}Sr$ data from 202 produced water samples, high-frequency lithologic Th/U and Rb/Sr measurements from three cored intervals, and daily water and gas production rates, demonstrate that a subset of Marcellus wells are producing out-of-zone fluid. The approach developed here has potential utility for identifying instances of cross-formation flow in both natural and human induced scenarios.

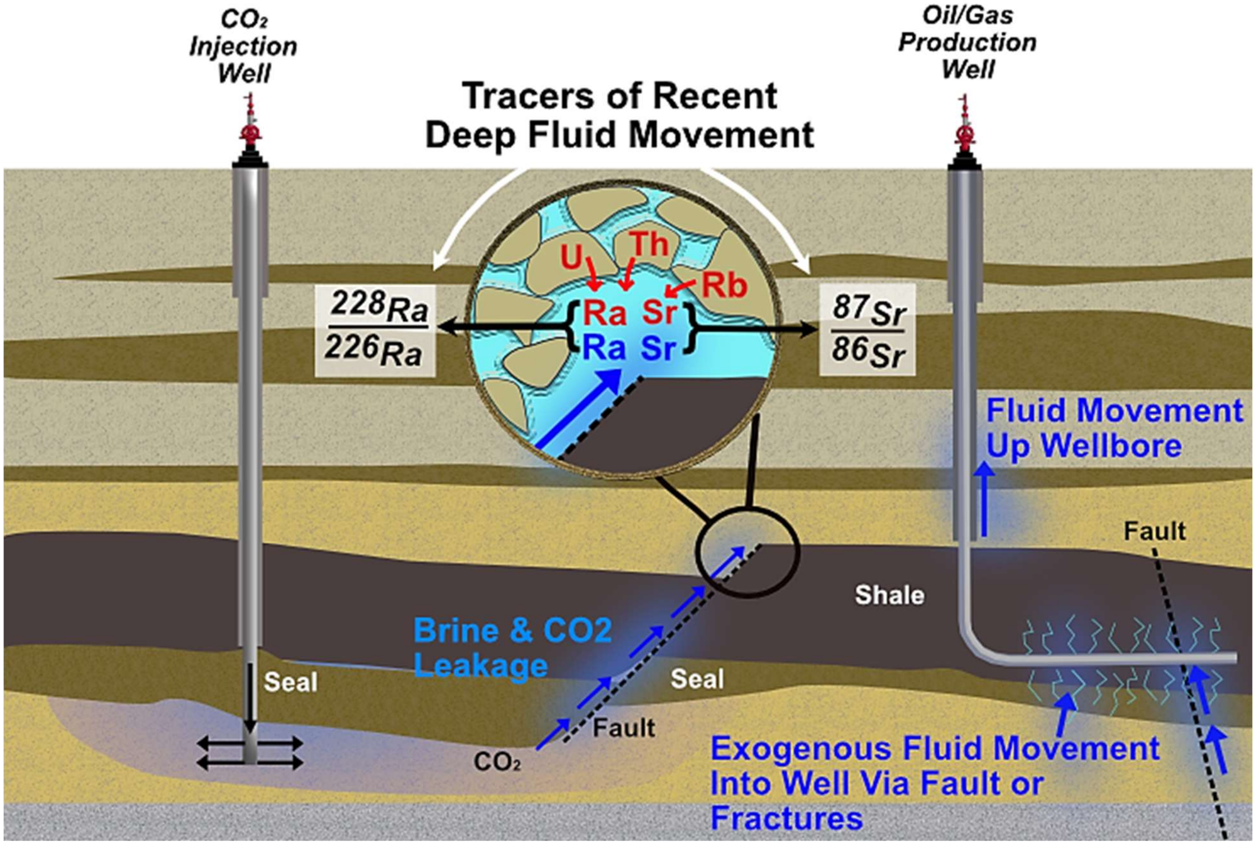

Illustration 3.1: Conceptual model of cross-formation fluid movement.

INTRODUCTION

The origin of water in deep sedimentary basins is complex and governed by a variety of processes, including hydrocarbon expulsion and movement, diagenesis, tectonic forcings, and isostatic changes (Bein and Dutton, 1993; Bethke and Marshak, 1990; Engle et al., 2020; Mcintosh et al., 2004; McNeal, 1965; Nicot et al., 2020, 2018). Previous investigations to interpret the history and origin of water in deep (>500 m) sedimentary basin hydrologic systems have relied on a range of physical evidence (e.g., fluid pressure, hydrologic flow parameters) and hydrologic chemical and isotopic tracers (e.g., δ^{2}H and $\delta^{18}O_{H2O}$, $\delta^{13}C_{DIC}$, δ^{34}S and $\delta^{18}O_{SO4}$, δ^{37}Cl, ^{87}Sr/^{86}Sr, δ^{7}Li, δ^{11}B, ^{228}Ra/^{226}Ra, ^{3}H, ^{14}C, ^{36}Cl, ^{81}Br) (Birkle, 2016; Blondes et al., 2020; Engle et al., 2020; Engle and

Rowan, 2014; Nicot et al., 2020, 2018; Phan et al., 2016; Rostron and Arkadakskiy, 2014; Rowan et al., 2011; Saller and Stueber, 2021; Stotler et al., 2021; Warner et al., 2012). Success of these various tools to identify water sources in a given system depend on the diversity of lithologies, fluids, and the corresponding tracers. For example, δ^2H and δ^{18}O can be a simple and effective system for distinguishing formation fluids with a significant meteoric water component from deep basin brines (Rostron and Arkadakskiy, 2014; Saller and Stueber, 2021). However, multiple processes (e.g., isotopic exchange with minerals, evaporation, etc.) and sources of water can produce over-lapping, and therefore, nonunique water isotopic compositions (Osborn and McIntosh, 2010). Thus, methods to distinguish between sources of fluids in sedimentary basins is still an active area of research (e.g., Phan et al., 2016; Stotler et al., 2021). Here, I present a new method to identify cross-formation flow in deep sedimentary units. This method relies on a combination of ^{228}Ra/^{226}Ra and ^{87}Sr/^{86}Sr in produced water samples, which reflect different fluid history timescales. More specifically, pairing of these isotope ratios was selected because I hypothesize that ^{228}Ra/^{226}Ra and ^{87}Sr/^{86}Sr in formation water should develop in predictable ways, as follows:

1. ^{228}Ra and ^{226}Ra form naturally in the decay chains of ^{232}Th ($t^{1/2}$=14 billion years, 99.98% of Th) and ^{238}U ($t^{1/2}$=4.5 billion years, 99.27% of U), respectively. These Ra isotopes are the first soluble species in their corresponding decay chains, and thus are the first to be present in detectable concentrations in water. Within water, dissolved Th and U concentrations (and concentrations of other intermediate isotopes in the decay chain) are too low to support measurable ^{228}Ra and ^{226}Ra (Fisher, 1998); therefore, aqueous Ra originates from the host rock via partial or complete dissolution, chemical leaching, and alpha-recoil damage to the formation (Kraemer and Reid, 1984). ^{228}Ra and ^{226}Ra also

decay, but with much shorter half-lives of 5.75 and 1,600 years, respectively. Because ^{232}Th and ^{238}U have extremely long half-lives relative to their daughter isotopes, systems that are relatively closed eventually reach secular equilibrium, where the production rates of ^{228}Ra and ^{226}Ra equal their decay rates (as long as fluid flow through the system is relatively slow). Secular equilibrium for ^{228}Ra/^{226}Ra from ^{232}Th/^{238}U is obtained after approximately 2.45 million years (a small period of time relative to the age of most hydrocarbon bearing formations), at which point the ^{228}Ra/^{226}Ra ratio can be predicted by the following relationship: Th/U (weight ratio in source material) × 0.245 / 0.745 (Engle et al., 2020; Kraemer and Reid, 1984; Rowan et al., 2011). Note that because ^{232}Th comprises 99.98% of Th and ^{238}U comprises 99.27% of U, it is reasonable to assume that the bulk Th/U ratio is good approximation of the ^{232}Th/^{238}U ratio within a mineral or rock. When a fluid travels from one formation with a specific Th/U ratio and enters a formation with a different Th/U ratio, the ^{228}Ra/^{226}Ra ratio of the original host rock rapidly changes (i.e., within well under 10 half-lives, or ~60 years for ^{228}Ra, the Ra isotope with the shorter half-life). In this way, the ^{228}Ra/^{226}Ra ratio measured in formation water from relatively closed hydrologic systems should predictably reflect the Th/U content of the Th- and U-bearing phases of the host rock. Assuming that ^{228}Ra and ^{226}Ra are equally accessible to formation water from the various Th- and U- bearing phases (an assumption discussed in more detail below), the ^{228}Ra/^{226}Ra composition of the water should approach that of the bulk Th/U activity of the formation in which it resides.

2. ^{87}Sr/^{86}Sr ratios in formation waters reflect a history of rock-water interaction, fluid migration, and fluid mixing. ^{87}Sr is the stable radiogenic daughter of ^{87}Rb ($t^{1/2}$=49.23 billion years, 27.9% of Rb), while ^{86}Sr is a stable isotope (9.86% of Sr) with no radiogenic

source. Because neither ^{87}Sr nor ^{86}Sr decay, the ^{87}Sr/^{86}Sr ratio of a fluid reflects the cumulative Sr input from all sources to the fluid over its lifetime. Therefore, the Sr isotope system serves as a useful contrast to the Ra isotope system. In minerals, Rb readily substitutes for K (e.g., in illite, K-feldspar, hornblende, biotite, or muscovite), and formations characterized by these minerals often exhibit more radiogenic (higher ^{87}Sr/^{86}Sr) ratios than formations where carbonate minerals predominate (Clark and Fritz, 1997). Sr in fluids originates from the dissolution of soluble Sr-bearing minerals or ion exchange reactions. Fractionation of the ^{87}Sr/^{86}Sr ratio as a result of mineral dissolution or precipitation, ion exchange, evaporation, or biologic processes is negligible relative to the radiogenic input. As a result, the ^{87}Sr/^{86}Sr ratio is a relatively conservative tracer of fluid-rock interactions and mixing of different fluid sources, and represents a cumulative history of the soluble Sr-bearing minerals that the fluid has been in contact with, assuming the fluid is not yet saturated with respect to Sr. Therefore, unlike the ^{228}Ra/^{226}Ra ratio, the ^{87}Sr/^{86}Sr ratio of a fluid cannot be predicted based on simple knowledge of the Rb/Sr ratios of minerals the fluid is currently in contact with. Kharaka and Hanor (2007) and Chaudhuri and Clauer (1992) note that the ^{87}Sr/^{86}Sr ratio in produced waters with a marine influence is almost always much more radiogenic than seawater of the period, suggesting that these compositions reflect a mixture of strontium from the original source of salinity (typically paleoseawater) and contributions from minerals in host rocks. Formation waters in many oil and gas basins share a common parent (same ^{87}Sr/^{86}Sr ratio) in deep brines formed during the evaporation of paleoseawater from one or two stratum (Blondes et al., 2020; Iampen and Rostron, 2000; Saller and Stueber, 2021). For such formation waters, it may be possible to link the relative difference in present-day $^{87}Sr/^{86}Sr$ with the different Rb/Sr ratios of reservoir rocks.

As noted above, fluids within sedimentary basins are mobile over geologic time, and fluid geochemistry reflects both the parent water and rock-water interactions (e.g., mineral diagenesis, thermal breakdown of kerogen, and radioactive decay). With only one to two proposed parent brine sources, the Appalachian Basin is an excellent place to apply the combined use of the $^{228}Ra/^{226}Ra$ and $^{87}Sr/^{86}Sr$ systems to identify cases of cross-formation fluid flow. Specifically, the salinity in Silurian and Devonian formation fluids in the Appalachian Basin is largely thought to share a common end-member, expelled brines from the underlying Silurian Salina evaporite sequence (Dresel and Rose, 2010; Rowan et al., 2015; Stewart et al., 2015). More recently, Blondes et al. (2020) proposed another possible source of salinity in the Appalachian Basin – the Ordovician Beekmantown dolomite, concluding that it was the likely origin of high-salinity fluids in the Upper Ordovician Utica Shale. Within the Appalachian Basin, the Marcellus Shale is a tremendously productive shale gas play, yielding 97×10^{7} m^3 (34×10^{9} ft^3) of gas per day, and a wealth of new produced water data over the past decade. Information on the chemical and isotopic composition of Marcellus produced water provides a unique opportunity to evaluate the origin of formation fluids produced alongside the gas.

The Marcellus Shale commonly only returns between 8% and 12% of the volume of injected fluids back to surface (U.S. EPA, 2015a), much of that during the first 30 days of flowback. The balance of injected water remains trapped in the formation, where it was imbibed as a result of the joint action of spontaneous imbibition, in which capillary suction draws the wetting fluid into the pore space, and forced imbibition, in which the external pressure gradient overcomes the capillary entry pressure of various pore sizes (Engelder et al., 2014; Wang and Fu, 2023). This imbibed water remains largely unable to drain without a similarly high external pressure (Rowan et al., 2015; Wang and Fu, 2023). During gas production, reservoir pressure decreases over time as fluid is withdrawn from the reservoir, and the production of injected fracturing fluids rapidly diminishes. At this time, many Marcellus wells transition to producing a smaller volume of high salinity water, commonly thought to be dominated by formation fluid that is drained under lower pressures from the hydraulically induced fracture networks (Rowan et al., 2015). However, a subset of Marcellus wells consistently produce larger volumes of high-salinity water (e.g.>15 to 20% of injected fluid volume) over time, leading some to speculate a fluid origin in more transmissive underlying or overlying formations (i.e., "out-of-zone" water). The identification of out-of-zone water is complicated by the fact that formation waters throughout much of the Appalachian Basin exhibit a similar major elemental composition (e.g., Dresel and Rose, 2010). It is also confounded by a lack of reliable geochemical measurements for an unadulterated Marcellus Shale formation fluid end-member, which are exceedingly difficult to obtain from shale with low water content and nano- to micro-Darcy permeability. Marcellus produced water composition is also influenced to varying degrees throughout the well's lifecycle by the presence of injected hydraulic fracturing fluids. Fracturing fluids commonly contain 80% or more freshwater, with the balance comprised of recycled produced water and <1% additives by mass (U.S. EPA, 2015b), and by water condensing out of the gas phase ("water of condensation"), which almost exclusively impacts produced water composition in gas wells with low water production rates (Molofsky et al. 2022).

In this study, I propose that ^{228}Ra/^{226}Ra and ^{87}Sr/^{86}Sr ratios can be reliable tracers of the formation fluid endmember in formations where flow rates are slow and there is the potential for cross-formation flow. Specifically, because formation fluids typically contain Ra and Sr concentrations that are an order of magnitude or more higher than injection fluids or water of condensation, $^{228}Ra/^{226}Ra$ and $^{87}Sr/^{86}Sr$ ratios of produced water principally reflect the formation fluid endmember, even within the first few days of flowback of injected fracturing fluids (e.g., Chapman et al., 2012; Rowan et al., 2011). I hypothesize that ratios of Th/U and Rb/Sr in lithologic samples in the Appalachian Basin can be used to broadly predict the $^{228}Ra/^{226}Ra$ and $^{87}Sr/^{86}Sr$ ratios of formation waters. Coupled with information on water production rates over time, this approach can effectively inform our understanding of in-zone versus out-of-zone formation fluid production, and more generally, cross-formation fluid flow over short versus long geologic timeframes in deep sedimentary basins. From a larger perspective, the combined use of $^{228}Ra/^{226}Ra$ and $^{87}Sr/^{86}Sr$ ratios holds promise for identifying relatively recent leaks of deep fluids from targeted reservoirs for CO_2 sequestration, wastewater injection, or hydrocarbon production.

GEOLOGY AND FLUID SOURCES

The Marcellus was deposited in the foreland basin of the Acadian orogenic belt approximately 390 million years ago, and is dominated by black shale, but also contains interbedded limestone and lighter shales (Walker-Milani, 2011). For the purposes of this paper, the Marcellus is divided into the following sub-units (from top to bottom): Upper Marcellus Shale, Purcell Limestone, Lower Marcellus Shale, and the Union Springs (exhibiting the highest relative organic and uranium content), which includes a limestone rich section towards the base referred to as the Union Springs Lime (Figure 3.1). Marcellus gas wells target one or more of the above units. Adjacent Middle Devonian formations that serve as possible sources of exogenous fluids in the Marcellus Shale include the overlying Mahantango Formation, composed of siltstone and shale with interbedded fine-grained sandstone, and the underlying Onondaga Limestone. The Onondaga is underlain by the Needmore Shale and beneath that, the Oriskany (Ridgely) Sandstone, which is characterized as a calcareous sandstone/siltstone or silty limestone. The lower intrinsic permeability of siltstones and shales make the Mahantango and Needmore shales less likely sources of out-of-zone fluids, though does not necessarily preclude the production of fluids from more permeable lenses or "stringers" within these units. By comparison, the Onondaga Limestone and Oriskany Sandstone are sufficiently permeable to support conventional gas production in parts of Pennsylvania and New York (e.g., NYSDEC, 2009; PA DEP, 1992), and the Oriskany has been proposed as a source of out-of-zone fluids in Marcellus gas wells in North Central Pennsylvania (Glick, 2017). Because the majority of Marcellus wells in the region target production from the Lower Marcellus or Union Springs members directly overlying the Onondaga Limestone, I consider the Onondaga to be the most likely source of out-of-zone fluids. As such, our evaluation primarily tests the hypothesis that the Onondaga Limestone is the source of exogenous formation fluids in Marcellus gas wells producing higher relative daily rates of water-to-gas production. Nevertheless, the Oriskany remains a possible source of out-of-zone fluids via pre-existing faults that extend through the Oriskany to the base of the Salina, thought it will not be investigated herein.

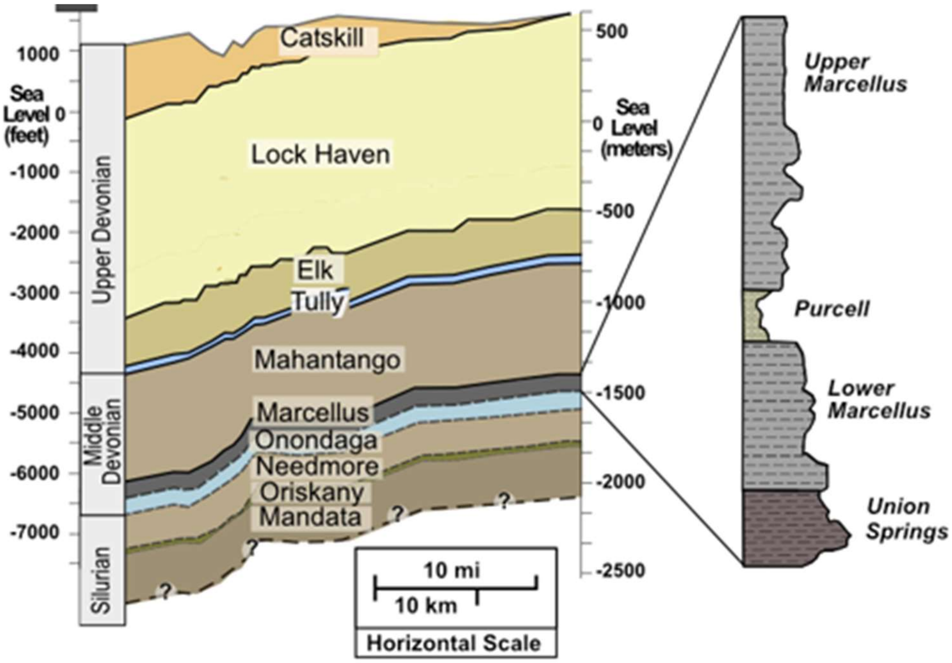

Figure 3.1: Generalized cross section of Devonian formations in study area with Marcellus sub-unit stratigraphy.

RA MODELING

As described above, secular equilibrium between ^{232}Th/^{238}U (effectively Th/U) and ^{228}Ra/^{226}Ra is attained in ~ 2.45 million years, assuming that the hydrologic system is relatively closed (Figure 3.2). This timeframe is calculated based on the assumption that only ^{238}U and ^{232}Th (the primary parents) are initially present, with in-growth of the daughters over time. However, virtually all formations contain some concentration of intermediate isotopes in these decay chains. For formations >2.45 Ma that are hydraulically closed (i.e., oil and gas-bearing formations which do not leak at appreciable rates), isotopes in the $^{232}\text{Th} \rightarrow {}^{228}\text{Ra}$ and $^{238}\text{U} \rightarrow {}^{226}\text{Ra}$ decay chains will have already have attained secular equilibrium (i.e., $\lambda_1 N_1 = \lambda_2 N_2 = \lambda_3 N_3$, where $\lambda = \ln(2)/t_{1/2}$, and N=number of atoms). Ra is the first largely soluble ion in either decay chain, and therefore, in formations where secular equilibrium is already achieved, the Ra isotopic composition

(^{228}Ra/^{226}Ra) of formation fluid can be assumed to reflect secular equilibrium with the Th/U ratio of the host rock. Though not all radium generated during the decay process is accessible by water, as long as a portion of the Ra can be leached and there is no major difference in the accessibility of ^{228}Ra vs. ^{226}Ra within that portion, then the water should inherit a signature equivalent to that produced in the host rock, which agrees with field observations (Kraemer and Reid, 1984; Rowan et al., 2011; Engle et al., 2021). I assume that the pore fluid ^{228}Ra/^{226}Ra reflects the bulk Th/U ratio of the host rock, rather than a specific fraction (e.g., the mineral phase vs. organic phase), an assumption which is discussed in greater detail below.

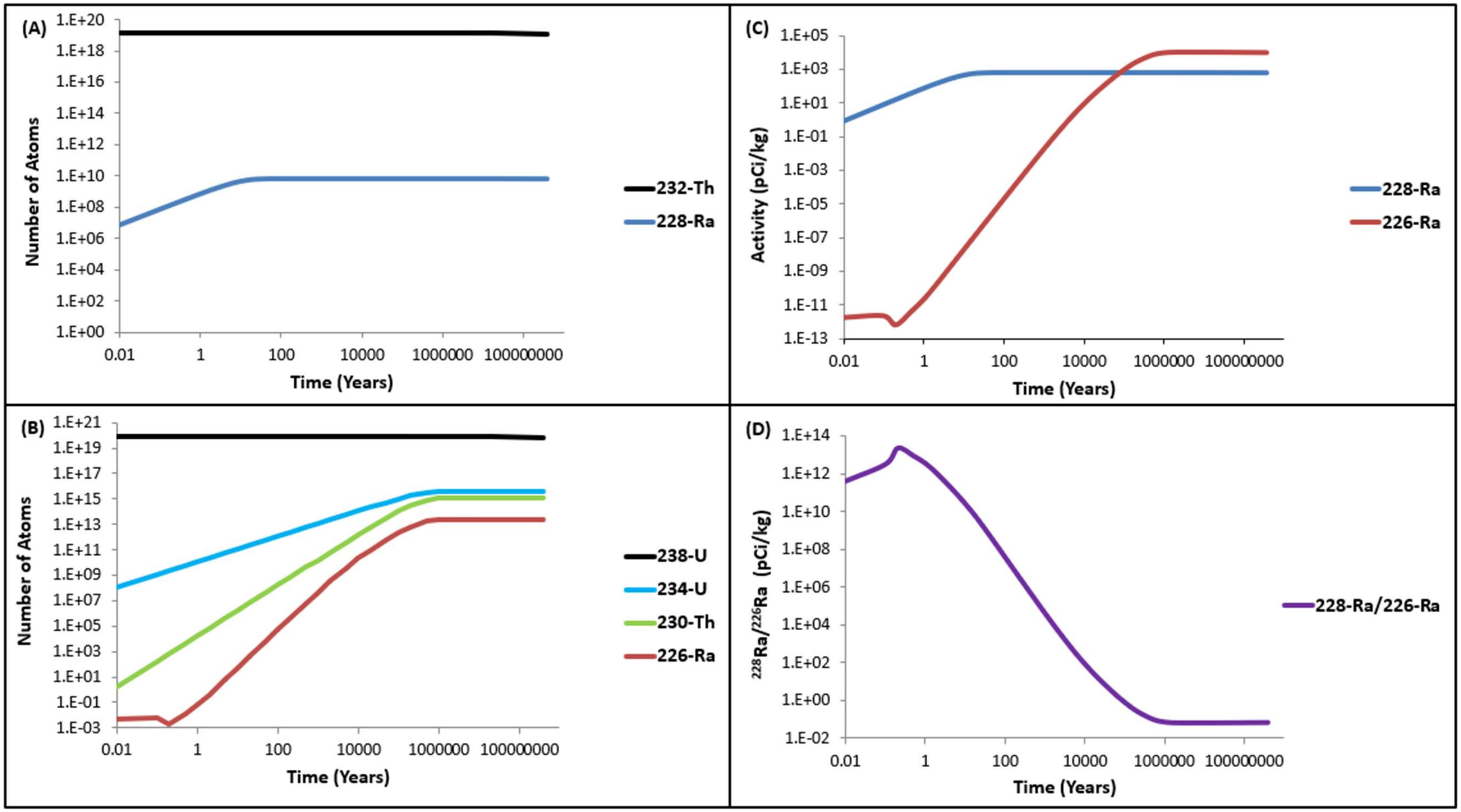

Figure 3.2: Model of Th/U approaching secular equilibrium with ^{228}Ra/^{226}Ra, assuming an initial number of ^{232}Th and ^{238}U atoms based on median Th and U concentrations in the Union Springs member of Core 1, and using the equations set forth in Bateman (2015): A) N versus time for the ^{232}Th→^{228}Ra decay chain, B) N versus time for the ^{238}U→^{226}Ra decay chain, C) ^{228}Ra and ^{226}Ra activity versus time, and D) ^{228}Ra/^{226}Ra activity ratio versus time.

If a fluid crosses formations, it carries the $^{228}Ra/^{226}Ra$ of the original host rock (assuming Th/U secular equilibrium in the host) into the new formation. Given the higher solubility of Ra than most other isotopes in their respective decay chains, ^{228}Ra and ^{226}Ra are likely the only isotopes not in secular equilibrium with the new host rock at the time of fluid entry. A key question I seek to answer in this modeling exercise is: How long does it take for an exogenous fluid to lose the $^{228}Ra/^{226}Ra$ ratio of its original host, and attain that of the new host? To better understand how the activity ratio of ^{228}Ra and ^{226}Ra in formation waters change as a function of time when fluid moves from one reservoir to another, a numerical radioactivity model was utilized in three different exercises in which an exogenous fluid moves into a new host-rock. For the purposes of this example, I assume that the exogenous fluid is either moving from the Onondaga Limestone into the Marcellus Shale, or vice-versa. Assumed total Ra ($^{228}Ra+^{226}Ra$) and $^{228}Ra/^{226}Ra$ ratios of Onondaga and Marcellus formation fluids are shown in Table 3.1, and the basis for these assumptions is discussed in Appendix B.

Table 3.1: Assumed total Ra (228Ra+226Ra) and 228Ra/226Ra ratios of formation fluids, and Th and U concentrations, in the Onondaga and Marcellus Formations used in the radium modeling exercise.

	Formation Fluids		**Avg. Whole Rock Conc.**	
Formation	**Total Ra (pCi/L)**	**$^{228}Ra/^{226}Ra$ (activity)**	**Th (mg/kg)**	**U (mg/kg)**
Onondaga	150	0.4	1.83	1.52
Marcellus	5000	0.1	5.80	28.94

While some of these scenarios are unlikely to occur (e.g., the migration of formation fluid from the relatively non-transmissive Marcellus Shale into the Onondaga Limestone), they serve as useful illustrations of how different assumptions about initial total Ra concentrations and

^{228}Ra/^{226}Ra ratios of fluids, and Th and U abundances and ratios of host rocks, affect the evolution of the ^{228}Ra/^{226}Ra in an exogenous fluid entering a new host formation:

1. Onondaga water moves into the Marcellus Shale, where all isotopes in the ^{232}Th$\rightarrow$^{228}Ra and ^{238}U $\rightarrow$^{226}Ra decay chains in the shale are in secular equilibrium. In this scenario, the resultant mixture of formation fluids yields a surplus of ^{228}Ra and ^{226}Ra relative to secular equilibrium conditions in the Marcellus Shale.
2. Onondaga water moves into the Marcellus Shale, where all isotopes in the ^{232}Th$\rightarrow$^{228}Ra and ^{238}U $\rightarrow$^{226}Ra decay chains in the shale are in secular equilibrium except for soluble ^{228}Ra and ^{226}Ra. Instead, these Ra isotopes are assumed to be lost with the expulsion of the original Marcellus formation fluid (e.g., assuming much of the moveable water was extracted during the early stages of gas production). Because Onondaga formation water is Ra-poor relative to Marcellus formation water, there is now an overall deficit of ^{228}Ra and ^{226}Ra relative to secular equilibrium conditions in the Marcellus.
3. Marcellus water moves into the Onondaga Limestone, where all isotopes in the ^{232}Th$\rightarrow$^{228}Ra and ^{238}U $\rightarrow$^{226}Ra decay chains in the limestone are in secular equilibrium.

The model also assumes that parent products to ^{228}Ra and ^{226}Ra are insoluble, parent products are homogeneous in the reservoir, sorption and desorption of ^{228}Ra and ^{226}Ra are negligible, and up to the point of Fluid A entry into Formation B, the rate of fluid movement through Formation B was much slower than the time required to achieve secular equilibrium. Additionally, the model must assume some rate of transfer of Ra daughters from the reservoir material to the aqueous phase, as well as an effective porosity of Formation B (i.e., the fraction of formation that is accessible to water, which in this case was enhanced by hydraulic fracturing). Together, these two factors have the effect of reducing the overall mass of total Ra that is readily accessible to water in Formation B, either presently or in the future as ^{228}Ra and ^{226}Ra in-grow over time. The effective porosity will also affect the volume of exogenous water that is assumed to be in contact with the rock. For the purposes of this example, Exercises 1 through 3 were modeled assuming a) a host rock effective porosity of 5% (per the 3% average effective porosity of organic-rich shale core samples cited in Balashov et al. (2015) and Gu et al. (2015), and assuming some connectivity enhancement related to hydraulic fracturing), b) that 15% of the radium in the host rock is transferred to the water virtually immediately (e.g., within a few hours, an assumption that is reasonably supported by experimental leaching work by Landis et al. (2018b)). I assume that the remaining ^{228}Ra and ^{226}Ra in the host rock is locked in the rock matrix (non-transferrable). Calculations utilized to model the radioactive decay and ingrowth of ^{228}Ra and ^{226}Ra in the three exercises above are described in Appendix B.

Exercise results

For the three exercises, the ^{228}Ra and ^{226}Ra activities, as well as the ^{228}Ra/^{226}Ra activity ratios over time are shown in Figures 3.3A, B, and C. In all exercises, secular equilibrium between ^{232}Th in the host-rock and ^{228}Ra in the fluid is re-established after ~60 years (~10 half-lives of ^{228}Ra), and secular equilibrium between ^{238}U in the host-rock and ^{226}Ra in the fluid is re-established after ~16,000 years (~10 half-lives of ^{226}Ra). This result indicates that, irrespective of whether there is a surplus or deficit of ^{228}Ra and ^{226}Ra relative to parent isotopes in their respective decay chains, in situations where insoluble parent isotopes are already in secular equilibrium in the host-rock, the timing of ^{228}Ra and ^{226}Ra stabilization in the fluid is a function of their decay rates. This finding also suggests that differences in ^{228}Ra and ^{226}Ra availability from the solid rock matrix to water, whether related to effective porosity, or the rate of Ra transfer from the mineral phase to the liquid phase, do not affect the time it takes to re-establish secular equilibrium.

That being said, additional information on the timing of exogenous fluid incursion into Formation B can be gleaned by evaluating the change in fluid ^{228}Ra/^{226}Ra activity ratio prior to 16,000 years. During the first month, the ^{228}Ra/^{226}Ra ratio is relatively stable in all three exercises, shifting marginally between 1 month and 1 year, and then more significantly thereafter, not necessarily in a uniform direction, until stabilization at ~16,000 years. The magnitude and direction of change in the ^{228}Ra/^{226}Ra ratio during that timeframe depends on both the initial ^{228}Ra/^{226}Ra ratio and whether there is a surplus or deficit of Ra as compared to secular equilibrium conditions

In scenarios where there is a surplus of Ra relative to secular equilibrium conditions in the host rock (Exercises 1 and 3), the ^{228}Ra/^{226}Ra ratio will exhibit an initial decline in the first 60 years, followed by an increase until stabilization at 16,000 years. This pattern is largely attributable to the respective decay rates of ^{228}Ra and ^{226}Ra. Specifically, because ^{228}Ra decays faster, the ^{228}Ra/^{226}Ra drops to a minimum around 60 years (ten half-lives of ^{228}Ra, at which point 99.9% of initial ^{228}Ra will have decayed). Thereafter, the ^{228}Ra/^{226}Ra ratio increases as ^{226}Ra continues to decay, until stabilization at ~16,000 years (ten half-lives of ^{226}Ra).

This pattern is apparent in both Exercises 1 and 3, but would likely be undetectable (given standard laboratory measurement errors) in Exercise 1, where the fluid exhibits relatively small changes in the ^{228}Ra/^{226}Ra ratio over time. In that scenario, there is several orders of magnitude more Ra in the host formation (either in the original formation fluid or transferrable from the host rock) than in the exogenous fluid. Consequently, the ^{228}Ra/^{226}Ra ratio is dominated by that of the host-rock both initially and over time as ^{228}Ra and ^{226}Ra in-grow from Th and U in the host-rock, with only minor changes related to the decay of excess Ra from the exogenous fluid. By comparison, in Exercise 3, there is significantly more Ra in the exogenous fluid than in the host rock. In this situation, the ^{228}Ra/^{226}Ra ratio changes notably from that of the exogenous fluid (initially) to that of the host-rock (at ~16,000 years).

In scenarios where there is a deficit of Ra relative to secular equilibrium conditions in the host rock (Exercise 2), the ^{228}Ra/^{226}Ra ratio exhibits the opposite trend over time: an initial increase associated with the in-growth of ^{228}Ra, peaking at ~60 years, followed by a decrease associated with the in-growth of ^{226}Ra, until stabilization at ~16,000 years. As before, the timing of the directional changes in the ^{228}Ra/^{226}Ra ratio reflect the respective decay rates of the numerator and denominator.

Overall, this modeling exercise demonstrates that when a fluid moves into a hydraulically closed system >2.45 Ma, the re-attainment of secular equilibrium between ^{228}Ra/^{226}Ra in fluid and Th/U of the new host formations takes only as long as it takes 99.99 % of ^{228}Ra and ^{226}Ra to decay (16,000 years), During that timeframe, the direction of change in the ^{228}Ra/^{226}Ra ratio can inform whether incursion of the exogenous fluid created:

a) a surplus of Ra relative to secular equilibrium conditions in the host rock, resulting in a decrease in the ^{228}Ra/^{226}Ra ratio during the first 60 years (e.g., as would occur from mixing of exogenous and endogenous fluids, or if a Ra-rich exogenous fluid replaced a Ra-poor endogenous fluid), or

b) a deficit of Ra relative to secular equilibrium conditions, resulting in an increase in the ^{228}Ra/^{226}Ra during the first 60 years (e.g., as would occur if a Ra-poor fluid replaced a Ra-rich fluid).

In sedimentary basins that contain U-rich formations characterized by orders of magnitude more Ra than other abutting formations, tracking the ^{228}Ra/^{226}Ra ratio of fluid during consecutive years may help inform the nature of fluid migration or mixing within formations, and the origin of exogenous fluid. Of note, this modeling exercise assumes that an exogenous fluid moves into a new host-rock and remains there. If, instead, an exogenous fluid moves through a new host rock relatively rapidly (e.g., during ongoing oil and gas production), we can assume that there is insufficient time for ^{228}Ra and ^{226}Ra to either in-grow or decay. In that case, the ^{228}Ra/^{226}Ra ratio of the produced fluid will largely reflect a simple mixing ratio between a) ^{228}Ra and ^{226}Ra in the exogenous fluid, and b) any ^{228}Ra and ^{226}Ra picked up during rapid transit through the new host rock (from the rock itself or endogenous pore fluids).

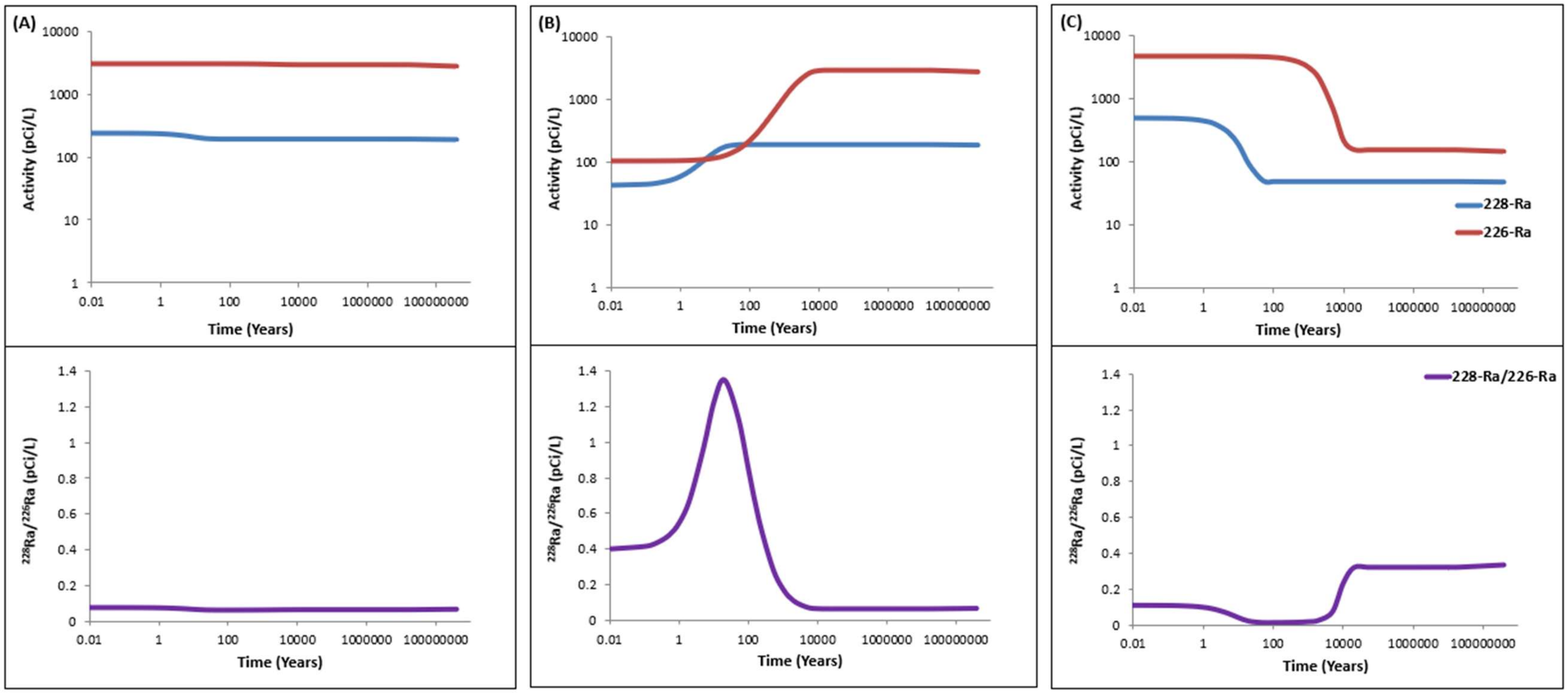

Figure 3.3: Model of Th/U re-approaching secular equilibrium with ^{228}Ra/^{226}Ra in A) Exercise 1, in which Onondaga water moves into the Marcellus Shale, where all isotopes in the ^{232}Th→^{228}Ra and ^{238}U →^{226}Ra decay chains are in secular equilibrium, B) Exercise 2, in which Onondaga water moves into the Marcellus Shale, where all isotopes in the ^{232}Th→^{228}Ra and ^{238}U →^{226}Ra decay chains are in secular equilibrium except for soluble Ra, which was entirely lost with the expulsion of the original Marcellus formation water (e.g., assuming much of the moveable water was extracted during earlier production), and C) Exercise 3, in which Marcellus water moves into the Onondaga Limestone, where all isotopes in the ^{232}Th→^{228}Ra and ^{238}U →^{226}Ra decay chains are in secular equilibrium: (top) ^{228}Ra and ^{226}Ra activity versus time, and (bottom) ^{228}Ra/^{226}Ra activity ratio versus time.

^{228}RA/^{226}RA AND ^{87}SR/^{86}SR MARCELLUS PRODUCED WATER DATA IN THE LITERATURE

Ra isotope characterization of Marcellus Shale produced water (Rowan et al., 2015, 2011) demonstrate that Marcellus produced waters commonly exhibit a distinctly lower ^{228}Ra/^{226}Ra activity ratio (generally less than 0.3) than the median ^{228}Ra/^{226}Ra for produced water samples from other reservoirs in the Appalachian Basin. This low ratio has been attributed to the high U concentrations, and low Th/U ratios, in the organic-rich black Marcellus Shale. This U control on the ratio is supported by data from sequential leaching experiments (Landis et al., 2018b, 2018a), which showed that the U-rich organic fraction of the Marcellus is characterized by exchangeable ^{226}Ra and a low ^{228}Ra/^{226}Ra activity ratio (~0.03). Due to the hydrophobicity and poor water-accessibility of organic pore networks, this organic phase is largely thought to be physically isolated from pore water within the shale (Landis et al., 2018b, 2018a). In contrast, Th-rich mineral surfaces in the Marcellus contain labile ^{228}Ra and a notably higher ^{228}Ra/^{226}Ra activity ratio (~1.11).

The different Ra-bearing fractions in the Marcellus were found to be preferentially accessed depending on the fluid composition, with the organic-rich fraction accessed by a 1M $CaCl_2$ solution, and the exchangeable fraction by low-ionic strength water (e.g., surface water). The same study also observed that ^{228}Ra/^{226}Ra ratios decreased as [Ca]/[Na] ratios increased in Marcellus produced water time-series data. Based on these findings, Landis et al. (2018a) proposed that increasing Ca^{2+} content of downhole fluid from the initiation of flowback over time drives the rapid release of Ra^{2+} from the ^{226}Ra-rich organic phase (where Ca^{2+} readily substitutes for Ra^{2+} due to similar size and charge). The authors also proposed that an exogenous source of Ca^{2+} rich formation fluids could potentially drive Ra^{2+} desorption from the Marcellus as out-of-zone fluids came in contact with the shale (assuming sufficient contact). The presence of different isolated sources of ^{228}Ra and ^{226}Ra within the bulk rock, which may be preferentially accessed depending on the evolving composition of the fluid itself, complicates the ability to predict the formation water ^{228}Ra/^{226}Ra ratio based on the bulk rock composition alone. This idea will be explored further in this paper.

Sr isotope data for Marcellus produced water have largely demonstrated a relatively narrow range of ^{87}Sr/^{86}Sr ratios in the northcentral and northeastern Appalachian Basin (0.7101 to 0.7121) (Capo et al., 2014; Chapman et al., 2012; Kolesar Kohl et al., 2014; Warner et al., 2012). This restricted range of values is largely lower than those reported for brines from conventional Upper Devonian reservoirs and acid mine drainage in the same area, with some minor overlap (>0.7108 to >0.7190) (Chapman et al., 2012). Sequential leaching experiments have also been utilized to characterize the ^{87}Sr/^{86}Sr ratios of different components of the Marcellus Shale, as well as formations immediately underlying the Marcellus that could serve as sources of exogenous fluids during well production (e.g., the Onondaga Limestone or Oriskany Sandstone) (e.g., Phan et al., 2020, 2018; Stewart et al., 2015). Using this approach, Stewart et al. (2015) reported that the ^{87}Sr/^{86}Sr ratios of the water soluble and exchangeable cation fraction (0.7094 to 0.7109) of Marcellus Shale cuttings were largely consistent with that of Marcellus produced waters, where the water-soluble fraction represents trapped fluid or salt residues from fluid evaporation after cuttings were brought to surface, and the exchangeable fraction reflects later Marcellus fluid compositions imprinted on exchange sites and trapped within pores (Stewart et al., 2015). By comparison, the ^{87}Sr/^{86}Sr ratios of the water soluble and exchangeable cation fraction of Onondaga Limestone and Oriskany Sandstone cuttings were generally lower, collectively less than 0.7010 (i.e., 0.7093 to 0.7099).

METHODS

Produced water data presented in this study (^{87}Sr/^{86}Sr, ^{228}Ra/^{226}Ra, δ^{18}O, δ^{2}H, Sr, Ra, Ca, Na, Cl, Br, total dissolved solids (TDS), and average ratios of daily water vs. gas production (Table 3.2) originate from Marcellus Shale gas wells in Pennsylvania, in the northern Appalachian basin.. Data include: 1) individual produced water samples from 123 gas wells collected at a single point in time, and 2) time-series produced water samples from three gas wells (Well A – 24 samples, Well B - 24 samples, and Well C - 23 samples) that started producing the same month from different vertical intervals within the Marcellus at a single geographic location. This study also presents analysis of blended injection fluid utilized during hydraulic fracturing of Wells A, B, and C (3 samples total, 1 per well), comprised of >90% freshwater and <10% treated produced water. These injection fluid samples were collected before fracturing additives were added. Lastly, two freshwater samples were collected from permitted freshwater sources that were regularly utilized by the operator for fracturing fluid water supply.

Of the 123 individual produced water samples, 111 originated from wells that had been in production for over 6 months (~180 days, i.e., "later-stage" production) or more at the time of sample collection. For the purposes of this study, if multiple samples were available from these wells, the most recent sample from each well that met data quality assurance criteria (±10% charge balance) was utilized. The time-series data from the three Marcellus wells (A–C) primarily represent produced water composition during the first three months following initial production (i.e., "initial production"), as well as three additional samples collected at 28 months after production begin. All produced water samples were collected directly from the water discharge port of the sealed gas-water separator into specified bottle ware provided by the respective analytical laboratories. In accordance with the operator's standard of practice, water samples were not filtered prior to collection.

Ra isotope analysis (^{226}Ra and ^{228}Ra) was performed at TestAmerica Laboratories (Earth City, Missouri) using gamma spectroscopy by EPA Method 901.1. ^{228}Ra and ^{226}Ra measurements are reported herein as activities in pCi/L. Accuracy varied by analysis, with 2σ values reported in Table 3.2. The relative standard deviation (RSD) for ^{228}Ra/^{226}Ra was calculated from the individual isotope measurement uncertainty following propagation of sample measurement variance for each isotope (Caldwell and Vahidsafa, 2020). Water isotope analysis (δ^{18}O and δ^{2}H) was performed at Isotech Laboratories (Champaign, Illinois) by vacuum distillation followed by continuous flow-isotope ratio mass spectrometry, with reported 2σ values of ±0.2‰ and ±4.0‰ for δ^{18}O and δ^{2}H, respectively. Sr isotope analysis (^{87}Sr and ^{86}Sr) was performed on a Thermo Scientific Neptune multiple collector-inductively coupled plasma-mass spectrometer (MC-ICP-MS) in the EARTH Core Facility at the University of Utah. The accuracy was assessed via comparison of the average measured value of the internal standard SRM 987 of 0.71029 to the certified value of 0.71034 ± 0.00026. The external precision as 2σ was ±0.00002 based on repeated measurements of SRM 987 for all analyses. Samples were analyzed for Cl, Na, and Br at Environmental Service Laboratories, Inc. (Indiana, Pennsylvania) or at Green Analytical Laboratories (Durango, Colorado). Total dissolved solids concentrations (TDS) were calculated as the sum of all major ions. Br data was available for all time-series data, and 91 of the 123 individual produced water samples.

Average daily water and gas production, measured at the well head with an Emerson R100 Coriolis meter and ABB Totalflow XMV meter, respectively, was evaluated for each well in this study for the relevant sampling dates. Specifically, daily water and gas measurements for the 7 days prior to the sampling event, the day of the sampling event itself, and the 7 days after the sampling event were averaged. The ratio of daily water production and gas production was then calculated based on these respective 15-day moving averages.

In addition to produced water data, Energy-Dispersive X-ray Fluorescence (ED-XRF) concentration data were generated for three cores obtained during the drilling of Marcellus gas wells in the study area. Specifically, ED-XRF concentration measurements were obtained using a portable Bruker Tracer 5i instrument every 0.1 to 10 ft from strata spanning the Upper Marcellus Shale to the Needmore Shale (Core 1), the Upper Marcellus Shale to the Onondaga Limestone (Core 2), and the Purcell Limestone to the Onondaga Limestone (Core 3). For this purposes of this study, concentrations of Th, U, Rb, and Sr were evaluated to characterize the Th/U and Rb/Sr ratios of each formation (i.e., minimum, 25th percentile, median, 75th percentile, and maximum ratios).

Deionized water extractions were performed on 31 discrete core and cuttings samples from the three cored intervals to evaluate the $^{87}Sr/^{86}Sr$ ratio of pore water and water-soluble salts (per the procedures described in Stewart et al., 2015) (Table 3.3). To minimize drilling mud residue, the outer 8 mm of each core was removed prior to sample extraction. Cuttings samples were obtained using a freshwater-based drilling mud, and prior to the water extraction, were washed in deionized water in a sieve to remove residue and fines. After rinsing, the core and cuttings samples were dried and crushed to 150-250 um under clean conditions. Ultrapure (18.2 MΩ/cm) water was then added at a water:sample mass ratio of ~60:1. The water amended aliquots were shaken for 24 hours, centrifuged, and the water solution was removed and filtered using a 0.45 μm filter. Following this step, for a subset of core and cuttings samples, a 1M ultrapure ammonium acetate extraction was performed in sequence using an identical volume and shaking, centrifuging, and filtering procedure as the ultrapure water step. Finally, for eight core or cuttings samples, a full four-step sequential extraction procedure was performed using ultrapure water, 1M ultrapure ammonium acetate, 1M ultrapure acetic acid and 0.1M ultrapure HCl using identical procedures to those described above. All filtered fluids were acidified with ultrapure nitric acid (HNO_3) and analyzed for $^{87}Sr/^{86}Sr$ at the EARTH Core Facility at the University of Utah in the same manner as produced water samples.

RESULTS

Na-Cl-Br systematics

The origin of produced water salinity (e.g., evaporated seawater versus salt dissolution) can be evaluated through use of the Na-Cl-Br system (e.g., Dresel and Rose, 2010). Specifically, brine originating from seawater evaporated past halite saturation is enriched in Br and depleted in Na and Cl, resulting in high Br/Na and Br/Cl ratios relative to the original seawater. If brine instead originates from the dissolution of halite, the opposite will be true, i.e., it will be depleted in Br relative to Na and Cl, resulting in lower Br/Na/ and Br/Cl ratios relative to seawater. Based on this conceptual model, researchers commonly utilize plots of Cl vs. Br and Cl/Br vs. Na/Br to assess brine origin. However, such compositional data plots are potentially subject to misinterpretation (e.g., false correlations), as changes in the abundance of one component necessarily changes the abundance of another. To address this issue, plots of isometric log ratio (ILR) transformations for molar Na and Cl concentrations ($1/\sqrt{2}*\ln[Na]/[Cl]$) and Na, Cl, and Br concentrations ($\sqrt{2}/\sqrt{3}*\ln([Na]/[Cl])^{0.5}/[Br]$) have been proposed (Engle and Rowan, 2014, 2013). ILR plots are not subject to the same potential numerical errors as compositional data plots. On a simple plot of the Cl vs. Br molar concentration, none of the Marcellus produced water samples plot above the seawater evaporation line, indicating halite dissolution is not a source of salinity (Figure 3.4A).

Instead, samples with elevated salinity (i.e., TDS≥100,000 mg/L) plot along a general trend line from evaporated Salina seawater past the point of halite saturation (Point A) to relatively fresh water. This trend is interpreted to represent mixing of evaporated paleoseawater and one or more of the following water sources: injection fluid, water of condensation, unevaporated seawater, and meteoric water. Samples with TDS <100,000 mg/L could represent an extension of this trend, or alternatively, water independently progressing along the seawater evaporation path. The ILR plot informs a more detailed interpretation (Figure 3.4B). Specifically, all produced water samples, regardless of salinity, exhibit Na-Cl and Na-Cl-Br ILR ratios consistent with seawater evaporated past the point of halite saturation, indicating that even the freshest produced water samples represent seawater evaporated past the point of halite saturation that has been diluted with a fresher water source (where dilution with relatively fresh water would not affect Na-Cl and Na-Cl-Br ILR ratios). As in Figure 3.4A, none of the produced water samples in Figure 3.4B exhibit ILR ratios consistent with halite dissolution and appear to represent a common origin (evaporated paleoseawater diluted by varying amounts).

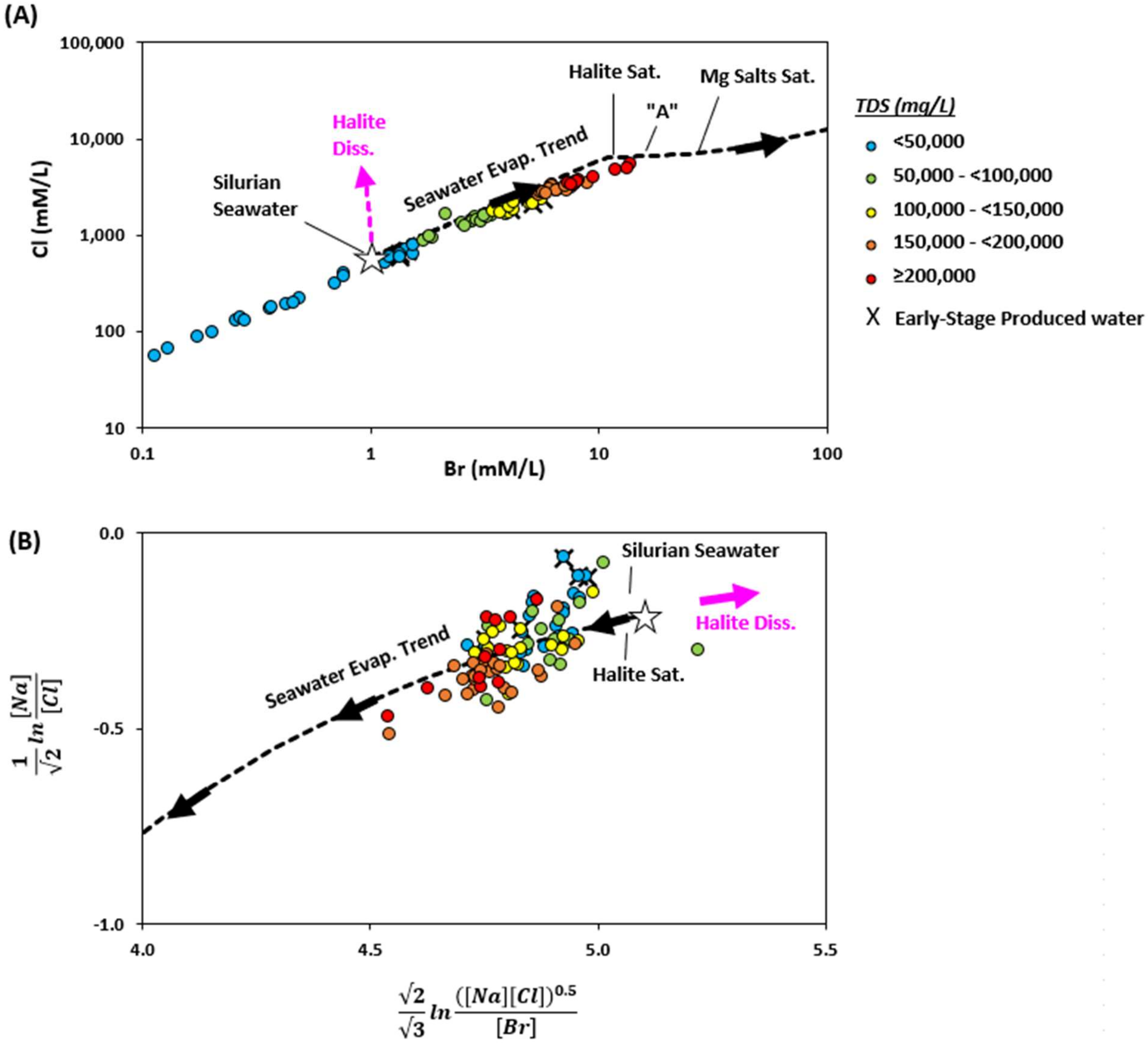

Figure 3.4: A) Cl vs. Br (mM/L), and B) $\frac{1}{\sqrt{2}} ln \frac{[Na]}{[Cl]}$ vs. $\frac{\sqrt{2}}{\sqrt{3}} ln \frac{([Na][Cl])^{0.5}}{[Br]}$ for 91 produced water samples with both Br and Cl measurements from Marcellus Shale gas wells sampled once each in the study area.

Time-series data

Time-series produced water data from Wells A, B, and C show that samples collected on the first day of flowback immediately exhibit different (higher) $^{87}Sr/^{86}Sr$ ratios than the respective injection fluids (Figure 3.5A). The $^{87}Sr/^{86}Sr$ ratio in samples from all three wells marginally increases thereafter (e.g., from 0.71147 to 0.71153 at Well A) until the last day of sampling (day 844 of production), where Wells A, B, and C exhibit a virtually identical $^{87}Sr/^{86}Sr$ ratio (0.71151 to 0.71152). Over this same timeframe, however, there is a continuous and significant increase in TDS concentrations in samples from Wells A (from 33,900 to 79,700 mg/L) and B (from 24,400 to 73,600 mg/L). Sr concentrations in Well A and B samples also continuously increase by a factor of 3 or more during production (Figure 3.5B, Figure B.1A). By comparison, Well C samples exhibited relatively constant TDS (35,000 to 40,000 mg/L) and Sr (520 to 750 mg/L) concentrations over the first 3 months of production (~89 days), with notably lower (more dilute) TDS and Sr concentrations on day 844. Overall, samples from all three wells exhibited a narrow range of $^{87}Sr/^{86}Sr$ ratios (from 0.7114 to 0.7115) within the larger overall range of study area produced water $^{87}Sr/^{86}Sr$ ratios (from 0.7101 to 0.7118).

As with $^{87}Sr/^{86}Sr$, the $^{228}Ra/^{226}Ra$ ratio of initial flowback samples differ notably (in this case, lower) from the respective injection fluids. However, the produced water $^{228}Ra/^{226}Ra$ ratios over time at Wells A, B, and C do not approach a similar value (Figure 3.5C), although they remain individually stable. During the first 88 days, Well C exhibits $^{228}Ra/^{226}Ra$ ratios within a narrow range of 0.05 to 0.08 (note that ^{228}Ra was not detected in the sample from Well C collected after 28 months of production, and therefore, the $^{228}Ra/^{226}Ra$ ratio is not shown). The $^{228}Ra/^{226}Ra$ ratios of Wells A and B produced waters exhibit significantly more variability than Well C; however, the central trend in the $^{228}Ra/^{226}Ra$ ratio at these wells is consistently between ~0.4 and 0.5 (an order of magnitude higher than Well C, without overlapping error bars). The increased ^{228}Ra/^{226}Ra variability in Well A and B relative to Well C is associated with larger analytical errors at lower ^{228}Ra and ^{226}Ra activities. The stability of ^{228}Ra/^{226}Ra ratios persists in samples from Wells A and B even as total Ra (^{228}Ra+^{226}Ra) concentrations increase by an order of magnitude (Figure 3.5D and Figure B.1B), TDS concentrations double to triple (Figure 3.6A and Figure B.2A), and the [Ca]/[Na] ratio almost doubles (from ~0.05 to ~0.09) during the same timeframe (Figure 3.6B and Figure B.2B). Well C, which exhibits a lower ^{228}Ra/^{226}Ra ratio than Wells A and B (median ~0.07), displays more stable total Ra (~2100 to ~3300 pCi/L), TDS (35,100 to 37,600 mg/L) and [Ca]/[Na] ratios (~0.06) over the first 3 months of production, with a maximum Ca concentration of 1260 mg/L (0.03 M). The last sample from Well C on day 844 (28 months of production) is significantly more dilute, associated with a strong contribution from water of condensation as confirmed by a lighter, non-meteoric δ^{18}O and δ^{2}H composition (see Molofsky et al., 2022), and exhibits a notably higher [Ca]/[Na] ratio (0.09). As noted previously, Landis et al. (2018b, 2018a) suggested that Marcellus produced water ^{228}Ra/^{226}Ra less than 0.1 reflect the preferential extraction of Ra^{2+} from the organic phase in association with increasing [Ca2+]/[Na+] ratios and a high Ca^{2+} content (1M). This relationship is not observed in this particular dataset, either in Well C time-series data or the larger dataset of single produced water samples (Figures B.2A, B and C).

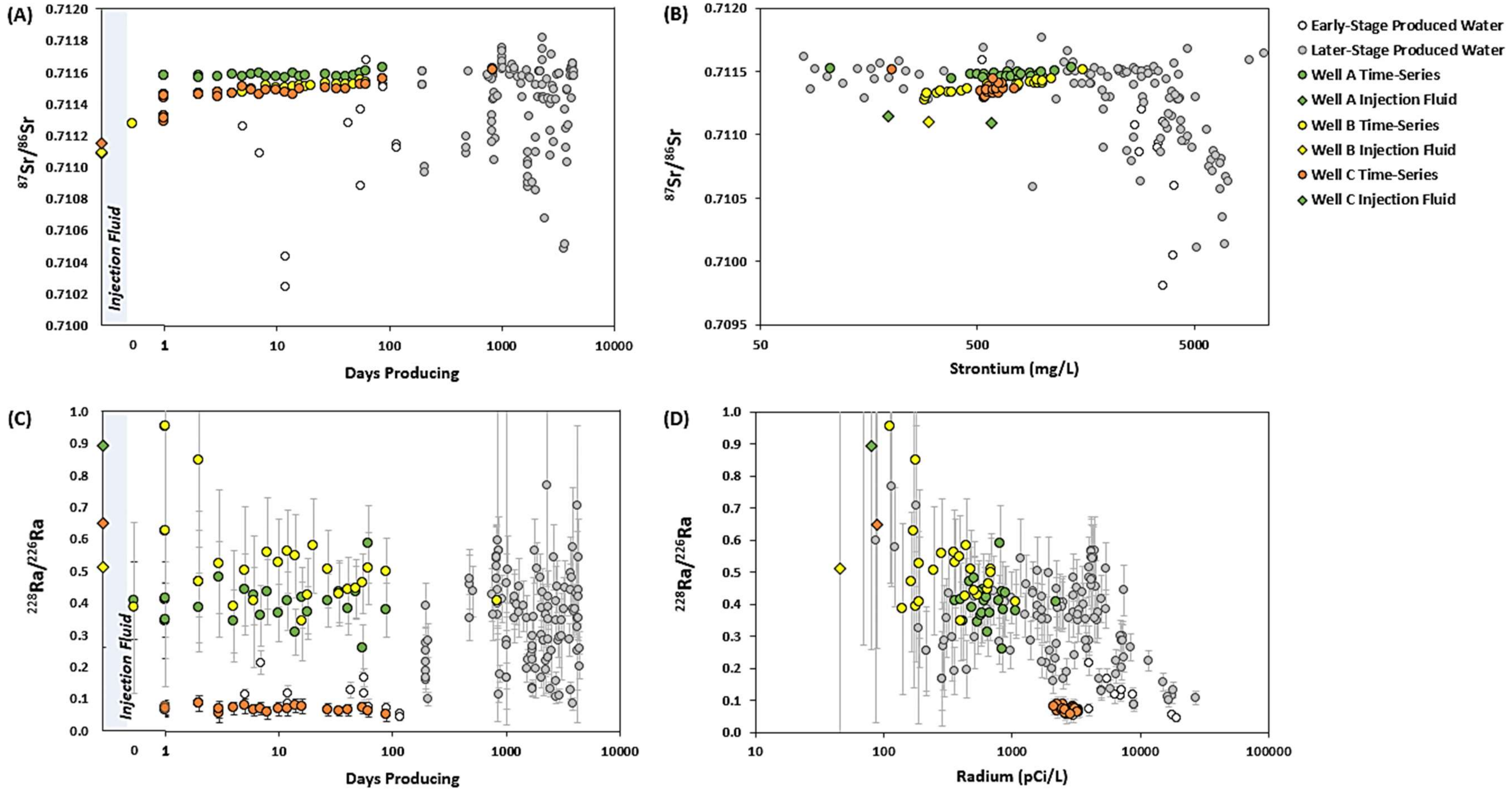

Figure 3.5: A) $^{87}Sr/^{86}Sr$ vs. days producing, B) $^{87}Sr/^{86}Sr$ vs. strontium concentration C) $^{228}Ra/^{226}Ra$ vs. days producing, and D) $^{228}Ra/^{226}Ra$ vs. total radium concentration for Well A, B, and C time-series data and 123 produced water samples from Marcellus Shale gas wells sampled once each in the study area. 2σ errors for $^{228}Ra/^{226}Ra$ are shown as gray error bars. 2σ errors for $^{87}Sr/^{86}Sr$ are smaller than symbol (<±0.00002).

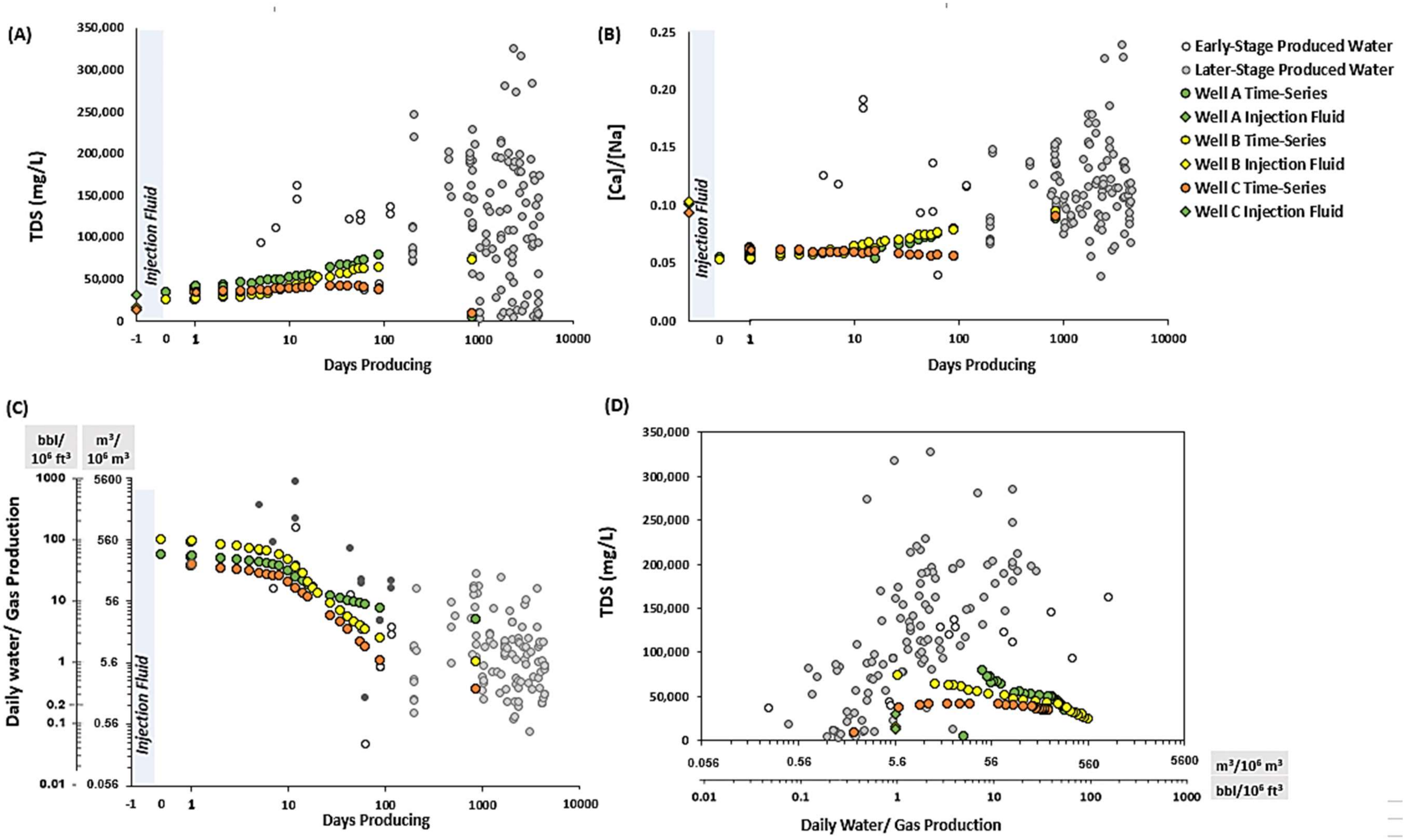

Figure 3.6: A) TDS vs. days producing, B) [Ca]/[Na] vs. days producing, C) Rate of daily water-to-gas production vs. days producing, and D) TDS vs rate of daily water-to-gas production for Well A, B, and C time-series data and 123 produced water samples from Marcellus Shale gas wells sampled once each in the study area.

Ratio of water-to-gas production

The average daily water-to-gas production ratio for each of the 123 individual produced water samples, as well as the time-series from Wells A, B, and C is shown on Figure 3.6C. During initial flowback, wells A, B, and C exhibit elevated daily water-to-gas ratios (upwards of 168 m^3 water/10^6 m^3 gas per day, or 30 bbls water/10^6 ft^3 gas), declining rapidly during the first 100 days of production. By the last day of sampling (day 844), the daily water-to-gas ratios for these wells plots within the bulk of later-stage individual produced water samples (water-to-gas ratios ranging from 0.45 to 163 m^3 water/10^6 m^3 gas per day per day, or 0.08 to 29 bbls water/10^6 ft^3 gas). By this stage of production, there is no clear relationship in the study area between the number of days producing and the water-to-gas ratio. There is a strong positive association, however, between the water-to-gas ratio and TDS concentration (Figure 3.6D).

^{228}Ra/^{226}Ra and ^{87}Sr/^{86}Sr distribution in larger dataset of individual produced water samples

Individual produced water samples exhibit ^{87}Sr/^{86}Sr ratios ranging from 0.71177 on the high end to 0.70981 on the low end (Figure 3.7A). This is similar to the range of ^{87}Sr/^{86}Sr ratios reported by Chapman et al. (2012) for Marcellus produced water from Bradford, Westmoreland, Washington, and Green Counties in Pennsylvania (0.7101 to 0.7121). Of note, TDS concentrations less than 100,000 mg/L are almost entirely associated with ^{87}Sr/^{86}Sr ratios >0.7112 (Figure 3.7A). A handful of these samples originate from wells that have only been producing a few days and their low Sr concentration likely reflects dilution by injection fluid, as is the case for earlier production from Wells A, B, and C. However, the majority of data comprising this trend come from samples that were collected 6 months or more into production (later-stage production). These samples also exhibit the lowest ratios of water-to-gas production, the lowest TDS concentrations (Figure 3.7A), and the most negative water isotope (δ^2H and δ^{18}O) compositions (Figure B.3).

^{228}Ra/^{226}Ra ratios for the individual produced water samples range from 0.04 to 0.78, with the majority exhibiting ratios <0.6 (Figure 3.7B). Almost half (46) of the individual produced water samples exhibit ^{228}Ra/^{226}Ra ratios less than 0.3, the range reported to characterize Marcellus produced waters across Pennsylvania and New York by Rowan et al. (2011). These samples also, on average, exhibit higher total Ra concentrations (average of 5928 pCi/L) than samples with ^{228}Ra/^{226}Ra ratios >0.3 (average of 2703 pCi/L). Unlike ^{87}Sr/^{86}Sr, there is no clear association between the ^{228}Ra/^{226}Ra ratio and the daily water-to-gas production ratio or TDS concentration (Figure 3.7B).

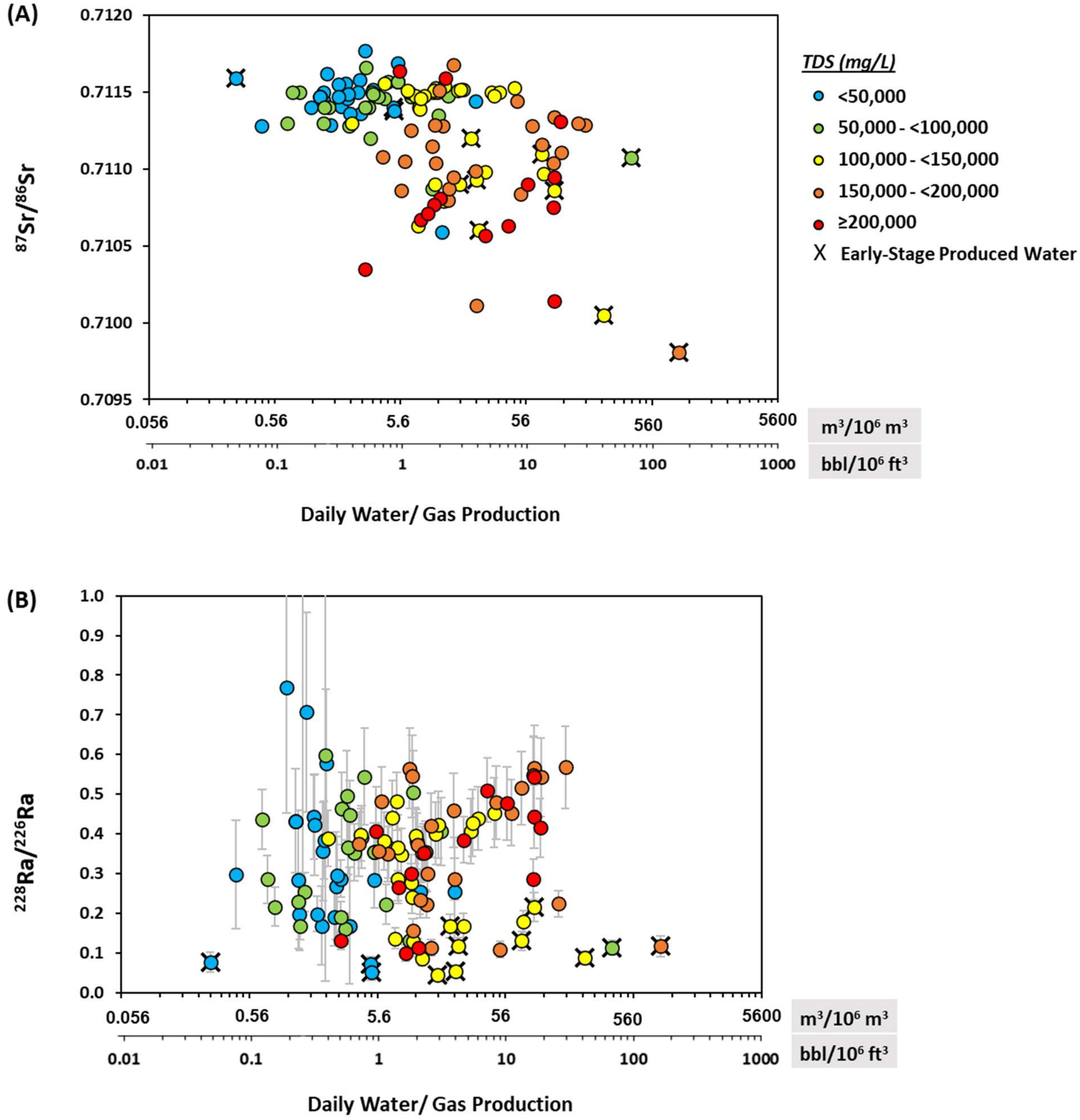

Figure 3.7: A) ^{7}Sr/^{86}Sr vs. TDS, and B) ^{228}Ra/^{226}Ra vs. rate of daily water-to-gas production for 123 produced water samples from Marcellus Shale gas wells sampled once each in the study area. 2σ errors for ^{228}Ra/^{226}Ra are shown as gray error bars. 2σ errors for ^{87}Sr/^{86}Sr are smaller than symbol (<±0.00002).

Development of characteristic $^{228}Ra/^{226}Ra$ and $^{87}Sr/^{86}Sr$ ranges for the Marcellus and other formations in cored intervals

Information on the Th, U, Rb, and Sr concentrations of different formations can serve as a powerful tool for estimating the $^{228}Ra/^{226}Ra$ and $^{87}Sr/^{86}Sr$ ratios of pore fluids from these formations. As described previously, assuming secular equilibrium, the rock Th/U ratio can be used to infer the $^{228}Ra/^{226}Ra$ of the formation and potentially the co-mingled formation water (Kraemer and Reid, 1984). Our evaluation of time-series produced water data from Wells A, B, and C shows that the $^{228}Ra/^{226}Ra$ ratios consistently fall along a central trend (i.e., ratios do not increase or decrease over time), even when fluid salinity and Ca content changes notably, suggesting a single primary source of Ra^{2+} in water samples collected from these wells. For the purposes of this exercise, I assume that Ra isotope composition of pore fluids directly reflects the bulk rock Th/U composition, which assumes that the rate of transfer of Ra from the rock to the water is not rate-limiting and that the uptake rate and relative abundance of ^{228}Ra and ^{226}Ra in the whole rock is equally transferred to the water. Among all three cores, the median predicted $^{228}Ra/^{226}Ra$ ratio of the Union Springs unit (including the Union Springs lime) is remarkably consistent (within the narrow range of 0.04 to 0.07) (Figure 3.8), reflecting the high U content (median > 20 mg/kg) in the Union Springs formation. Of note, the Upper Onondaga Limestone in all three cores exhibits median predicted $^{228}Ra/^{226}Ra$ ratios similar to the Union Springs formation. For the purposes of this study, the “Upper Onondaga” is characterized as the upper ~6 m (20 ft) of the Onondaga formation, and may be considered to exhibit some transitional features between the two units. Specifically, comparison of U content in the Upper Onondaga to that in the Lower Onondaga (where ED-XRF data is available for a 115 ft portion of Core 1) show that the Upper Onondaga exhibits higher U concentrations, and lower Th/U ratios and predicted $^{228}Ra/^{226}Ra$ ratios, than the underlying Onondaga (median $^{228}Ra/^{226}Ra = 0.42$). Above the Union Springs, the

Lower Marcellus Shale, Purcell Limestone, and Upper Marcellus Shale display median predicted $^{228}Ra/^{226}Ra$ ratios >0.1, consistent with a higher Th/U ratio, although there is notable variability among the cores. This variability in Th/U ratios may reflect differences in the depositional environment, organic and mineralogical content, and diagenetic history of the local core environments (Adams and Weaver, 1958).

Although the Rb and Sr bulk rock composition cannot be directly converted to $^{87}Sr/^{86}Sr$ ratios (additional information is required for that exercise, including the initial bulk rock $^{87}Sr/^{86}Sr$ ratio and ^{87}Rb composition, as well as the decay time), the Rb/Sr ratio can inform our general understanding of higher vs. lower $^{87}Sr/^{86}Sr$ ratios. Specifically, higher Rb/Sr ratios are typically associated with more radiogenic ^{87}Sr, and higher $^{87}Sr/^{86}Sr$ ratios in whole rock samples. Median Rb/Sr ratios for each formation exhibit similar ranges across the three cores. For example, in the two cores with available Upper Marcellus ED-XRF data, the median Rb/Sr ratio is the highest of all formations (1.25 to 1.28), followed by the Lower Marcellus (0.43 to 0.81). The Purcell limestone, the Union Springs and Union Springs Lime formations exhibit similar median Rb/Sr ratios in all three cores between (0.09 and 0.25), and the Upper Onondaga and Lower Onondaga Limestone exhibits the lowest median Rb/Sr ratios of all formations (0.01 to 0.06) (Figure 3.8).

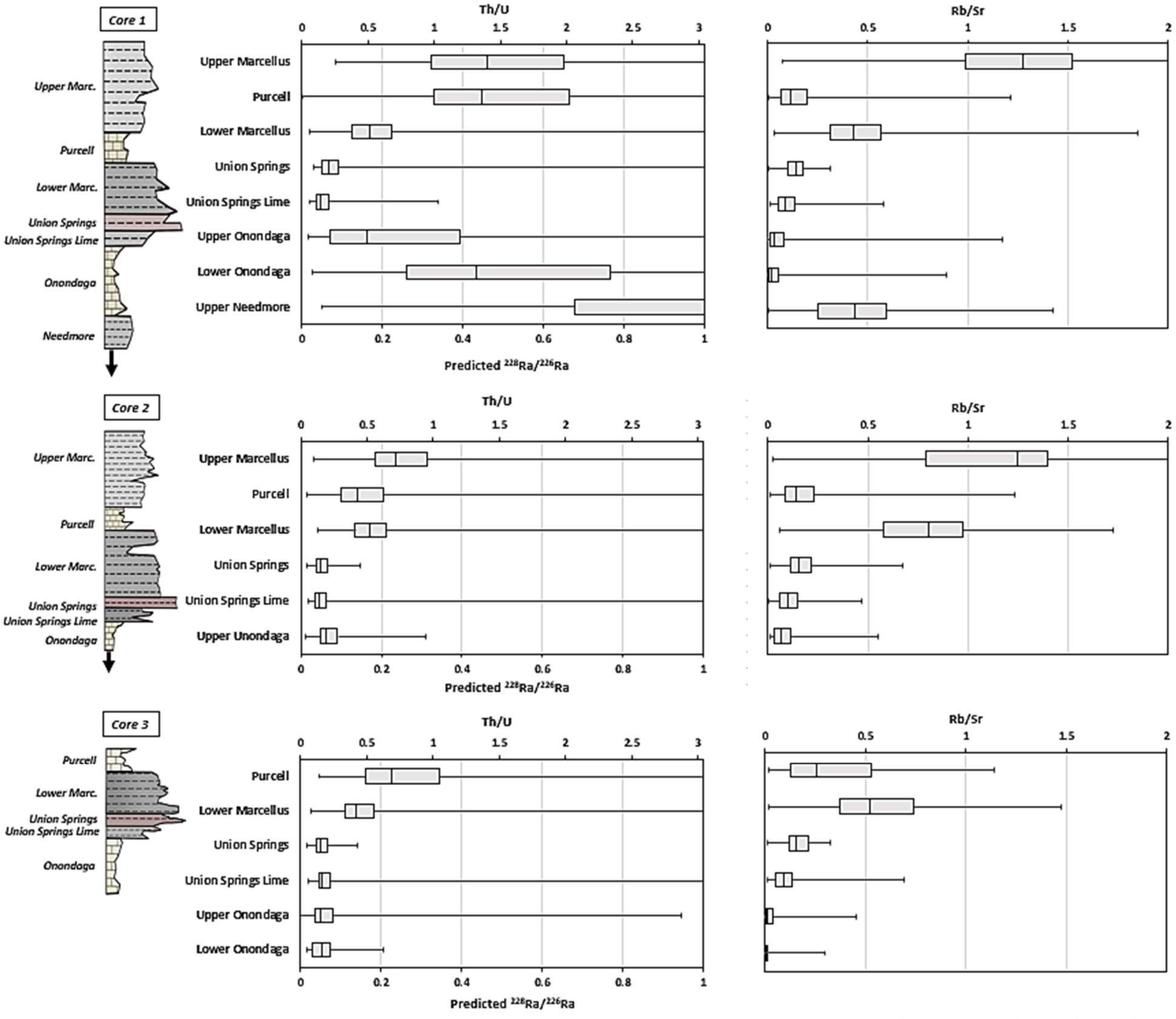

Figure 3.8: Distribution of measured Th/U and Rb/Sr ED-XRF measurements and predicted ^{228}Ra/^{226}Ra ratios for each formation in Cores 1, 2, and 3. Predicted ^{228}Ra/^{226}Ra ratios are directly calculated from Th/U measurements.

In addition to ED-XRF measurements of Rb/Sr, water extractions were obtained from discreet sampling intervals within each formation in the three cores and associated cuttings and analyzed for the $^{87}Sr/^{86}Sr$ ratio and Sr concentration (Table 3.3). Sequential ammonium acetate, acetic acid, and hydrochloric acid extractions were also performed on a subset of samples and are discussed further in the Supporting Information. The $^{87}Sr/^{86}Sr$ ratio of water leachates was plotted against the average ED-XRF Rb/Sr ratio (weighted by the Sr concentration) of the respective discrete sampling interval (Figure 3.9) to evaluate the relationship between bulk rock Rb/Sr and $^{87}Sr/^{86}Sr$ of water-soluble components. Stewart et al. (2105) reported that the $^{87}Sr/^{86}Sr$ of water-soluble and exchangeable components of the Marcellus Shale exhibit a similar range to those of Marcellus produced water. I postulate that the $^{87}Sr/^{86}Sr$ ratio of water-soluble components reflects that of Marcellus pore water (liquid or evaporated), which contains Sr from the original fluid source (e.g., the Salina) and the water soluble/exchangeable fraction of other intermediate formations and the Marcellus itself. As shown in Figure 3.9, formations with higher bulk Rb/Sr largely exhibit more radiogenic (higher) $^{87}Sr/^{86}Sr$ of water-soluble components. In this case, a logarithmic model ($^{87}Sr/^{86}Sr = 0.0003\ln(Rb/Sr) + 0.7116$) was found to better predict and capture the data across the full range of $^{87}Sr/^{86}Sr$ ratios than a linear model, accounting for approximately 44% of the total variability. Variations in reservoir rock composition and the accessibility of different Sr-bearing fractions are likely a significant contributor to the uncertainty in the regression relationship; nevertheless, the uncertainty is not so large to warrant discounting the predicted value, and the regression demonstrates that simple water-rock interaction produces fluids with $^{87}Sr/^{86}Sr$ ratios that increase when Rb/Sr ratios in the whole rock are elevated.

Using this simple relationship, the $^{87}Sr/^{86}Sr$ ratio of water-soluble components was estimated for all available ED-XRF Rb/Sr measurements in the three cored intervals. Summary predicted $^{87}Sr/^{86}Sr$ ratios were then calculated for formations within each core (Figure 3.10). As with the median Rb/Sr ratios, the median predicted $^{87}Sr/^{86}Sr$ ratios exhibit similar trends among formations. Specifically, the Upper Marcellus consistently exhibits the highest median predicted $^{87}Sr/^{86}Sr$ ratio (0.7117 in both cores with available Upper Marcellus data), followed by the Lower Marcellus (0.7113 to 0.7115), the Purcell (0.7110 to 0.7112), the Union Springs (0.7109 to 0.7111) and the Onondaga (0.7102 to 0.7108).

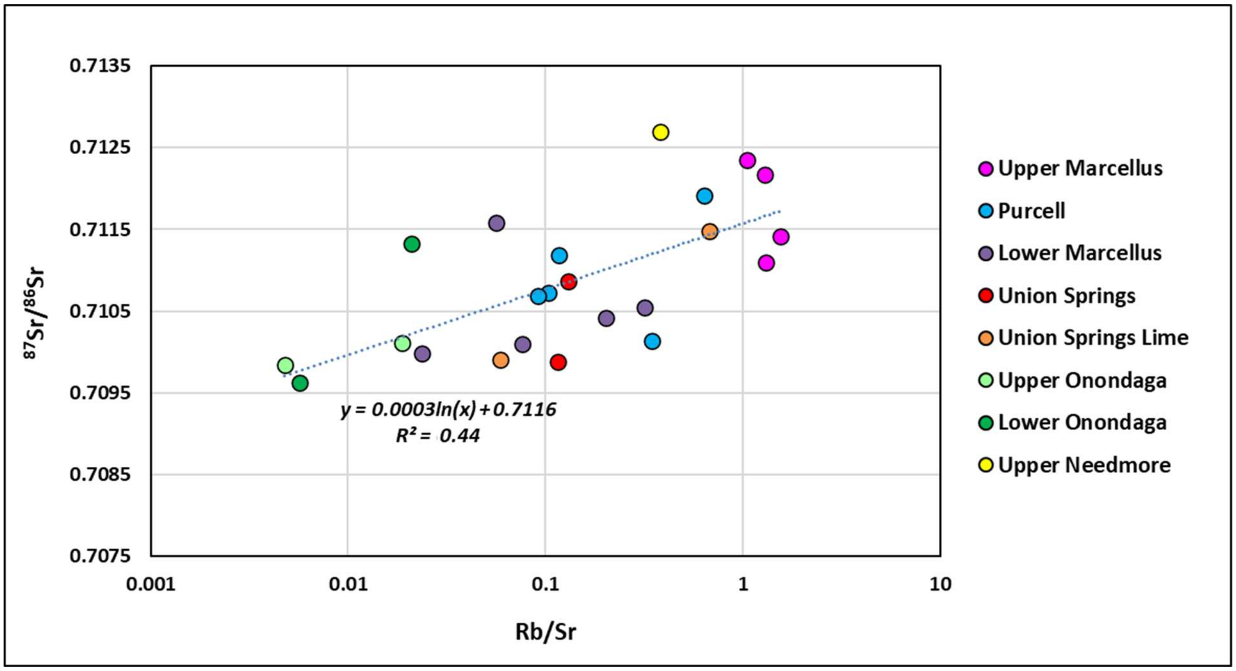

Figure 3.9: $^{87}Sr/^{86}Sr$ of ultrapure water leachates of discreet core samples vs. weighted average XRF Rb/Sr measurements of that same core interval (weighted by Sr concentration).

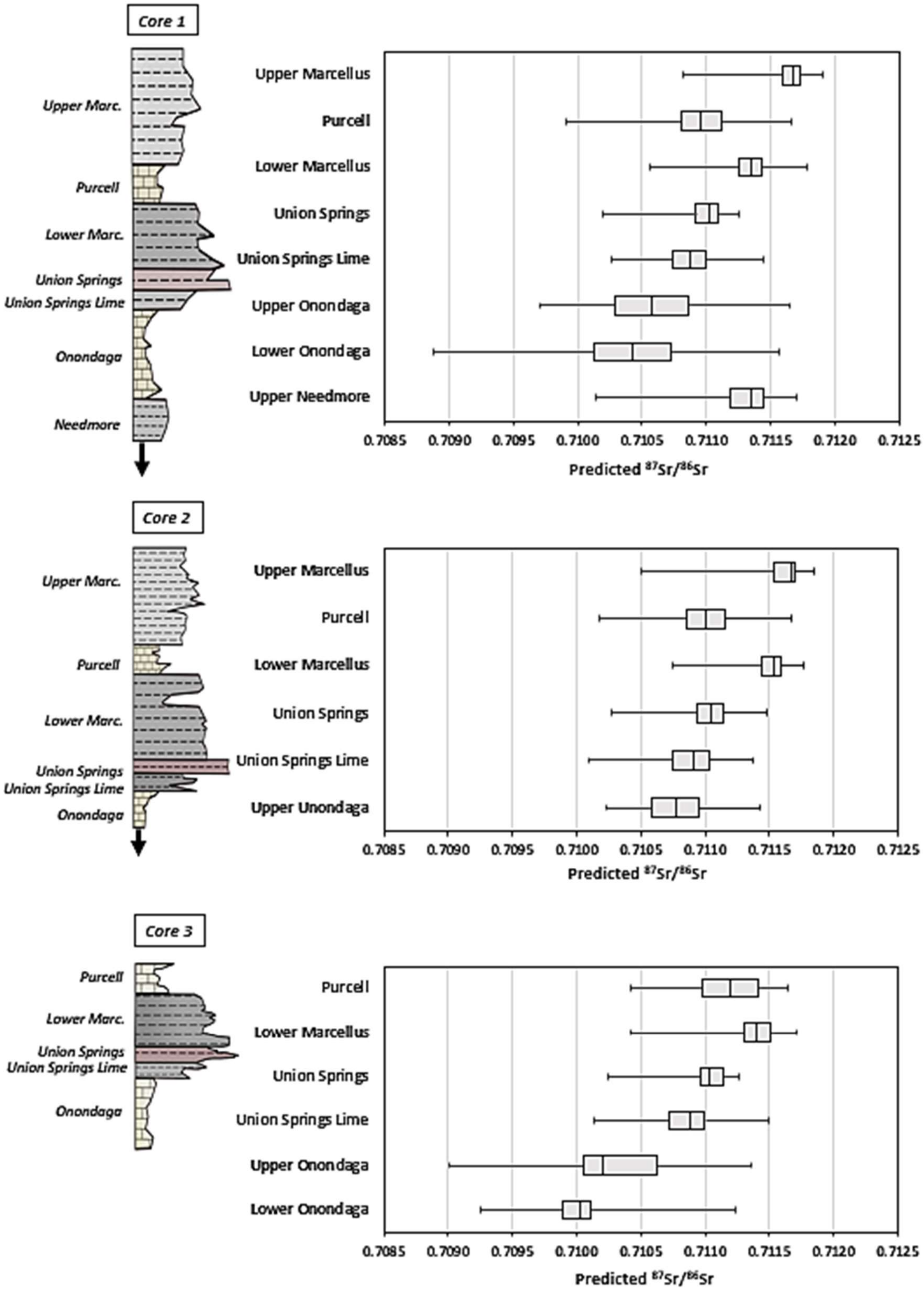

Figure 3.10: Distribution of predicted ^{7}Sr/^{86}Sr measurements for each formation in Cores 1, 2, and 3.

DISCUSSION

In this study, both compositional and ILR plots of Cl, Br, and Na data (Figures 3.4A and B) show that, regardless of TDS concentration, salinity in produced water samples from the study area is consistent with seawater evaporated past the point of halite saturation, rather than halite dissolution. This suggests that salinity in produced water is originating from pore fluids, diluted with variable amounts of fresher water sources (e.g., injection fluid, water of condensation, unevaporated sweater, and meteoric water), as suggested by Dresel and Rose (2010), Rowan et al. (2015), and others.

The fact that produced water samples collected on the first day of flowback immediately exhibit different $^{87}Sr/^{86}Sr$ ratios and $^{228}Ra/^{226}Ra$ ratios than injection fluids (Figures 3.5A and C) is interpreted to reflect input from Sr-rich and Ra-rich downhole pore fluids (with possible contributions of water-soluble/exchangeable formation components) mixing with the relatively fresh injection fluids. This conclusion is further supported by the observation that $^{87}Sr/^{86}Sr$ ratios increase only slightly over time, and $^{228}Ra/^{226}Ra$ ratios are relatively stable, while TDS, Sr, and Ra concentrations increase substantially in Wells A and B (Figure 3.6A, Figures B.2A and B), suggesting that the primary source of strontium and radium remained constant, even as the mixing relationship between injection fluid and pore fluids evolves. Of note, Well C exhibits relatively constant TDS, Sr, and Ra concentrations during the first 3 months of production, indicating that this well produces a consistent mixture of injection fluid and formation fluid throughout that time period. This well also exhibits the lowest daily water-to-gas production rates of all three wells with time-series data after 3 months of production (6.2 m^3 water/10^6 m^3 gas per day, or <1.1 bbl water/10^6 ft^3 gas per day). Combined, these data suggest that the targeted formation in Well C contained a relatively small volume of movable water that, when diluted by hydraulic fracturing fluid, formed a uniform mixture that continued to drain from the hydraulically induced fracture network in low volumes over time. The sample from day 844 of production from Well C is notably more dilute (lower TDS, Sr, and Ra) than samples collected during the first three months. This is interpreted to represent later-stage dilution of a small volume of downhole fluids (comprised of the aforementioned formation fluid/ fracturing fluid mixture) with water condensing out of the gas phase, a phenomenon discussed in more detail below. The lack of a clear relationship between $^{228}Ra/^{226}Ra$ and TDS (Figure B.2A), [Ca]/[Na] (Figure 3.6B and Figure B.2B), or the Ca concentration (Figure B.2C) suggests that the controls on the $^{228}Ra/^{226}Ra$ ratio of produced waters for our particular time-series are not impacted significantly by these factors (at least, in the range of TDS, Ca, and [Ca]/[Na] observed), and instead follow a model of a singular primary contributing Ra source within the formation.

As noted above, ratios of daily water-to-gas production volumes provide additional insight into the origin of produced fluids. Formations with low volumes of movable water and relatively low permeability (i.e., much of the Marcellus) are anticipated to produce lower daily water-to-gas ratios than formations that are relatively saturated with higher permeability (e.g., out-of-zone limestone or sandstone formations). Specifically, while the permeability of the Marcellus is enhanced by hydraulic fracturing, formation water in pores (pore water) not in contact with fractures is still thought to be largely inaccessible (Balashov et al., 2015). Based on this assumption, Marcellus Shale gas wells can, at most, produce a finite amount of water equal to the pore spaces encountered by the fracturing network (assuming no out-of-zone water). If the formation contains a low volume of movable water to begin with, that finite volume of water will be relatively small, and water-to-gas production can be miniscule (e.g., <5.6 m^3 water/10^6 m^3 gas per day, or <1 bbl water/10^6 ft^3 gas per day). Even if a low-permeability formation is relatively water saturated, and therefore produces a significant volume of pore fluid early on, I suggest that once that fracture-accessed pore water is depleted, the lack of native permeability will preclude sustained production of formation fluids over time. Thus, these wells should still show a decline in water-to-gas production ratios over time. By contrast, wells drawing water from relatively permeable water saturated formations (i.e., out-of-zone water) can sustain larger volumes of water production over time.

In this study, the strong positive relationship between water-to-gas ratio and TDS concentration, particularly during later-stage production (6 months or more) (Figure 3.6D), indicates that that higher daily water-to-gas production ratios are related to the sustained production of formation fluids over time. The likelihood that these formation fluids originate out-of-zone is bolstered by the observation that samples with higher TDS concentrations (>100,000 mg/L) exhibit $^{87}Sr/^{86}Sr$ ratios that span the entire range of values (0.7098 to 0.7117), pointing to two or more possible sources of movable water (Figure 3.7A). In contrast, wells exhibiting lower TDS concentrations (<100,000 mg/L) during later-stage production (e.g., Wells A, B, and C) are characterized by lower ratios of water-to-gas production rates and $^{87}Sr/^{86}Sr$ ratios within a limited range of higher values (0.7112 to 0.7117). These observations suggest that an elevated $^{87}Sr/^{86}Sr$ ratio is characteristic of pore fluids from one or more low-permeability formation(s) that contains little movable water. Later-stage produced water samples exhibiting lower TDS concentrations (<100,000 mg/L) also exhibit more negative water isotope (δ^2H and $\delta^{18}O$) compositions (Figure B.4). I suggest the depleted water isotopic composition reflects the dilution of downhole fluids with water condensing out of the gas phase, i.e. "water of condensation", which is characterized by low TDS (freshwater) and isotopically light but non-meteoric compositions of δ^2H and $\delta^{18}O$. As described in Molofsky et al. (2022) every 10^6 m^3 of Marcellus gas at typical reservoir temperature (~60°C) is anticipated to contain 1.1 m^3 of water vapor (or ~0.2 bbl of water vapor per 10^6 ft^3 of gas), which condenses as gas leaves the reservoir or at the surface. As such, wells with low ratios of water-to-gas production (e.g., <5.6 m^3 water/10^6 m^3 gas per day, or <1 bbl water/10^6 ft^3 gas per day) necessarily exhibit a produced water that contains a significant fraction of water of condensation.

In contrast to $^{87}Sr/^{86}Sr$, there is no clear relationship between the $^{228}Ra/^{226}Ra$ ratio and the daily water-to-gas production ratio or TDS concentration (Figure 3.7B), suggesting that either formations with different amounts of movable water exhibit similar $^{228}Ra/^{226}Ra$ ratios, or possibly, that $^{228}Ra/^{226}Ra$ ratios in Marcellus fluids are changing over time after the incursion of exogenous fluid. As detailed in the "Geology and Fluid Sources" section, although the Oriskany Sandstone and permeable stringers remain possible sources of exogenous brine in the Marcellus, the Onondaga Limestone is considered to be the most likely source of out-of-zone fluid in the study area, and is the primary focus of our evaluation of potential exogenous fluid production herein. Discussions with oil and gas operators in the region indicate that pre-existing structural features (i.e., faults and fractures) are a potential conduit for the cross-formation flow of Onondaga formation water. Additionally, faults and fractures that are enhanced/created by hydraulic fracturing could serve as pathways for Onondaga fluid migration into the Marcellus. If an exogenous Onondaga fluid were to enter the Marcellus, I propose that one of three scenarios could occur:

1) **Exogenous Onondaga fluid moves through the Marcellus quickly (little to no residence time):** Onondaga fluid moves through fractures in the Marcellus to the wellbore in relatively rapid fashion. In this case, I assume that there is negligible in-growth and decay of Ra during transport, and that the majority of accessible Ra and Sr in the shale matrix (either in pore fluid or the water-soluble/exchangeable fraction) is "flushed through" after some initial period of consistent Onondaga fluid production.

Thereafter, the ^{228}Ra/^{226}Ra and ^{87}Sr/^{86}Sr of later-stage produced water largely reflects that of Onondaga exogenous fluid.

2) **Exogenous Onondaga fluid moves through the Marcellus moderately quickly (some residence time in Marcellus):** Onondaga fluid is transported through fractures and pore spaces (i.e, matrix flow) into and through the Marcellus (with some residence time in the Marcellus associated with matrix flow). As with the scenario above, I assume that the majority of accessible Ra and Sr in the shale matrix (either in pore fluid or the water-soluble/exchangeable fraction) is "flushed through" after some initial period of Onondaga fluid production. However, there is some in-growth and decay of Ra during transport of exogenous Onondaga fluid. In this case, the ^{87}Sr/^{86}Sr of later-stage produced water largely reflects that of Onondaga exogenous fluid, but the ^{228}Ra/^{226}Ra would either be equal to or higher than Onondaga water (where the increase is primarily related to the in-growth of ^{228}Ra, similar to "Exercise 2" in the Radium Modeling Section).
3) **Exogenous Onondaga fluid moves through the Marcellus slowly (relative to the scenarios above), mixing with Marcellus formation fluids:** Onondaga fluid is transported through fracture and pore spaces into the Marcellus, where it thoroughly mixes with Marcellus fluid before production. In this case, the Ra-rich Marcellus pore fluid dominates the ^{228}Ra/^{226}Ra composition (similar to "Exercise 1" in the Radium Modeling Exercise), while the ^{87}Sr/^{86}Sr reflects a mixture of Sr from the two sources, according to their relative contributions.

Lastly, I envision a scenario that does not involve exogenous fluid at all (perhaps the most common), where endogenous Marcellus formation fluid is produced, and the ^{228}Ra/^{226}Ra and ^{87}Sr/^{86}Sr ratios of produced water exclusively reflects that of Marcellus formation water.

Based on this conceptual model, the origin of formation fluids in Marcellus gas wells in the study area were evaluated by comparing produced water ^{228}Ra/^{226}Ra and ^{87}Sr/^{86}Sr ratios from this study to the characteristic predicted ^{228}Ra/^{226}Ra and ^{87}Sr/^{86}Sr ranges (25th to 75th%) for the Marcellus and other formations from core samples (Figure 11). Of the 123 individual produced water samples, 7 samples exhibit ^{228}Ra/^{226}Ra <0.1, consistent with the predicted ^{228}Ra/^{226}Ra for pore fluids from the Union Springs formation or the immediately underlying upper-most part of the Onondaga formation. These could represent endogenous pore fluids from these formations, or exogenous Onondaga water that “picked up” the Marcellus ^{228}Ra/^{226}Ra as it passed through the formation (either from water-soluble Ra in the rock matrix, or from mixing with Marcellus pore fluids).

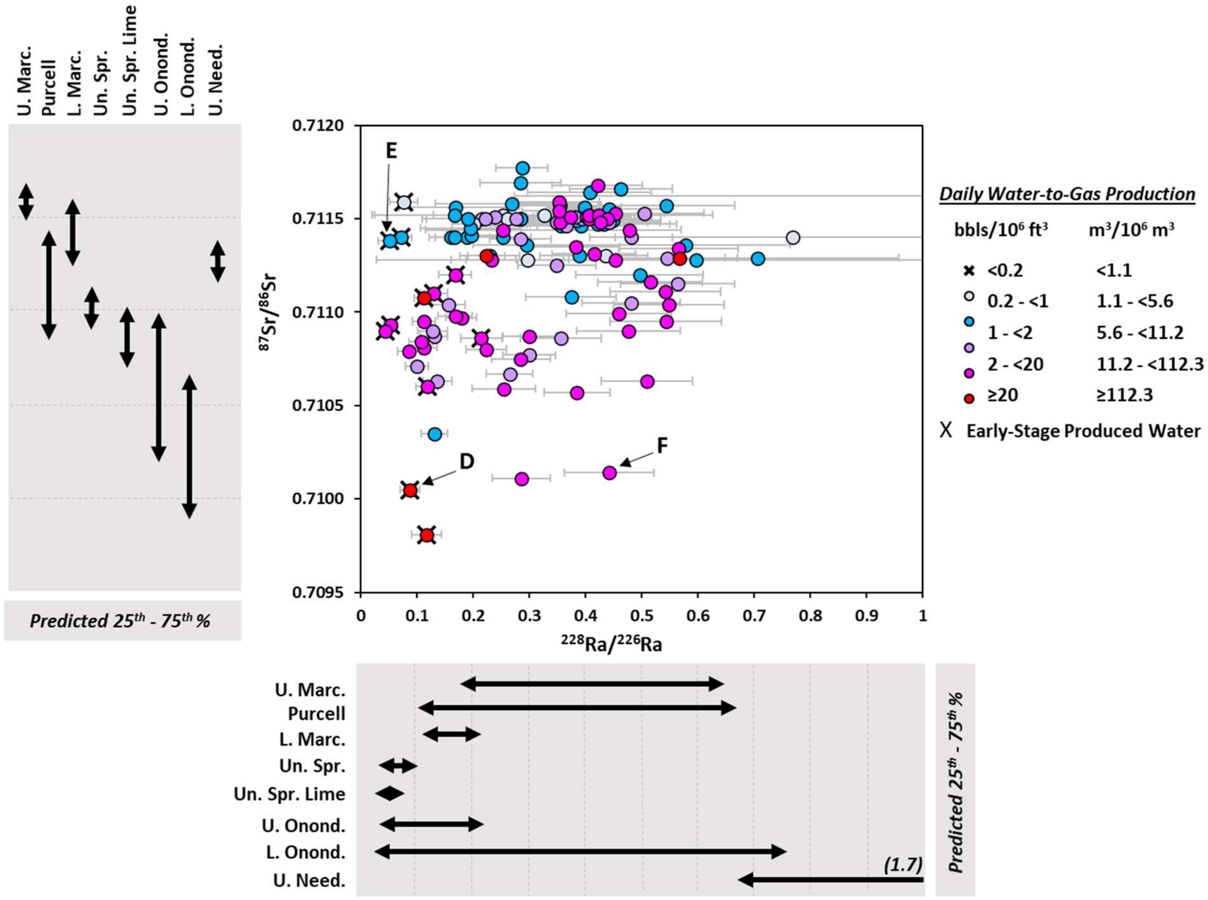

Figure 3.11: ^{228}Ra/^{226}Ra vs. ^{87}Sr/^{86}Sr for 123 produced water samples from Marcellus Shale gas wells sampled once each in the study area, as compared to predicted 25th to 75th percentile ranges of ^{228}Ra/^{226}Ra and ^{87}Sr/^{86}Sr for different formations in Cores 1, 2, and 3. 2σ errors for ^{228}Ra/^{226}Ra are shown as gray error bars. 2σ errors for ^{87}Sr/^{86}Sr are smaller than symbol (<±0.00002). Predicted 25th to 75th percentile ranges of ^{228}Ra/^{226}Ra and ^{87}Sr/^{86}Sr for different formations based on ED-XRF measurements of Th/U and Rb/Sr in Cores 1, 2, and 3 are shown as bold black arrows.

The $^{87}Sr/^{86}Sr$ ratio of these same fluids can provide multi-level information about their genetic history, and/or mixtures of one or more fluid sources. For example, for the sample from Well D, the low $^{87}Sr/^{86}Sr$ ratio approaching 0.7100 provides compelling evidence for pore fluids in contact with the Onondaga Limestone, either in the geologic past or presently. Of note, Well D was only producing for 12 days prior to sampling; yet exhibited a relatively elevated produced water TDS of 146,000 mg/L compared to time-series samples collected 12 days into production from Wells A, B, and C (TDS <55,000 mg/L) (Figure 3.7A). In addition, at the time of sample collection, Well D exhibited a daily water-to-gas production ratio of 230 m^3 water/10^6 m^3 gas, or 41 bbls water/10^6 ft^3 gas, which was similar or higher than that for Wells A, B, and C during the same timeframe (<275 m^3 water/10^6 m^3 gas, or <49 bbls water/10^6 ft^3 gas). Combined, this information suggests that Well D was producing a significant volume of saline formation fluids with a present-day origin in either 1) the upper part of the Onondaga Limestone which exhibits $^{228}Ra/^{226}Ra$ <0.1, and/or 2) the underlying Lower Onondaga Limestone, which exhibits a median $^{228}Ra/^{226}Ra$ of ~0.43, but could have picked up Ra^{2+} from the Marcellus during transport to the well. Either way, this data appears to support a significant out-of-zone source of fluids.

In contrast, the sample from Well E also exhibits a low $^{228}Ra/^{226}Ra$ ratio of ~0.05, characteristic of the Union Springs or Upper Onondaga, but a significantly higher $^{87}Sr/^{86}Sr$ ratio of 0.7114, characteristic of the Lower or Upper Marcellus. In addition, unlike Well D, Well E is characterized by remarkably low daily water-to-gas ratio (5 m^3 water/10^6 m^3 gas, or 0.9 bbls water/10^6 ft^3 gas) 89 days into production. Based on this combined information, I propose that the salinity in Well E produced water represents a mixture of formation fluids from the Union Springs (primary source of Ra^{2+}) and immediately overlying Lower Marcellus (primary source of Sr^{2+}) where both formations are water-poor in the production area.

Finally, the sample from Well F exhibits a $^{228}Ra/^{226}Ra$ ratio of 0.44 and a $^{87}Sr/^{86}Sr$ ratio of 0.7101. Both of these values are consistent with a present-day fluid source in the Lower Onondaga Limestone (where the median predicted $^{228}Ra/^{226}Ra$ and $^{87}Sr/^{86}Sr$ ratios of the complete Lower Onondaga interval in Core 1 is 0.43 and 0.7104, respectively). Combined with the elevated water-to-gas ratio of ~95 m^3 water/10^6 m^3 gas (~17 bbls water/10^6 ft^3 gas) 3,671 days into production, the source of fluids in this well is almost certainly not the Marcellus.

There are a number of produced water samples that exhibit mid-range $^{87}Sr/^{86}Sr$ ratios (e.g., between 0.7110 and 0.7105). These are characterized by a spectrum of $^{228}Ra/^{226}Ra$ ratios (<0.1 to >0.5), and water-to-gas ratios generally between ~5 to 112 m^3 water/10^6 m^3 gas (1 and 20 bbls water/10^6 ft^3 gas). I propose that these samples represent varying mixtures between present-day Onondaga and Union Springs/Lower/Upper Marcellus and Purcell fluids. Such mixtures could be produced from wells with laterals that access multiple Marcellus sub-units and/or underlying units, which is common in the study area, or reflect the extension of hydraulic fractures into zones adjacent to the targeted unit. In localized areas where the Marcellus is more water saturated (e.g., in the southeast), it is possible that some wells are producing formation fluids that infiltrated into the Marcellus over geologic time from the Onondaga or other underlying formations downdip, where there may be more connectivity. In this scenario, if at least 16,000 years have passed, I expect the fluid to exhibit a $^{228}Ra/^{226}Ra$ ratio consistent with the respective Marcellus sub-unit host rock, and a $^{87}Sr/^{86}Sr$ ratio consistent with the relative contributions of Sr from the exogenous fluid and the Marcellus (in the form of pore water and water-soluble/exchangeable Sr). The ability to sustain longer-term production of this fluid several months or more would, however, still be limited by the stimulated rock volume and intrinsic permeability of the Marcellus host rock (i.e., the volume of fluid directly accessed by the hydraulic fracturing network, and that which is able to subsequently flow into those fractures via pre-existing water-connected porosity).

Assumptions and limitations of method

Both $^{87}Sr/^{86}Sr$ and $^{228}Ra/^{226}Ra$ have been used independently to evaluate the origin of formation fluids. Herein, I propose that their combined use allows practitioners to not only evaluate the origin of formation fluids, but also potentially the timing of fluid migration. This approach is most effective at identifying cross-formation flow where the following criteria are met:

1) The Th/U ratio differs among host rocks, and/or the $^{87}Sr/^{86}Sr$ ratio differs among formation fluids or water-soluble/exchangeable Sr in host rocks.
2) Formations are at least 2.45 Ma (at least Tertiary in age), and thus have attained secular equilibrium between $^{232}Th/^{238}U$ and $^{228}Ra/^{226}Ra$.
3) Formations are hydraulically closed (i.e., fluid movement within the formation is relatively slow, as is the case with many oil- and gas-bearing formations that do not leak appreciably), with exception of the event resulting in cross-formation flow.
4) Cross-formation flow occurred less than 16,000 years ago. Thereafter, given the short half-lives of ^{228}Ra and ^{226}Ra, very little trace of radium will remain from the exogenous fluid.

As such, this approach is particularly relevant where cross-formation flow in deep sedimentary basins is stimulated by a relatively recent event (at least, relative to geologic time), including but not limited to: hydraulic fracturing to stimulate shale/tight oil or gas production, fluid migration via an artificial pathway including an underground injection well or well integrity issue, and the intrusion of fluids from a targeted storage reservoir into overlying formations via new or existing faults or fractures. The latter is of heightened concern at CO_2 enhanced oil recovery (EOR) sites and permanent carbon storage reservoirs (e.g., Gardiner et al., 2020), where the potential migration of fluids from targeted reservoirs into overlying groundwater-bearing units is the focus of extensive measurement, monitoring, and verification (MMV) as established in regulations for U.S. EPA Class VI geologic sequestration wells, and the California Low Carbon Fuel Standard (LCSF) (CARB, 2018; U.S. EPA, 2016, 2013).

In such scenarios, the timing of fluid migration may be inferred based on modeling of how the ^{228}Ra/^{226}Ra ratio would change over time as an exogenous fluid moves into a new host formation. This modeling exercise requires information on the average ^{228}Ra and ^{226}Ra content of the exogenous fluid (either measured or predicted from Th and U or the original host rock), as well as the average Th and U content of the new host rock. Use of the bulk rock Th and U concentrations to approximate the ^{228}Ra and ^{226}Ra content of soluble radium at secular equilibrium assumes that a) the relative abundance of Ra isotopes within all rock fractions are equally transferred to the water, and b) the rate of transfer of Ra from the rock to the water is not rate-limiting. While both assumptions may not always be the case, this study demonstrates that the bulk Th/U ratio can serve as a useful general approximation of the ^{228}Ra/^{226}Ra of formation fluids.

If the system if physically open, or very young (e.g., oil and gas basins in California), secular equilibrium will not have been attained in either the original source-rock of the exogenous fluid or the new host-rock. In this case, the bulk Th/U ratio cannot be used to predict the ^{228}Ra/^{226}Ra content of pore fluids. However, in most oil and gas producing regions, because systems do not leak oil and gas at appreciable rates, we can generally assume that formations are hydraulically closed, and this approach may therefore apply to many deep groundwater systems.

CONCLUSIONS

The combined application of ^{228}Ra/^{226}Ra and ^{87}Sr/^{86}Sr data from fluid samples can inform the recent (<16,000 years) flow of formation fluids across formations in deep sedimentary basins, and holds particular promise for identifying recent leaks of deep fluids from reservoirs utilized for CO_2 sequestration, wastewater injection, or hydrocarbon production. This study uses a synthesis of $^{228}Ra/^{226}Ra$ and $^{87}Sr/^{86}Sr$ data from produced water samples, Th/U and Rb/Sr measurements from three cored intervals, and daily water and gas production rates from Marcellus gas wells to evaluate the endogenous vs. exogenous origin of produced fluids from Marcellus gas wells in the northeastern Appalachian Basin. Key findings include:

1. Bulk rock Th/U and Rb/Sr ratios, in concert with fresh water $^{87}Sr/^{86}Sr$ leachates, can be used to develop predicted $^{228}Ra/^{226}Ra$ and $^{87}Sr/^{86}Sr$ ratios of formation waters residing within different formations in deep sedimentary basins. This approach assumes that formations are >2.45 Ma (the time required to achieve secular equilibrium between Th/U and $^{228}Ra/^{226}Ra$), and hydraulically closed (i.e., little leakage with relatively slow fluid movement).
2. The $^{228}Ra/^{226}Ra$ ratio of deep formation fluids reflects the mineralogical composition of the host rock that the water has interacted with very recently (e.g., less than 1 month, with diminishing influence up to 16,000 years), whereas the $^{87}Sr/^{86}Sr$ ratio reflects both fluid origin (e.g., Silurian seawater) and Sr contributions from formations that the fluid has been in contact with over geologic time.
3. The $^{228}Ra/^{226}Ra$ and $^{87}Sr/^{86}Sr$ ratios of Marcellus produced water are dominated by the Ra^{2+} and Sr^{2+} content of downhole formation fluids. Specifically, $^{228}Ra/^{226}Ra$ and $^{87}Sr/^{86}Sr$ ratios of produced water are distinctly different from injection fluid on the first day of flowback, with $^{228}Ra/^{226}Ra$ ratios stabilizing around a central trend immediately, and $^{87}Sr/^{86}Sr$ ratios increasing only marginally thereafter.

4. For relatively non-transmissive shale oil and gas formations, the sustained production of a larger volume of exogenous fluid is suggested to "flush out" water-soluble and exchangeable Ra and Sr during early production, yielding a later-stage produced water composition that largely reflects that of the exogenous brine with negligible contributions from endogenous pore fluids.
5. Marcellus wells sampled in this study exhibit a wide range of later-stage (6 months or more) daily water-to-gas production ratios, $^{87}Sr/^{86}Sr$ ratios, and $^{228}Ra/^{226}Ra$ ratios that likely reflect a combination of in-zone and out-of-zone production. Several wells with higher water-to-gas production ratios (e.g. >5.6 m^3 water/10^6 m^3 gas, or >1 water/10^6 ft^3 gas) and elevated TDS (>100,000 mg/L) exhibit lower $^{87}Sr/^{86}Sr$ ratios, consistent with a significant contribution from exogenous Onondaga pore fluids. $^{228}Ra/^{226}Ra$ ratios provide more nuanced information on the origin of these waters, where lower $^{228}Ra/^{226}Ra$ ratios (<0.1) suggest an origin in the Upper Onondaga, or possibly Ra^{2+} that desorbed from the Union Springs during contact with exogenous Onondaga water, and higher $^{228}Ra/^{226}Ra$ ratios (>0.1) suggest an origin in the larger lower vertical extent of the Onondaga Formation.
6. The combined use of $^{87}Sr/^{86}Sr$ and $^{228}Ra/^{226}Ra$ systems can inform the in-zone versus out-of-zone origin of deep formation fluids where cross-formation flow is stimulated by a recent event, such as hydraulic fracturing, wellbore integrity issues, or reservoir pressurization resulting in intrusion of reservoir fluids into overlying formations. In particular, with new economic incentives for carbon storage, the joint application of these isotope systems holds promise for monitoring programs seeking to understand the

unintended migration of fluids from CO_2 EOR and permanent CO_2 sequestration reservoirs into overlying formations.

Table 3.2: Data presented in this study for 1) individual produced water samples from 123 gas wells collected at a single point in time, 2) time-series produced water samples from three gas wells (Well A – 24 samples, Well B - 24 samples, and Well C - 23 samples), and 3) two freshwater samples collected from permitted freshwater sources utilized for fracturing fluid water supply.

			Daily Water/Gas 15 Day Moving Avg.																
Sample No.	Sample Date	Days Producing	$m^3/10^6m^3$	$bbl/10^6ft^3$	Calcium (mg/L)	Sodium (mg/L)	Strontium (mg/L)	Chloride (mg/L)	Bromide (mg/L)	$\delta^{18}O$ H_2O (‰ VSMOW)	δ^2H H_2O (‰ VSMOW)	$^{87}Sr/^{86}Sr$	^{226}Ra (pCi/L)	^{226}Ra ±2σ Error	^{228}Ra (pCi/L)	^{228}Ra ±2σ Error	^{226}Ra + ^{228}Ra (pCi/L)	$^{228}Ra/^{226}Ra$	$^{228}Ra/^{226}Ra$ ±2σ Error
123 Individual Produced Water Samples																			
1	5/2/2019	5	1.5	68.0	5850	27200	2680	52400	--	-5.32	-55.1	0.711075146	6250	635	708	89.1	6958	0.11	0.02
2	7/25/2019	7	3.1	16.7	5920	29400	2800	64400	488	-4.48	-51.3	0.71086	3310	344	711	96.6	4021	0.21	0.04
3	10/22/2018	43	0.9	13.4	5930	37300	3580	65400	--	-3.32	-42.6	0.7111	6360	647	828	129	7188	0.13	0.02
4	10/15/2018	56	2.9	3.7	5300	32800	2870	66000	--	-4.09	-49.9	0.7112	4690	481	789	110	5479	0.17	0.03
5	10/15/2018	56	1.4	4.2	7800	33500	4030	72600	--	-4.66	-53.3	0.7106	7860	798	930	121	8790	0.12	0.02
6	10/9/2019	89	10.2	0.9	1310	13600	762	24600	172	-5.84	-55.5	0.7114	3740	386	268	65.4	4008	0.07	0.02
7	10/9/2019	89	11.1	0.9	1180	12400	634	22400	160	-5.93	-54.9	0.71138	2870	297	150	59	3020	0.05	0.02
8	9/12/2020	62	2.2	0.0	827	12300	528	20800	160	-6.2	-66.5	0.71159	2420	295	187	56.6	2607	0.08	0.03
9	12/18/2019	116	6.8	4.0	6840	34400	3450	82200	674	-3.65	-46	0.71093	16700	3020	890	146	17590	0.05	0.01
10	12/18/2019	116	7.4	3.0	6590	32900	3380	74800	614	-4.25	-50.6	0.7109	18300	3230	814	118	19114	0.04	0.01
11	2/17/2020	12	16.1	162.6	13500	42900	3580	96600	--	-4.99	-55	0.70981	5700	589	668	134	6368	0.12	0.03
12	2/17/2020	12	29.9	41.4	11600	35400	4000	85400	--	-4.79	-53.9	0.71005	8230	836	722	119	8952	0.09	0.02
13	10/23/2018	198	164.4	0.3	3330	24000	1670	45900	--	-4.73	-54.1	0.7114	1560	165	396	64.5	1956	0.25	0.05
14	10/23/2018	198	11.6	0.6	2370	20900	1400	37600	--	-5.53	-59.1	0.7114	1790	191	289	62.6	2079	0.16	0.04
15	10/23/2018	198	77.5	0.2	2500	20600	1330	41400	--	-5.09	-55.5	0.7115	1520	170	329	64.2	1849	0.22	0.05
16	10/23/2018	198	2.1	0.5	2950	24900	1660	48000	--	-4.78	-55.5	0.7114	2260	236	428	79.3	2688	0.19	0.04
17	10/23/2018	198	3.4	0.2	2670	22700	1530	43600	--	-5.12	-58.9	0.7114	2170	229	362	61.1	2532	0.17	0.03
18	10/23/2018	198	1.5	1.8	4830	31600	2350	62600	--	-3.93	-50.7	0.7115	1740	183	481	69.4	2221	0.28	0.05
19	10/23/2018	198	5.3	2.0	4620	31600	2260	61000	--	-4.19	-51.6	0.7115	1130	126	446	62.8	1576	0.39	0.07
20	11/2/2021	844	2.7	0.4	2300	14600	1160	33200	225	-7.82	-72.8	0.71128	54.7	20.9	32.7	28.5	87.4	0.60	0.57
21	11/2/2021	844	3.0	1.2	3300	20000	1660	46000	301	-4.89	-57.2	0.71147	1150	146	420	70.1	1570	0.37	0.08
22	11/2/2021	844	10.7	1.3	4820	28900	2360	66200	420	-4.35	-54.9	0.71148	1000	131	442	70.9	1442	0.44	0.09
23	11/2/2021	844	13.4	2.9	5000	28900	2330	68400	445	-2.11	-38.8	0.71151	1740	217	698	106	2438	0.40	0.08
24	11/2/2021	844	17.6	5.3	6150	34700	2850	66400	442	-2.54	-43.9	0.7115	1790	223	727	115	2517	0.41	0.08
25	11/16/2021	852	16.8	16.8	10000	43000	3970	110000	838	-1.99	-43.8	0.71134	2810	353	1590	223	4400	0.57	0.11
26	11/16/2021	852	4.2	29.3	11000	47100	3870	116000	916	-1.82	-42.9	0.71129	2660	328	1510	203	4170	0.57	0.10
27	11/30/2017	865	11.4	2.1	14900	56300	6700	133000	--	-1.93	-47.6	0.71081	15900	1610	1800	306	17700	0.11	0.02
28	1/18/2018	871	45.6	13.8	8290	38600	3530	84600	--	-2.11	-44.6	0.71097	5520	561	992	112	6512	0.18	0.03
29	12/23/2019	1002	4.2	0.4	372	2060	178	4470	30.9	-6.73	-74.4	0.71156	244	36.1	41.1	23.6	285.1	0.17	0.10
30	12/23/2019	1002	1.9	0.6	326	2540	141	6010	43.1	-8.57	-71.7	0.71152	245	36.6	41.1	35.5	286.1	0.17	0.15
31	12/23/2019	1017	3.7	0.3	138	953	79.6	1940	13.6	-7.23	-78.2	0.71162	25.3	16.5	44.8	24.1	70.1	1.77	1.50
32	12/23/2019	1017	145.2	0.9	1060	6300	532	14000	91.5	-4.75	-66.9	0.71169	622	75.4	177	39.3	799	0.28	0.07
33	12/23/2019	1017	10.4	0.5	448	3260	218	6290	44	-6.56	-75.7	0.71158	229	32.6	61.6	29.8	290.6	0.27	0.14
34	12/23/2019	1017	12.0	0.5	2820	15200	1300	30200	205	-4.6	-64.4	0.71166	889	101	412	66.4	1301	0.46	0.09
35	10/27/2021	1036	13.5	1.9	3550	21500	1740	53700	342	-4.48	-53.7	0.71153	1050	135	530	87.6	1580	0.50	0.11

Notes: -- = Not analyzed

Table 3.2: Continued.

			Daily Water/Gas 15 Day Moving Avg.																
Sample No.	**Sample Date**	**Days Producing**	**$m^3/10^6m^3$**	**$bbl/10^6ft^3$**	**Calcium (mg/L)**	**Sodium (mg/L)**	**Strontium (mg/L)**	**Chloride (mg/L)**	**Bromide (mg/L)**	**$\delta^{18}O$ H_2O (‰ VSMOW)**	**δ^2H H_2O (‰ VSMOW)**	**$^{87}Sr/^{86}Sr$**	**^{226}Ra (pCi/L)**	**^{226}Ra ±2σ Error**	**^{228}Ra (pCi/L)**	**^{228}Ra ±2σ Error**	**^{226}Ra + ^{228}Ra (pCi/L)**	**$^{228}Ra/^{226}Ra$**	**$^{228}Ra/^{226}Ra$ ±2σ Error**
36	10/27/2021	1180	7.7	2.4	3240	22600	1640	47900	332	-2.94	-43.2	0.71148	1320	169	469	81.3	1789	0.36	0.08
37	10/27/2021	1180	10.0	3.1	4480	29400	2260	50800	347	-2.77	-45.9	0.71152	1680	212	682	116	2362	0.41	0.09
38	10/27/2021	1180	10.3	3.0	4300	27500	2230	61800	411	-3.59	-48.2	0.71152	1210	156	512	78.5	1722	0.42	0.08
39	12/7/2017	1240	8.2	0.7	6350	43900	4070	73050	--	-3.07	-53.1	0.71156	2560	272	1020	131	3580	0.40	0.07
40	11/1/2021	1303	2.1	2.0	6850	36700	3040	92800	698	-2.61	-43.1	0.71151	2170	266	811	136	2981	0.37	0.08
41	11/1/2021	1303	10.0	8.1	5670	31600	2640	79600	607	-2.09	-41.8	0.71153	2200	274	997	146	3197	0.45	0.09
42	11/3/2021	1410	1.4	0.8	3890	23500	2000	48200	366	-4.24	-58.5	0.71146	1760	222	690	107	2450	0.39	0.08
43	11/28/2017	1510	40.6	0.3	1170	7380	643	16000	--	-5.18	-64.5	0.71141	1700	185	336	66.8	2036	0.20	0.04
44	11/3/2021	1532	7.9	0.7	3460	18600	1670	43100	311	-5.4	-60.5	0.71147	1390	175	491	77.1	1881	0.35	0.07
45	12/7/2017	1541	13.7	25.9	11700	49000	5090	120000	--	-0.72	-44.8	0.7113	9390	950	2100	218	11490	0.22	0.03
46	12/21/2017	1672	26.3	1.9	6050	35500	2690	73800	--	-3.4	-49.6	0.71151	2490	259	597	82	3087	0.24	0.04
47	12/26/2019	1703	26.6	2.1	2470	9370	908	21800	185	-7.12	-56.3	0.71059	777	90.5	198	37.4	975	0.25	0.06
48	12/26/2019	1703	0.7	2.4	12700	48000	6000	115000	911	-2.68	-49.8	0.7108	5330	546	1190	146	6520	0.22	0.04
49	12/26/2019	1703	0.8	1.4	6240	27700	2850	60200	484	-4.71	-53.1	0.71063	5140	524	700	112	5840	0.14	0.03
50	12/26/2019	1703	1.4	1.8	5210	26200	2450	56800	472	-4.97	-54.4	0.71087	4360	448	571	86.3	4931	0.13	0.02
51	12/26/2019	1703	2.6	1.8	16600	56600	6620	119000	945	-2.17	-49.7	0.71077	5570	568	1670	201	7240	0.30	0.05
52	12/26/2019	1703	3.3	1.5	15800	51600	7040	122000	940	-2.11	-51.3	0.71067	6590	670	1750	208	8340	0.27	0.04
53	11/16/2021	1742	6.6	0.4	164	1400	102	3350	24.3	-7.49	-79	0.71146	227	36.4	80.9	25.1	307.9	0.36	0.12
54	11/8/2021	1765	1.1	1.8	9730	37300	3950	102000	786	-3.23	-52.1	0.71115	2640	325	1490	194	4130	0.56	0.10
55	11/20/2017	1806	2.3	0.2	308	3270	197	6050	--	-4.02	-76.6	0.71145	373	50.4	73.2	32.2	446.2	0.20	0.09
56	11/20/2017	1880	14.7	7.2	19500	63700	7150	160000	--	-1.02	-45.5	0.71063	3570	374	1820	217	5390	0.51	0.08
57	10/22/2018	2009	12.9	1.4	7640	37300	3310	76800	--	-2.61	-44.6	0.7114	2010	212	968	107	2978	0.48	0.07
58	12/26/2019	2037	2.9	2.4	12500	45100	6150	112000	903	-2.53	-50.4	0.71087	5390	551	1620	195	7010	0.30	0.05
59	12/26/2019	2037	1.4	4.7	5750	28400	2630	62900	510	-4.57	-51.7	0.71098	4090	422	688	104	4778	0.17	0.03
60	12/26/2019	2037	12.1	4.7	14200	48600	6590	118000	932	-2.3	-48.8	0.71057	3920	405	1510	171	5430	0.39	0.06
61	11/8/2018	2088	2.9	0.1	4320	20800	2060	44800	--	-4.21	-60.1	0.7113	1010	111	440	58.4	1450	0.44	0.08
62	10/22/2018	2144	22.3	0.1	2270	14400	1310	29000	--	-4.01	-65.3	0.7115	1080	118	308	55.7	1388	0.29	0.06
63	10/22/2018	2144	10.5	0.2	394	2850	234	5850	--	-4.87	-66.2	0.7115	231	49.2	65.8	37.9	296.8	0.28	0.17
64	10/23/2018	2226	50.8	0.5	519	8020	353	12300	--	-6.7	-60.6	0.7115	299	40.2	57.2	20.5	356.2	0.19	0.07
65	10/23/2018	2226	6.8	0.6	2970	20700	1420	38500	--	-4.98	-58.4	0.7115	917	102	336	50.6	1253	0.37	0.07
66	10/23/2018	2226	10.6	1.2	3540	23000	1870	41900	--	-5.25	-54.1	0.7115	1410	158	312	61.5	1722	0.22	0.05
67	10/29/2018	2305	5.5	0.2	203	1520	120	2810	--	-6.15	-75.8	0.7114	64.9	18	49.9	15.1	114.8	0.77	0.32
68	11/8/2018	2329	62.1	0.4	6330	27700	2910	57100	--	-4.25	-60.3	0.7113	1620	174	630	91.3	2250	0.39	0.07
69	12/23/2019	2338	8.0	2.6	9970	52300	4650	106000	755	-5.86	-81.3	0.71168	700	81.1	295	45.2	995	0.42	0.08
70	12/23/2019	2338	2.7	2.3	18500	92100	9000	193000	1640	-3.86	-81.7	0.71159	1270	137	448	77.9	1718	0.35	0.07

Notes: -- = Not analyzed

Table 3.2: Continued.

			Daily Water/Gas 15 Day Moving Avg.																
Sample No.	**Sample Date**	**Days Producing**	**$m^3/10^6m^3$**	**$bbl/10^6ft^3$**	**Calcium (mg/L)**	**Sodium (mg/L)**	**Strontium (mg/L)**	**Chloride (mg/L)**	**Bromide (mg/L)**	**$\delta^{18}O$ H_2O (‰ VSMOW)**	**δ^2H H_2O (‰ VSMOW)**	**$^{87}Sr/^{86}Sr$**	**^{226}Ra (pCi/L)**	**^{226}Ra ±2σ Error**	**^{228}Ra (pCi/L)**	**^{228}Ra ±2σ Error**	**^{226}Ra + ^{228}Ra (pCi/L)**	**$^{228}Ra/^{226}Ra$**	**$^{228}Ra/^{226}Ra$ ±2σ Error**
71	12/23/2019	2338	14.7	0.5	2210	12000	993	27400	184	-4.42	-61.7	0.71177	3110	324	893	111	4003	0.29	0.05
72	11/18/2017	2352	0.4	0.2	4300	20500	1970	48200	--	-4.88	-60.5	0.7113	1760	195	404	81.6	2164	0.23	0.05
73	11/16/2021	2365	8.7	2.2	9020	44500	4220	116000	919	-2.32	-46.6	0.71128	6060	731	1410	210	7470	0.23	0.04
74	11/10/2021	2447	2.2	0.5	23500	60300	6730	164000	1430	-1.9	-48.2	0.71035	15900	1880	2090	280	17990	0.13	0.02
75	10/29/2019	2533	3.4	4.0	598	3880	169	7620	58.6	-6.64	-52.3	0.71144	171	30.2	43.3	22.2	214.3	0.25	0.14
76	11/8/2021	2602	22.5	1.9	9380	39400	4290	110000	902	-2.98	-50.6	0.71129	2660	327	1450	208	4110	0.55	0.10
77	11/3/2021	2717	93.5	9.0	13100	51100	6290	118000	752	-1.01	-47.6	0.71084	24600	2940	2640	395	27240	0.11	0.02
78	11/9/2021	2739	3.2	1.2	6600	34000	2930	92300	657	-3.54	-50.1	0.71125	3380	419	1180	185	4560	0.35	0.07
79	12/1/2021	2749	10.6	1.9	11700	43800	5740	114000	750	-2.04	-50.2	0.71104	12900	1540	2020	288	14920	0.16	0.03
80	12/6/2017	2760	6.1	1.0	25000	78300	10500	189000	--	-8.51	-156.2	0.71164	621	80.6	253	60.4	874	0.41	0.11
81	11/16/2021	2796	11.3	11.1	8650	41400	4230	109000	879	-1.92	-44	0.71128	3110	381	1410	189	4520	0.45	0.08
82	11/8/2021	2851	2.2	1.4	5600	29500	2630	76400	603	-4.2	-53.3	0.71139	2930	359	835	123	3765	0.28	0.05
83	11/3/2021	2914	12.4	0.5	354	3400	230	6620	51.3	-5.33	-67.8	0.71136	395	59	117	33.8	512	0.30	0.10
84	11/16/2021	2934	4.0	2.6	9570	38700	4570	98300	659	-3.05	-51.5	0.71095	14600	1750	1640	224	16240	0.11	0.02
85	11/1/2021	3045	6.3	0.1	580	5300	297	11100	83.9	-5.67	-68.2	0.71128	266	40.3	79	34.2	345	0.30	0.14
86	12/1/2021	3105	1.3	1.5	6690	34000	3090	84800	606	-3.27	-52.6	0.71148	2440	298	850	119	3290	0.35	0.06
87	10/27/2021	3242	0.0	0.4	1520	8990	754	17900	138	-3.53	-67.9	0.71149	461	64.4	177	37.4	638	0.38	0.10
88	11/3/2021	3297	0.0	0.6	5080	25800	2460	56500	404	-4.22	-64.5	0.71149	1520	191	681	100	2201	0.45	0.09
89	11/10/2021	3582	1.6	4.0	15300	37400	5150	120000	1070	-4.15	-52.9	0.71011	5550	670	1590	214	7140	0.29	0.05
90	11/10/2021	3671	12.6	16.7	22700	58000	6940	174000	1610	-2.12	-48.1	0.71014	5150	630	2280	303	7430	0.44	0.08
91	11/4/2021	3682	4.4	0.6	4380	18800	1920	53200	389	-4.64	-68.5	0.7112	1280	172	636	117	1916	0.50	0.11
92	11/3/2021	3715	1.8	1.9	4360	23900	1910	60300	443	-3.91	-48.5	0.7109	4370	526	559	96.7	4929	0.13	0.03
93	11/10/2021	3746	1.8	1.1	8450	35800	3780	104000	725	-2.74	-53.3	0.71105	2680	329	1290	172	3970	0.48	0.09
94	11/2/2021	3822	5.3	2.0	4260	23100	1900	56500	374	-4.59	-54.9	0.71135	1240	158	474	77.9	1714	0.38	0.08
95	11/2/2021	3823	0.0	0.4	187	1460	85.2	3010	20.9	-9.57	-82	0.71136	77.8	22.5	45	6.19	122.8	0.58	0.19
96	11/3/2021	3824	0.0	2.2	5700	25200	2590	69700	484	-3.74	-50.4	0.71079	8280	1000	713	140	8993	0.09	0.02
97	11/3/2021	3915	47.3	0.7	8000	35600	3700	98300	679	-3.2	-56	0.71108	3390	439	1270	219	4660	0.37	0.08
98	12/1/2021	4073	34.3	1.1	6630	32900	3290	81400	590	-3.07	-54.1	0.71151	2420	296	924	139	3344	0.38	0.07
99	10/27/2021	4120	104.5	0.2	541	2930	272	6820	55.1	-5.5	-67.8	0.71147	223	37.8	96.5	24	319.5	0.43	0.13
100	11/2/2021	4196	74.6	0.0	175	1160	89.5	2270	15.5	-7.2	-103.2	0.71152	172	35.1	43.6	19.4	215.6	0.25	0.12
101	12/15/2021	4219	106.0	0.0	303	2130	163	4790	32.3	-5.1	-89.1	0.71152	142	32.6	46.3	41.3	188.3	0.33	0.30
102	11/3/2021	4227	92.9	0.3	327	2040	151	4510	33.8	-6.47	-80.5	0.71129	106	22.3	74.9	21.5	180.9	0.71	0.25
103	12/1/2021	4227	93.3	2.2	7150	37200	3290	87200	639	-2.09	-51.7	0.71154	2780	339	981	139	3761	0.35	0.07
104	11/1/2021	4277	8.1	0.8	2600	14700	1260	33500	218	-6.09	-66.9	0.71157	757	105	412	72.5	1169	0.54	0.12
105	11/1/2021	4287	22.1	0.3	1420	8200	708	20500	144	-5.93	-59.3	0.71155	497	68	220	43.5	717	0.44	0.11

Notes: -- = Not analyzed

Table 3.2: Continued.

			Daily Water/Gas 15 Day Moving Avg.																
Sample No.	**Sample Date**	**Days Producing**	**$m^3/10^6m^3$**	**$bbl/10^6ft^3$**	**Calcium (mg/L)**	**Sodium (mg/L)**	**Strontium (mg/L)**	**Chloride (mg/L)**	**Bromide (mg/L)**	**$\delta^{18}O$ H_2O (‰ VSMOW)**	**δ^2H H_2O (‰ VSMOW)**	**$^{87}Sr/^{86}Sr$**	**^{226}Ra (pCi/L)**	**^{226}Ra ±2σ Error**	**^{228}Ra (pCi/L)**	**^{228}Ra ±2σ Error**	**^{226}Ra + ^{228}Ra (pCi/L)**	**$^{228}Ra/^{226}Ra$**	**$^{228}Ra/^{226}Ra$ ±2σ Error**
106	12/1/2021	4327	5.7	0.3	1150	5640	494	13200	90.9	-5.87	-69.4	0.71147	362	51.2	153	40.6	515	0.42	0.13
107	11/1/2021	4333	57.7	0.9	2760	24000	1390	56600	256	-6.77	-61.7	0.71157	2030	249	721	118	2751	0.36	0.07
108	11/1/2021	4390	30.9	0.0	5640	31900	2880	74900	598	-3.63	-47.7	0.7115	3060	375	798	122	3858	0.26	0.05
109	11/1/2021	4455	92.8	0.0	7930	41200	4240	103000	872	-8.48	-115	0.71147	5940	710	1200	185	7140	0.20	0.04
110	11/8/2021	827	9.3	8.4	8100	38100	3730	100000	782	-1.86	-42.8	0.71144	2840	347	1360	200	4200	0.48	0.09
111	11/3/2021	512	0.0	6.1	7570	37600	3420	89100	671	-2.35	-43.7	0.7115	2460	304	1080	142	3540	0.44	0.08
112	11/16/2021	918	0.0	18.6	9790	47500	4120	128000	974	-1.67	-43	0.71131	3540	431	1470	192	5010	0.42	0.07
113	11/16/2021	815	0.0	13.3	10600	44600	3830	116000	913	-1.89	-39.8	0.71116	2640	326	1360	178	4000	0.52	0.09
114	11/16/2021	815	0.0	18.9	11300	45900	4340	117000	913	-2.07	-44.5	0.71111	2820	346	1530	204	4350	0.54	0.10
115	11/16/2021	815	0.0	16.5	11300	44300	4360	123000	953	-2.57	-43.1	0.71104	2810	347	1540	201	4350	0.55	0.10
116	11/16/2021	815	0.0	16.6	12400	47500	4390	124000	960	-2.69	-48.6	0.71095	2760	339	1500	204	4260	0.54	0.10
117	11/3/2021	775	0.0	1.4	6170	32400	2860	75400	509	-2.44	-44.1	0.71146	2370	305	867	160	3237	0.37	0.08
118	11/3/2021	479	0.0	3.9	10500	44900	4700	111000	851	-2.66	-47.6	0.71099	2850	377	1310	203	4160	0.46	0.09
119	11/3/2021	479	0.0	1.0	8670	37700	3520	94400	708	-3.69	-57.6	0.71086	3230	403	1150	181	4380	0.36	0.07
120	11/3/2021	479	0.0	10.3	10600	45200	4890	120000	877	-1.89	-45.3	0.7109	2790	349	1330	198	4120	0.48	0.09
121	11/16/2021	751	0.0	5.5	6950	37400	3090	89200	662	-2.12	-42.2	0.71148	2120	263	905	138	3025	0.43	0.08
122	9/16/2020	206	0.0	16.5	16000	64600	5860	137000	1130	-2.61	-50.2	0.71075	5720	687	1630	224	7350	0.28	0.05
123	9/16/2020	206	0.0	1.7	15200	60000	6050	118000	902	-3.39	-53	0.71071	15100	1810	1510	258	16610	0.10	0.02
Well A Time-Series Produced Water Data																			
124	5/7/2019	Fracturing Fluid	0.0	No Gas Production	1840	10400	582	17400	134	-7.67	-57.3	0.711089187	42.1	16.6	37.6	28.8	79.7	0.89	0.77
125	7/12/2019	0	0.0	57.1	1070	11200	382	19600	--	-5.32	-48.8	0.71144	260	36	106	27.8	366	0.41	0.12
126	7/13/2019	1	0.0	53.5	1240	13100	469	22300	--	-5.17	-49.1	0.71147	284	40.9	117	29	401	0.41	0.12
127	7/13/2019	1	0.0	53.5	1310	13500	506	23300	--	-4.85	-47.9	0.71147	310	40.9	107	29	417	0.35	0.12
128	7/14/2019	2	0.0	50.7	1400	14200	539	24200	160	-4.84	-48.7	0.71147	320	44.6	150	27.9	470	0.47	0.11
129	7/14/2019	2	0.0	50.7	1380	13900	534	22900	161	-4.8	-47.5	0.71145	351	44.6	136	27.9	487	0.39	0.11
130	7/15/2019	3	0.0	48.2	1510	14800	590	26600	175	-4.67	-47.2	0.71146	347	46.5	167	32.3	514	0.48	0.11
131	7/16/2019	4	0.0	46.1	1460	14900	599	26100	--	-4.77	-47.8	0.71148	407	56.3	140	35	547	0.34	0.10
132	7/17/2019	5	0.0	44.2	1570	16000	647	26800	182	-4.58	-48.1	0.71146	415	57.6	184	38.9	599	0.44	0.11
133	7/18/2019	6	0.0	42.5	1690	16800	706	27500	192	-4.56	-46.8	0.71148	434	53.8	184	31.3	618	0.42	0.09
134	7/19/2019	7	0.0	40.9	1660	16500	694	28400	190	-4.42	-46.3	0.71149	425	52.8	154	35.3	579	0.36	0.09
135	7/20/2019	8	0.0	39.6	1650	16200	689	28700	195	-4.45	-46.1	0.71146	385	50.2	168	32.2	553	0.44	0.10
136	7/22/2019	10	0.0	31.9	1750	16900	724	29700	201	-4.67	-47.9	0.71146	430	55.1	159	32.4	589	0.37	0.09
137	7/24/2019	12	0.0	26.1	1860	17900	783	29900	201	-4.18	-46.8	0.71145	434	55.2	177	33.5	611	0.41	0.09
138	7/26/2019	14	0.0	22.2	1890	17800	778	30000	210	-4.24	-46.7	0.71149	494	62.5	153	29.9	647	0.31	0.07
139	7/28/2019	16	0.0	19.7	1770	19600	894	30000	212	-4.25	-45.9	0.71146	449	57.1	188	35	637	0.42	0.09
140	7/30/2019	18	0.0	17.7	1940	17900	802	30700	213	-4.24	-47.9	0.71147	499	63.2	185	34.9	684	0.37	0.08

Notes: -- = Not analyzed

Table 3.2: Continued.

			Daily Water/Gas 15 Day Moving Avg.																
Sample No.	**Sample Date**	**Days Producing**	**m^3/10^{6}m^3**	**bbl/10^{6}ft^3**	**Calcium (mg/L)**	**Sodium (mg/L)**	**Strontium (mg/L)**	**Chloride (mg/L)**	**Bromide (mg/L)**	**δ^{18}O H_2O (‰ VSMOW)**	**δ^{2}H H_2O (‰ VSMOW)**	**^{87}Sr/^{86}Sr**	**^{226}Ra (pCi/L)**	**^{226}Ra ±2σ Error**	**^{228}Ra (pCi/L)**	**^{228}Ra ±2σ Error**	**^{226}Ra + ^{228}Ra (pCi/L)**	**^{228}Ra/^{226}Ra**	**^{228}Ra/^{226}Ra ±2σ Error**
141	8/8/2019	27	0.0	12.8	2340	21000	880	36000	231	-4.05	-45.9	0.71148	563	69.8	230	36.4	793	0.41	0.08
142	8/15/2019	34	0.0	11.6	2490	21800	896	37900	241	-3.93	-46.1	0.71146	591	71.3	258	47.8	849	0.44	0.10
143	8/22/2019	41	0.0	10.6	2530	21400	1010	37600	252	-4.02	-45.5	0.71146	623	72.9	238	42	861	0.38	0.08
144	8/29/2019	48	0.0	10.0	2260	18300	975	39800	262	-3.9	-45.9	0.71147	626	73.8	272	41.2	898	0.43	0.08
145	9/5/2019	55	0.0	9.5	2860	23300	994	40600	267	-3.84	-46.4	0.71149	671	75.8	174	44.9	845	0.26	0.07
146	9/12/2019	62	0.0	9.2	2870	22400	1140	42000	279	-3.74	-44.8	0.7115	513	67.4	301	48.1	814	0.59	0.12
147	10/9/2019	89	0.0	8.0	3180	23500	1370	46800	303	-3.51	-45.2	0.71153	780	89.9	295	57.1	1075	0.38	0.09
148	11/2/2021	844	0.0	5.2	166	1100	106	2410	15.5	-2.68	-43.4	0.71152	1580	198	642	90.4	2222	0.41	0.08
Well B Time-Series Produced Water Data																			
149	5/2/2019	Fracturing Fluid	0.0	No Gas Production	931	5180	299	9670	--	-8.33	-58.7	0.711098493	30.3	9.1	15.5	18.7	45.8	0.51	0.64
150	7/12/2019	0	0.0	99.9	753	8240	287	13700	--	-6.84	-55.2	0.71127	102	24.1	39.3	25.7	141.3	0.39	0.27
151	7/13/2019	1	0.0	93.1	763	8380	292	14800	101	-6.45	-53.3	0.7113	57.9	19.4	55.2	21.4	113.1	0.95	0.49
152	7/13/2019	1	0.0	93.1	742	7950	293	15200	--	-6.46	-53.2	0.71132	106	19.4	66.4	21.4	172.4	0.63	0.49
153	7/14/2019	2	0.0	87.1	857	8990	328	15700	--	-6.39	-51.8	0.71132	113	26	53	21.6	166	0.47	0.22
154	7/14/2019	2	0.0	87.1	945	9560	370	17000	--	-6.3	-52.7	0.71133	96.9	26	82.3	21.6	179.2	0.85	0.22
155	7/15/2019	3	0.0	81.0	893	9160	341	16600	110	-6.39	-52.6	0.71134	125	25.4	65.6	25.6	190.6	0.52	0.23
156	7/16/2019	4	0.0	75.8	931	9650	381	18700	122	-6.21	-52.7	0.71133	128	24.1	50.1	20.1	178.1	0.39	0.17
157	7/17/2019	5	0.0	71.5	1020	10200	424	18100	127	-6.2	-52.3	0.71134	165	26.3	83.1	30.3	248.1	0.50	0.20
158	7/18/2019	6	0.0	67.5	1110	10600	454	18800	132	-6.34	-53.3	0.71136	136	28	55.2	25.5	191.2	0.41	0.21
159	7/20/2019	8	0.0	60.3	1100	11100	559	21200	146	-5.92	-51.5	0.71139	183	30	102	26.9	285	0.56	0.17
160	7/22/2019	10	0.0	49.0	1440	13100	631	23100	158	-5.76	-49.9	0.71137	239	35.7	126	27.3	365	0.53	0.14
161	7/24/2019	12	0.0	38.1	1480	13300	653	24500	164	-5.62	-50	0.71137	228	31.2	128	24.2	356	0.56	0.13
162	7/26/2019	14	0.0	29.4	1520	13200	664	25400	171	-5.62	-51.2	0.71138	252	36.9	138	25.9	390	0.55	0.13
163	7/28/2019	16	0.0	21.6	1580	14800	766	25100	179	-5.24	-49.9	0.71139	301	45	104	33.7	405	0.35	0.12
164	7/30/2019	18	0.0	17.0	1740	15000	771	26100	183	-5.37	-50.5	0.71138	307	43	130	31.3	437	0.42	0.12
165	8/1/2019	20	0.0	13.9	1780	15200	787	30100	192	-5.42	-51.8	0.71139	282	41.3	164	34.2	446	0.58	0.15
166	8/8/2019	27	0.0	9.5	1950	16300	880	29200	196	-5.23	-49.8	0.71141	317	42.4	161	32.6	478	0.51	0.12
167	8/15/2019	34	0.0	7.3	2060	17100	924	31600	205	-5.16	-50	0.7114	381	49.2	163	30.8	544	0.43	0.10
168	8/22/2019	41	0.0	5.8	2100	16700	955	33100	217	-5.04	-49.1	0.7114	356	48.8	157	30.2	513	0.44	0.10
169	8/29/2019	48	0.0	4.9	2260	17900	1000	35400	224	-4.92	-49.4	0.7114	449	55	200	33.1	649	0.45	0.09
170	9/5/2019	55	0.0	4.1	2380	18800	948	35600	225	-4.83	-48.8	0.71143	450	54.6	208	34.1	658	0.46	0.09
171	9/12/2019	62	0.0	3.6	2410	18500	1010	36300	234	-4.87	-49.3	0.71142	458	58.5	233	42.3	691	0.51	0.11
172	10/9/2019	89	0.0	2.6	2570	19200	1100	36800	245	-4.79	-50.3	0.71144	462	57.5	230	40.1	692	0.50	0.11
173	11/2/2021	844	0.0	1.1	3080	19000	1540	43200	282	-5.61	-62.7	0.71151	759	99.3	308	65.8	1067	0.41	0.10

Notes: -- = Not analyzed

Table 3.2: Continued.

			Daily Water/Gas 15 Day Moving Avg.																
Sample No.	**Sample Date**	**Days Producing**	**$m^3/10^6m^3$**	**$bbl/10^6ft^3$**	**Calcium (mg/L)**	**Sodium (mg/L)**	**Strontium (mg/L)**	**Chloride (mg/L)**	**Bromide (mg/L)**	**$\delta^{18}O$ H_2O (‰ VSMOW)**	**δ^2H H_2O (‰ VSMOW)**	**$^{87}Sr/^{86}Sr$**	**^{226}Ra (pCi/L)**	**^{226}Ra ±2σ Error**	**^{228}Ra (pCi/L)**	**^{228}Ra ±2σ Error**	**^{226}Ra + ^{228}Ra (pCi/L)**	**$^{228}Ra/^{226}Ra$**	**$^{228}Ra/^{226}Ra$ ±2σ Error**
Well C Time-Series Produced Water Data																			
174	5/17/2019	Fracturing Fluid	0.0	No Gas Production	682	4190	195	7760		-8.84	-63.3	0.711149994	54.1	19	35.1	16.9	89.2	0.65	0.39
175	7/13/2019	1	0.0	38.6	1230	11400	574	19200	75.6	-6.24	-54.1	0.71132	2120	223	140	45.9	2260	0.07	0.02
176	7/13/2019	1	0.0	38.6	1170	11200	544	18500	136	-6.14	-52.7	0.71129	2410	223	179	45.9	2589	0.07	0.02
177	7/13/2019	1	0.0	38.6	1160	10900	549	19000	73.5	-6.46	-53.4	0.71131	2320	223	160	45.9	2480	0.07	0.02
178	7/14/2019	2	0.0	35.9	1130	10800	531	19100	141	-6.18	-53.2	0.71133	2290	240	197	52.8	2487	0.09	0.02
179	7/14/2019	2	0.0	35.9	1170	11300	550	20200	54.9	-6.16	-52.5	0.71132	2100	240	181	52.8	2281	0.09	0.02
180	7/15/2019	3	0.0	33.5	1080	10500	523	19700	148	-6.01	-52.6	0.71134	2530	265	136	69.5	2666	0.05	0.03
181	7/15/2019	3	0.0	33.5	1150	11100	546	20000	146	-6.16	-52.3	0.7113	2490	265	168	69.5	2658	0.07	0.03
182	7/16/2019	4	0.0	31.7	1150	11400	563	20300	154	-6.06	-52.9	0.71133	2360	249	171	42.3	2531	0.07	0.02
183	7/17/2019	5	0.0	30.1	1200	11900	570	21000	151	-6.04	-51.3	0.71138	1960	208	154	42.8	2114	0.08	0.02
184	7/18/2019	6	0.0	28.7	1130	11200	553	20200	149	-6.16	-52.3	0.71135	2490	258	162	41.4	2652	0.07	0.02
185	7/19/2019	7	0.0	27.4	1180	11700	595	21600	155	-6.06	-51.3	0.71132	2690	278	190	50	2880	0.07	0.02
186	7/20/2019	8	0.0	26.3	1190	11700	597	21600	154	-6.04	-51.5	0.71135	2460	255	140	43.4	2600	0.06	0.02
187	7/22/2019	10	0.0	21.4	1220	12100	620	22100	158	-5.85	-50.9	0.71135	2600	272	178	51.9	2778	0.07	0.02
188	7/24/2019	12	0.0	16.8	1220	12300	629	22100	159	-5.86	-52	0.71134	2430	254	166	49.4	2596	0.07	0.02
189	7/26/2019	14	0.0	14.2	1240	12400	632	22100	168	-4.81	-49.8	0.71132	2770	289	223	55	2993	0.08	0.02
190	7/28/2019	16	0.0	11.9	1240	12100	619	23800	57.4	-5.81	-51	0.71136	2830	295	217	59.3	3047	0.08	0.02
191	8/8/2019	27	0.0	6.1	1260	12800	660	23100	163	-5.58	-50.3	0.71137	3130	323	210	52.5	3340	0.07	0.02
192	8/15/2019	34	0.0	4.7	1250	13000	749	23400	168	-5.6	-50.5	0.71136	3130	322	194	38.9	3324	0.06	0.01
193	8/22/2019	41	0.0	3.5	1230	12700	661	23800	166	-5.53	-50.3	0.71136	3080	321	205	51.4	3285	0.07	0.02
194	9/5/2019	55	0.0	2.2	1230	12900	652	23000	161	-5.59	-52.1	0.7114	2930	303	215	44.9	3145	0.07	0.02
195	9/12/2019	62	0.0	1.8	1200	12300	632	22800	162	-5.63	-52.8	0.7114	3050	316	190	46.7	3240	0.06	0.02
196	10/9/2019	89	0.0	1.1	1100	11700	595	20900	143	-5.91	-54.1	0.71144	2760	286	146	63.6	2906	0.05	0.02
197	11/2/2021	844	0.0	0.4	380	2460	204	5170	34.5	-7.74	-79.8	0.71151	29	17.6	28.4	22.2	57.4	#N/A	0.97
Freshwater Samples																			
1	6/6/2019	N/A	0.0	#N/A	10.3	5.36	0.035	12	--	-8.88	-58.6	0.71368	37.7	15.4	26	19.9	63.7	0.69	0.60
2	6/6/2019	N/A	0.0	#N/A	11.2	6.24	0.064	6.85	0.0309	-8.65	-56.1	0.71331	44.4	16.1	24.9	18.1	69.3	0.56	0.46

Notes: -- = Not analyzed

Table 3.3: ^{87}Sr/^{86}Sr ratios of leachates of core and cuttings samples.

Sample Name	**Cored Interval**	**Formation**	**Top of Sampling Interval (ft bgs)**	**Bottom of Sampling Interval (ft bgs)**	**^{87}Sr/^{86}Sr**	**Sr (mg/L)**	**Leaching Media**	**SE (1σ)**	**SD (1σ)**
Core-1-7210-UpperMarcellus	Core 1	Upper Marcellus	7210	7211	0.71217	10.2	water	0.00001	0.00001
Core-1-7275-MiddleMarcellus	Core 1	Middle Marcellus	7275	7276	0.71235	7.9	water	0.00001	0.00001
Core-1-7319-Purcell	Core 1	Purcell	7319.55	7315.55	0.71118	5.1	water	0.00001	0.00001
Core-1-7333-Purcell	Core 1	Purcell	7333.55	1334.45	0.71013	2.1	water	0.00001	0.00001
Core-1-7346-Purcell	Core 1	Purcell	7346	7346.85	0.71192	1.5	water	0.00001	0.00001
Core-1-7399-LowerMarcellus	Core 1	Lower Marcellus	7399.6	7400.4	0.71159	9.8	water	0.00001	0.00001
Core-1-7464-UnionSprings	Core 1	Union Springs	7464	7465	0.71087	9.0	water	0.00001	0.00001
Core-1-7493-UnionSprings	Core 1	Union Springs	7493.05	7493.85	0.71148	1.2	water	0.00001	0.00001
Core-1_7560-Onondaga	Core 1	Onondaga	7560	7561	0.71132	7.8	water	0.00001	0.00001
Core-1-7641-Needmore	Core 1	Needmore	7641	7642	0.71269	2.5	water	0.00001	0.00001
Core-2-6594-UpperMarcellus	Core 2	Upper Marcellus	6594	6595	0.71142	13.8	water	0.00000	0.00001
Core-2-6594-UpperMarcellus	Core 2	Upper Marcellus	6594	6595	0.71140	23.2	1 M ammonium acetate	0.00001	0.00001
Core-2-6650-UpperMarcellus	Core 2	Upper Marcellus	6650	6651	0.71110	11.8	water	0.00001	0.00001
Core-2-6650-UpperMarcellus	Core 2	Upper Marcellus	6650	6651	0.71104	27.9	1 M ammonium acetate	0.00001	0.00001
Core-2-6650-UpperMarcellus	Core 2	Upper Marcellus	6650	6651	0.71028	181.0	1 M acetic acid	0.00001	0.00001
Core-2-6650-UpperMarcellus	Core 2	Upper Marcellus	6650	6651	0.71000	59.1	0.1 M hydrochloric acid	0.00000	0.00001
Core-2-6787-Purcell	Core 2	Purcell	6787	6788	0.71073	8.2	water	0.00001	0.00001
Core-2-6787-Purcell	Core 2	Purcell	6787	6788	0.70918	48.3	1 M ammonium acetate	0.00001	0.00001
Core-2-6881-FaultedPurcell	Core 2	Faulted Purcell	6881	6882	0.71068	5.2	water	0.00001	0.00001
Core-2-6881-FaultedPurcell	Core 2	Faulted Purcell	6881	6882	0.70936	23.1	1 M ammonium acetate	0.00001	0.00001
Core-2-6986.5-LowerMarcellus	Core 2	Lower Marcellus	6986.5	6987.5	0.70998	10.5	water	0.00001	0.00001
Core-2-6986.5-LowerMarcellus	Core 2	Lower Marcellus	6986.5	6987.5	0.70892	34.9	1 M ammonium acetate	0.00000	0.00001
Core-2-6986.5-LowerMarcellus	Core 2	Lower Marcellus	6986.5	6987.5	0.70848	1306.2	1 M acetic acid	0.00000	0.00001
Core-2-6986.5-LowerMarcellus	Core 2	Lower Marcellus	6986.5	6987.5	0.70844	77.7	0.1 M hydrochloric acid	0.00000	0.00001
Core-2-7003-UnionSprings	Core 2	Union Springs	7003	7004	0.70988	16.3	water	0.00000	0.00001
Core-2-7003-UnionSprings	Core 2	Union Springs	7003	7004	0.70882	83.2	1 M ammonium acetate	0.00001	0.00001
Core-2-7011-UnionSprings	Core 2	Union Springs	7011	7012	0.70990	14.9	water	0.00001	0.00001
Core-2-7011-UnionSprings	Core 2	Union Springs	7011	7012	0.70922	33.2	1 M ammonium acetate	0.00000	0.00001
Core-2-7011-UnionSprings	Core 2	Union Springs	7011	7012	0.70847	386.1	1 M acetic acid	0.00001	0.00001
Core-2-7011-UnionSprings	Core 2	Union Springs	7011	7012	0.70893	69.3	0.1 M hydrochloric acid	0.00000	0.00001
Core-3-7485-LowerMarcellus	Core 3	Lower Marcellus	7485	7486	0.71042	8.7	water	0.00001	0.00001
Core-3-7485-LowerMarcellus	Core 3	Lower Marcellus	7485	7486	0.70938	44.4	1 M ammonium acetate	0.00001	0.00001

Table 3.3: Continued.

Sample Name	Cored Interval	Formation	Top of Sampling Interval (ft bgs)	Bottom of Sampling Interval (ft bgs)	^{87}Sr/^{86}Sr	Sr (mg/L)	Leaching Media	SE (1σ)	SD (1σ)
Core-3-7500.5-LowerMarcellus	Core 3	Lower Marcellus	7500.5	7501.5	0.71055	9.6	water	0.00000	0.00001
Core-3-7500.5-LowerMarcellus	Core 3	Lower Marcellus	7500.5	7501.5	0.70946	43.7	1 M ammonium acetate	0.00001	0.00001
Core-3-7500.5-LowerMarcellus	Core 3	Lower Marcellus	7500.5	7501.5	0.70869	375.0	1 M acetic acid	0.00001	0.00001
Core-3-7500.5-LowerMarcellus	Core 3	Lower Marcellus	7500.5	7501.5	0.70887	75.5	0.1 M hydrochloric acid	0.00001	0.00001
Core-3-7512-LowerMarcellus	Core 3	Lower Marcellus	7512	7513	0.71009	11.2	water	0.00001	0.00001
Core-3-7512-LowerMarcellus	Core 3	Lower Marcellus	7512	7513	0.70913	47.3	1 M ammonium acetate	0.00000	0.00001
Core-3-7567-Onondaga	Core 3	Onondaga	7567	7568	0.71011	8.7	water	0.00001	0.00001
Core-3-7567-Onondaga	Core 3	Onondaga	7567	7568	0.70910	35.8	1 M ammonium acetate	0.00001	0.00001
Core-3-7567-Onondaga	Core 3	Onondaga	7567	7568	0.70838	1095.9	1 M acetic acid	0.00000	0.00001
Core-3-7567-Onondaga	Core 3	Onondaga	7567	7568	0.70845	67.7	0.1 M hydrochloric acid	0.00000	0.00001
Core-3-7581-Onondaga	Core 3	Onondaga	7581	7582	0.70985	5.3	water	0.00001	0.00001
Core-3-7581-Onondaga	Core 3	Onondaga	7581	7582	0.70909	25.3	1 M ammonium acetate	0.00000	0.00001
Core-3-7585-Onondaga	Core 3	Onondaga	7585	7586	0.70962	4.6	water	0.00001	0.00001
Core-3-7585-Onondaga	Core 3	Onondaga	7585	7586	0.70881	41.4	1 M ammonium acetate	0.00000	0.00001
Core-3-7857-Needmore	Core 3	Needmore	7587	7588	0.71169	29.5	water	0.00001	0.00001
Core-3-7857-Needmore	Core 3	Needmore	7587	7588	0.71166	80.3	1 M ammonium acetate	0.00001	0.00001
Core-3-7932-Needmore	Core 3	Needmore	7932	7933	0.71164	50.8	water	0.00001	0.00001
Core-3-7932-Needmore	Core 3	Needmore	7932	7933	0.71162	67.2	1 M ammonium acetate	0.00000	0.00001
Core-3-7952-Needmore	Core 3	Needmore	7952	7953	0.71159	33.0	water	0.00001	0.00001
Core-3-7952-Needmore	Core 3	Needmore	7952	7953	0.71160	47.0	1 M ammonium acetate	0.00000	0.00001
Core-3-7952-Needmore	Core 3	Needmore	7952	7953	0.71097	47.4	1 M acetic acid	0.00001	0.00001
Core-3-7952-Needmore	Core 3	Needmore	7952	7953	0.71064	9.1	0.1 M hydrochloric acid	0.00000	0.00001
Core-3-Cuttings-8135-8140-Oriskany	Core 3	Oriskany	8135	8140	0.71096	2.1	water	0.00000	0.00001
Core-3-Cuttings-8135-8140-Oriskany	Core 3	Oriskany	8135	8140	0.71082	12.3	1 M ammonium acetate	0.00001	0.00001
Core-3-Cuttings-8135-8140-Oriskany	Core 3	Oriskany	8135	8140	0.70977	339.4	1 M acetic acid	0.00001	0.00001
Core-3-Cuttings-8135-8140-Oriskany	Core 3	Oriskany	8135	8140	0.71026	14.3	0.1 M hydrochloric acid	0.00000	0.00001
Core-3-Cuttings-8150-8155-Oriskany	Core 3	Oriskany	8150	8155	0.71095	2.9	water	0.00001	0.00001
Core-3-Cuttings-8150-8155-Oriskany	Core 3	Oriskany	8150	8155	0.71077	14.6	1 M ammonium acetate	0.00000	0.00001
Core-3-Cuttings-8190-8195-Oriskany	Core 3	Oriskany	8190	8195	0.71072	3.2	water	0.00001	0.00001
Core-3-Cuttings-8190-8195-Oriskany	Core 3	Oriskany	8190	8195	0.71056	15.3	1 M ammonium acetate	0.00001	0.00001
Core-3-Cuttings-8350-8360-Mandata	Core 3	Mandata	8350	8360	0.71087	6.3	water	0.00001	0.00001
Core-3-Cuttings-8350-8360-Mandata	Core 3	Mandata	8350	8360	0.71072	21.4	1 M ammonium acetate	0.00001	0.00001
Core-3-Cuttings-8350-8360-Mandata	Core 3	Mandata	8350	8360	0.70936	123.3	1 M acetic acid	0.00001	0.00001
Core-3-Cuttings-8350-8360-Mandata	Core 3	Mandata	8350	8360	0.70948	23.7	0.1 M hydrochloric acid	0.00000	0.00001
Core-3-Cuttings-8460-8465-Mandata	Core 3	Mandata	8460	8465	0.71086	14.1	water	0.00001	0.00001
Core-3-Cuttings-8460-8465-Mandata	Core 3	Mandata	8460	8465	0.71049	43.3	1 M ammonium acetate	0.00000	0.00001

REFERENCES

Adams, J.A., Weaver, C.E., 1958. Thorium-to-uranium ratios as indicators of sedimentary processes: example of concept of geochemical facies. Am. Assoc. Pet. Geol. Bull. 42, 387–430. https://doi.org/10.1306/0BDA5A89-16BD-11D7-8645000102C1865D

Balashov, V.N., Engelder, T., Gu, X., Fantle, M.S., Brantley, S.L., 2015. A model describing flowback chemistry changes with time after Marcellus Shale hydraulic fracturing. Am. Assoc. Pet. Geol. Bull. 99, 143–154. https://doi.org/10.1306/06041413119

Bein, A., Dutton, A.R., 1993. Origin, distribution, and movement of brine in the Permian Basin (U.S.A.): A model for displacement of connate brine. Geol. Soc. Am. Abstr. with Programs 44, 337. https://doi.org/10.1130/0016-7606(1993)105<0695:ODAMOB>2.3.CO;2

Bethke, C.M., Marshak, S., 1990. Brine Migrations Across North America - the Plate Tectonics of Groundwater. Annu. Rev. Earth Planet. Sci. 18, 287–315. https://doi.org/10.1146/annurev.earth.18.1.287

Birkle, P., 2016. Recovery rates of fracturing fluids and provenance of produced water from hydraulic fracturing of Silurian Qusaiba hot shale, northern Saudi Arabia, with implications on fracture network. Am. Assoc. Pet. Geol. Bull. 100. https://doi.org/10.1306/02101615120

Blondes, M.S., Shelton, J.L., Engle, M.A., Trembly, J.P., Doolan, C.A., Jubb, A.M., Chenault, J.C., Rowan, E.L., Haefner, R.J., Mailot, B.E., 2020. Utica shale play oil and gas brines: Geochemistry and factors influencing wastewater management. Environ. Sci. Technol. 54, 13917–13925. https://doi.org/10.1021/acs.est.0c02461

Caldwell, J. (UC D., Vahidsafa, A. (UC D., 2020. Propagation of Error [WWW Document]. Chem. Libr. URL https://chem.libretexts.org/Bookshelves/Analytical_Chemistry/Supplemental_Modules_(Analytical_Chemistry)/Quantifying_Nature/Significant_Digits/Propagation_of_Error?bc=0

Capo, R.C., Stewart, B.W., Rowan, E.L., Kolesar Kohl, C.A., Wall, A.J., Chapman, E.C., Hammack, R.W., Schroeder, K.T., 2014. The strontium isotopic evolution of Marcellus Formation produced waters, southwestern Pennsylvania. Int. J. Coal Geol. 126, 57–63. https://doi.org/10.1016/j.coal.2013.12.010

CARB, 2018. Carbon Capture and Sequestration Protocol under the Low Carbon Fuel Standard, California Air Resources Board.

Chapman, E.C., Capo, R.C., Stewart, B.W., Kirby, C.S., Hammack, R.W., Schroeder, K.T., Edenborn, H.M., 2012. Geochemical and strontium isotope characterization of produced waters from Marcellus Shale natural gas extraction. Environ. Sci. Technol. 46, 3545–3553. https://doi.org/10.1021/es204005g

Chaudhuri, S., Clauer, N., 1992. History of marine evaporites: constraints from radiogenic isotopes. In: Isotopic Signatures and Records, in: Lecture Notes in Earth Sciences. Springer-Verlag, Verlin/Heidelberg, pp. 177–198. https://doi.org/10.1007/ BFb0009865

Clark, I., Fritz, P., 1997. Environmental Isotopes in Hydrogeology, 1st ed. CRC Press LLC.

Dresel, P., Rose, A.W., 2010. Chemistry and origin of oil and gas well brines in western Pennsylvania. Pennsylvania Geol. Surv., 4th Ser. Open File Rep. OFOG 10-01.0 48.

Engelder, T., Cathles, L.M., Bryndzia, L.T., 2014. The fate of residual treatment water in gas shale. J. Unconv. Oil Gas Resour. 7, 33–48. https://doi.org/10.1016/j.juogr.2014.03.002

Engle, M.A., Doolan, C.A., Pitman, J.A., Varonka, M.S., Chenault, J., Orem, W.H., Mcmahon, P.B., Jubb, A.M., 2020. Origin and geochemistry of formation waters from the lower Eagle Ford Group, Gulf Coast Basin, south central Texas. Chem. Geol. 550, 119754. https://doi.org/10.1016/j.chemgeo.2020.119754

Engle, M.A., Rowan, E.L., 2014. Geochemical evolution of produced waters from hydraulic fracturing of the Marcellus Shale, northern Appalachian Basin: A multivariate compositional data analysis approach. Int. J. Coal Geol. 126, 45–56. https://doi.org/10.1016/j.coal.2013.11.010

Engle, M.A., Rowan, E.L., 2013. Interpretation of Na–Cl–Br Systematics in Sedimentary Basin Brines: Comparison of Concentration, Element Ratio, and Isometric Log-ratio Approaches. Math Geosci. 45, 87–101. https://doi.org/10.1007/s11004-012-9436-z

Fisher, R.S., 1998. Geological and Geochemical Controls on Naturally Occurring Radioactive Materials (NORM) in Produced water from Oil, Gas, and Geothermal Operations. Environ. Geosci. 5, 139–150. https://doi.org/1075-9565/98/$10.50/0

Gardiner, J., Thomas, R.B., Phan, T.T., Stuckman, M., Wang, J., Small, M., Lopano, C., Hakala, J.A., 2020. Applied Geochemistry Utilization of produced water baseline as a groundwater monitoring tool at a CO2-EOR site in the Permian Basin, Texas, USA. Appl. Geochemistry 121, 104688. https://doi.org/10.1016/j.apgeochem.2020.104688

Glick, E., 2017. Connectivity of the Oriskany Sandstone with the Marcellus Shale: Effects on Shale Gas Operations in North Central Pennsylvania. University of Pittsburgh.

Gu, X., Cole, D.R., Rother, G., Mildner, D.F.R., Brantley, S.L., 2015. Pores in Marcellus Shale : A Neutron Scattering and FIB-SEM Study. Energy Fuels 29, 1295–1308. https://doi.org/10.1021/acs.energyfuels.5b00033

Iampen, H.T., Rostron, B.J., 2000. Hydrogeochemistry of pre-Mississippian brines, Williston Basin, Canada – USA. J. Geochemical Explor. 70, 29–35. https://doi.org/10.1016/S0375-6742(00)00007-8

Kharaka, Y.K., Hanor, J.S., 2007. Deep fluids in the continents: 1. Sedimentary Basins, in: Treatise on Geochemistry. Pergamon, Oxford, pp. 1–48.

Kolesar Kohl, C.A., Capo, R.C., Stewart, B.W., Wall, A.J., Schroeder, K.T., Hammack, R.W., Guthrie, G.D., 2014. Strontium isotopes test long-term zonal isolation of injected and

Marcellus formation water after hydraulic fracturing. Environ. Sci. Technol. 48, 9867–9873. https://doi.org/10.1021/es501099k

Kraemer, T.F., Reid, D.F., 1984. The occurrence and behavior of radium in saline formation water of the U.S. Gulf Coast region. Chem. Geol. 46, 153–174. https://doi.org/10.1016/0009-2541(84)90186-4

Landis, J.D., Sharma, M., Renock, D., 2018a. Rapid desorption of radium isotopes from black shale during hydraulic fracturing. 2. A model reconciling radium extraction with Marcellus wastewater production. Chem. Geol. 500, 194–206. https://doi.org/10.1016/j.chemgeo.2018.08.001

Landis, J.D., Sharma, M., Renock, D., Niu, D., 2018b. Rapid desorption of radium isotopes from black shale during hydraulic fracturing. 1. Source phases that control the release of Ra from Marcellus Shale. Chem. Geol. 496, 1–13. https://doi.org/10.1016/j.chemgeo.2018.06.013

Mcintosh, J.C., Walter, L.M., Martini, A.M., 2004. Extensive microbial modification of formation water geochemistry: Case study from a Midcontinent sedimentary basin, United States. Geol. Soc. Am. Bull. 116, 743–759. https://doi.org/10.1130/B25371.1

McNeal, R.P., 1965. Hydrodynamics of the Permian Basin, in: Young, A., Galley, J.E. (Eds.), AAPG Memoir: Fluids in Subsurface Environments. American Association of Petroleum Geologists. https://doi.org/https://doi.org/10.1306/M4360C12

Molofsky, L.J., Engle, M.A., Wylie, A.S., Wagner, T., Daniels, E.J., Connor, J.A., 2022. Evidence for water of condensation: A third source of water in shale gas wells. Am. Assoc. Pet. Geol. Bull. In Press.

Nicot, J., Eichhubl, P., Scanlon, B.R., 2020. Origin of low salinity, high volume produced waters in the Wolfcamp Shale (Permian), Delaware Basin, USA. Appl. Geochemistry 122, 104771. https://doi.org/10.1016/j.apgeochem.2020.104771

Nicot, J., Gherabati, A., Darvari, R., Mickler, P., 2018. Salinity Reversal and Water Freshening in the Eagle Ford Shale, Texas, USA. ACS Earth Sp. Chem. 2, 1087–1094. https://doi.org/10.1021/acsearthspacechem.8b00095

NYSDEC, 2009. Draft Supplemental Generic Environmental Impact Statement (SGEIS) on the oil, gas, and solution mining regulatory program (September 2009), Well permit issuance for horizontal drilling and high-volume hydraulic fracturing to develop the Marcellus Shale...

Osborn, S.G., McIntosh, J.C., 2010. Chemical and isotopic tracers of the contribution of microbial gas in Devonian organic-rich shales and reservoir sandstones, northern Appalachian Basin. Appl. Geochemistry 25, 456–471. https://doi.org/10.1016/j.apgeochem.2010.01.001

PA DEP, 1992. NORM survey summary, September 1, 1992; reproduced in IOGA NEWS (Independent Oil and Gas Association of Pennsylvania), April 1995.

Phan, T.T., Capo, R.C., Stewart, B.W., Macpherson, G.L., Rowan, E.L., Hammack, R.W., 2016. Factors controlling Li concentration and isotopic composition in formation waters and host rocks of Marcellus Shale, Appalachian Basin. Chem. Geol. 420, 162–179. https://doi.org/10.1016/j.chemgeo.2015.11.003

Phan, T.T., Gardiner, J.B., Capo, R.C., Stewart, B.W., 2018. Geochemical and multi-isotopic (87Sr/86Sr, 143Nd/144Nd, 238U/235U) perspectives of sediment sources, depositional conditions, and diagenesis of the Marcellus Shale, Appalachian Basin, USA. Geochim. Cosmochim. Acta 222, 187–211. https://doi.org/10.1016/j.gca.2017.10.021

Phan, T.T., Hakala, J.A., Sharma, S., 2020. Application of isotopic and geochemical signals in unconventional oil and gas reservoir produced waters toward characterizing in situ geochemical fluid-shale reactions. Sci. Total Environ. 714, 1–17.

https://doi.org/10.1016/j.scitotenv.2020.136867

Rostron, B., Arkadakskiy, S., 2014. Fingerprinting “stray” formation fluids associated with hydrocarbon exploration and production. Elements 10, 285–290. https://doi.org/10.1190/ice2015-2211363

Rowan, E.L., Engle, M.A., Kirby, C.S., Kraemer, T.F., 2011. Radium Content of Oil- and Gas-Field Produced Waters in the Northern Appalachian Basin (USA): Summary and Discussion of Data, USGS Scientific Investigations Report 2011–5135.

Rowan, E.L., Engle, M.A., Kraemer, T.F., Schroeder, K.T., Hammack, R.W., Doughten, M.W., 2015. Geochemical and isotopic evolution of water produced from Middle Devonian Marcellus shale gas wells, Appalachian Basin, Pennsylvania. Am. Assoc. Pet. Geol. Bull. 99, 181–206. https://doi.org/10.1306/07071413146

Saller, A.H., Stueber, A.M., 2021. Evolution of formation waters in the Permian Basin, United States: Late Permian evaporated seawater to Neogene meteoric water. Am. Assoc. Pet. Geol. Bull. 102, 401–428. https://doi.org/10.1306/0504171612517157

Stewart, B.W., Chapman, E.C., Capo, R.C., Johnson, J.D., Graney, J.R., Kirby, C.S., Schroeder, K.T., 2015. Origin of brines, salts and carbonate from shales of the Marcellus Formation: Evidence from geochemical and Sr isotope study of sequentially extracted fluids. Appl. Geochemistry 60, 78–88. https://doi.org/10.1016/j.apgeochem.2015.01.004

Stotler, R.L., Kirk, M.F., David Newell, K., Goldstein, R.H., Frape, S.K., Gwynne, R., 2021. Stable bromine isotopic composition of coal bed methane (CBM) produced water, the occurrence of enriched 81Br, and implications for fluid flow in the midcontinent, USA. Minerals 11. https://doi.org/10.3390/min11040358

U.S. EPA, 2016. Geologic Sequestration of Carbon Dioxide Underground Injection Control (UIC) Program Class VI Well Plugging, Post-Injection Site Care, and Site Closure

Guidance, EPA/816/R-16/006.

U.S. EPA, 2015a. Case Study Analysis of the Impacts of Water Acquisition for Hydraulic Fracturing on Local Water Availability, EPA/600/R-14/179.

U.S. EPA, 2015b. Analysis of Hydraulic Fracturing Fluid Data from the FracFocus Chemical Disclosure Registry 1.0, EPA/601/R-14/003.

U.S. EPA, 2013. Geologic Sequestration of Carbon Dioxide Underground Injection Control (UIC) Program Class VI Well Testing and Monitoring Guidance, U.S. Environmental Protection Agency Office of Water, EPA/816/R-13/001.

Walker-Milani, M.E., 2011. Outcrop Lithostratigraphy and Petrophysics of the Middle Devonian Marcellus Shale in West Virginia and Adjacent States.

Wang, F., Fu, J., 2023. A capillary bundle model for the forced imbibition in the shale matrix with dual-wettability. Can. J. Chem. Eng. 2330–2340. https://doi.org/10.1002/cjce.24635

Warner, N.R., Jackson, R.B., Darrah, T.H., Osborn, S.G., Down, A., Zhao, K., White, A., Vengosh, A., 2012. Geochemical evidence for possible natural migration of Marcellus Formation brine to shallow aquifers in Pennsylvania. Proc. Natl. Acad. Sci. U. S. A. 109, 11961–11966. https://doi.org/10.1073/pnas.1121181109

Chapter 4: A Geochemical Conceptual Model for Onshore Natural Gas Seepage in Oil and Gas Provinces

ABSTRACT

California exhibits one of the highest densities of natural oil and gas seeps in the world. However, there is limited information regarding the chemistry of the emitted gas and the changes occurring during transport from the source reservoir. This chapter presents the framework utilized for the first large-scale examination and synthesis of the molecular and isotopic composition of natural gas seepage in California. Specifically, this chapter reviews data from the literature on the chemistry of natural gas seeps throughout the state, and outlines the sampling and analytical strategies implemented during a focused program to significantly expand that dataset. The objectives of this research were twofold: 1) to evaluate whether there are common post-genetic changes in gas chemistry during natural gas seepage that could differentiate natural gas seeps from anthropogenic releases of reservoir gas; and 2) to assess the chemistry and origin of any water observed to be co-migrating with naturally seeping gas. Collectively, the methods presented herein can be applied to the interpretation of monitoring data in oil and gas fields with historical and/or ongoing natural gas seepage.

INTRODUCTION

California, USA is characterized by extensive natural hydrocarbon seepage, with over 540 instances of natural oil and/or gas migration from reservoir(s) to surface identified in 29 separate counties (Hodgson, 1987). The earliest documentation of these natural seeps can be traced to Native Americans, who used petroleum products and tar for necklaces, paint, and waterproofing (Hodgson, 1987; Takahashi and Gautier, 2004). Natural seeps were also the foundation for early hydrocarbon exploration in the state. More than 50 oil and gas fields in California have been discovered by drilling in the vicinity of natural hydrocarbon seeps (Table 4.1, Hodgson, 1987). These include the three most prolific oil producing fields in the state: Midway-Sunset, Kern River, and South Belridge (California Department of Conservation, 2020). Because oil and gas production is commonly co-located with areas of natural hydrocarbon seepage, understanding the chemical characteristics of natural seeping fluids (oil, gas, and/or water) is important for discerning, if possible, these natural phenomena from potential hydrocarbon releases associated with oil and gas extraction and associated activities. With numerous proposed carbon sequestration projects in active or depleted oil and gas fields under review in California (U.S. EPA, 2023), this research may also assist in discerning natural conditions from the unintended leakage of fluids or gases from CO_2 sequestration reservoirs. In particular, natural gas seepage is of high interest, both because gas can be transported significant distances from the original source owing to its low density and viscosity (several orders of magnitude less than that of oil or water (Bird et al., 2006; Heald, 1988)), and because natural gas seepage is a potentially important source of methane to the atmosphere (e.g., Etiope, 2009; Etiope et al., 2004; Etiope and Ciccioli, 2009; Farrell et al., 2013; Peischl et al., 2013; Weber et al., 2017). However, despite a wealth of available information on the location of onshore natural hydrocarbon seeps in California, only a select few have been sampled for the chemistry of gases emerging from the surface (Duffy et al., 2007; Etiope et al., 2017; Jeffrey et al., 1991; Lorenson et al., 1998; Weber et al., 2017; Weed et al., 2020). This chapter focuses on expanding the present understanding of the molecular and isotopic composition of natural gas seepage throughout California, and specifically, the post-genetic changes that occur during gas migration from reservoir to surface. Given the pervasive and ubiquitous nature of these seeps, this work has the potential to provide insights into sources of near-surface hydrocarbons in petroleum-bearing basins around the world.

Table 4.1: Oil and gas fields in California discovered in the vicinity of seeps. Based on table presented in Hodgson (1987).

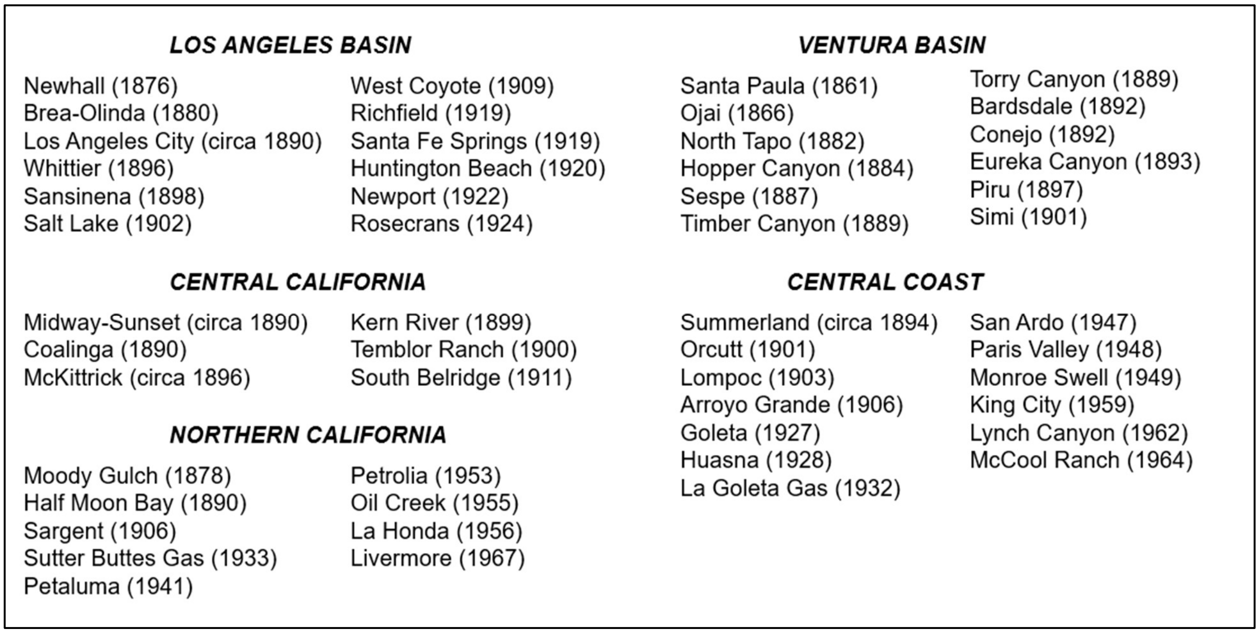

LOS ANGELES BASIN

Newhall (1876)
Brea-Olinda (1880)
Los Angeles City (circa 1890)
Whittier (1896)
Sansinena (1898)
Salt Lake (1902)
West Coyote (1909)
Richfield (1919)
Santa Fe Springs (1919)
Huntington Beach (1920)
Newport (1922)
Rosecrans (1924)

CENTRAL CALIFORNIA

Midway-Sunset (circa 1890)
Coalinga (1890)
McKittrick (circa 1896)
Kern River (1899)
Temblor Ranch (1900)
South Belridge (1911)

NORTHERN CALIFORNIA

Moody Gulch (1878)
Half Moon Bay (1890)
Sargent (1906)
Sutter Buttes Gas (1933)
Petaluma (1941)
Petrolia (1953)
Oil Creek (1955)
La Honda (1956)
Livermore (1967)

VENTURA BASIN

Santa Paula (1861)
Ojai (1866)
North Tapo (1882)
Hopper Canyon (1884)
Sespe (1887)
Timber Canyon (1889)
Torry Canyon (1889)
Bardsdale (1892)
Conejo (1892)
Eureka Canyon (1893)
Piru (1897)
Simi (1901)

CENTRAL COAST

Summerland (circa 1894)
Orcutt (1901)
Lompoc (1903)
Arroyo Grande (1906)
Goleta (1927)
Huasna (1928)
La Goleta Gas (1932)
San Ardo (1947)
Paris Valley (1948)
Monroe Swell (1949)
King City (1959)
Lynch Canyon (1962)
McCool Ranch (1964)

Natural gas seepage is the non-anthropogenic flow of gaseous hydrocarbons from subsurface sources to Earth's surface. This flow may be fast or slow, consistent or sporadic, and visible or invisible (Abrams, 2017; Etiope, 2015). Natural gas seeps traditionally occur in oil- and gas-bearing sedimentary basins, where hydrocarbon gases, primarily methane (CH_4 or "C1"), but also ethane (C_2H_6 or "C2"), propane (C_3H_8 or "C3"), butane (C_4H_{10} or "C4"), pentane (C_5H_{12} or "C5") and hexane (C_6H_{14} or "C6"), form from the thermal breakdown of more complex organic molecules in source rocks (i.e., "thermogenic" gas). In addition, natural seeps may contain "microbial" gas, which is primarily comprised of methane (>99%) formed by the microbial degradation of organic material at depth in source rocks, or in the shallow subsurface. Non-hydrocarbon gases (CO_2, N_2, He, and H_2S) are also often co-present as minor components (Etiope, 2015).

Natural gas seeps are largely classified into two categories: macroseepage and microseepage (Abrams, 2020, 2017, 2005; Asadzadeh and de Souza Filho, 2017; Etiope, 2015).

Macroseepage is the surface expression of hydrocarbon or hydrocarbon-bearing fluids (oil, gas, and gas-bearing springs) related to advective flow, most commonly via major faults or fractures (Abrams, 2020). Macroseeps are generally characterized by hydrocarbon gas concentrations in excess of 10% by volume (100,000 ppmv) (Abrams, 2005), although fluxes from individual macroseeps or larger macroseep areas can exhibit a wide range of values (e.g., from 10^{-1} to $>10^3$ tonnes per year (Etiope, 2015)). By contrast, microseepage describes the invisible, but constant transport of light alkanes (C1-C5) and volatiles vertically or near-vertically from the source pool. Buoyancy of microbubbles, or "continuous phase buoyancy-driven gas flow," is the commonly proposed migration mechanism for microseepage (Abrams, 2020; Etiope, 2015; Klusman and Saeed, 1996; Krooss, 1996; Rice, 2022). This research focuses on macroseeps, which are readily identified and sampled at the surface.

Natural gas macroseepage can co-occur with other petroleum hydrocarbons (oil) and/or deep formation waters. However, because gas can rapidly move vertically or laterally through complex pathways that may have little or no hydraulic connection (Molofsky et al., 2021), it is not unusual to observe natural gas seepage without surface expression of oil or other reservoir fluids (e.g., deep formation waters). Hydrocarbon (gas or oil) seeps most commonly occur in convergent basins with petroleum source rocks. Specifically, of 2,699 natural seeps of gas and/or oil worldwide, Ciotoli et al. (2020) found that 72% (1,941 seeps) were located in convergent basins. Seepage is primarily associated with reverse faults, or more broadly, any type of brittle tectonic structure (Ciotoli et al., 2020). In particular, seeps prevail along the outer edge of petroleum fields, which are generally characterized by a higher density of faults and fractures.

With numerous petroleum-bearing basins and its location along a convergent plate margin, California is a prime example of a geologic setting conducive to natural hydrocarbon seepage. Much of California geology is shaped by the subduction of the Farallon Plate (now complete) beneath the westward-moving North American Plate, and by the present-day subduction of the Juan de Fuca plate beneath North America in northern California. Within this setting, multiple marine basins developed adjacent to the active continental margin, and gas flow is so dynamic that mantle-derived helium has been identified migrating along the San Andres fault system (Boles et al., 2015; Kennedy et al., 1997). These basins contain sedimentary organic rich formations, which serve as oil and gas source rocks, including the Miocene Monterey Formation, considered to be the source rock for the majority of oil produced in California (Behl, 2012). Hydrocarbon migration is significant in California's oil and gas basins, with lateral transport in excess of 50 km (Peters et al., 2007). In addition, many of these basins are located along the margins of thrust-and-fold belts or shallow decollement layers that have ruptured to surface. The latter is associated with short-cuts, back-thrusts, and ancillary high-angle fracturing, all which can serve as seepage pathways (Ciotoli et al., 2020; Macgregor, 1993).

Accordingly, California exhibits a particularly high density of natural hydrocarbon seeps. Of the 543 seeps identified within the state by Hodgson (1987), 132 were reported to produce natural gas (Figure 4.1). Nevertheless, gas molecular and isotopic data from natural gas seeps in California are limited. Research by Duffy et al. (2007), Etiope et al. (2017), Weber et al. (2017) and Weed et al. (2020) quantified emission rates from natural gas seeps located in the Los Angeles, Ventura, and San Joaquin Basins in Southern California (i.e., the La Brea, Upper Ojai Valley, Carpinteria, and McKittrick natural seeps). These studies also reported the molecular composition of hydrocarbon gases, and in some cases, one or more of the following isotopic values: $\delta^{13}C$ of C1, C2, C3, CO_2 and $\delta^{2}H$ of C1. In addition, compositional and isotopic data are available for nine samples of natural gas surface seepage in Los Angeles (Jeffrey et al., 1991) and four samples collected from natural gas seeps in the Eel River Basin in Northern California (Lorenson et al., 1998). Collectively, these data show that natural gas seepage in California is characterized by C1, as well as the presence of C2+ light alkanes, consistent with a significant thermogenic gas component (i.e., natural gas seepage originating from underlying oil and gas-bearing reservoirs). Where data for reservoir gases are available for comparison, seepage gas commonly shows C2+ loss relative to reservoir gas, as well as changes in the $\delta^{13}C$ composition of C1 and/or CO_2, and ratio of isobutane to n-butane relative to reservoir gas (Duffy et al., 2007; Etiope et al., 2017; Jeffrey et al., 1991; Lorenson et al., 1998; Weber et al., 2017). These changes were interpreted as post-genetic processes that can affect gas chemistry during transport, including microbial oxidation of hydrocarbon gases, mixing with microbial gas, and secondary methanogenesis, among others.

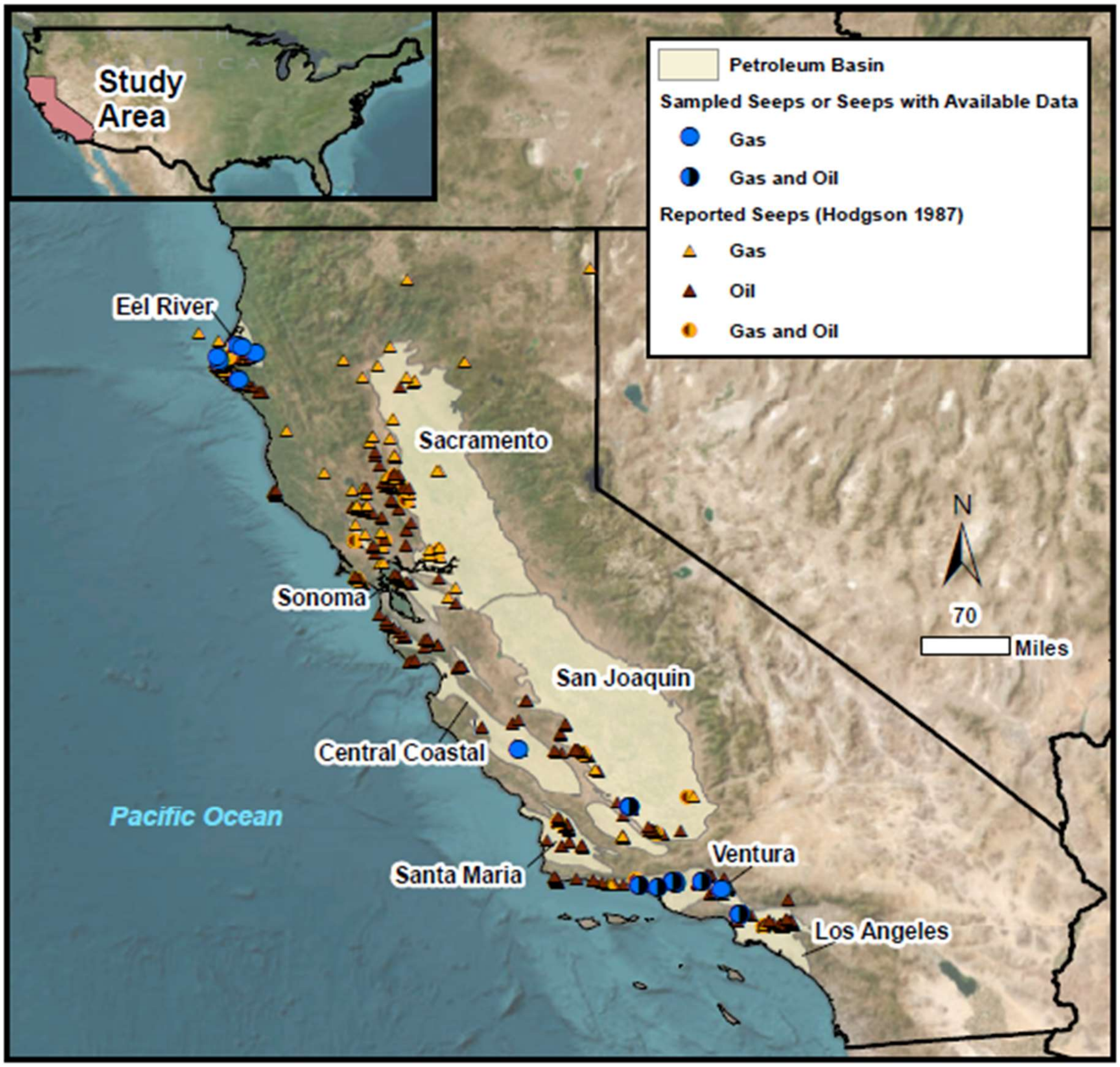

Figure 4.1: Map of California study area, including natural gas seeps that have been sampled previously or were sampled as part of this research program, as well as 543 natural gas and/or oil seeps reported in Hodgson (1987), and the outlines of major petroleum basins.

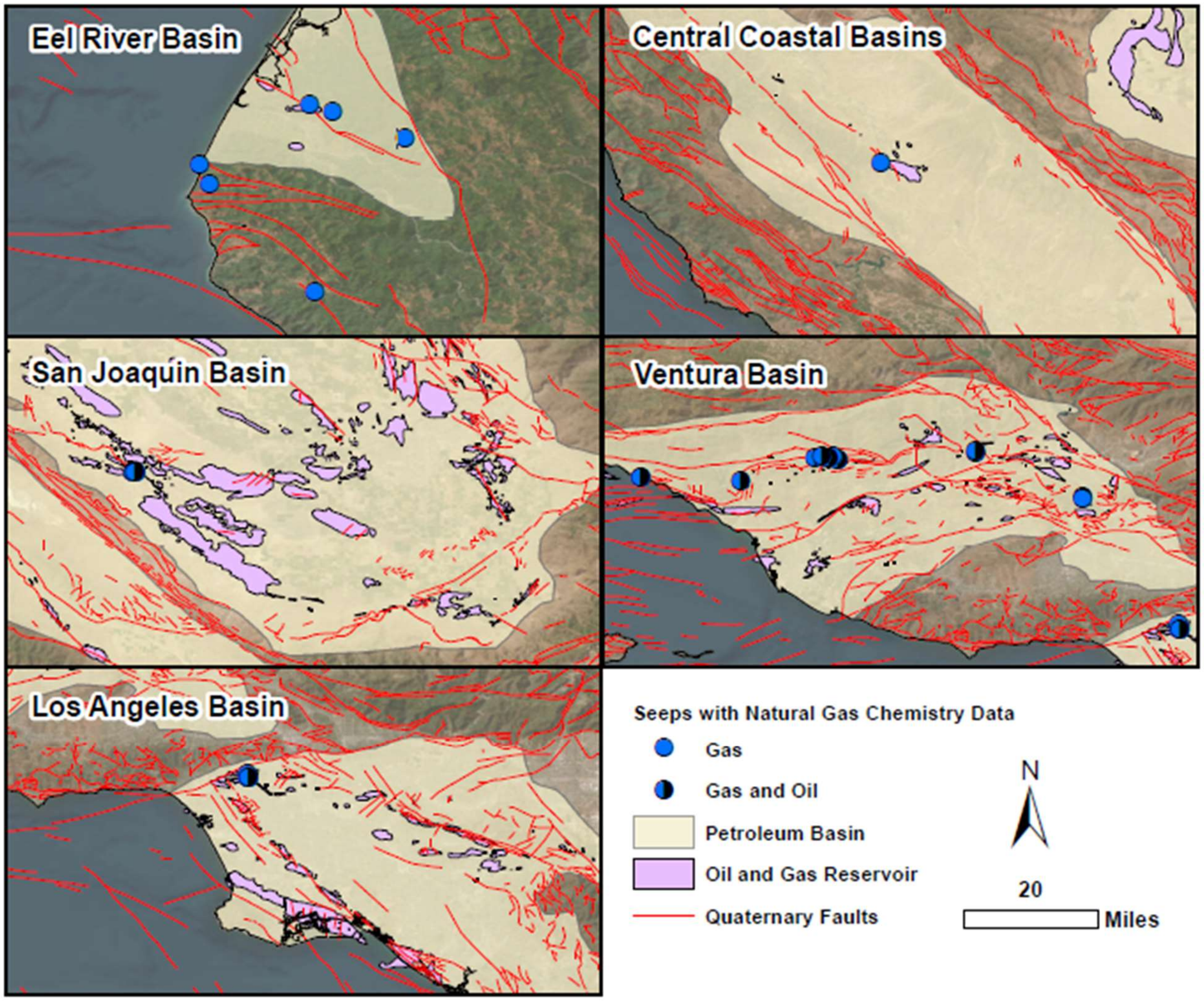

Figure 4.2: Location of natural gas seeps sampled in this research program relative to oil and gas reservoirs and quaternary faults in major petroleum bearing basins.

This study presents the strategy for the evaluation of existing gas data (i.e., the molecular and isotopic composition), as well as the collection of new gas data, from natural gas seeps located in a wide-range of geologic settings in California, including the Los Angeles, Ventura, San Joaquin, Central Coastal, and Eel River Basins (Figures 4.1 and 4.2). Methods for sampling and evaluating water chemistry are also presented that can be used when water is co-migrating with the gas. The purpose of this research was to evaluate whether natural seeps consistently exhibit either any shared chemical characteristics of gases or post-genetic changes that occur during transport from reservoir to surface. If so, such information could assist in differentiating natural seepage from potential unintended releases of gas in areas of oil and gas extraction. This research was also designed to inform the co-seepage of reservoir formation fluids with natural gas. The data collected during this program will be presented elsewhere.

BACKGROUND

Post-genetic processes affecting natural gas molecular and isotopic composition

As a framework for comparing natural gas seepage to local reservoir gas(es), it is important to understand the various chemical and physical processes that can affect the molecular and isotopic composition of gases during transport from reservoir to surface:

- Molecular fractionation due to loss of free-phase hydrocarbon gases to solution in water ("solubility fractionation"), exsolution of gases out of water ("evaporation fractionation"), or sorption to mineral or organic surfaces ("sorption fractionation");
- Aerobic and anaerobic microbial oxidation of hydrocarbon gases;
- Abiogenic oxidation;
- Secondary methanogenesis following anaerobic petroleum degradation;
- Gas mixing; and
- Isotopic and molecular fractionation by diffusion.

The potential effects of these processes on the chemistry of natural gas seepage are described below and summarized in Table 4.2. Key processes acting on macroseepage gas chemistry are illustrated in Figure 4.3.

Table 4.2: Post-genetic processes potentially affecting natural seepage gas chemistry.

Post-Genetic Process	**Effect on Molecular or Isotopic Composition of Free-Phase Gas**
Solubility Fractionation Function of different solubility properties of C1 – C5	• Loss of C2 and C3
Evaporation Fractionation Function of different volatilities of C1 – C5	• Minimal effect on free-phase gas, results in C2 and C3 enrichment of dissolved gas
Sorption Fractionation Function of different sorption properties of C1 – C5	• Loss of C2+, if organic sorption, loss in order of mass (C5 loss>C4 loss >C3 loss>C2 loss)
Aerobic and anaerobic microbial oxidation of C1 – C6+	• Increased (heavier) $\delta^{13}C$ and $\delta^{2}H$ values; • High C2/C3 and iC4/nC4 ratios due to preferential degradation of C3 and n-alkanes; • Large isotopic separation between n-alkanes
Abiogenic oxidation Thermochemical sulfate reduction (TSR) or oxidation by Fe^{3+} bearing minerals at high temperatures (80 to 400°C)	• High H_2S concentrations (>5%) • Increased (heavier) $\delta^{13}C$ values of C1-C5
Secondary methanogenesis following anaerobic biodegradation of petroleum	• Positive $\delta^{13}C$-CO_2
Gas mixing	• Depends on gas end-members
Isotopic fractionation by diffusion Slow gas movement driven by concentration gradients results in depletion of ^{13}C in diffusing CH_4	• Decreasing (lighter) $\delta^{13}C$-CH_4 in migrating gas

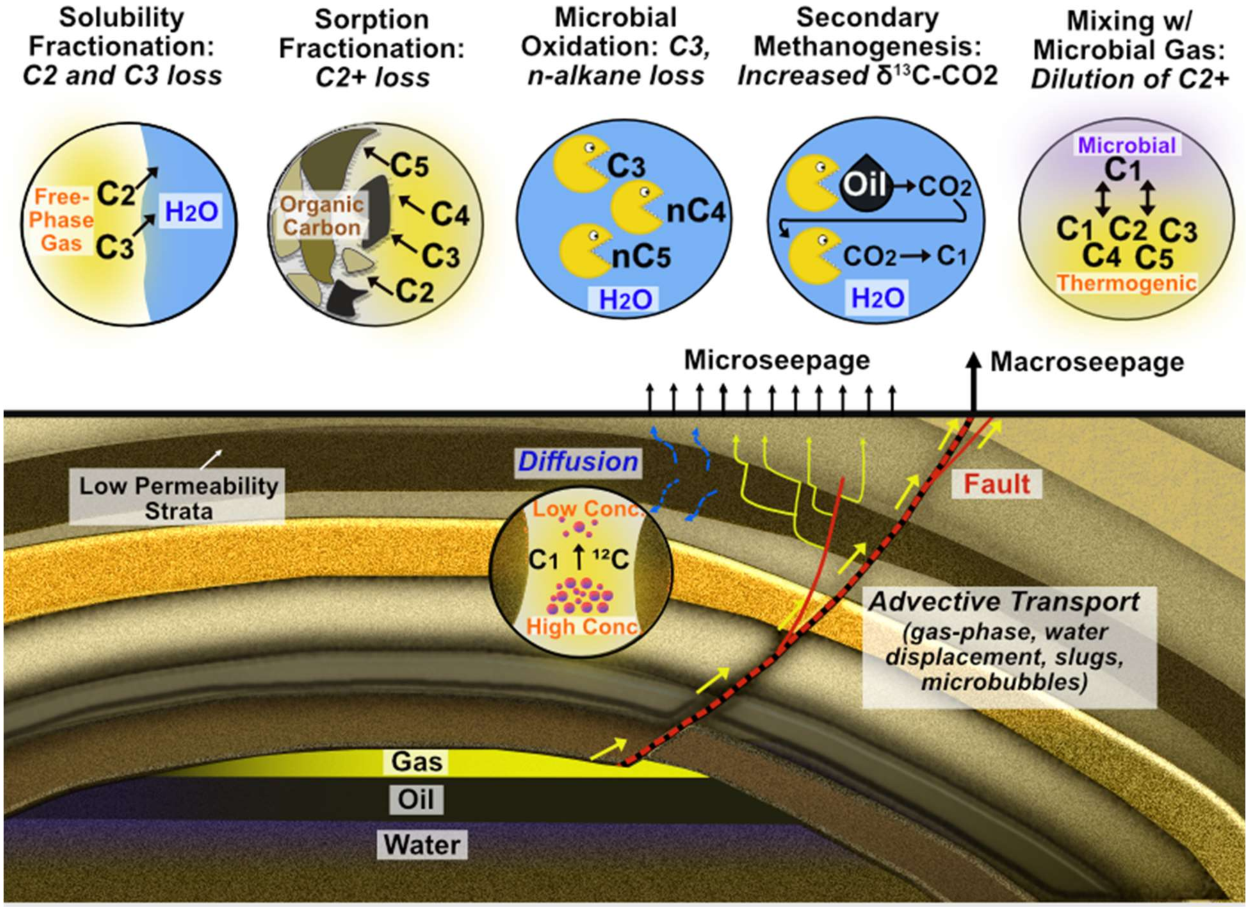

Figure 4.3: Conceptual model of key post-genetic processes that affect geochemistry of gas macroseepage.

Solubility fractionation, or the enhanced free-phase loss of a specific hydrocarbon gases to adjacent formation water over others, occurs because C2 and C3 exhibit higher solubilities than C1 (e.g., Klusman and Saeed, 1996). As a result, these components are more readily dissolved in water (i.e., lost from the gas phase) during free-phase gas transport. Conversely, evaporative fractionation describes the preferential volatilization (i.e., off-gassing) of dissolved C1 relative to C2 and C3 from a rapid and significant change in the local pressure regime. It was initially described in studies of the exsolution of gas from oil in U.S. Gulf Coast reservoirs (Thompson, 1987), but the same process may occur during dissolved gas transport, resulting in increased dissolved gas wetness (Abrams, 1996).

Sorption fractionation is described as the preferential adsorption of C2+ hydrocarbons to organic matter or sediments/minerals, or entrapment in structured water or authigenic carbonate inclusions, resulting in C2+ loss from the migrating gas (Abrams, 2020, 2017; Abrams and Dahdah, 2010; Bernard et al., 2001; Bjoroy and Ferriday, 2001; Deville et al., 2003; Etiope, 2015; Horvitz, 1985, 1972; Whiticar, 2001). This in part reflects the greater affinity for heavier hydrocarbon gases (relative to lighter hydrocarbon gases) to sorb to and accumulate within organic carbon, as reflected in the increasing octanal-water coefficients (Log K_{ow} values) with mass: C1= 1.2, C2 = 1.81, C3 = 2.36, C4= 2.89, and C5 = 3.39 (Bhatnagar et al., 2011; Ulrich et al., 2021). There is debate about the extent of molecular fractionation related to adsorption to sediments, with recent literature suggesting that the enrichment of C2+ in sediment adsorbed gases (relative to free-phase gas) may be an artifact of the approach to sample collection or adsorbed gas extraction (Abrams and Dahdah, 2010). Of note, sorption fractionation, solubility fractionation and evaporative fractionation require significant interaction with water, organics, or sediments; as such, the effects of these processes are not typically observed in high-flow macroseeps where natural gas is the only ascending fluid (Etiope et al., 2009).

Aerobic and anaerobic oxidation of hydrocarbon gases affects both the isotopic and molecular composition of migrating natural gas. During microbial oxidation, lighter isotopes are metabolized by microbes slightly faster than heavier isotopes (i.e., the bonds with lighter isotopes are more readily dissolved). This oxidation process leaves the remaining hydrocarbon gases enriched in the heavier carbon and hydrogen isotopes (i.e., more ^{13}C relative to ^{12}C, and more ^{2}H relative to ^{1}H). C3 and n-alkanes are preferentially oxidized (degraded) by microbes over other hydrocarbon gases (Pallasser, 2000; Whiticar, 1999). As a result, microbial oxidation can result in high C2/C3 and isobutane/n-butane (iC4/nC4) ratios and large isotopic separations between successive n-alkanes relative to the starting gas composition (Pallasser, 2000). Aerobic microbial oxidation can proceed in both the vadose zone (i.e., above the water table) and in oxygenated water, although deeper waters are almost universally anaerobic (e.g., Freeze and Cherry, 1979). Anaerobic oxidation of hydrocarbon gases exclusively occurs in water, where NO_3^{-1}, Fe^{2+}, Mn^{4+}, and SO_4^{2-} are utilized as electron acceptors in the oxidation process (e.g., Kelly et al., 1985; Van Stempvoort et al., 2005). In either case (anaerobic or aerobic oxidation), CO_2 is produced as a byproduct of the oxidation reaction. The CO_2 is characterized by a $\delta^{13}C$ composition that is depleted (isotopically lighter) than the parent hydrocarbon gas.

In deep reservoirs with high temperatures (80°C to 400°C), hydrocarbon gases may also be consumed by abiogenic oxidation associated with thermochemical sulfate or iron reduction (Etiope et al., 2009). Abiogenic oxidation results in enriched (more positive) $\delta^{13}C$ of C1-C5, and elevated H_2S concentrations. This process primarily occurs in seepage systems close to geothermal or volcanic systems (Etiope, 2015). Such conditions are generally not present in the seepage areas evaluated in this study, with the possible exception of the Eel River Basin, which contains several geothermal hot springs (Ogle, 1953).

In secondary methanogenesis following petroleum hydrocarbon degradation, the CO_2 produced from microbial oxidation of petroleum hydrocarbons is consumed by microbes (i.e., via the anaerobic CO2 reduction pathway), producing methane as a byproduct (Pallasser, 2000; Whiticar, 1999). Secondary methanogenesis yields residual CO_2 with an enriched (isotopically heavier) $\delta^{13}C$ composition, commonly exceeding +10‰ (Etiope et al., 2009). This process may occur in both petroleum reservoirs and during natural seepage if both gas and oil are migrating concurrently through same pathways.

Gas mixing, or the mixing of gases of two or more different sources, may affect the molecular and isotopic composition of hydrocarbon gases. Such mixing may occur within reservoirs and during gas transport. Because microbial gas commonly lacks C2+ hydrocarbons, mixtures of microbial and thermogenic gas are primarily evident in the isotopic composition of methane and the abundance of methane relative to C2+. However, gas mixtures may also include mixtures of two or more thermogenic gases, both which contain C2+ hydrocarbons. As such, the presence of mixing is typically evaluated through a combination of C1/(C2+C3) and δ^{13}C-C1, or δ^{13}C-C1, δ^{13}C-C2, and δ^{13}C-C3, or other similar plots (e.g., Bernard et al., 1977; Chung et al., 1988; Coleman, 1995; Etiope et al., 2009).

Isotopic and molecular fractionation by diffusion is reported to occur when concentration gradients, rather than pressure gradients, are the driver of slow gas movement. Lighter molecules (C1) and isotopes (^{12}C) diffuse quicker than heaver molecules (C2+) and isotopes (^{13}C), resulting in "lightening" of the molecular and isotopic composition from source rock to reservoir, or reservoir to surface (Prinzhofer and Battani, 2003). However, isotope and molecular fractionation by diffusion is not a significant process in macroseeps, where advection rather than diffusion is the primary transport mechanism (e.g., Etiope et al., 2009). Additionally, even in microseeps, diffusion does not appear to be the dominant transport mechanism through the saturated zone (Klusman and Saeed, 1996). Accordingly, this process is not discussed further.

GEOLOGIC SETTING

The seep sampling locations selected for this project (Figure 4.2) represent a significant geographic spread and diversity of geologic settings, as well as variation in occurrence (i.e., seeps where natural gas was the sole fluid vs. natural gas, oil and/or water). Specifically, the selected seeps are located in the Eel River, San Joaquin, Central Coastal, Ventura, and Los Angeles Basins in California, USA (Figure 4.1). The geologic setting of each basin is summarized below.

Eel River Basin

The Eel River Basin of northern California is a westerly trending Cenozoic basin containing over 4,000 m (13,000 ft.) of marine sedimentary rock, including the Miocene through Pleistocene sediment fill referred to as the Wildcat Group (Ogle, 1953). Within the Wildcat Group, gas is presently produced from several thin, permeable sands within the 900 to 1,800 m (3,000 to 6,000 ft.) thick Pliocene Rio Dell Formation, comprised of mudstone, siltstone and sandstone. The Anderson sandstones of the Rio Dell Formation are the most prolific gas reservoir, and the source of gas production in the Tompkins Hill gas field (Gordon, 2009). The source rock for Eel River Basin hydrocarbons is inconclusive, though some researchers have suggested that the Miocene Bear River Beds are a possible analog to the Miocene Monterey Formation of central California (Gordon, 2009; McLean, 1988). However, others have noted that the Bear River Beds likely never reached sufficient thermal maturities for hydrocarbon generation (Gordon, 2009). Alternatively, Underwood (1985) proposed the pre-Tertiary Yager Formation marine shales and sandstones as a likely source rock. The Yager is characterized by Type III kerogens and vitrinite reflectance (Ro) values as high as 1.26%, indicating thermal maturation within the gas window (Underwood, 1985). Located near the Mendocino Triple Junction of the North American, Pacific, and Gorda plates, the basin has experienced active tectonism and faulting and folding, resulting in structural features including the Eel River syncline and smaller anticlines in the South and North, and the Little Salmon fault (Tsai and Boessenecker, 2017), where several natural gas seeps present at surface. Seeps sampled in the Eel River Basin were located proximate to the Tompkins Hill gas field (northern Eel River Basin), and northwest and southeast of the Petrolia oil field (southern Eel River Basin).

San Joaquin Basin

The San Joaquin Basin is an asymmetrical trough, consisting of 7.6–10 km of Mesozoic and Cenozoic sediments infilling accommodation space created by a history of subsidence as a forearc basin (Franks et al., 2001). The petroleum system of the San Joaquin Basin consists of variable combinations of source, reservoir, and seal intervals. The most significant hydrocarbon source rock in the southern San Joaquin Basin is the Miocene Antelope Shale, which is part of the Monterey Formation as confirmed through comparison of biomarker ratios and $\delta^{13}C$ composition of aromatic and saturated hydrocarbons in oils vs. possible source rocks (Lillis et al., 2007). These source rocks migrate to and through reservoirs consisting of deep-sea channel and fan deposits with stratigraphic and structural/stratigraphic traps. Maturation of bitumen in sampled accumulation zones of Antelope Formation hydrocarbons at depths of 580m-1572m have also shown comparable maturity values to those found in the deepest non-production zone at 3,430m. Modeled vitrinite reflectance values of the Antelope Formation's Type II and Type IIS kerogen are within the oil window (>0.6), if not the gas window (>1.3) (Peters et al., 2007). There are three primary depocenters, including from north to south: the Northern Buttonwillow, Southern Buttonwillow, and Tejon depocenters. Thermal maturity modeling of the system by Peters et al. (2007) indicates that the highest potential for petroleum generation from the Antelope Shale existed in the Tejon depocenter, from which the majority of hydrocarbons were expelled in the last 0.6 Ma (roughly the time of maximum burial). Notably many of the present-day fields in the southern portion of the basin are distal to areas of primary hydrocarbon generation, suggesting significant hydrocarbon migration. Seeps sampled in the San Joaquin Basin are located along the southern border of the McKittrick oilfield, and are thought to be sourced from the Miocene Monterey Formation.

Central Coastal Basins

The Central Coastal Basins include three adjacent basins located in central California between the northwest-southeast trending San Andreas strike-slip fault to the east, and the parallel Sur-Nacimiento strike-slip fault to the west. These include the La Honda (northwest), Salinas (central) and Cuyama (southeast) Basins. These basins were formed during the Eocene and Miocene as a result of sea level changes and tectonically driven land movement associated with the triple junction between the North American, Pacific, and Farallon plates, which has since migrated north from central California (Isaacs, 1992; SVBGSA, 2019). One seep was sampled in the Central Coastal Basins, and specifically, within the Salinas Basin proximate to the San Ardo oilfield. The Salinas Basin formed during a 20 Ma period of major basin subsidence and sediment infilling during the Neogene. The principal source rock in the Salinas Basin is the Miocene Monterey Formation, associated with a 10 Ma period of major marine transgression, in which oil-generating (thermally mature) organic matter was reported to be present below the present-day depth of 4500 ft in the Salinas trough (Isaacs, 1992). Principal production is from the San Ardo field, and from upper Miocene sandstones in the Monterey or Santa Margarita Formations.

Ventura Basin

The Ventura Basin lies southeast of the San Joaquin Basin, separated by the San Andreas Fault zone and the Transverse Mountain Ranges. The basin is superposed on a Middle Miocene rift system and Mesozoic-Cenozoic forearc basin (Sorlien et al., 2000; Yeats et al., 1994), and presently represents the onshore portion of the main structural down-warp of a major thrust and fold belt that began forming during the late Pliocene (Keller, 1988). By comparison, the Santa Barbara Basin represents its offshore extension. The Ventura Basin contains mostly marine Cretaceous to Pleistocene sedimentary strata, including the Miocene Monterey-Modelo Formation, which represents the primary source rock from which hydrocarbon generation is ongoing (Gordon, 2020). Pliocene-Miocene sandstones comprise 75-80 percent of productive reservoirs (Keller, 1988). Within the Ventura Basin, seeps data originates from Carpinteria State Beach (western basin), the Upper Ojai Valley (west-central basin), Modelo Canyon (east-central basin), and Wiley Canyon (eastern basin). Carpinteria State Beach, located on the shoreline of the Pacific Ocean, is approximately equidistant from four oilfields: the onshore Rincon and Rincon Creek oil fields, and the offshore Summerland and Carpinteria oil fields (Weed et al., 2020). To the west, the Upper Ojai valley sits within a tectonic depression and is bordered by two opposing reverse faults: the north-dipping San Cayetano fault in the north and south-dipping Oak Ridge fault in the south (Huftile, 1988). Seeps evaluated in the Ojai Valley are located above or proximate to the North Sulphur Mountain and Silverthread oil fields, which produce from the Upper Miocene Mohnian sandstone and fractured shale (Huftile, 1988; Schwade and Fine, 1949). Modelo Canyon is located in the Modelo anticline within the Topatopa Mountains, part of the Tranverse Ranges of Southern California (Eldridge and Arnold, 1907). The rocks in the Modelo anticline are comprised of the lower and upper Miocene Modelo sandstones and intermediate and overlying shales, with historical production from accumulations within the Modelo sandstones (Eldridge and Arnold, 1907), Wiley Canyon is located on the Pico anticlinal uplift, which comprises a portion of the Santa Susana Mountains. At this location, the fractured Miocene Modelo Shale is exposed on the anticlinal axis, and numerous seeps of crude oil and gas occur in the fractured shale (Walling, 1934). Oil production in Wiley Canyon originate from accumulations within the Miocene Modelo Formation.

Los Angeles Basin

The Los Angeles Basin is located southeast of the Ventura Basin. Its tectonic history includes regional subsidence through the late Miocene followed by a NW-SE extensional period in the Pliocene transitioning to a north-south compressional period in the Pleistocene (Wright, 1991). The basin has significant Miocene source rocks, as well as thick sandstone reservoirs, and anticlinal traps which come together to generate on of the highest concentrations of crude oil in the world, with the Wilmington-Belmont field being the fourth largest oil field in the United States (Gautier et al., 2012). Geochemical analysis of the primary source rocks, including the Miocene Monterey Formation, reveals oil- and gas-prone Type II marine kerogens (Behl, 1999; Feinstein et al., 2015). Due to the substantial tectonic deformation in the region, the internal structure of the basin includes significant faulting, which could act as conduit pathways for hydrocarbon migration through the basin. As an example, mantle He has been transported to surface via the Newport-Englewood fault zone (NIFZ), a 1,300 km strike-slip system active through basement rock to the mantle which developed during early Miocene subduction and is a major fault in the San Andreas fault system (Boles et al., 2015). The presence of extensive faults would explain the fact that gas caps are almost nonexistent in the oil fields, as a result of hydrocarbon migration to the surface (Shonkoff and Gautier, 2015; Wright, 1991). Seeps evaluated in the Los Angeles Basin were located on or adjacent to the grounds of the La Brea Tar Pits and Museum. In this area, crude oil is thought to be surfacing via the 6th Street Fault, which serves as a likely conduit to the Salt Lake Oil Field (Etiope et al., 2017; Wright, 1987).

METHODS

Natural gas seeps in California were identified through review of the DOGGR Hodgson (1987) complication of "Onshore Oil & Gas Seeps in California." Hodgson (1987) compiled available reports of onshore oil and gas seeps in California in government and industry publications, and documented seep location, activity, and appearance, where possible. Of the 132 natural gas seeps reported in this publication, 69 were listed as active at the time. In addition, numerous scientific publications and public resources were reviewed for additional information on the location and nature of natural gas seeps throughout California (e.g., Duffy et al., 2007;

Etiope et al., 2017; Jeffrey et al., 1991; Lorenson et al., 1998; Weber et al., 2017; Weed et al., 2020).

Eight areas were identified for field reconnaissance. These included, from north to south: the Eel River Basin (which includes a northern and southern component), the areas proximate to the San Ardo oilfield in Monterey County, the McKittrick oilfield in Kern County, Carpinteria State Beach, the Upper Ojai Valley, Wiley Canyon, Modelo Canyon, and the La Brea Tar Pits. The reported locations of active natural seeps were visited in June and July of 2022. In some areas, natural seepage of oil was present across a wide area. To evaluate where and if natural gas was surfacing, I screened the area immediately overlying oil or water seepage for possible evidence of alteration (i.e., within 6 inches of the surface) using a Bascom-Turner Gas Explorer Detector, which utilizes dual catalytic methane sensors to provide measurements of combustible gases with 20 ppmv resolution, and an electrochemical sensor to provide H_2S measurements with 1 ppmv resolution. In some areas (e.g., Carpinteria State Beach), natural gas seepage was not identified during the field visit, despite previous reports. In one area (Sulphur Mountain, Upper Ojai Valley), natural gas seepage was identified that contained substantial H_2S (e.g., >1% by volume). Because the presence of H_2S can corrode the seal of the IsoBags™ utilized for sample collection and complicate molecular analysis, this seep was not sampled for this project.

Eighteen natural gas seep samples were collected (data to be published elsewhere), including: three within the northern Eel River Basin (Salmon Creek, Yager Creek, and Felt Springs), one in the vicinity of the San Ardo Oilfield (Los Lobos Spring), two in the vicinity of the McKittrick Oilfield (McKittrick seeps 1 and 2), three within the Upper Ojai Valley (Santa Paula Creek, Hemp Fee Battery, and Arco Pad 22), two within Modelo Canyon (Modelo seeps 1 and 2), two within Wiley Canyon (Wiley seeps 1 and 2), and five within or proximate to the La Brea Tarpits (Pit 91, Pit 3,4,61-7, La Brea pond, and the corner of Wilshire & Curson). Out of the

18 individual sampling locations, 12 seeps produced both oil and gas, and water was observed in association with hydrocarbon seepage at six locations.

Natural gas was concentrated prior to sampling using a sampling shield constructed from a stainless steel bowl, which could be placed directly above the seepage location. Bowls of various sizes were utilized depending on the size and nature of surface seepage expression. Each bowl was outfitted with a port on its apex, through which ¼-inch polyethylene tubing was threaded. Gas was allowed to naturally purge via this port while natural gas accumulated within the bowl. The concentration of combustible gases purging through the tubing was checked at regular intervals using the Bascom Turner Gas Explorer Detector. When combustible gas concentrations were sufficiently high (e.g. greater than 1% v/v), a hand squeeze bulb was used to fill a pre-evacuated IsoBag™ from Isotech Laboratories (Isotech) with approximately 300 cm^3 of gas. At select locations with lower relative gas production rates, IsoBags™ were filled at lower accumulated combustible gas concentrations (e.g., greater than 500 parts per million by volume (ppmv)). At a single seepage location (Los Lobos Spring), a dissolved gas sample was collected in an IsoFlask™ per the methods described in Molofsky et al. (2016). In addition to samples of natural gas seepage, a single sample of dissolved reservoir gas was collected using an IsoFlask™ container from a tank containing a mixture of produced water from multiple oil wells in San Ardo field.

Gas samples were analyzed for C1-C6+ hydrocarbons and non-hydrocarbon gases (CO_2, Ar, O_2, N_2) by Isotech Laboratories (Isotech), in Champaign, Illinois on a Shimadzu 2010 Gas Chromatograph (GC) equipped with both a thermal conductivity detector (TCD) and flame ionization detector (FID). Reported analytical errors of external standards are as follows: C1-C4: ±5%, C6-C6+: ±10%, N_2, CO_2, O_2, Ar: ±10%. For samples where gas concentrations were sufficient, samples were analyzed for $\delta^{13}C$ and $\delta^{2}H$ analysis of C1, and $\delta^{13}C$ of C2, C3, and CO_2 via dual-inlet isotope ratio mass spectrometer (DI-IRMS) using a Finnigan MAT Delta S Isotope

Ratio Mass Spectrometer (δ^{13}C of C1, C2, C3, and CO_2) and a Finnigan Delta Plus XL isotope ratio mass spectrometer (δ^{2}H of C1). Two-sigma errors for δ^{13}C and δ^{2}H measurements of gases are ±0.2‰ and ±7‰. For select samples where concentrations of C1, C2, C3 or CO2 were insufficient for isotopic analysis by DI-IRMS, samples were analyzed using gas chromatograph combustion isotope ratio mass spectrometry (GC-C-IRMS) at Isotech for δ^{13}C and δ^{2}H with 2-sigma errors of ±0.6‰ and ±10‰, respectively.

All natural seepage samples exhibited some degree of atmospheric contamination, i.e., the presence of non-hydrocarbon gases such as nitrogen, oxygen, and argon in concentrations and proportions consistent with an atmospheric origin. The presence of atmospheric gases is an artifact of the sample collection method, caused when atmospheric gases are present within the sampling shield prior to sampling. The contribution of atmospheric gases was estimated and corrected for based on the known abundances of nitrogen, oxygen, argon, and carbon dioxide in the atmosphere.

For the six seeps where water was present in association with natural hydrocarbon seepage, water samples were collected using a peristaltic pump. Field parameters (temperature, pH, specific conductance, dissolved oxygen (DO), oxidation-reduction potential (ORP), sample appearance) were recorded prior to sample collection using a YSI multiparameter unit, and water samples were collected in appropriate bottles with preservatives supplied by the laboratories. For all but the Los Lobos Spring seep (see following paragraph), samples were analyzed for major anions and cations at the University of Texas (UT) at El Paso by Inductively Coupled-Plasma-Optical Emissions Spectrometry (Horiba Ultima Expert) and ion chromatography (Dionex ICS 2100), with errors of external standards of generally <10%. Water isotope analysis (δ^{18}O and δ^{2}H) was also performed at the UT El Paso by cavity ring-down spectrometry (CRDS) using a Los Gatos Research (LGR) Liquid Water Isotope Analyzer with reported 2-sigma errors of ±0.04‰ and ±0.30‰ for δ^{18}O and δ^{2}H, respectively. δ^{13}C of dissolved inorganic carbon (DIC) was performed at Isotech by continuous flow-isotope ratio mass spectrometry (CF-IRMS) on a Gas Bench II connected to a Thermo-Delta V+ IRMS, with a two-sima error of ±0.40‰. In addition, samples were analyzed for total petroleum hydrocarbons (TPH) gasoline range organics (GRO), diesel range organics (DRO), and motor oil range organics (MRO) by EPA Method 8015M/D, benzene, toluene, ethylbenzene, and xylenes (BTEX) by EPA Method 8260B, and ammonia by SM 4500 at Hall Environmental Analysis Laboratory (Albuquerque, New Mexico). Reported two-sima errors were: TPH-GRO: ±0.098 mg/L, TPH-DRO: ±0.252 mg/L, benzene: ±0.152 ug/L, toluene: ±0.084 ug/L, ethylbenzene: ±0.198 ug/L, total xylenes: ±0.097 ug/L, and ammonia: ± 0.035 mg/L.

The sixth water seepage sample from Los Lobos Spring, and a single sample of produced water from the San Ardo oilfield, were analyzed for a virtually identical analytical suite to the other water seepage samples at: Oilfield Environmental and Compliance in Santa Monica, California (inorganic and organic water chemistry), and Isotech (water isotope). Analytical errors are similar to those reported for UT El Paso and Hall Environmental Analysis Laboratory. Select water samples were also collected for noble gas analysis per the procedure described in Cey et al. (2008) and Rademacher et al. (2001), and analyzed at Lawrence Livermore National Laboratory per the methods detailed in Visser et al. (2013). At least one duplicate sample was collected and analyzed for every ten samples.

Available data on the molecular and isotopic composition of natural gas seepage was compiled from the scientific literature for seeps within and near the La Brea tar pits and Los Angeles area (Etiope et al., 2017; Jeffrey et al., 1991; Weber et al., 2017), the Upper Ojai Valley (Duffy et al., 2007; Weed et al., 2020), and the Eel River Basin (Lorenson et al., 1998). That data is provided in Table 4.3. Available molecular and isotopic data on reservoir gases in the literature was also compiled for the Salt Lake oil field in the Los Angeles Basin (Jeffrey et al., 1991), the Tompkins Hill gas field in the northern Eel River Basin, the Petrolia oil field in the southern Eel

River Basin (Lorenson et al., 1998), and the North Sulphur Mountain and Silverthread oil fields in the Upper Ojai Valley (Duffy et al., 2007). In addition, molecular analysis of reservoir gases from the Oat Mountain oil field, approximately 1.5 miles southwest of the Wiley Canyon oil field, was provided by Termo Company. These reservoir gas data are also provided in Table 4.3.

CONCLUSIONS

In this study, I present the framework implemented for the collection and evaluation of compositional and isotopic data for gases (and water, if present) from natural gas seeps throughout California. This approach lays the groundwork for the characterization of naturally seeping gases from a variety of geologic and geographic settings, by which common differences between natural gas seepage at the surface and anthropogenic releases of reservoir gases may be identified. In the development of this approach, I identified tracers that have high potential for revealing post-genetic changes indicative of natural seepage, and also are readily accessible to operators, regulators and the public (i.e., can be implemented anywhere in the world at commercial laboratories). This strategy focused on California, where there are many oil and gas fields and which exhibits one of the highest densities of natural hydrocarbon seeps in the world (Ciotoli et al., 2020). However, this approach would likely also be applicable to other hydrocarbon bearing sedimentary basins in similar geologic settings (i.e., convergent basins and/or regions with brittle tectonic structures). Such areas include Western Russia, Caucasus and Eastern Europe, China, and the Arabian Peninsula (Ciotoli et al., 2020). With new financial incentives for carbon sequestration in the United States and elsewhere, this framework may also prove important for monitoring for leakage of mixed CO_2 and hydrocarbon gases from geologic carbon sequestration reservoirs, which are commonly located in depleted oil and gas reservoirs. Finally, the methods and tracers presented herein hold promise for improving the attribution of atmospheric methane to geogenic versus anthropogenic sources, which is important for understanding and predicting the radiative forcing of the atmosphere (Allen, 2016; Etiope et al., 2019).

Table 4.3: Data from the literature: molecular and isotopic composition of natural gas seepage and local reservoir gases.

Data Source	Study Area	Sample Description	Sample Date	He (%)	H_2 (%)	Ar (%)	O_2 (%)	CO_2 (%)	N_2 (%)	C1 (%)	C2 (%)	C3 (%)	iC4 (%)	nC4 (%)	iC5 (%)	nC5 (%)	C6+ (%)
Natural Seeps																	
Etiope et al. 2017	La Brea	Circular sidewalk degassing soil (no. 160)	May 2017	--	--	--	--	11.4	--	68.5	0.1	0.02	0.013	0.002	Nd	Nd	
		*Circular sidewalk degassing soil (no. 160)	May 2017	--	--	--	--	--	--	0.6377	0.0051	0.00006	0.00012	<0.00001	0.00011	<0.0000001	
		Bubbling Oil Seep (no. 8)	May 2017	--	--	--	--	12.2	--	75	0.4	0.1	0.017	0.001	0.004	0.002	
		Wilshire-Curson corner	May 2017	--	--	--	--	13.5	--	78	1.3	0.5	0.02	0.03	0.008	0.006	
		Wilshire-Curson corner	May 2017	--	--	--	--	--	--	8.93	0.112	0.096	0.016	0.022	0.007	0.002	
		La Brea average oil seep by Weber et al. (2017)	May 2017	--	--	--	--	--	--	19.63	0.153	0.067	0.021	0.002	0.001	<0.001	
Jeffrey et al. 1991	La Brea and Fairfax District	L.A.C. Well, Ogden & 3rd (Sample No. 1057)	1985 - 1987	--	--	0.146	1.13	2.12	10.5	82.6	0.734	0.238	0.034	0.035	0.073	0.038	--
		L.A.C. Well, Ogden & 3rd (Sample No. 1058)	1985 - 1987	Nd	--	0.034	0.324	6.18	2.27	87.1	0.998	0.373	0.05	0.059	0.108	0.06	--
		L.A.C. Well, Ogden & 3rd (Sample No. 1059)	1985 - 1987	0.002	--	--	--	6.26	2.04	91	0.99	0.383	0.046	0.055	0.113	0.062	--
		Fairfax District (Sample No. 1053)	1985 - 1987	Nd	--	0.172	2.88	1.36	8.80	82.5	1.09	0.381	0.048	0.073	0.163	0.08	--
		Fairfax District (Sample No. 1054)	1985 - 1987	0.003	--	0.845	16.3	0.389	68.0	10.6	0.794	0.257	0.019	0.04	0.006	0.004	--
		Fairfax District (Sample No. 1055)	1985 - 1987	Nd	--	0.841	16.4	1.78	62.0	14.3	0.158	0.034	0.004	0.004	0.01	0.009	--
		Fairfax District (Sample No. 1056)	1985 - 1987	Nd	--	0.145	2.33	8.93	6.33	78.1	0.992	0.371	0.043	0.053	0.09	0.05	--
		Lake Pit, Rancho La Brea (Sample No. 1060)	1985 - 1987	Nd	--	0.159	2.67	13.0	12.9	66.7	0.604	0.149	0.019	0.002	0.003		--
		Lake Pit, Rancho La Brea (Sample No. 1061)	1985 - 1987	Nd	--	0.029	0.405	14.5	1.28	82.7	0.675	0.163	0.021				--
*Lorenson et al. 1998	Eel River Basin	Salmon Creek gas seep	8/27/1997	--	--	--	--	0.13	--	96.03	2.64	0.041	0.004301	0.002676	0.000461	0.000142	0.000054
		False Cape outcrop	8/14/1997	--	--	--	--	0.03	--	0.00514	0.000199	0.000174	0.000042	0.000108	0.000046	0.000053	0.000469
		Helen Branstedter Bridge	8/13/1997	--	--	--	--	0.13	--	91.2	3.56	1.48	0.347	0.428	0.136	0.085	0.0554
		Mattole River Gas seep	8/13/1997	--	--	--	--	0.05	--	58	0.009	0.000908	0.000052	0	0.000011	0	0.000005
Duffy et al. 2007	Upper Ojai Valley	Seep I	9/4/2003	--	--	--	--	74.1	--	25.8	0.07	0.02	--	<0.01	--	--	--
		Seep I	3/8/2004	--	--	--	--	78.1	--	21.2	0.08	Nd	--	<0.01	--	--	--
		Seep I	3/16/2004	--	--	--	--	78.6	--	21.4	0.07	Nd	--	<0.01	--	--	--
		Seep I	4/9/2004	--	--	--	--	77.2	--	22.8	0.04	Nd	--	<0.01	--	--	--
		Seep II	9/4/2003	--	--	--	--	74.4	--	25.5	0.07	0.04	--	<0.01	--	--	--
		Seep II	9/4/2003	--	--	--	--	74.4	--	25.5	0.07	0.04	--	<0.01	--	--	--
		Seep II	3/8/2004	--	--	--	--	76.7	--	22.4	0.09	0.06	--	<0.01	--	--	--
		Seep II	3/16/2004	--	--	--	--	75.7	--	24.2	0.08	0.05	--	<0.01	--	--	--
		Seep II	3/16/2004	--	--	--	--	75.5	--	24.3	0.09	0.06	--	<0.01	--	--	--
		Seep II	4/9/2004	--	--	--	--	74.5	--	25.4	0.06	0.03	--	<0.01	--	--	--
		Seep III	9/4/2003	--	--	--	--	25.7	--	73.9	0.39	0.05	--	<0.01	--	--	--
		Seep III	3/8/2004	--	--	--	--	27.8	--	71.6	0.42	0.19	--	<0.01	--	--	--
		Seep III	3/16/2004	--	--	--	--	28.7	--	70.9	0.36	0.07	--	<0.01	--	--	--
		Seep III	3/16/2004	--	--	--	--	28.6	--	71	0.34	0.08	--	<0.01	--	--	--
		Seep III	4/9/2004	--	--	--	--	26.6	--	73	0.39	0.03	--	<0.01	--	--	--
		Seep IV	4/9/2004	--	--	--	--	27.2	--	72.5	0.28	0.07	--	<0.01	--	--	--

Notes:

1) *Data from Lorenson et al. 1998 and select data from Etiope et al. 2017 were reported as ppmv and converted to % volume
2) ** = Data from Weed et al. 2020 were reported as flux magnitudes by mass (ug/hour), and converted to % volume/hour
3) Not all data reported in the literature were corrected for atmospheric contamination
4) < = Compound not detected above specified detection limit
5) Nd = Not detected; detection limit not provided
6) -- = Data not available
7) Data for Oat Mountain reservoir gas provided by The Termo Co. (Long Beach, CA)

Table 4.3: Continued.

Data Source	Study Area	Sample Description	Sample Date	He (%)	H_2 (%)	Ar (%)	O_2 (%)	CO_2 (%)	N_2 (%)	C1 (%)	C2 (%)	C3 (%)	iC4 (%)	nC4 (%)	iC5 (%)	nC5 (%)	C6+ (%)
**Weed et al. 2020	McKittrick, Carpinteria, Upper Ojai Valley	McKittrick 1	May/June 2019	--	--	--	--	--	--	3.68E-05	8.98E-09	8.39E-09	8.95E-10	1.63E-09	1.80E-09	2.63E-09	--
		McKittrick 3	May/June 2019	--	--	--	--	--	--	6.61E-07	5.99E-08	6.58E-08	1.05E-08	1.14E-08	1.22E-08	1.80E-08	--
		McKittrick 4	May/June 2019	--	--	--	--	--	--	2.24E-05	3.06E-08	8.39E-08	1.51E-08	1.22E-08	1.22E-08	1.52E-08	--
		McKittrick 5	May/June 2019	--	--	--	--	--	--	5.11E-04	6.65E-07	4.31E-08	5.33E-09	3.10E-09	2.36E-09	3.88E-09	--
		Carpinteria 11	May/June 2019	--	--	--	--	--	--	5.24E-02	2.13E-04	2.36E-06	3.61E-07	1.86E-08	4.57E-09	4.85E-09	--
		Carpinteria 20	May/June 2019	--	--	--	--	--	--	2.06E-04	7.32E-08	1.56E-07	2.58E-07	1.89E-08	5.13E-07	1.04E-08	--
		Carpinteria 21	May/June 2019	--	--	--	--	--	--	1.43E-03	1.03E-07	1.59E-07	2.75E-07	9.12E-09	3.33E-07	5.41E-09	--
		Carpinteria 22	May/June 2019	--	--	--	--	--	--	4.68E-04	7.98E-08	1.47E-07	2.41E-07	1.19E-08	3.74E-07	6.10E-09	--
		Carpinteria 23	May/June 2019	--	--	--	--	--	--	6.86E-04	1.03E-07	2.13E-07	3.96E-07	1.91E-08	6.10E-07	9.29E-09	--
		Ojai 13	May/June 2019	--	--	--	--	--	--	2.06E-04	3.72E-08	3.40E-08	7.23E-09	1.72E-08	9.42E-09	1.48E-08	--
		Ojai 14	May/June 2019	--	--	--	--	--	--	9.98E-06	4.66E-08	4.08E-08	7.91E-09	2.24E-08	5.96E-09	4.02E-08	--
		Ojai 15	May/June 2019	--	--	--	--	--	--	1.81E-05	1.16E-08	1.52E-08	1.77E-09	6.02E-09	1.80E-09	1.37E-09	--
		Ojai 17	May/June 2019	--	--	--	--	--	--	2.37E-04	4.99E-08	1.13E-08	8.95E-11	9.81E-09	2.08E-09	4.16E-09	--
		Ojai 18	May/June 2019	--	--	--	--	--	--	5.67E-05	6.32E-08	4.99E-08	1.02E-08	1.63E-08	7.90E-09	1.30E-08	--
		Ojai 19	May/June 2019	--	--	--	--	--	--	6.86E-06	2.86E-08	2.24E-08	4.65E-10	2.06E-08	2.08E-09	4.30E-09	--
Local Reservoir Gas(es)																	
Jeffrey et al. 1991	La Brea and Fairfax District	Salt Lake oil field, Puente Formation (Sample No. 1093)	1985 - 1987	Nd	--	--	0.154	0.269	0.575	80.5	1.59	0.6	0.23	0.38	0.17	0.07	--
Duffy et al. 2007	Upper Ojai Valley	North Sulphur Mountain Oil Field	4/15/2005	--	--	--	--	23.3	--	69.3	3.5	2.4	--	1.5	--	--	--
		North Sulphur Mountain Oil Field	11/15/2005	--	--	--	--	22.7	--	69.3	3.9	3	--	1.1	--	--	--
		Silverthread Oil Field	11/15/2005	--	--	--	--	20.8	--	69.5	5.3	3.3	--	1.2	--	--	--
Termo Co. 2022	Wiley Canyon (Oat Mountain)	Oat Mountain DA 1-1	3/29/2016	--	0.004	--	0.094	0.069	0.512	91.369	4.160	1.803	0.324	0.469	0.172	0.12	0.902
		Oat Mountain 1-2	3/29/2016	--	0.007	--	0.109	0.042	0.477	87.364	5.502	2.916	0.590	0.886	0.328	0.226	1.553
		Oat Mountain DA 1-3	3/29/2016	--	0.002	--	0.102	0.075	0.492	91.909	3.978	1.653	0.308	0.444	0.165	0.114	0.758
		Oat Mountain 1-4		--	0.016	--	0.099	0.074	0.762	93.956	3.202	1.110	0.165	0.218	0.064	0.044	0.290
Lorenson et al. 1998	North Eel River Basin	Tompkins Hill Discovery Well (Tompkins Hill Gas Field)	8/22/1997	--	--	--	--	0.09	--	98.28	1.07	0.413	0.064	0.089	0.0197	0.0112	0.009345
	South Eel River Basin	Hidden Valley no.1, API no. 023-20027 (Petrolia # 1)	8/15/1997	--	--	--	--	0.78	--	88.27	4.16	2.34	0.475	0.761	0.237	0.178	0.0938
		Shelby Woods no.1, API no. 023-00097 (Petrolia # 2)	8/15/1997	--	--	--	--	0.17	--	84.82	4.07	3.2	0.82	1.58	0.0679	0.0573	0.0504
		Whitchurch no.1A, API no. 023-20065 (Petrolia #3)	8/15/1997	--	--	--	--	0.72	--	79.03	6.92	4.34	0.706	0.984	0.0258	0.0198	0.0322
		Otto Clark Matthews no.1 Petrolia	8/16/1997	--	--	--	--	0.02	--	92.2	2.94	2.35	0.538	0.8572	0.32	0.215	0.14

Notes:

1) *Data from Lorenson et al. 1998 and select data from Etiope et al. 2017 were reported as ppmv and converted to % volume
2) ** = Data from Weed et al. 2020 were reported as flux magnitudes by mass (ug/hour), and converted to % volume/hour
3) Not all data reported in the literature were corrected for atmospheric contamination
4) < = Compound not detected above specified detection limit
5) Nd = Not detected; detection limit not provided
6) -- = Data not available
7) Data for Oat Mountain reservoir gas provided by The Termo Co. (Long Beach, CA)

Table 4.3: Continued.

Data Source	Study Area	Sample Description	Sample Date	δ^{13}C-CO$_2$ (‰)	δ^{13}C-C1 (‰)	δ^{2}H-C1 (‰)	δ^{13}C-C2 (‰)	δ^{13}C-C3 (‰)	δ^{13}C-iC4 (‰)	δ^{13}C-nC4 (‰)	δ^{13}C-iC5 (‰)	δ^{13}C-nC5 (‰)
Natural Seeps												
Etiope et al. 2017	La Brea	Circular sidewalk degassing soil (no. 160)	May 2017	--	--	--	--	--	--	--	--	--
		*Circular sidewalk degassing soil (no. 160)	May 2017	--	--	--	--	--	--	--	--	--
		Bubbling Oil Seep (no 8)	May 2017	--	--	--	--	--	--	--	--	--
		Wilshire-Curson corner	May 2017	--	--	--	--	--	--	--	--	--
		Wilshire-Curson corner	May 2017	--	--	--	--	--	--	--	--	--
		La Brea average oil seep by Weber et al. (2017)	May 2017	--	-38.9	--	--	--	--	--	--	--
Jeffrey et al. 1991	La Brea and Fairfax District	L.A.C. Well, Ogden & 3rd (Sample No. 1057)	1985 - 1987	-13.5	-44.1	-199	-29.6	-23.6	--	--	--	--
		L.A.C. Well, Ogden & 3rd (Sample No. 1058)	1985 - 1987	3	-43.1	-189	-29.7	-23.7	--	--	--	--
		L.A.C. Well, Ogden & 3rd (Sample No. 1059)	1985 - 1987	3.1	-43.3	-196	-29.6	-23.5	--	--	--	--
		Fairfax District (Sample No. 1053)	1985 - 1987	-22.9	-41.9	-189	-29.9	-24.1	--	--	--	--
		Fairfax District (Sample No. 1054)	1985 - 1987	-3.9	-44.4	-186	-30.3	-26.1	--	--	--	--
		Fairfax District (Sample No. 1055)	1985 - 1987	20.2	-42.4	-191	-29.7	--	--	--	--	--
		Fairfax District (Sample No. 1056)	1985 - 1987	-11.3	-42	-189	-30	-22.7	--	--	--	--
		Lake Pit, Rancho La Brea (Sample No. 1060)	1985 - 1987	25.9	-42.4	-178	-29.1	-19.6	--	--	--	--
		Lake Pit, Rancho La Brea (Sample No. 1061)	1985 - 1987	25.4	-42.4	-183	-29.3	-19	--	--	--	--
*Lorenson et al. 1998	Eel River Basin	Salmon Creek gas seep	8/27/1997	Nd	-31.0	-137.0			--	--	--	--
		False Cape outcrop	8/14/1997	Nd	Nd	Nd			--	--	--	--
		Helen Branstedter Bridge	8/13/1997	Nd	-38.4	-153.0			--	--	--	--
		Mattole River Gas seep	8/13/1997	Nd	Nd	Nd			--	--	--	--
Duffy et al. 2007	Upper Ojai Valley	Seep I	9/4/2003	23.9	-45.9	--	-26.9	-2.4	--	--	--	--
		Seep I	3/8/2004	--	--	--	--	--	--	--	--	--
		Seep I	3/16/2004	--	--	--	--	--	--	--	--	--
		Seep I	4/9/2004	23	-46	--	--	--	--	--	--	--
		Seep II	9/4/2003	16.1	-44.1	--	-28.2	-12	-9.7	-12.5	-20.0	-13.9
		Seep II	9/4/2003	--	--	--	--	--	--	--	--	--
		Seep II	3/8/2004	--	--	--	--	--	--	--	--	--
		Seep II	3/16/2004	--	--	--	--	--	--	--	--	--
		Seep II	3/16/2004	--	--	--	--	--	--	--	--	--
		Seep II	4/9/2004	15.4	-47.4	--	--	--	--	--	--	--
		Seep III	9/4/2003	27.2	-41.3	--	-28.1	-5.4	-21.8	-19.5	--	--
		Seep III	3/8/2004	--	--	--	--	--	--	--	--	--
		Seep III	3/16/2004	--	--	--	--	--	--	--	--	--
		Seep III	3/16/2004	--	--	--	--	--	--	--	--	--
		Seep III	4/9/2004	26.6	-41.5	--	--	--	--	--	--	--
		Seep IV	4/9/2004	25.4	-41.7	--	--	--	--	--	--	--

Notes:

1) *Data from Lorenson et al. 1998 and select data from Etiope et al. 2017 were reported as ppmv and converted to % volume
2) ** = Data from Weed et al. 2020 were reported as flux magnitudes by mass (ug/hour), and converted to % volume/hour
3) Not all data reported in the literature were corrected for atmospheric contamination
4) < = Compound not detected above specified detection limit
5) Nd = Not detected; detection limit not provided
6) -- = Data not available
7) Data for Oat Mountain reservoir gas provided by The Termo Co. (Long Beach, CA)

Table 4.3: Continued.

Data Source	Study Area	Sample Description	Sample Date	δ^{13}C-CO$_2$ (‰)	δ^{13}C-C1 (‰)	δ^{2}H-C1 (‰)	δ^{13}C-C2 (‰)	δ^{13}C-C3 (‰)	δ^{13}C-iC4 (‰)	δ^{13}C-nC4 (‰)	δ^{13}C-iC5 (‰)	δ^{13}C-nC5 (‰)
**Weed et al. 2020	McKittrick, Carpinteria, Upper Ojai Valley	McKittrick 1	May/June 2019	--	--	--	--	--	--	--	--	--
		McKittrick 3	May/June 2019	--	--	--	--	--	--	--	--	--
		McKittrick 4	May/June 2019	--	--	--	--	--	--	--	--	--
		McKittrick 5	May/June 2019	--	--	--	--	--	--	--	--	--
		Carpinteria 11	May/June 2019	--	--	--	--	--	--	--	--	--
		Carpinteria 20	May/June 2019	--	--	--	--	--	--	--	--	--
		Carpinteria 21	May/June 2019	--	--	--	--	--	--	--	--	--
		Carpinteria 22	May/June 2019	--	--	--	--	--	--	--	--	--
		Carpinteria 23	May/June 2019	--	--	--	--	--	--	--	--	--
		Ojai 13	May/June 2019	--	--	--	--	--	--	--	--	--
		Ojai 14	May/June 2019	--	--	--	--	--	--	--	--	--
		Ojai 15	May/June 2019	--	--	--	--	--	--	--	--	--
		Ojai 17	May/June 2019	--	--	--	--	--	--	--	--	--
		Ojai 18	May/June 2019	--	--	--	--	--	--	--	--	--
		Ojai 19	May/June 2019	--	--	--	--	--	--	--	--	--
Local Reservoir Gas(es)												
Jeffrey et al. 1991	La Brea and Fairfax District	Salt Lake oil field, Puente Formation (Sample No. 1093)	1985 - 1987	15.6	-42.5	-181	-29.4	-21.1	--	--	--	--
Duffy et al. 2007	Upper Ojai Valley	North Sulphur Mountain Oil Field	4/15/2005	10.3	-46.7	--	-29.6	-27.8	--	-26.3	--	--
		North Sulphur Mountain Oil Field	11/15/2005	10.6	-47.9	--	-30.1	-27.9	-23.6	-25.7	-20.7	-26.9
		Silverthread Oil Field	11/15/2005	8.8	-45.6	--	-29.2	-27.2	-26.2	-25.0	-23.8	-26.5
Termo Co. 2022	Wiley Canyon (Oat Mountain)	Oat Mountain DA 1-1	3/29/2016	--	--	--	--	--	--	--	--	--
		Oat Mountain 1-2	3/29/2016	--	--	--	--	--	--	--	--	--
		Oat Mountain DA 1-3	3/29/2016	--	--	--	--	--	--	--	--	--
		Oat Mountain 1-4		--	--	--	--	--	--	--	--	--
Lorenson et al. 1998	North Eel River Basin	Tompkins Hill Discovery Well (Tompkins Hill Gas Field)	8/22/1997	Nd	-33.5	-149.0	--	--	--	--	--	--
	South Eel River Basin	Hidden Valley no.1, API no. 023-20027 (Petrolia # 1)	8/15/1997	Nd	-36.4	-151.0	--	--	--	--	--	--
		Shelby Woods no.1, API no. 023-00097 (Petrolia # 2)	8/15/1997	Nd	-34.0	-158.0	--	--	--	--	--	--
		Whitchurch no.1A, API no. 023-20065 (Petrolia #3)	8/15/1997	Nd	-42.0	-149.0	--	--	--	--	--	--
		Otto Clark Matthews no.1 Petrolia	8/16/1997	Nd	-53.6	-180.0	--	--	--	--	--	--

Notes:

1) *Data from Lorenson et al. 1998 and select data from Etiope et al. 2017 were reported as ppmv and converted to % volume
2) ** = Data from Weed et al. 2020 were reported as flux magnitudes by mass (ug/hour), and converted to % volume/hour
3) Not all data reported in the literature were corrected for atmospheric contamination
4) < = Compound not detected above specified detection limit
5) Nd = Not detected; detection limit not provided
6) -- = Data not available
7) Data for Oat Mountain reservoir gas provided by The Termo Co. (Long Beach, CA)

REFERENCES

Abrams, M.A., 2020. Marine seepage variability and its impact on evaluating the surface migrated hydrocarbon seep signal. Mar. Pet. Geol. 121, 104600. https://doi.org/10.1016/j.marpetgeo.2020.104600

Abrams, M.A., 2017. Evaluation of near-surface gases in marine sediments to assess subsurface petroleum gas generation and entrapment. Geosci. 7. https://doi.org/10.3390/geosciences7020035

Abrams, M.A., 2005. Significance of hydrocarbon seepage relative to petroleum generation and entrapment. Mar. Pet. Geol. 22, 457–477. https://doi.org/10.1016/j.marpetgeo.2004.08.003

Abrams, M.A., 1996. Distribution of subsurface hydrocarbon seepage in near-surface marine sediments, in: Schumacher, D., Abrams, M.A. (Eds.), Hydrocarbon Migration and Its Near-Surface Expression: AAPG Memoir 66. pp. 1–14.

Abrams, M.A., Dahdah, N.F., 2010. Surface sediment gases as indicators of subsurface hydrocarbons - examining the record in laboratory and field studies. Mar. Pet. Geol. 27, 273–284. https://doi.org/10.1016/j.marpetgeo.2009.08.005

Allen, D., 2016. Attributing Atmospheric Methane to Anthropogenic Emission Sources. Acc. Chem. Res. 49, 1344–1350.

Asadzadeh, S., de Souza Filho, C.R., 2017. Spectral remote sensing for onshore seepage characterization: A critical overview. Earth-Science Rev. 168, 48–72. https://doi.org/10.1016/j.earscirev.2017.03.004

Behl, R.J., 2012. The Monterey Formation of California: New Research Directions. AAPG Annu. Conv. Exhib. 10435, 1–42.

Behl, R.J., 1999. Since Bramlette (1946): The Miocene Monterey Formation of California revisited." Classic Cordilleran Concepts: A View from California. Geol. Soc. Am. Spec. Pap. 338 301–313.

Bernard, B., Brooks, J.M., Sackett, W.M., 1977. A geochemical model for characterization of hydrocarbon gas sources in marine sediments, in: Proceedings of the Annual Offshore Technology Conference, Houston, Texas, May 1977. https://doi.org/10.4043/2934-ms

Bernard, B.B., Brooks, J.M., Zumberge, J., 2001. Determining the Origin of Gases in Near-Surface Sediments, in: AAPG Hedberg Conference "Near-Surface Hydrocarbon Migration: Mechanisms and Seepage Rates" September 16-19, 2001, Vancouver, BC, Canada. pp. 1–4.

Bhatnagar, N., Kamath, G., Chelst, I., Potoff, J.J., 2011. Direct calculation of 1-octanol–water partition coefficients from adaptive biasing force molecular dynamics simulations. J. Chem. Phys. 137, 014502. https://doi.org/https://doi.org/10.1063/1.4730040

Bird, R.B., Stewart, W.E., Lightfoot, E.N., 2006. Transport Phenomena, Revised 2nd Edition. John Wiley Sons, Inc.

Bjoroy, M., Ferriday, I., 2001. Surface geochemistry as an exploration tool: A comparison of results using different analytical techniques. Near-Surface Hydrocarb. Migr. Mech. Seepage Rates.

Boles, J.R., Garven, G., Camacho, H., Lupton, J.E., 2015. Mantle helium along the Newport-Inglewood fault zone, Los Angeles Basin, California: A leaking paleo-subduction zone. Geochem. Geophys. Geosyst. 16, 2364–2381.

California Department of Conservation, 2020. 2019 Annual Report of the State Oil and Gas Supervisor. Sacramento.

Cey, B.D., Hudson, G.B., Moran, J.E., Scanlon, B.R., 2008. Impact of Artificial Recharge on Dissolved Noble Gases in Groundwater in California. Environ. Sci. Technol. 42, 1017–

1023.

Chung, H.M., Gormly, J.R., Squires, R.M., 1988. Origin of gaseous hydrocarbons in subsurface environments: Theoretical considerations of carbon isotope distribution. Chem. Geol. 71, 97–104. https://doi.org/10.1016/0009-2541(88)90108-8

Ciotoli, G., Procesi, M., Etiope, G., Fracassi, U., Ventura, G., 2020. Influence of tectonics on global scale distribution of geological methane emissions. Nat. Commun. 11, 1–8. https://doi.org/10.1038/s41467-020-16229-1

Coleman, D., 1995. Advances in the Use of Geochemical Fingerprinting for Gas Identification. Soc. Pet. Eng. Contin. Educ. Semin. "Engineering Appl. Michigan," Mt. Pleasant, MI, April 11-12, 1995.

Deville, E., Battani, A., Griboulard, R., Guerlais, S., Lallemant, S., Mascle, A., Prizhofer, A., Schmitz, J., Statement, G., Setting, S., 2003. Processes of Mud Volcanism in the Barbados-Trinidad Compressional System : New structural , Thermal and Geochemical Data. AAPG Search and Discovery Article #30017.

Duffy, M., Kinnaman, F.S., Valentine, D.L., Keller, E.A., Clark, J.F., 2007. Gaseous emission rates from natural petroleum seeps in the Upper Ojai Valley, California. Environ. Geosci. 14, 197–207. https://doi.org/10.1306/eg.07110707010

Eldridge, G.H., Arnold, R., 1907. The Santa Clara Valley, Puente Hills and Los Angeles Oil Districts, Southern California.

Etiope, G., 2015. Natural Gas Seepage: The Earth's Hydrocarbon Degassing. Springer International Publishing, Switzerland.

Etiope, G., 2009. Natural emissions of methane from geological seepage in Europe. Atmos. Environ. 43, 1430–1443. https://doi.org/10.1016/j.atmosenv.2008.03.014

Etiope, G., Caracausi, A., Favara, R., Italiano, F., Baciu, C., 2004. New Directions: GEM—Geologic Emissions of Methane, the missing source in the atmospheric methane budget. Atmos. Environ. 38, 3099–3100. https://doi.org/10.1029/2002gl016287

Etiope, G., Ciccioli, P., 2009. Earth's degassing: A missing ethane and propane source. Science (80-.). 323, 478. https://doi.org/10.1126/science.1165904

Etiope, G., Ciotoli, G., Schwietzke, S., Schoell, M., 2019. Gridded maps of geological methane emissions and their isotopic signature. Earth Syst. Sci. Data 11, 1–22.

Etiope, G., Doezema, L.A., Pacheco, C., 2017. Emission of Methane and Heavier Alkanes From the La Brea Tar Pits Seepage Area, Los Angeles. J. Geophys. Res. Atmos. 122, 12,008-12,019. https://doi.org/10.1002/2017JD027675

Etiope, G., Feyzullayev, A., Milkov, A. V., Waseda, A., Mizobe, K., Sun, C.H., 2009. Evidence of subsurface anaerobic biodegradation of hydrocarbons and potential secondary methanogenesis in terrestrial mud volcanoes. Mar. Pet. Geol. 26, 1692–1703. https://doi.org/10.1016/j.marpetgeo.2008.12.002

Farrell, P., Culling, D., Leifer, I., 2013. Transcontinental methane measurements: Part 1. A mobile surface platform for source investigations. Atmos. Environ. 74, 422–431. https://doi.org/10.1016/j.atmosenv.2013.02.014

Feinstein, L., Gautier, D., Heberger, M., Philips, S., Ulrich, C., Brandt, A., Foxall, W., 2015. Case study of the potential development of source rock in the Monterey Formation, in: Technology, C.C. on S. and (Ed.), An Independent Scientific Assessment of Well Stimulation in California, Volume III. pp. 112–198.

Franks, S.G., Dias, R.F., Freeman, K.H., Boles, J.R., Holba, A.H., Fincannon, A.L., Jordan, E.D., 2001. Carbon isotopic composition of organic acids in oil field waters , San Joaquin

Basin , California , USA. Geochim. Cosmochim. Acta 65, 1301–1310.

Freeze, R.A., Cherry, J.A., 1979. Groundwater. Prentice Hall, Englewood Cliffs, NJ.

Gautier, D.L., Tennyson, M.E., Cook, T.A., Charpentier, R.R., Klett, T.R., 2012. Remaining recoverable petroleum in ten giant oil fields of the Los Angeles Basin, Southern California. U.S. Geological Survey Fact Sheet 2012–3120.

Gordon, G.S., 2009. Stratigraphic and Sedimentologic Controld on Reservoir Quality and Distribution: Middle Wildcat Group, Grizzly Bluff Gas Field, Humboldt County, California. California State University, Bakersfield.

Gordon, S., 2020. Ventura Basin Oil Generation, Timing, Migration, and Entrapment. AAPG Search and Discovery Article #11333. https://doi.org/10.1306/11333Gordon2020

Heald, C.C. (Ed.), 1988. Cameron Hydraulic Data: A Handy Reference on the Subject of Hydraulics and Steam - 17th Edition. Ingersoll-Rand.

Hodgson, S.F., 1987. Onshore Oil & Gas Seeps in California, Publication No. TR26.

Horvitz, L., 1985. Geochemical exploration for petroleum. Science (80-.). 229, 821–827. https://doi.org/10.1126/science.229.4716.821

Horvitz, L., 1972. Vegetation and Geochemical Prospecting for Petroleum. Am. Assoc. Pet. Geol. Bull. 56, 925–940. https://doi.org/10.1306/819a409a-16c5-11d7-8645000102c1865d

Huftile, G.J., 1988. Geologic structure of the Upper Ojai Valley and Chaffee Canyon areas, Ventura County, California. Oregon State University.

Isaacs, C.M., 1992. Petroleum Geology of the Central Coastal Basins Assessment Province, California, 1987 National Assessment of Undiscovered Oil and Gas Resources. Open-File Report 89-450 D.

Jeffrey, A.W.A., Alimi, H.M., Jenden, P.D., 1991. Geochemistry of Los Angeles Basin oil and gas systems: Chapter 6, Active Margin Basins.

Keller, B.M.A., 1988. Geologic Basis for the Assessment of Undiscovered Oil and Gas Resources of the Ventura Basin Province, California, 1987 National Assessment. Open-File Report 87-450 M.

Kelly, W.R., Matisoff, G., Fisher, J.B., 1985. The effects of a gas well blow out on groundwater chemistry. Environ. Geol. Water Sci. 7, 205–213. https://doi.org/10.1007/BF02509921

Kennedy, B.M., Kharaka, Y.K., Evans, W.C., Ellwood, A., DePaolo, D.J., Thordsen, J., Ambats, G., Mariner, R.H., 1997. Mantle fluids in the San Andreas fault system, California. Science (80-.). 278, 1278–1281. https://doi.org/10.1126/science.278.5341.1278

Klusman, R.W., Saeed, M.A., 1996. Comparison of Light Hydrocarbon Microseepage Mechanisms, in: Schumacher, D., Abrams, M.A. (Eds.), Hydrocarbon Migration and Its Near-Surface Expression: AAPG Memoir 66. pp. 157–158.

Krooss, B.M., 1996. Molecular Diffusion of Light Hydrocarbons in Sedimentary Rocks and Its Role in Migration and Dissipation of Natural Gas, in: Schumacher, D., Abrams, M.A. (Eds.), Hydrocarbon Migration and Its Nearsurface Expression: AAPG Memoir. pp. 173–183.

Lillis, P.G., Warden, A., Claypool, G.E., Magoon, L.B., 2007. Petroleum systems of the San Joaquin Basin Province, California—Geochemical characteristics of gas types. Chapter 10, in: A.H., S. (Ed.), Petroleum Systems and Geologic Assessment of Oil and Gas in the San Joaquin Basin Province, California, U.S. Geological Survey Professional Paper 1713. p. 30.

Lorenson, T.D., McLaughlin, R.J., Kvenvolden, K.A., Orange, D. l., Davisson, M.L., Brewer, P.G., Martin, J.B., 1998. Comparison of Offshore and Onshore Gas Occurrences, Eel River Basin, Northern California.

Macgregor, D.S., 1993. Relationships between seepage, tectonics and subsurface petroleum reserves. Mar. Pet. Geol. 10.

McLean, H., 1988. Open-File Report 87-450 I. Federal Lands Assesment Program: Eel River (Humboldt) Basin, California (Province 80).

Molofsky, L.J., Connor, J.A., Van De Ven, C.J.C., Hemingway, M.P., Richardson, S.D., Strasert, B.A., McGuire, T.M., Paquette, S.M., 2021. A review of physical, chemical, and hydrogeologic characteristics of stray gas migration: Implications for investigation and remediation. Sci. Total Environ. 779, 146234. https://doi.org/10.1016/j.scitotenv.2021.146234

Molofsky, L.J., Richardson, S.D., Gorody, A.W., Baldassare, F., Black, J.A., McHugh, T.E., Connor, J.A., 2016. Effect of Different Sampling Methodologies on Measured Methane Concentrations in Groundwater Samples. Groundwater 54, 669–680. https://doi.org/10.1111/gwat.12415

Ogle, B.A., 1953. Geology of Eel River Valley area, Humboldt County, California: California Division of Mines Bulletin 164.

Pallasser, R.J., 2000. Recognizing biodegradation in gas/oil accumulations through the δ13C compositions of gas components. Org. Geochem. 31, 1363–1373. https://doi.org/10.1016/S0146-6380(00)00101-7

Peischl, J., Ryerson, T.B., Brioude, J., Aikin, K.C., Andrews, A.E., Atlas, E., Blake, D., Daube, B.C., De Gouw, J.A., Dlugokencky, E., Frost, G.J., Gentner, D.R., Gilman, J.B., Goldstein, A.H., Harley, R.A., Holloway, J.S., Kofler, J., Kuster, W.C., Lang, P.M., Novelli, P.C., Santoni, G.W., Trainer, M., Wofsy, S.C., Parrish, D.D., 2013. Quantifying sources of methane using light alkanes in the Los Angeles basin, California. J. Geophys. Res. Atmos.

118, 4974–4990. https://doi.org/10.1002/jgrd.50413

Peters, K.E., Magoon, L.B., Lampe, C., Hosford Scheirer, A., Lillis, P.G., Gautier, D.L., 2007. A four-dimensional petroleum systems model for the San Joaquin Basin Province, California. USGS Prof. Pap. 1713, 35pp.

Prinzhofer, A., Battani, A., 2003. Gas isotopes tracing: An important tool for hydrocarbons exploration. Oil Gas Sci. Technol. 58, 299–311. https://doi.org/10.2516/ogst:2003018

Rademacher, L.K., Clark, J.F., Hudson, G.B., Erman, D.C., Erman, N.A., 2001. Chemical evolution of shallow groundwater as recorded by springs, Sagehen basin; Nevada County, California. Chem. Geol. 179, 37–51.

Rice, G.K., 2022. Special section: Hydrocarbon migration, near-surface seepage, and petroleum system assessment. Vertical migration in theory and in practice. Interpretation 10, 17–26. https://doi.org/10.1190/INT-2020-0216.1

Schwade, I.T., Fine, S., 1949. Geology of North Sulphur Mountain Field, Ventura County. Am. Assoc. Pet. Geol. Bull. 33, 2061.

Shonkoff, S., Gautier, D.L., 2015. A case study of the petroleum geological potential and potential public health risks associated with hydraulic fracturing and oil and gas development in the Los Angeles Basin., in: An Independent Scientific Assessment of Well Stimulation in California, Volume III. pp. 199–211.

Sorlien, C.C., Gratier, J.P., Luyendyk, B.P., Hornafius, J.S., Hopps, T.E., 2000. Map restoration of folded and faulted late Cenozoic strata across the Oak Ridge fault, onshore and offshore Ventura basin, California. Bull. Geol. Soc. Am. 112, 1080–1090. https://doi.org/10.1130/0016-7606(2000)112<1080:MROFAF>2.0.CO;2

SVBGSA, 2019. Draft Chapter 4 Salinas Valley Basin Integrated Sustainability Plan.

Takahashi, B.K.I., Gautier, D.L., 2004. A Brief History of Oil and Gas Exploration in the Southern San Joaquin Valley of California. Pet. Syst. Geol. Assess. Oil Gas San Joaquin Basin Prov. Calif. 1–24.

Tsai, C., Boessenecker, R.W., 2017. The Earliest-Known Fin Whale, Balaenoptera Physalus, From the Early Pleistocene of Northern California, U.S.A. J. Vertebr. Paleontol. 37, e1306536.

U.S. EPA, 2023. Class VI Wells Permitted by EPA [WWW Document]. URL https://www.epa.gov/uic/class-vi-wells-permitted-epa (accessed 3.2.23).

Ulrich, N., Goss, K.U., Ebert, A., 2021. Exploring the octanol–water partition coefficient dataset using deep learning techniques and data augmentation. Commun. Chem. 4, 1–10. https://doi.org/10.1038/s42004-021-00528-9

Underwood, M.B., 1985. Sedimentology and hydrocarbon potential of Yager structural complex—possible Paleogene source rocks in Eel River basin, northern California. Am. Assoc. Pet. Geol. Bull. 69, 1088–1100.

Van Stempvoort, D., Maathuis, H., Jaworski, E., Mayer, B., Rich, K., 2005. Oxidation of fugitive methane in ground water linked to bacterial sulfate reduction. Ground Water 43, 187–199. https://doi.org/10.1111/j.1745-6584.2005.0005.x

Visser, A., Singleton, M.J., Hillegonds, D.J., Velsko, C.A., Moran, J.E., Esser, B.K., 2013. A membrane inlet mass spectrometry system for noble gases at natural abundances in gas and water samples. Rapid Commun. Mass Spectrom. 2472–2482. https://doi.org/10.1002/rcm.6704

Walling, R.W., 1934. Summary of Operations: California Oil Fields. Report on Newhall Oil-field. Q. Chapter, Twent. Annu. Rep. State Oil Gas Superv. 20, 1–221.

Weber, D., Marquez, B.A., Taylor, C., Raya, P., Contreras, P., Howard, D., Nwachuku, I., Fusco, K., Morales, F., Doezema, L.A., 2017. Macroseepage of methane and light alkanes at the La Brea tar pits in Los Angeles. J. Atmos. Chem. 74, 339–356. https://doi.org/10.1007/s10874-016-9346-4

Weed, B.M., Brambila, G.D., Doezema, L.A., 2020. Natural seepage of methane and light alkanes at three locations in Southern California. Atmosphere (Basel). 11. https://doi.org/10.3390/atmos11090979

Whiticar, M.J., 2001. Characterization and Application of Sorbed Gas by Microdesorption CF-IRMS, in: AAPG Hedberg Conference “Near-Surface Hydrocarbon Migration: Mechanisms and Seepage Rates” September 16-19, 2001, Vancouver, BC, Canada. pp. 1–3.

Whiticar, M.J., 1999. Carbon and hydrogen isotope systematics of bacterial formation and oxidation of methane. Chem. Geol. 161, 291–314. https://doi.org/10.1016/S0009-2541(99)00092-3

Wright, T.L., 1991. Structural Geology and Tectonic Evolution of the Los Angeles Basin, California: Chapter 3: PART 1. Geology.

Wright, T.L., 1987. Geological setting of the Rancho La Brea Tar Pits, in: Wright, T., Heck, R. (Eds.), Petroleum Geology of Coastal California, Pacific Section, American Assoc. Petrol. Geologist Guidebook (Vol. 60). pp. 87–91.

Yeats, R.S., Huftile, G.J., Stitt, L.T., 1994. Late Cenozoic tectonics of the east Ventura Basin, Transverse Ranges, California, American Association of Petroleum Geologists Bulletin. https://doi.org/10.1306/a25fe42d-171b-11d7-8645000102c1865d

Chapter 5: Conclusions

This work utilized newly available produced water data from the Marcellus Shale in northeastern Pennsylvania, as well as geochemical data from natural gas seeps throughout California, to identify new information about the behavior of subsurface fluids (including natural gases) in deep hydrocarbon-bearing sedimentary basins. Specifically, research in the second chapter provided the first evidence of the effects of water condensing out of the gas phase, i.e., water of condensation, on the chemistry of produced water from a shale gas reservoir. The third chapter proposed a new method to identify cross-formation flow of deep fluids using the combined behavior of ^{228}Ra/^{226}Ra and ^{87}Sr/^{86}Sr in waters. Lastly, the fourth chapter presents a framework for characterizing the chemistry of natural gas seepage from a variety of geographic and geologic settings in California, where post-genetic changes in gas chemistry during migration from reservoir to surface may be helpful in distinguishing natural seepage from stray gas releases.

Prior to this study, it was generally thought that later-stage (i.e., six months or more) produced water chemistry from shale gas wells primarily represented that of formation fluids, as opposed to injected hydraulic fracturing fluids (Chapman et al., 2012; Haluszczak et al., 2013; Rowan et al., 2015). This assumption was based, in large part, on time-series produced water data from shale gas wells, which showed a pattern of rapidly increasing salinity and changes in δ^{18}O-H_2O, δ^{2}H-H_2O, and ^{87}Sr/^{8S}Sr. These data were interpreted to represent the transition from relatively fresh injected fluids to saline formation fluids. However, my second chapter demonstrates evidence of a surprising reversal in this trend, i.e., a later-stage transition from higher salinity and enriched δ^{18}O and δ^{2}H water to lower salinity and isotopically light water. This was observed in the majority of Marcellus Shale gas produced water samples from the study area in northeastern Pennsylvania. This ‘freshening’ during later-stage production is interpreted to represent the increasingly important influence of a third source of water, water of condensation, on produced water chemistry. Water of condensation becomes a significant, and even dominant, component of produced water as the production of other water sources (formation fluid and hydraulic fracturing fluid) declines. This conclusion is supported by a simple end-member mixing model between injected fluid, formation water, and water of condensation.

The dominance of water of condensation on later-stage produced water composition has important implications for studies on the nature and composition of shale formation fluids, which must now consider the possibility of a third water source affecting later-stage produced water chemistry. Understanding the potential for a later-stage salinity reversal could also inform the development of improved produced water management strategies, with concomitant reductions in treatment and/or disposal and associated costs.

Water of condensation has been observed in deep conventional Gulf Coast reservoirs by Kharaka et al. (1977a, 1977b) and Poulson et al., (1995). However, the effects of water of condensation on later-stage produced water chemistry in shale gas wells outside of the study area are unclear. While water condensing out of the gas phase occurs in virtually all natural gas production wells, it only becomes a significant contributor to produced water composition when the contributions from other water sources are very low. This is common during mature production within high-quality shale gas reservoirs, which typically have low permeability and/or water saturation (e.g. ranging from <35% to irreducible water content) and high imbibition rates (Cheng et al., 2017; Singh, 2016). The Marcellus Shale fits this description, as do several other shale gas reservoirs in the United States (e.g., the Woodford, Fayetteville, and Haynesville Shales). Therefore, it is likely that water of condensation is an important player in produced water composition in other parts of the Marcellus, and other shale-gas plays, as well as some conventional gas plays. With broader sampling in the future, there will be an opportunity to evaluate whether this is the case.

The third chapter of this dissertation proposes a new method to evaluate the origin of produced water from a subset of Marcellus Shale gas wells that continue to produce anomalously large volumes of saline water well into later-stage production. As noted above, because the Marcellus is thought to contain relatively little mobile water, the production of larger volumes of water from Marcellus wells has puzzled researchers. In many cases, this water exhibits high salinity (>150,000 mg/L total dissolved solids), and high radionuclide content (e.g., radium> 10,000 pCi/L), which increase the costs for water treatment and waste disposal. In almost all cases, these larger volumes of water are associated with lower gas production. Whether these are examples of out-of-zone waters, or higher permeability lenses within the Marcellus, is therefore a significant question that affects produced water management and production.

To address this question, I demonstrate that the combined behavior of ^{228}Ra/^{226}Ra and ^{87}Sr/^{86}Sr in waters can be used to identify relatively recent (<16,000 years) cross-formation flow in deep sedimentary basin fluids. Specifically, because ^{87}Sr and ^{86}Sr are stable (i.e., do not decay), the ^{87}Sr/^{86}Sr ratio of formation fluids reflects the cumulative Sr inputs to those fluids over time. These inputs would include the ^{87}Sr/^{86}Sr ratio of the originating fluid (e.g., seawater), and Sr contributions from formations the water has contacted (Chaudhuri and Clauer, 1992; Kharaka and Hanor, 2007). By contrast, ^{226}Ra and ^{228}Ra do decay and have relatively short half-lives (1,600 and 5.75 years, respectively). Therefore the ^{228}Ra/^{226}Ra ratio of formation fluids would be most strongly affected by water-rock interactions within the last month prior to sampling, with a diminishing influence detectable up to 16,000 years.

These characteristics can allow one to develop a predictive method for estimating $^{87}Sr/^{86}Sr$ and $^{228}Ra/^{226}Ra$ ratios of formation fluids. With known information on the U/Th ratio of lithologic samples from potential host formations, the $^{228}Ra/^{226}Ra$ ratio of present-day pore fluids within those formations can be estimated. Similarly, information on the Rb/Sr ratio of lithologic samples, in combination with $^{87}Sr/^{86}Sr$ values for freshwater leachates from those same formations, can be used to predict the $^{87}Sr/^{86}Sr$ ratio of fluids presently residing in different formations.

Within the study area of my third chapter, I demonstrate that, even when strongly diluted by hydraulic fracturing fluid or water of condensation, the Ra^{2+} and Sr^{2+} content of formation fluids is the primary determinant of the $^{228}Ra/^{226}Ra$ and $^{87}Sr/^{86}Sr$ ratios in Marcellus produced water. Based on that finding, the $^{228}Ra/^{226}Ra$ and $^{87}Sr/^{86}Sr$ ratios of Marcellus produced water are used to identify the production of out-of-zone water within a subset of Marcellus Shale gas wells. By comparing these ratios to predicted ratios for different formations, the Onondaga Limestone was identified as the likely source of exogenous fluid.

This approach is likely to be most successful where brines in oil and gas basins share a common parent source of salinity (i.e., with the same $^{87}Sr/^{86}Sr$ ratio), such as paleoseawater or expelled brines from underlying evaporite sequences. In such settings, the differences in the $^{87}Sr/^{86}Sr$ ratio of formation waters largely reflect rock-water interaction and the Rb/Sr ratios of host rocks, without the variable of different fluid origins.

Within these basins, this approach holds particular promise for identifying sudden and recent cross-formation flow events stimulated by anthropogenic activities. These activities could include hydraulic fracturing, in which exogenous formation fluids may move into the wellbore via newly created fractures or a combination of pre-existing faults and enhanced permeability. Similarly, formation pressurization associated with CO_2 or wastewater injection could mobilize fluids, and wellbore integrity issues such as compromised cement or casing strings can connect formations formerly isolated by geologic seals. In these scenarios, cross-formation flow has important implications for produced water management, as well as for potential environmental impacts associated with unintended fluid migration. Future work may also incorporate other isotope tracers to confirm the efficacy of the combined ^{228}Ra/^{226}Ra and ^{87}Sr/^{86}Sr approach to discerning cross formation flow. Such tracers could include δ^{7}Li, where Li isotope fractionation is associated with processes including clay formation and secondary mineralization (Phan et al., 2016); ^{129}I, which can be a tracer of the spontaneous fission of ^{238}U in organic-rich shales (Osborn et al., 2012); and δ^{11}B, which becomes depleted (isotopically light) when associated with kerogen maturation (Williams et al., 2001). Additionally, laboratory experiments could be used to confirm the modeling results for the predicted changes in the ^{228}Ra/^{226}Ra ratio over time following the rapid migration of formation fluid from one host-rock into another (e.g., where the two host-rocks exhibit different Th/U ratios and abundances).

The fourth chapter of this dissertation focuses on geochemical methods to better characterize the natural migration of hydrocarbon gases in sedimentary basins. Natural gas seeps are commonly found in oil and gas fields; indeed many of these fields were discovered specifically because of the presence of such seeps (e.g., Hodgson, 1987). However, recent concerns about unintended releases of natural gas to the shallow subsurface and surface via artificial pathways (e.g., oil and gas wells) have prompted interest in distinguishing natural gas seepage from reservoir gas, if possible. With multiple petroleum-bearing basins, and a location along a convergent plate margin characterized by extensive faulting and fracturing, California exhibits an exceptionally high density of natural hydrocarbon seeps (Ciotoli et al., 2020; Hodgson, 1987). To better understand whether natural seeps exhibit commonalities in the chemical characteristics of gases, or in the post-genetic changes that occur during transport from reservoir to surface, my fourth chapter presents the framework utilized for the collection and evaluation of chemical data from natural gas seeps throughout California. Specifically, I identify molecular and isotopic tracers that are likely to demonstrate the effects of gas alteration during transport, and are also widely accessible to the public, i.e., analyzed in commercial laboratories worldwide. I also present an approach to evaluating whether there is evidence for the co-migration of deep formation water with naturally seeping gas, which could result from multi-component transport along seepage pathways. On a local scale, this work has important implications for differentiating naturally seeping gas and water from anthropogenic releases of fluids associated with oil and gas exploration. It also holds promise for discerning elevated CO_2 associated with natural seeps, which may prove important during monitoring at CO_2 sequestration sites in California. On a more global scale, the framework I present may aid in the ability to identify and quantify geogenic methane emissions, which are a potentially important component of the greenhouse gas budget (e.g., Allen, 2016; Etiope et al., 2019).

REFERENCES

Allen, D., 2016. Attributing Atmospheric Methane to Anthropogenic Emission Sources. Acc. Chem. Res. 49, 1344–1350.

Chapman, E.C., Capo, R.C., Stewart, B.W., Kirby, C.S., Hammack, R.W., Schroeder, K.T., Edenborn, H.M., 2012. Geochemical and strontium isotope characterization of produced waters from Marcellus Shale natural gas extraction. Environ. Sci. Technol. 46, 3545–3553. https://doi.org/10.1021/es204005g

Chaudhuri, S., Clauer, N., 1992. History of marine evaporites: constraints from radiogenic isotopes. In: Isotopic Signatures and Records, in: Lecture Notes in Earth Sciences. Springer-Verlag, Verlin/Heidelberg, pp. 177–198. https://doi.org/10.1007/ BFb0009865

Cheng, P., Tian, H., Xiao, X., Gai, H., Li, T., Wang, X., 2017. Water Distribution in Overmature Organic-Rich Shales : Implications from Water Adsorption Experiments. https://doi.org/10.1021/acs.energyfuels.7b01531

Ciotoli, G., Procesi, M., Etiope, G., Fracassi, U., Ventura, G., 2020. Influence of tectonics on global scale distribution of geological methane emissions. Nat. Commun. 11, 1–8. https://doi.org/10.1038/s41467-020-16229-1

Etiope, G., Ciotoli, G., Schwietzke, S., Schoell, M., 2019. Gridded maps of geological methane emissions and their isotopic signature. Earth Syst. Sci. Data 11, 1–22.

Haluszczak, L.O., Rose, A.W., Kump, L.R., 2013. Geochemical evaluation of flowback brine from Marcellus gas wells in Pennsylvania, USA. Appl. Geochemistry 28. https://doi.org/10.1016/j.apgeochem.2012.10.002

Hodgson, S.F., 1987. Onshore Oil & Gas Seeps in California, Publication No. TR26.

Kharaka, Y.K., Callender, E., Carothers, W.W., 1977a. Geochemistry of geopressured geothermal waters from the Texas Gulf Coast. Third Geopress. Energy Conf. 1, 121–166.

Kharaka, Y.K., Callender, E., Wallace, R.H., 1977b. Geochemistry of geopressured geothermal waters from the Frio Clay in the Gulf Coast region of Texas. Geology 5, 241–244. https://doi.org/10.1130/0091-7613(1977)5<241:GOGGWF>2.0.CO;2

Kharaka, Y.K., Hanor, J.S., 2007. Deep fluids in the continents: 1. Sedimentary Basins, in: Treatise on Geochemistry. Pergamon, Oxford, pp. 1–48.

Osborn, S.G., McIntosh, J.C., Hanor, J.S., Biddulph, D., 2012. Iodine-129, 87Sr/86Sr, and trace elemental geochemistry of northern Appalachian Basin brines: Evidence for basinal-scale fluid migration and clay mineral diagenesis. Am. J. Sci. 312, 263–287.

Phan, T.T., Capo, R.C., Stewart, B.W., Macpherson, G.L., Rowan, E.L., Hammack, R.W., 2016. Factors controlling Li concentration and isotopic composition in formation waters and host rocks of Marcellus Shale, Appalachian Basin. Chem. Geol. 420, 162–179. https://doi.org/10.1016/j.chemgeo.2015.11.003

Poulson, S.R., Ohmoto, H., Ross, T.P., 1995. Stable isotope geochemistry of waters and gases (CO2, CH4) from the overpressured Morganza and Moore-Sams fields, Louisiana Gulf Coast. Appl. Geochemistry 10, 407–417. https://doi.org/10.1016/0883-2927(95)00014-B

Rowan, E.L., Engle, M.A., Kraemer, T.F., Schroeder, K.T., Hammack, R.W., Doughten, M.W., 2015. Geochemical and isotopic evolution of water produced from Middle Devonian Marcellus shale gas wells, Appalachian Basin, Pennsylvania. Am. Assoc. Pet. Geol. Bull. 99, 181–206. https://doi.org/10.1306/07071413146

Singh, H., 2016. Journal of Natural Gas Science and Engineering A critical review of water uptake by shales. J. Nat. Gas Sci. Eng. 34, 751–766. https://doi.org/10.1016/j.jngse.2016.07.003

Williams, L.B., Hervig, R.L., Wieser, M.E., Hutcheon, I., 2001. The Influence of organic matter on the boron isotope geochemistry of the Gulf Coast sedimentary basin, USA. Chem. Geol. 174, 445–461. https://doi.org/10.1016/S0009-2541(00)00289-8

Appendix A: Supporting Information for Chapter 2

Evidence for water of condensation: A third source of water in shale gas wells

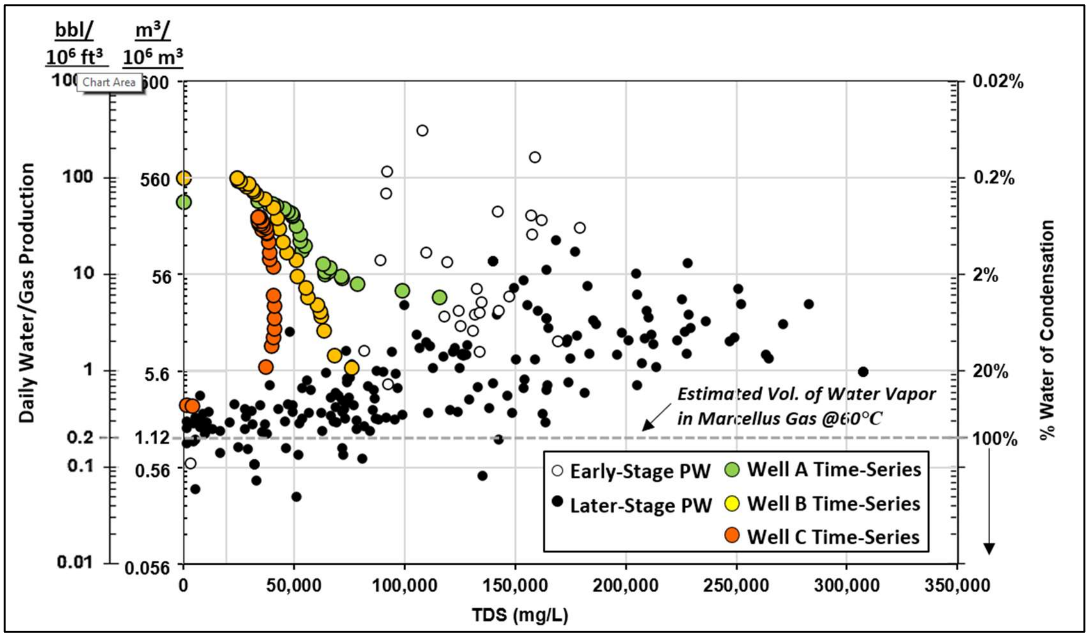

Figure A.1: Daily water to gas production ratio (15 day moving average) vs. TDS concentration vs. days producing for Well A, B, and C time-series data and 230 produced water samples from Marcellus shale gas wells sampled once each in Susquehanna County.

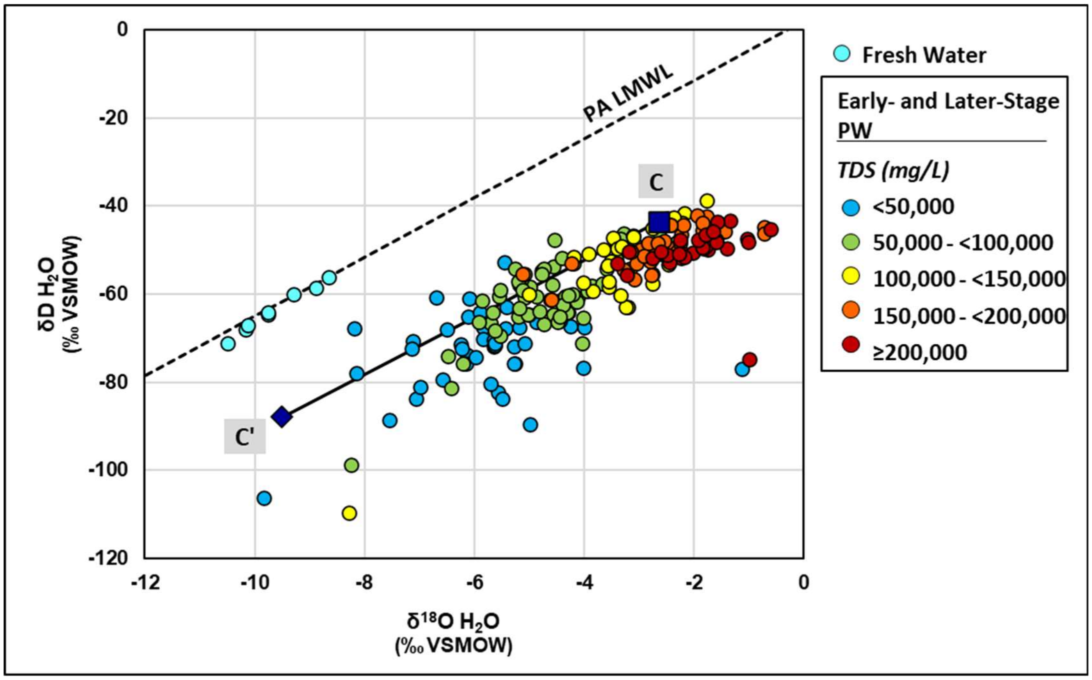

Figure A.2: Hypothetical mixing line C-C' (navy), where Point C is defined as downhole fluid with chloride = 60,000 mg/L, $\delta^{18}O$ = -2.6‰, $\delta^{2}H$ = -43.5‰, and Point C' is calculated based on the isotopic composition of water vapor assumed to be in isotopic equilibrium with downhole fluid at typical reservoir temperature (60°C). Water $\delta^{2}H$ vs. $\delta^{18}O$ values are also shown for 230 produced water samples from Marcellus shale gas wells sampled once each in Susquehanna County.

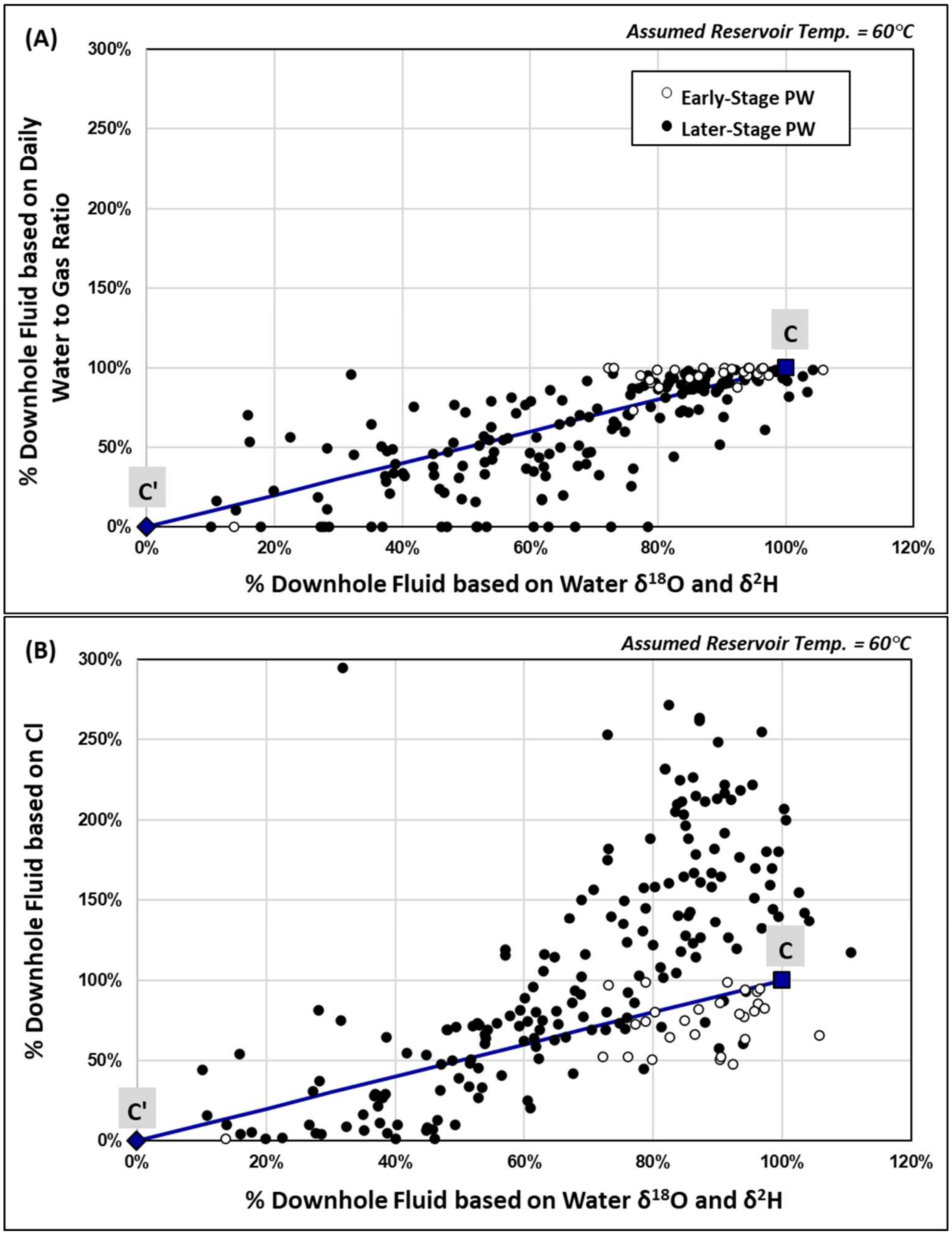

Figure A.3: Estimated percentages of formation fluids based on A) the daily ratios of water-to-gas production and B) conservative Cl concentrations, versus the δ^{18}O and δ^{2}H composition of produced water using endmember mixing model C-C' in Figure A2. Values with negative proportions removed for plotting purposes. Due to variability in downhole fluid composition, in rare instances, the calculated percentage of downhole fluid based on the δ^{18}O and δ^{2}H composition and Cl concentration was greater than 100%.

Table A.1: Temperature-dependence of estimated water content of natural gas and isotopic composition of water vapor end-member assuming downhole water $\delta^{18}O$ and $\delta^{2}H$ values of -0.9‰ and -39.9‰, respectively.

			Vapor End-member	
Reservoir Temp. (°C)	bbls water/ 10^6 ft^3 gas	m^3 water/ 10^6 m^3 gas	$\delta^{18}O$ (‰ VSMOW)	$\delta^{2}H$ (‰ VSMOW)
45	0.1	0.6	-8.8	-94.4
60	0.2	1.1	-7.8	-84.5
70	0.3	1.7	-6.7	-76.3

Notes:

1. Water content of natural gas at different reservoir temperatures is estimated using the chart for the water content of natural gases provided in McKetta and Wehe (1958).
2. Isotopic composition of water vapor is calculated from the downhole water isotopic composition using the temperature-dependent equilibration fractionation factors provided in Majoube (1971) and incorporated in Beaudoin and Therrien (2021).

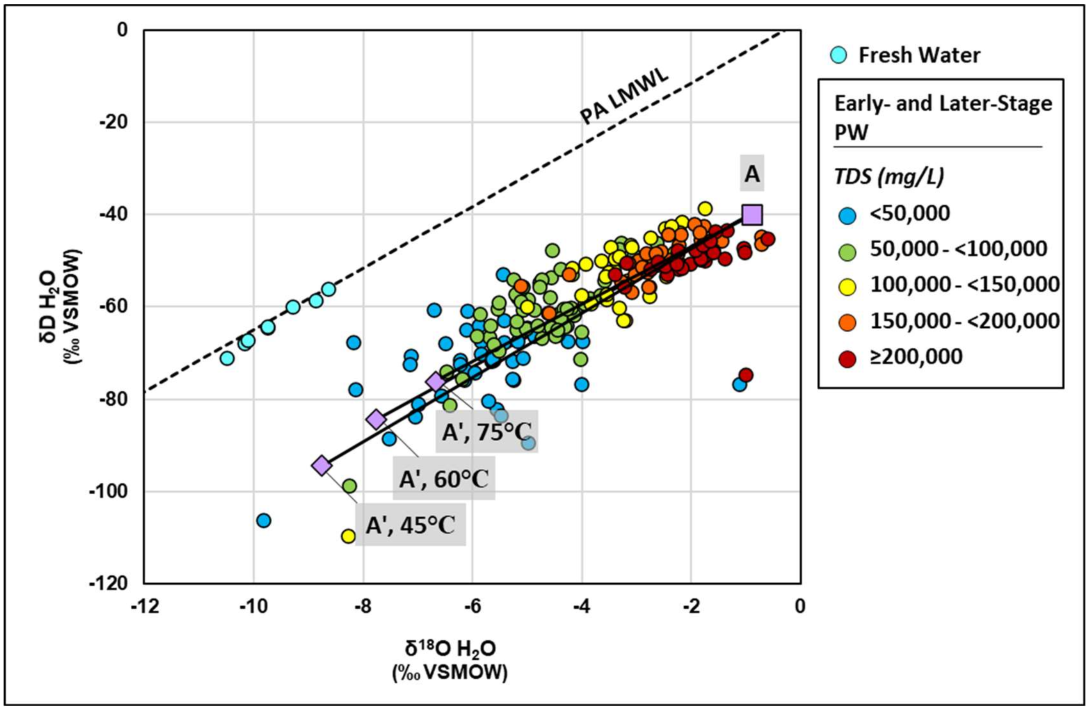

Figure A.4: Differences in hypothetical mixing line A-A’ (purple) based on a range of reservoir temperatures (45°C, 60°C, and 75°C), as compared to water $\delta^{2}H$ vs. $\delta^{18}O$ values for 230 produced water samples from Marcellus shale gas wells sampled once each in Susquehanna County.

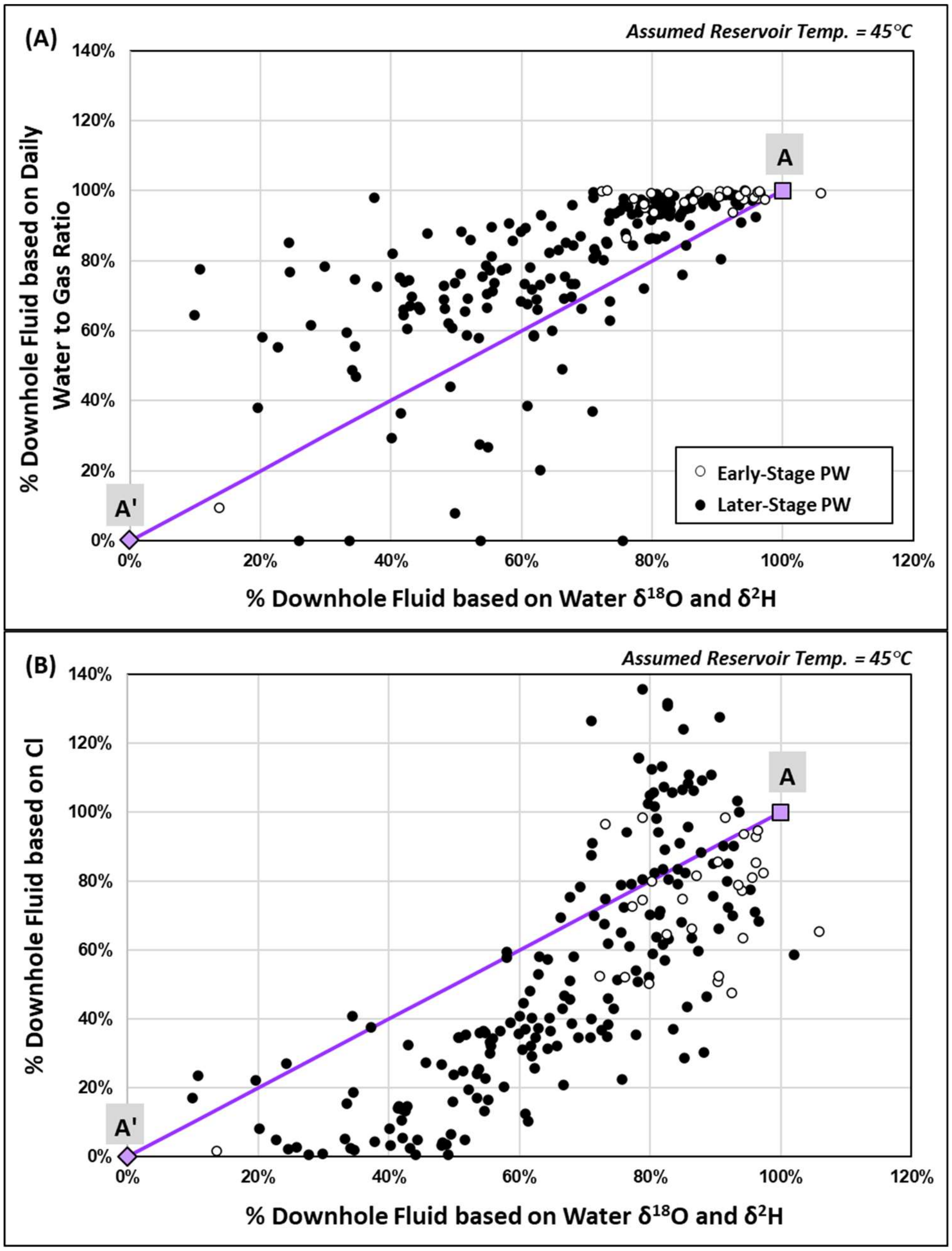

Figure A.5: Estimated percentages of formation fluids based on A) the daily ratios of water-to-gas production and B) conservative Cl concentrations, versus the $\delta^{18}O$ and $\delta^{2}H$ composition of produced water using endmember mixing model A-A' with A' calculated assuming a reservoir temperature of 45°C. Values with negative proportions removed for plotting purposes. Due to variability in downhole fluid composition, in rare instances, the calculated percentage of downhole fluid based on the $\delta^{18}O$ and $\delta^{2}H$ composition and Cl concentration was greater than 100%.

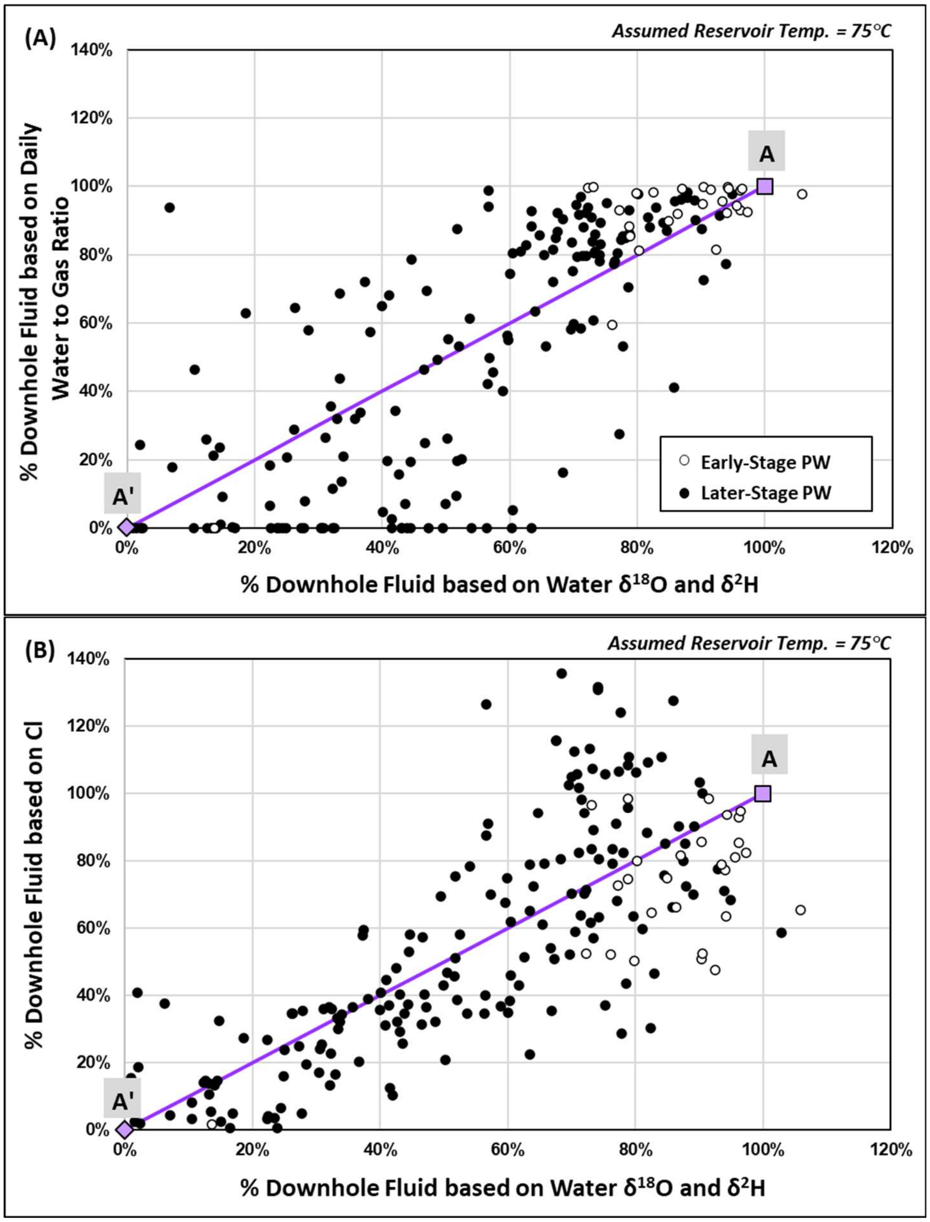

Figure A.6: Estimated percentages of formation fluids based on A) the daily ratios of water-to-gas production and B) conservative Cl concentrations, versus the $\delta^{18}O$ and $\delta^{2}H$ composition of produced water using endmember mixing model A-A’ with A’ calculated assuming a reservoir temperature of 75°C. Values with negative proportions removed for plotting purposes. Due to variability in downhole fluid composition, in rare instances, the calculated percentage of downhole fluid based on the $\delta^{18}O$ and $\delta^{2}H$ composition and Cl concentration was greater than 100%.

References

Beaudoin, G., Therrien, P., 2021. AlphaDelta Stable Isotope Fractionation Calculator [WWW Document]. URL http://www2.ggl.ulaval.ca/cgi-bin/alphadelta/alphadelta_4alpha.cgi

Majoube, M., 1971. Fractionnement en oxygene-18 et en deuterium entre l'eau et sa vapeur. J. Chem. Phys. 1423–1436. https://doi.org/10.1051/jcp/1971681423

McKetta, J.J., Wehe, A.H., 1958. Use this chart for the water content of natural gases. Pet. Refin. 37, 153–154.

Appendix B: Supporting Information for Chapter 3

A combined ^{228}Ra/^{226}Ra and ^{87}Sr/^{86}Sr approach to identify cross-formation flow in sedimentary basin systems

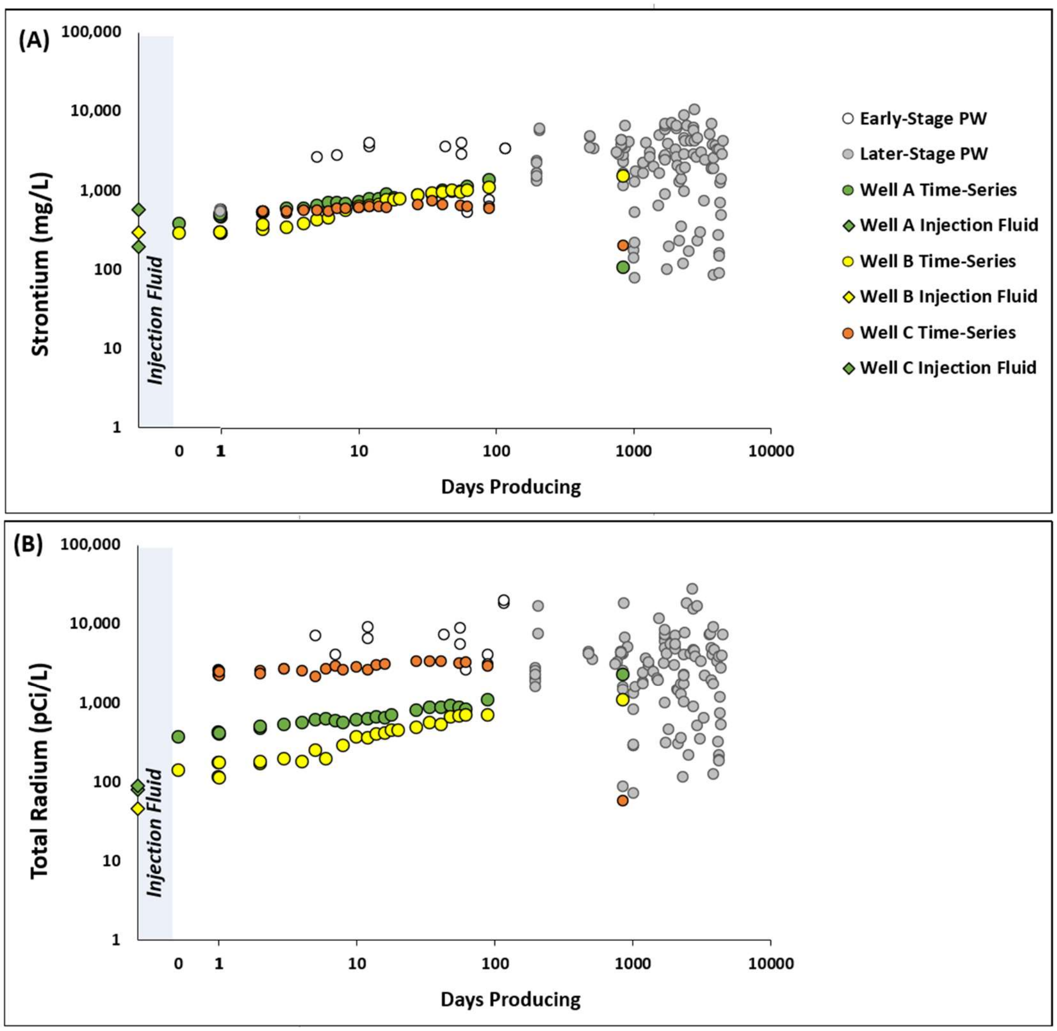

Figure B.1: (A) Strontium vs. days producing; (B) Radium vs. days producing, for Well A, B, and C time-series data and 123 produced water samples from Marcellus shale gas wells sampled once each in the study area. PW= Produced water.

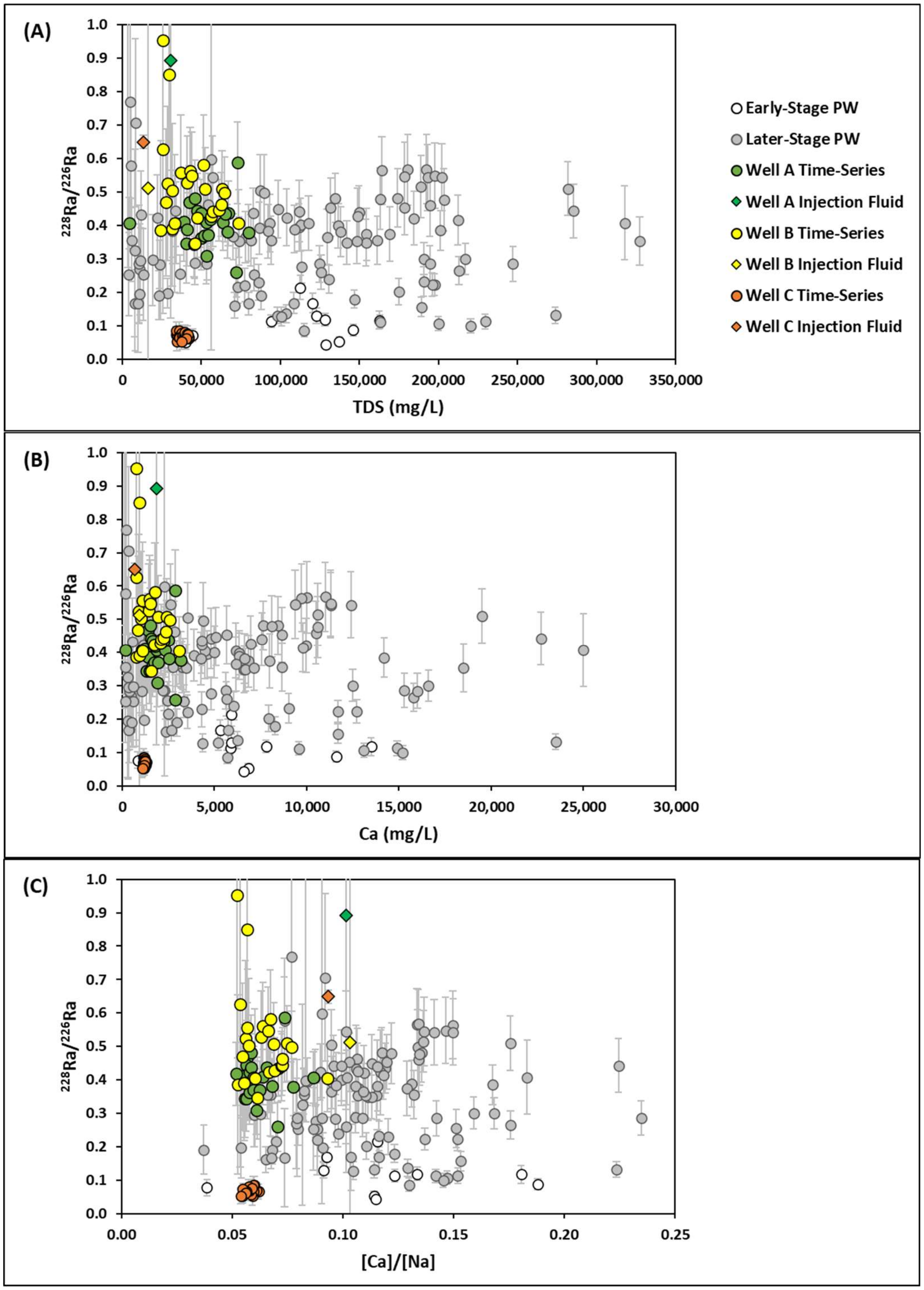

Figure B.2: (A) ^{228}Ra/^{226}Ra vs. TDS, (B) ^{228}Ra/^{226}Ra vs. [Ca]/[Na], and C) ^{228}Ra/^{226}Ra vs. Ca, for Well A, B, and C time-series data and 123 produced water samples from Marcellus shale gas wells sampled once each in the study area. 2σ errors for ^{228}Ra/^{226}Ra are shown as gray error bars. 2σ errors for ^{87}Sr/^{86}Sr are smaller than symbol (<±0.00002). PW= Produced water.

.

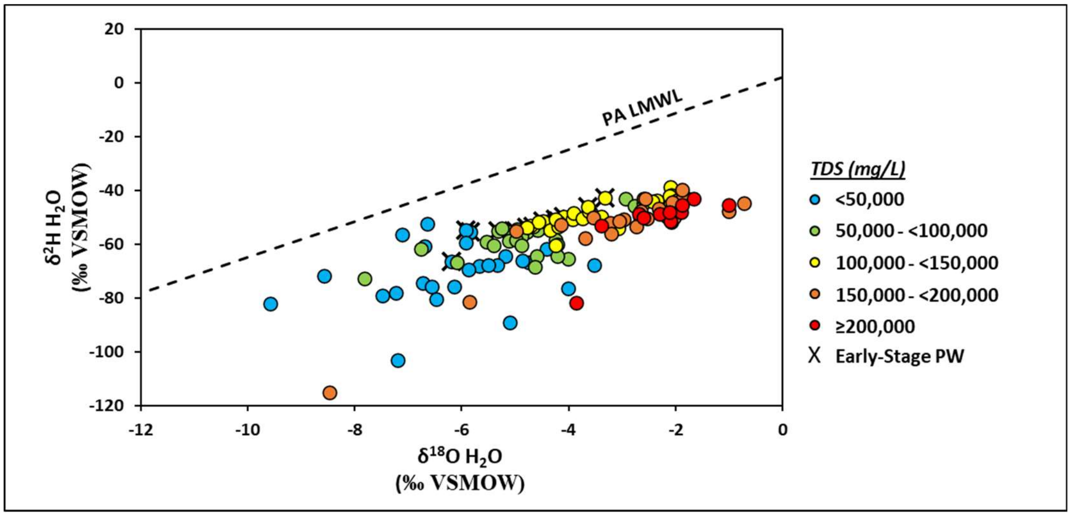

Figure B.3: δ^2H vs. δ^{18}O of water for 123 produced water samples from Marcellus shale gas wells sampled once each in the study area. Local meteoric water line for Pennsylvania from Kendall and Coplen (2001). PW= Produced water

RA MODELING METHODS

Calculations and parameter values utilized to model the radioactive decay and ingrowth of ^{228}Ra and ^{226}Ra in Exercises 1, 2, and 3 are described below.

Total Ra and ^{228}Ra/^{226}Ra values for Marcellus formation fluids were selected based on produced water data from the study area, as well as reported values in Marcellus produced water from the north-central and north-eastern Appalachian Basin (e.g., Rowan et al., 2015). Onondaga produced water data is not available for the study area. Instead, the total Ra value for Onondaga Formation fluid is based on a sample of Onondaga produced water from Erie County, NY (Blondes et al., 2019), and the ^{228}Ra/^{226}Ra value is based on the median predicted ^{228}Ra/^{226}Ra value of Onondaga Formation fluids in Core 1 in the study area (Figure 3.8). Characteristic Th and U abundances and ratios of both Onondaga and Marcellus (Union springs sub-unit) host rocks are based on median measured values for the respective units in Core 1.

In both scenarios, we assume that the water-connected porosity (enhanced by hydraulic fracturing) of the Union Springs Formation is 5% (per the 3% average effective porosity of organic-rich shale core samples cited in Balashov et al., 2015; Gu et al., 2015, and assuming some connectivity enhancement related to hydraulic fracturing). Therefore, we assume that only 5% of the initial abundance of isotopes (number of atoms per kg rock) in the $^{232}Th \rightarrow ^{228}Ra$ and $^{238}U \rightarrow ^{226}Ra$ decay chains in the Union Springs Formation is available for interaction with an invading exogenous fluid. Of that 5%, we assume that only 15% of the radium in the solid phase is transferred to the water virtually immediately (c.f., Landis et al., 2018). Lastly, we assume that an exogenous invading fluid will, at most, fill 5% of the pore space, or 25 cm^3/kg of rock. This equates to 0.025 L of water per kg of rock.

^{228}Ra

The number of atoms of ^{228}Ra (N_{228Ra}) at any time *t* is a function of its ingrowth from ^{232}Th (based on the number of atoms at time = 0, N^{o}_{232T}) with a given rate constant (λ_{232Th}); its own radioactive decay (with a rate constant of λ_{228Ra}); and the decay of any ^{228}Ra present in a) the migrating formation fluid, Fluid A ($N^{o}_{228Ra-FLUID.A}$), and b) the new host formation and/or pore fluid within that host formation ($N^{o}_{228Ra-FORMATI\quad .B}$), following the analytical solutions provided by Bateman (1910):

$$N_{228Ra} = \frac{\lambda_{232Th}}{\lambda_{228Ra} - \lambda_{232Th}} N^{o}_{232Th-FORMATIO\quad .B}\left(e^{-\lambda_{232Th}t}\right)$$

$$+ \left[\frac{\lambda_{232Th}}{\lambda_{232Th} - \lambda_{228Ra}} N^{o}_{232Th-FORMAT\quad .B} + N^{o}_{228Ra-FORMATI\quad .B}\right]\left(e^{-\lambda_{228Ra}t}\right)$$

$$+ N^{o}_{228Ra-FLUI\ .A}\left(e^{-\lambda_{228Ra}t}\right)$$

where time *t* = 0 corresponds to the point when the fluid moves from its initial formation to a secondary formation and becomes out-of-zone, and *t* is time in years (Bateman, 1910).

$N^{o}_{232Th-FORMAT\quad .B}$, $N^{o}_{228Ra-FORMA\quad .B}$, and $N^{o}_{228Ra-FLUI\ .A}$ were determined as follows:

- $N^{o}_{232Th-FORMATION.B}$= Median whole rock Th concentration in the Union Springs Formation in Core 1, as measured by ED-XRF in mg/kg, and converted to mols of ^{232}Th atoms by dividing by the atomic mass of Th, subsequently converted to atoms of ^{232}Th by multiplying by Avogadro's number.
- $N^{o}_{228Ra-FORMATI\quad .B}$= number of ^{228}Ra atoms in secular equilibrium with $N^{o}_{232Th-FORMATION.B}$.
- $N^{o}_{228Ra-FLUID.A}$ = ^{228}Ra activity (pCi/L) in produced water from the Onondaga Limestone, as reported in Rowan et al. 2011, converted to number of ^{228}Ra atoms by dividing by λ_{228Ra}.

^{226}Ra

A similar model can be developed for the decay and ingrowth of parent and daughter products in the ^{238}U decay chain system: $^{238}\mathrm{U} \rightarrow {}^{234}\mathrm{Th} \rightarrow {}^{234}\mathrm{Pa} \rightarrow {}^{234}\mathrm{U} \rightarrow {}^{230}\mathrm{Th} \rightarrow {}^{226}\mathrm{Ra} \rightarrow {}^{222}\mathrm{Rn}$. This model to determine the number of ^{226}Ra atoms at time *t* ($N_{226\mathrm{Ra}}$) is more complex as it requires ingrowth from multiple parent isotopes but can be simplified by ignoring short-lived parents (i.e., ^{234}Th and ^{234}Pa):

$$\begin{aligned}
\mathrm{N}_{226\mathrm{Ra}} = {} & \frac{\lambda_{238\mathrm{U}}\lambda_{234\mathrm{U}}\lambda_{230\mathrm{Th}}}{(\lambda_{234\mathrm{U}} - \lambda_{238}U)(\lambda_{230\mathrm{Th}} - \lambda_{238}U)(\lambda_{226\mathrm{Ra}} - \lambda_{238\mathrm{U}})} \mathrm{N}^{\mathrm{o}}_{238\mathrm{U-FORMATION.B}}\left(\mathrm{e}^{-\lambda_{238\mathrm{U}}\mathrm{t}}\right) \\
& + \left[\begin{array}{c} \dfrac{\lambda_{238\mathrm{U}}\lambda_{234\mathrm{U}}\lambda_{230\mathrm{Th}}}{(\lambda_{238\mathrm{U}} - \lambda_{234}U)(\lambda_{230\mathrm{Th}} - \lambda_{234}U)(\lambda_{226\mathrm{Ra}} - \lambda_{234\mathrm{U}})} \mathrm{N}^{\mathrm{o}}_{238\mathrm{U-FORMATIO\ \ .B}} \\ + \dfrac{\lambda_{234\mathrm{U}}\lambda_{230\mathrm{Th}}}{(\lambda_{230\mathrm{Th}} - \lambda_{234}U)(\lambda_{226\mathrm{Ra}} - \lambda_{234\mathrm{U}})} \mathrm{N}^{\mathrm{o}}_{234\mathrm{U-FO\ \ \ \ .B}} \end{array}\right]\left(\mathrm{e}^{-\lambda_{234\mathrm{U}}\mathrm{t}}\right) \\
& + \left[\begin{array}{c} \dfrac{\lambda_{238\mathrm{U}}\lambda_{234\mathrm{U}}\lambda_{230\mathrm{Th}}}{(\lambda_{238\mathrm{U}} - \lambda_{230}Th)(\lambda_{234\mathrm{U}} - \lambda_{230}Th)(\lambda_{226\mathrm{Ra}} - \lambda_{230\mathrm{Th}})} \mathrm{N}^{\mathrm{o}}_{238\mathrm{U-FORMATION.B}} \\ + \dfrac{\lambda_{234\mathrm{U}}\lambda_{230\mathrm{Th}}}{(\lambda_{234\mathrm{U}} - \lambda_{230}Th)(\lambda_{226\mathrm{Ra}} - \lambda_{230\mathrm{Th}})} \mathrm{N}^{\mathrm{o}}_{234\mathrm{U-FORMATION.B}} + \dfrac{\lambda_{230}}{(\lambda_{226\mathrm{Ra}} - \lambda_{230\mathrm{Th}})} \mathrm{N}^{\mathrm{o}}_{230\mathrm{Th-FORMATIO\ \ .B}} \end{array}\right]\left(\mathrm{e}^{-\lambda_{230\mathrm{Th}}\mathrm{t}}\right) \\
& + \left[\begin{array}{c} \dfrac{\lambda_{238\mathrm{U}}\lambda_{234\mathrm{U}}\lambda_{230\mathrm{Th}}}{(\lambda_{238\mathrm{U}} - \lambda_{226}Ra)(\lambda_{234\mathrm{U}} - \lambda_{226}Ra)(\lambda_{230\mathrm{Th}} - \lambda_{226}Ra)} \mathrm{N}^{\mathrm{o}}_{238\mathrm{U-FORMAT\ \ \ .B}} \\ + \dfrac{\lambda_{234\mathrm{U}}\lambda_{230\mathrm{Th}}}{(\lambda_{234\mathrm{U}} - \lambda_{226}Ra)(\lambda_{230\mathrm{Th}} - \lambda_{226\mathrm{Ra}})} \mathrm{N}^{\mathrm{o}}_{234\mathrm{U-FORMATION.B}} \\ + \dfrac{\lambda_{230\mathrm{Th}}}{(\lambda_{230\mathrm{Th}} - \lambda_{226\mathrm{Ra}})} \mathrm{N}^{\mathrm{o}}_{230\mathrm{Th-FORMATIO\ \ .B}} + \mathrm{N}^{\mathrm{o}}_{226\mathrm{Ra-FORMA\ \ \ .B}} \end{array}\right]\left(\mathrm{e}^{-\lambda_{226\mathrm{Ra}}\mathrm{t}}\right)
\end{aligned}$$

Where $N^{o}_{238U-FORMATION.B}$, $N^{o}_{234U-FORMATI \quad .B}$, $N^{o}_{230Th-FORMATION.B}$, $N^{o}_{226Ra-FORM \qquad .B}$, and $N^{o}_{228Ra-FLUID.A}$ were determined as follows:

- $N^{o}_{232Th-FORMAT \quad .B,}$ $N^{o}_{238U-FORMATIO \ .B}$,

  $N^{o}_{234U-FORMATION.B}$, $N^{o}_{230Th-FORMAT \quad .B}$, $N^{o}_{226Ra-FORMATI \quad .B}$= Median whole rock concentration in the Union Springs Formation in Core 1, as measured by ED-XRF in mg/kg, and converted to mols of the respective parent by dividing by the atomic mass of the parent, subsequently converted to atoms of the parent by multiplying by Avogadro's number.
- $N^{o}_{226Ra-FORMATIO \ .B}$= number of ^{226}Ra atoms in secular equilibrium with $N^{o}_{238U-FORMATIO \ .B}$.
- $N^{o}_{226Ra-FLUI \ .A}$ = ^{226}Ra activity (pCi/L) in produced water from the Onondaga Limestone, as reported in Rowan et al. 2011, converted to number of ^{228}Ra atoms by dividing by $\lambda_{228\text{Ra}}$.

^{87}SR/^{86}SR RESULTS OF AQUEOUS SEQUENTIAL EXTRACTION OF CORE/CUTTING SAMPLES

The ^{87}Sr/^{86}Sr results of the four-step aqueous sequential extraction procedure of eight core or cuttings samples are shown in Figure S4. As described in Stewart et al. (2015) the sequential extraction procedure targets different relatively accessible fractions of the samples, with ultrapure water targeting pore water and water-soluble salts (H_2O soluble), 1M ammonium acetate targeting exchangeable cations and interlayer cations from low-charge clay structures, 1M acetic acid targeting carbonate minerals, and 0.1 hydrochloric acid targeting acid-soluble phases. An additional subset of 13 core or cuttings samples were only subjected to the first two steps of the four-step extraction procedure above; the ^{87}Sr/^{86}Sr results for leachates of these samples, as well as those shown in Figure B.4, are provided in Table 3.2.

Trends in ^{87}Sr/^{86}Sr ratios in sequential extractions in this study are similar to those observed by Stewart et al. (2015). Specifically, the ultrapure water (H_2O soluble) leachate exhibits higher or equal ^{87}Sr/^{86}Sr ratios to the ammonium acetate (exchangeable fraction) leachate, which in turn exhibits higher ^{87}Sr/^{86}Sr ratios than the acetic acid (carbonate minerals) leachate. Lastly, the hydrochloric acid leachate (acid-soluble phases) largely exhibits an increase in the ^{87}Sr/^{86}Sr ratio, with the exception of two samples that show a decreasing ratio.

Both the water and ammonium acetate leachates exhibit a range of ^{87}Sr/^{86}Sr ratios (0.70990 to 0.71159, and 0.70892 to 0.71160, respectively) within those of Marcellus produced waters (Figure 3.11), suggesting that the ^{87}Sr/^{86}Sr composition of water-soluble and exchangeable fraction of the sampled formations are largely consistent with the ^{87}Sr/^{86}Sr composition of formation fluids produced in Marcellus Shale gas wells.

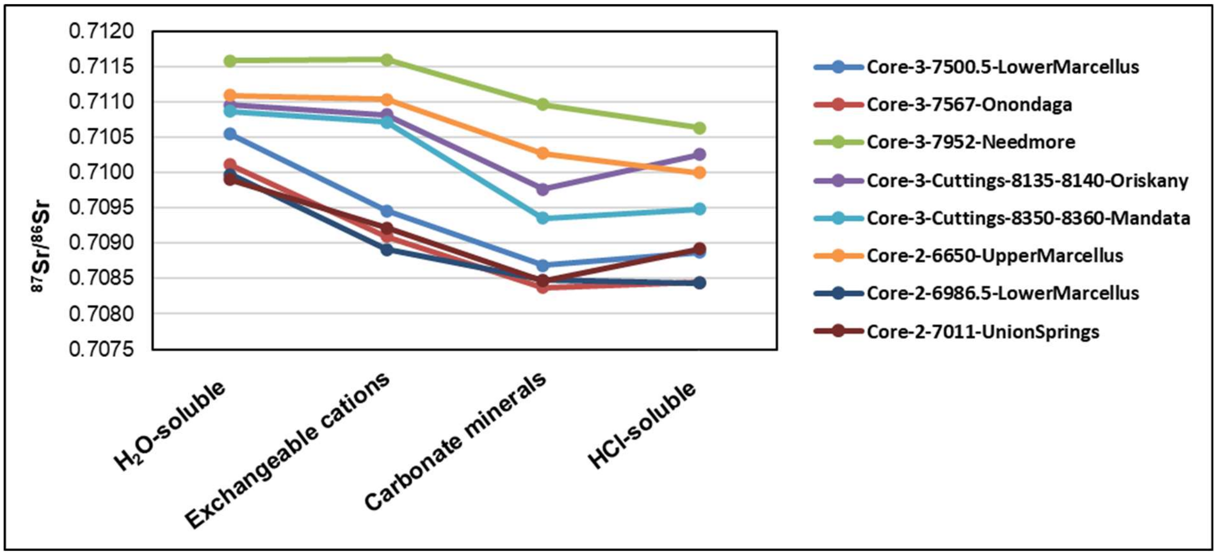

Figure B.4: $^{87}Sr/^{86}Sr$ of sequential leachates of Marcellus Shale and adjacent units. 2σ errors for $^{87}Sr/^{86}Sr$ are smaller than symbol (<±0.00002).

References

Balashov, V.N., Engelder, T., Gu, X., Fantle, M.S., Brantley, S.L., 2015. A model describing flowback chemistry changes with time after Marcellus Shale hydraulic fracturing. Am. Assoc. Pet. Geol. Bull. 99, 143–154. https://doi.org/10.1306/06041413119

Blondes, M.S., Gans, K.D., Engle, M.A., Kharaka, Y.K., Reidy, M.E., Saraswathula, V., Thordsen, J.J., Rowan, E.L., Morrissey, E.A., 2019. U.S. Geological Survey National Produced Waters Geochemical Database v2.3 [Data set]. U.S. Geological Survey [WWW Document]. USGS Data Source. https://doi.org/10.5066/F7J964W8

Gu, X., Cole, D.R., Rother, G., Mildner, D.F.R., Brantley, S.L., 2015. Pores in Marcellus Shale : A Neutron Scattering and FIB-SEM Study. Energy Fuels 29, 1295–1308.

https://doi.org/10.1021/acs.energyfuels.5b00033

Kendall, C., Coplen, T.B., 2001. Distribution of oxygen-18 and deuteriun in river waters across the United States. Hydrol. Process. 15, 1363–1393. https://doi.org/10.1002/hyp.217

Landis, J.D., Sharma, M., Renock, D., Niu, D., 2018. Rapid desorption of radium isotopes from black shale during hydraulic fracturing. 1. Source phases that control the release of Ra from Marcellus Shale. Chem. Geol. 496, 1–13. https://doi.org/10.1016/j.chemgeo.2018.06.013

Rowan, E.L., Engle, M.A., Kraemer, T.F., Schroeder, K.T., Hammack, R.W., Doughten, M.W., 2015. Geochemical and isotopic evolution of water produced from Middle Devonian Marcellus shale gas wells, Appalachian Basin, Pennsylvania. Am. Assoc. Pet. Geol. Bull. 99, 181–206. https://doi.org/10.1306/07071413146

Stewart, B.W., Chapman, E.C., Capo, R.C., Johnson, J.D., Graney, J.R., Kirby, C.S., Schroeder, K.T., 2015. Origin of brines, salts and carbonate from shales of the Marcellus Formation: Evidence from geochemical and Sr isotope study of sequentially extracted fluids. Appl. Geochemistry 60, 78–88. https://doi.org/10.1016/j.apgeochem.2015.01.004

Welch, S.A., Sheets, J.M., Daly, R.A., Hanson, A., Sharma, S., Darrah, T., Olesik, J., Lutton, A., Mouser, P.J., Wrighton, K.C., Wilkins, M.J., Carr, T., Cole, D.R., 2021. Comparative geochemistry of flowback chemistry from the Utica/Point Pleasant and Marcellus formations. Chem. Geol. 564. https://doi.org/10.1016/j.chemgeo.2020.120041

Vita

Lisa J. Molofsky completed her Bachelor of Arts in Earth and Planetary Sciences at Washington University in St. Louis in 2005. She later completed her Master of Science in Geochemistry at the University of Arizona in 2009, where she was a National Science Foundation IGERT fellow. Her M.S. research focused on the application of isotope geochemistry to determining the provenance of metals. In 2009, she joined GSI Environmental Inc. in Houston, Texas where she has worked for over a decade as a Professional Geologist in the practice area of forensic geochemistry. Specifically, she focused on the application of chemical and isotopic data to evaluate the origins of natural gas and salinity in groundwater, as well as associated risks and response actions. In 2020, she began her Ph.D. studies in Geological Sciences with Dr. Mark Engle at the University of Texas at El Paso. Her research centered on isotopic tools to decipher fluid origin, movement, and transformation in hydrocarbon-bearing sedimentary basins. She received her Ph.D. in May 2023.

Contact Information: Lisa.Molofsky@gmail.com